Defining the Multiscale Relationship between Subject-Specific Bone Strain and Structural Adaptation in the Distal Radius of Women

A Dissertation
Submitted to the Faculty of
WORCESTER POLYTECHNIC INSTITUTE
in Partial Fulfillment of the Requirements for the Degree of
DOCTOR OF PHILOSOPHY
in Biomedical Engineering

July 27th 2020

By:

Megan E. Mancuso

Approved by:

_____

Karen L. Troy, PhD
Associate Professor, Advisor
Biomedical Engineering
Worcester Polytechnic Institute

_____

Kristen L. Billiar, PhD
Professor, Department Head
Biomedical Engineering
Worcester Polytechnic Institute

_____

Songbai Ji, PhD
Associate Professor
Biomedical Engineering
Worcester Polytechnic Institute

_____

Nima Rahbar, PhD
Associate Professor
Civil & Environmental Engineering
Worcester Polytechnic Institute

_____

Julie Hughes, PhD
Research Physiologist
U.S. Army Research Institute
of Environmental Medicine

Acknowledgements

Thank you to my advisor, Dr. Karen Troy, for your mentorship over the past five years. Thank you for the opportunity to work on this exciting project, and for your consistent guidance, encouragement and patience. I am grateful to have an advisor invested in her students' success, and will carry all I have learned working with you throughout my career. I would also like to thank the members of my dissertation committee, Dr. Kristen Billiar, Dr. Songbai Ji, Dr. Nima Rahbar, and Dr. Julie Hughes, for their insight in developing this dissertation project.

I would like to thank all of the women who participated in the clinical trial at the foundation of this dissertation. Thank you to Dr. Joshua Johnson, Dr. Tiffiny Butler, and Sabahat Ahmed, PharmD, who I had the pleasure of working with directly on the study, as well as Michael DiStefano, Tyler Marshall, Aaron Rosenthal, Nicole Zaino, Julie Tevenan, and other students who worked on several aspects of this project. Thank you to Dr. Chris Nycz and Tess Meier for their help and expertise in the motion capture study. I would also like to thank the WPI Academic and Research Computing team, especially Dr. Spencer Pruitt and James Kingsley, for their consulting and technical support in high performance computing.

Thank you to all past and present members of the Musculoskeletal Biomechanics Lab, especially Dr. Joshua Johnson and Dr. Ying Fang. Joshua, your patience and generosity with your time were invaluable and immensely appreciated. Ying, thank you for being a great role model as well as a dear friend.

I want to thank all of the WPI graduate students who have become lifelong friends and made Gateway feel like home. Special thanks to Michelle McKee, who shared both Gateway and our apartment as home for three years and made both a lot more special.

Thank you to Dr. Jennifer Currey, my undergraduate research mentor at Union College, who sparked my captivation with bone adaptation as a sophomore and gave me the confidence to pursue a PhD.

Lastly, thank you to my friends and family, especially my parents Richard and Susan, and my fiancée Zachary, for your endless love and support. I could not have done this without you.

Table of Contents

Table of Figures

Table of Tables

List of Abbreviations and Symbols

armBLI	arm bone loading index
aBMD	areal bone mineral density
BLHQ	bone loading history questionnaire
BMC	bone mineral content
BMD	bone mineral density
BSI	bending strength index
BV	bone volume
BV/TV	bone volume fraction
CSA	cross-sectional area
CSI	compressive strength index
CT	computed tomography
Ct.BMD	cortical bone mineral density
Ct.Po	cortical porosity
Ct.Th	cortical thickness
CV	coefficient of variation
DXA	dual energy X-ray absorptiometry
ε_{eeq}	energy equivalent strain
FE	finite element
GRF	ground reaction force
HRpQCT	high resolution peripheral quantitative computed tomography
Micro-CT	micro-computed tomography
Micro-FE	micro-finite element
ND	non-dominant
RMSE	root mean square error
QCT	quantitative computed tomography
SD	standard deviation
SEM	standard error of the mean
Tb.BMD	trabecular bone mineral density
Tb.BMDinn	inner trabecular bone mineral density
Tb.BMDmeta	outer trabecular bone mineral density
Tb.N	trabecular number
Tb.Th	trabecular thickness
Tt.BMD	total bone mineral density
UD	ultradistal
vBMD	volumetric bone mineral density

Abstract

Over 1.5 million osteoporotic bone fractures occur each year in the United States, with annual treatment costs predicted to exceed $25.3 billion by 2025. Osteoporotic fractures are associated with skeletal fragility resulting from low bone mass and microstructural bone deterioration. While existing drug therapies slow bone loss, they cannot fully restore bone structure. Therefore, is it more effective to maximize peak bone mass in early adulthood, with each 1% increase in peak bone mass estimated to provide 1.3 years of osteoporosis-free life. Exercise is a potentially safe and cost-accessible strategy for increasing bone mass and preventing fractures. Several in vivo animal loading models have demonstrated that bone adapts to mechanical loading, with bone formation occurring in proportion to bone strain (relative deformation). In humans, elite athletes experience site-specific skeletal adaptations, and have higher bone density than their peers. Clinical studies have shown that high-impact and resistive exercise generally leads to consistent, modest increases in bone density. However, there are no evidence-based bone loading targets or methods to tune interventions for individuals. This is largely due to a lack of data relating human bone adaptation to bone strain, which is challenging to estimate non-invasively.

This Dissertation used an upper extremity bone loading model to establish quantitative relationships between bone strain and adaptation in the distal radius of healthy adult women. This was accomplished using a 12-month randomized controlled trial, in which participants performed a voluntary, cyclic forearm loading task or served in a control group. Computed tomography (CT) and high resolution peripheral quantitative CT (HRpQCT) were used to measure changes in bone structure and generate participant-specific finite element (FE) models to estimate bone strain during simulated forearm loading. We found that average changes in bone

structure parameters were correlated to a mechanical loading dose considering bone strain magnitude, strain rate, and number of loading sessions. Additionally, we observed at the microstructural level significant spatial relationships between low bone strain and bone resorption, and between high strains and both formation and resorption. Finally, we developed a forward simulation of strain-driven adaptation and compared predicted changes to experimentally measured bone adaptation. Overall, we have established a combined experimental-computational approach to systematically study the mechanism of human bone adaptation and inform the design of exercise interventions for the prevention of fractures.

Chapter 1: Introduction

Fragility bone fractures are experienced by 1 in 3 women over age 50 (Melton, 1995), leading to loss of mobility, extended hospital stays, and increased risk of death (U.S. Dept. of HHS, 2004). These low energy injuries are associated with osteoporosis, characterized by low bone density and deterioration of bone structure. Over 55 million Americans over age 50 have low bone density (Looker et al., 2017), and this number is expected to grow with the aging population. Several drug therapies are approved to treat low bone density, but concerns about side effects limit widespread use, and targeting high-risk individuals before they fracture is challenging (Schuit et al., 2004; Sornay-Rendu et al., 2005). Additionally, most drug therapies slow bone loss but cannot regain lost bone, and newer anabolic therapies cannot fully restore bone structure. Therefore, maximizing peak bone mass in early adulthood and maintaining healthy bone mass later in life is more effective than treating bone loss after it occurs. In fact, it has been predicted that increasing peak bone mass by just 1% provides up to 1.3 years of osteoporosis-free life (Hernandez et al., 2003).

Exercise is a potentially cost-effective, non-pharmacologic strategy for stimulating bone formation and preventing fractures. Elite athletes have improved bone density and structure compared to their peers (Bareither et al., 2008; Stewart and Hannan, 2000), and these benefits are sustained after retirement (Erlandson et al., 2012). Additionally, elite athletes experience site-specific adaptations, such as increased cortical thickness in the racquet arms of tennis players (Kontulainen et al., 2003) or throwing arms of baseball pitchers (Warden et al., 2019), suggesting that skeletal benefits can be attributed mechanical loading. In normal healthy adults, clinical exercise trials have shown that high-impact and resistive loading interventions elicit consistent, modest (~1-3%) increases in bone density at the hip (Ireland and Rittweger, 2017; Zhao et al.,

2017). However, there are no evidence-based targets for an optimal bone loading "dose" or methods to tune exercise interventions for individual patients.

A substantial effort has been made to develop effective bone-building exercises for the prevention of fragility fractures. This has consisted of mechanistic studies in animal models, as well as clinical exercise trials and observational studies in humans. In vivo animal loading models have been used to apply known, repeatable mechanical stimuli to bone and systematically quantify the relationship between specific loading parameters and adaptation. Models applying cyclic compressive loading to the turkey ulna (Lanyon and Rubin, 1984), rat ulna (Mosley et al., 1997), mouse tibia (De Souza et al., 2005), and other sites, have shown that the volume of loading-driven bone formation increases with bone strain magnitude (Rubin and Lanyon, 1985), rate (Mosley and Lanyon, 1998; Turner et al., 1995), and spatial gradient (Gross et al., 1997; Judex et al., 1997). These parameters of bone strain have been shown to govern bone adaptation at the global (cm) and local (μm) levels (Lambers et al., 2015; Schulte et al., 2013a; Webster et al., 2015). Quantitative datasets generated from bone loading animal models have been used to establish mathematical models of load-driven bone adaptation (Turner, 1998), which have been implemented with finite element (FE) modeling to drive predictive simulations of how bone changes in response to new loads (Fyhrie and Carter, 1986; Huiskes et al., 1987; Mullender and Huiskes, 1995). Looking at human studies, measuring bone strain directly requires the surgical implantation of strain gauges on the bone surface, and is not feasible to implement clinically. Therefore, previous human exercise trials have relied on indirect surrogate measures of bone loading or not measured loading at all. The lack of standardized methods for estimating bone loading has made it challenging to directly compare and learn from previous clinical exercise studies, creating a time-consuming and expensive cycle of trial and error. Fundamentally, animal

models and human exercise trials comprise two ends of a disconnected research spectrum, where quantitative relationships between strain and adaptation in animals are not fully translated to the clinic. Thus, there is a clear need for human bone loading models based on measures of bone strain and loading dose relevant to the biological mechanism of adaptation.

Previous work in the Musculoskeletal Biomechanics Laboratory established an upper-extremity human bone loading model. The primary goals of such a model are to deliver a diverse range of bone strain signals that can be quantified non-invasively and elicit measureable changes in bone structure. Our loading model uses a simple loading task, leaning on and off the palm of the hand, to deliver axial, compressive, and voluntary loading to the distal radius bone (Troy et al., 2013). The radius is appropriate because it is a clinically relevant fracture site (Nellans et al., 2012), and the distal radius can be scanned using the three most common bone imaging modalities: dual-energy X-ray absorptiometry (DXA), clinical resolution computed tomography (CT), and high resolution peripheral quantitative CT (HRPQCT). These imaging techniques can be used to measure regional and local adaptation of bone structure, and serve as the basis for image-based, patient-specific FE models. FE modeling is a numerical technique that enables computational stress analysis of structures, such as bone, with complex geometries and materials. When validated against cadaveric mechanical testing, FE models explain 60-94% of the variability in human bone strain (Anderson et al., 2005; Bhatia et al., 2014; Edwards et al., 2013; Fung et al., 2017; Gupta et al., 2004; Keyak et al., 1993). In our lab, Bhatia et al. (2014) and Johnson et al. (2017) developed and validated methods to estimate radius bone strain using FE models based on clinical resolution CT only and combining clinical CT and HRPQCT, respectively (Bhatia et al., 2014; Johnson and Troy, 2017a). These FE models can be applied to assign participant-specific target forces to achieve desired bone strains, as well as determine actual achieved bone strain based on real force

measurements. This is accomplished using a custom loading device that guides applied force via LED biofeedback, guides loading rate using auditory cues, and records applied force using a data logger. Therefore, our approach allows bone strain to be assigned, monitored, and correlated to structural bone changes within individual human participants. In an in vivo pilot study, nineteen women performed loading three days per week for twenty-eight weeks, and it was shown that loading led to small increases in bone mineral content and protection against bone losses observed for the non-loading control group (Troy et al., 2013). Additionally, it was shown using clinical resolution CT that regional changes in bone density were positively correlated with bone strain magnitude (Bhatia et al., 2015). These studies provided important preliminary evidence of the role bone strain plays in human bone adaptation.

The primary purpose of this Dissertation is to establish quantitative relationships between bone adaptation and bone strain magnitude, rate, and spatial gradient, at the macro- and microstructural levels, in the upper extremity of young healthy adult women. Additionally, we aim to develop a predictive bone adaptation simulation, driven by these quantitative relationships, with the long-term goal of designing improved bone-building interventions in silico. The foundation of this project is a 12-month randomized controlled trial in which participants performed axial forearm loading or served as non-loading controls. The mechanical strain stimulus within the radius bone was estimated using participant-specific FE models generated from density-calibrated CT scans with boundary conditions based on load cell recordings. Changes in radius bone structure were measured using CT and HRpQCT. The project objective was accomplished in the following three *Specific Aims*:

Aim 1: Quantify the relationship between mechanical loading history, bone structure, and FE-estimated bone strain in the human forearm.

The purpose of Aim 1 was to understand the factors influencing bone structure and strain using a cross-sectional analysis at baseline of the parent study. Second, we wanted to assess the ability of DXA to predict the between-participant variability in bone strain. Forearm loading history was quantified using a physical activity questionnaire, grip strength, and body mass. Bone structure was measured using DXA, quantitative CT, and HRPQCT, and CT-based FE models estimated bone strain under an arbitrary 300N force. We hypothesized that higher levels of mechanical loading would be associated with favorable bone structure and lower strain under a given force, and that bone density will not fully predict the observed variability in bone strain.

Aim 2: Quantify the effect of strain magnitude, rate, and spatial gradient on 12-month changes in bone macro- and microstructure in the distal radius.

Aim 2A: Relate changes in average bone macro- and microstructure in the distal radius to strain.

The purpose of Aim 2A, which comprised the primary analysis of the parent study, was to compare 12-month changes in bone structure between loading groups with varying target strain magnitudes and rates to the control group. Additionally, we related bone changes to achieved loading dose, based on participant-specific load cell recordings, across all participants. Bone changes were measured as change in average parameters measured using QCT and HRpQCT for the entire distal radius. We hypothesized that higher bone strain magnitude, rate, and protocol compliance would be associated with a greater adaptive response.

Aim 2B: Relate changes in bone microstructure to local strain parameters at the individual trabecular level.

The purpose of Aim 2B was to investigate the mechanism of bone adaptation by locally relating strain and adaptation. Image registration of baseline and 12-month HRpQCT scans was used to

identify local regions of bone formation and resorption, and multiscale FE models were used to calculate microstructural strain parameters during forearm loading. We hypothesized that bone strain magnitude and spatial gradient would be higher in regions of formation and lower in regions of bone resorption. Additionally, we hypothesized that formation would be more likely to occur near high versus low strain regions, and resorption near low versus high strain regions.

Aim 3: Develop a forward bone adaptation simulation for the human forearm loading model.

The purpose of Aim 3 was to establish an in silico simulation of load-driven bone adaptation, with a particular focus on the influence of boundary conditions. The variability in loading direction during the forearm loading task was quantified using three dimensional motion capture, and the influence of varying loads within the measured range on FE-estimated bone strain was quantified using a sensitivity analysis. Bone adaptation predictions from the in silico simulation, driven by FE strain with axial and tilted boundary conditions, were compared to experimentally measured changes. We hypothesized that the adaptation simulation would predict similar trabecular changes to those measured experimentally, and that boundary conditions would have a significant influence on FE-estimated strain and predicted adaptation.

This work represents an important step toward establishing an integrative, experimental-numerical pipeline to systematically study the mechanism of strain-driven bone adaptation. Our approach can be generalized to other activities, skeletal sites, and clinical populations. Long-term, estimating the osteogenic potential of activities *a priori* will avoid the trial-and-error approach to exercise trial design, lowering research costs and accelerating the translation of patient-specific prescription to the clinic.

Chapter 2: Background

2.1 Clinical Significance

Fragility bone fractures present a major clinical burden worldwide, affecting one in three women and one in five men over age fifty (Melton, 1995). It is estimated the 1.5 million osteoporotic fractures occur in the United States each year (Riggs and Melton, 1995), typically at the hip (proximal femur), spine (vertebrae), or wrist (distal radius). The annual direct cost of treating these fractures in the United States is approximately $17.9 billion as of 2002 (U.S. Dept. of HHS, 2004), and is predicted to exceed $25.3 billion by 2025 (National Osteoporosis Foundation, 2008). Fragility fractures disproportionately affect older individuals, which is particularly concerning in the context that the number of Americans over age 85 is expected to increase from 4 to 20 million between 2000 and 2050 (U.S. Dept. of HHS, 2004). Importantly, individuals who experience fractures often have worse health outcomes than their non-fractured peers: mortality is 2.8-4 times greater the first 3 months after a hip fracture (U.S. Dept. of HHS, 2004), and 20% of hip fracture patients require long-term care in nursing facilities (Salkeld et al., 2000).

Fragility fractures are low energy injuries resulting from a fall at standing height or lower. They are generally associated with osteoporosis, the deterioration of bone structure leading to increased skeletal fragility (Cosman et al., 2014). The World Health Organization (WHO) defines osteoporosis based on bone mineral density at the spine (lumbar vertebrae) or hip (proximal femur). Density is measured using dual energy X-ray absorptiometry (DXA), which generates a two-dimensional image from which bone area and bone mineral content are measured to calculate areal bone mineral density (aBMD, in g/cm^2). Density is converted to a statistical T-score comparing a patient to population data from healthy women ages 20-29, with a

T-score less than -2.5 indicating osteoporosis. It is estimated that 12 million (11%) Americans over age 50 meet the WHO diagnostic criteria of osteoporosis and another 47 million (45%) have low bone density. Prevalence is higher in women than men, with 16.5% of women versus 5.1% of men over age fifty having osteoporotic bone density (Looker et al., 2017).

While osteoporosis is associated with increased fracture risk at the population level, it is challenging to predict patient-specific fracture risk based on DXA. In fact, aBMD explains less than sixty percent of the variability in bone strength, and more than half of fragility fractures occur in individuals who do not meet the WHO bone density criteria for osteoporosis (Schuit et al., 2004; Sornay-Rendu et al., 2005). While drug therapies are available to treat bone loss, their high cost and potential side effects limits widespread use. Therefore, only high-risk patients receive therapies and, despite its shortcomings, DXA is typically used to decide who is treated. This has led to a situation where many people at a high risk of fracture go untreated. Additionally, the most commonly prescribed drug class, antiresorptives, slow bone loss but cannot regain lost bone. Newer anabolic therapies show potential to increase bone mass but cannot fully restore bone structure, limiting efficacy in improving bone strength. Clearly, there is a need for prevention strategies that minimize bone loss before it happens, and are safe and inexpensive enough for all individuals.

2.2 Definition of Bone Quality and Strength:

Bone fractures occur when applied loads exceed whole bone strength, and therefore maximizing bone strength is a key component of fracture prevention. Bone must be able to withstand high magnitude, high energy (impact), and repetitive loading at a minimal metabolic cost, requiring a material that is stiff, tough, and light. Bone tissue is a composite of hydroxyapatite mineral crystals bound to an organic matrix of type 1 collagen, proteoglycans,

and other proteins (Cowin, 2001). The mineral provides stiffness and compressive strength, and the organic components provide flexibility and toughness. The basic building blocks of the organic matrix are triple helix tropocollagen molecules that polymerize to form aligned collagen fibrils approximately 100 nm in length (Sabet et al., 2016). Hydroxyapatite mineral crystals form between adjacent collagen molecules. At the microscale, aligned collagen fibers form lamellar sheets 3-7 μm thick (Sabet et al., 2016), which are layered to form concentric osteons (200-300 μm diameter) in cortical bone and trabecular packets (50 μm thick) in trabecular bone (Sabet et al., 2016). Cortical bone forms the dense shaft and outer shell of long bones. Trabecular bone forms an interconnected lattice of individual struts, or trabeculae. Trabecular bone is found at the ends of long bones because its structure allows for absorption and transmission of joint loads away from the articular surface towards the cortex (Figure 2.1). The periosteal surface defines the outer boundary of the cortical shell, and the endocortical surface is the interface between the inner cortical boundary and trabecular compartment.

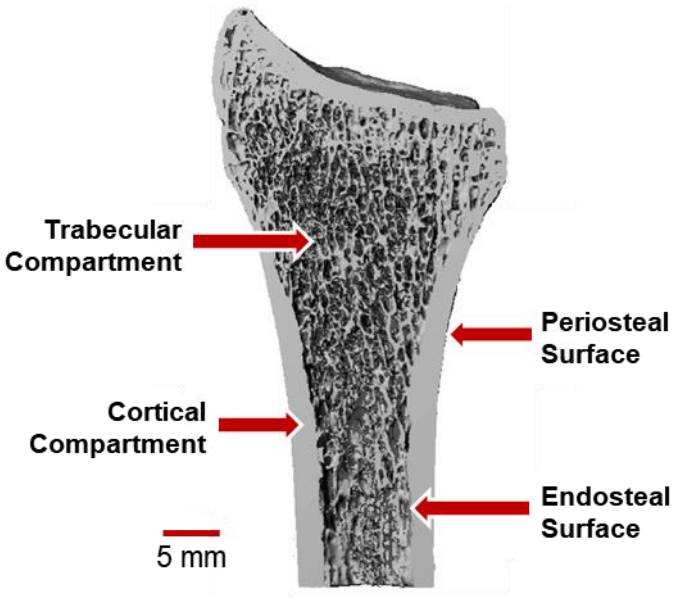

Figure 2.1: Definition of the trabecular and cortical bone compartments, shown for the distal radius bone in the forearm. The periosteal surface forms the outer bone surface, while the endosteal surface separates the cortical shell from the spongey trabecular compartment. Adapted from MacNeil (2008) *Bone.*

Bone strength is determined by the material properties, structure, and amount of tissue present. Tissue material properties reflect the composition and quality of the collagen and mineral composite, which depends on several factors. Enzymatic crosslinking of the collagen network prevents fibers from freely sliding, provides matrix stability, and contributes to bone stiffness. However, as bone matures, detrimental non-enzymatic crosslinks, referred to as advanced glycation end-products (AGEs), accumulate and decrease toughness (Poundarik et al., 2015; Willett et al., 2013). Heterogeneity in collagen fiber orientation between lamellar sheets and differences in mineralization between older and newer osteons increase fracture toughness by preventing crack propagation (Goff et al., 2015; Jimenez-Palomar et al., 2015; Torres et al., 2016). The amount of free and bound water within bone tissue also affects bone mechanical properties, with bound water in particular shown to be positively related to post-yield properties (Unal and Akkus, 2015). The size, maturity, and purity of mineral crystals also likely have an

influence on bone strength, but this relationship is not yet understood (Unal et al., 2018). Looking toward clinical measurement of bone tissue properties, microindentation is a relatively new technique that measures local (~350 μm) cortical bone stiffness in vivo at sites with minimal soft tissue such as the anterior tibia shaft. The Bone Material Strength index (tip depth in bone/tip depth into reference material) measured by the OsteoProbe indenter has been shown to be significantly lower for individuals with history of fragility fractures versus non-fractured controls (Rozental et al., 2018; Schoeb et al., 2020), but requires further validation.

Bone structure describes the geometric distribution of tissue within a bone. At the macrostructural level, cortical bone mechanics depend heavily on the inner and outer diameter, which together determine cortical thickness, area, and cross-sectional moment of inertia. Cortical thickness and area contribute to compressive and tensile stiffness, which is proportional to cross-sectional area (CSA). Cross sectional moment of inertia, which increases as material is distributed further from the neutral axis of the bone, is related to stiffness under bending loads. Given a constant CSA, a thinner cortex with greater inner and out diameter is better adapted to resist bending than a smaller bone. Cortical area and cross sectional moment of inertia have been shown to be significantly compromised in women with distal radius fracture versus non-fractured individuals (Schneider et al., 2001). Cortical bone microstructure is often described in terms of cortical porosity (Ct.Po; %), which increases with age (Bjørnerem et al., 2018; Vilayphiou et al., 2016), is inversely related to bone strength (Currey, 1988; Schaffler and Burr, 1988), and can discriminate osteopenic and osteoporotic women with and without fractures (Bala et al., 2014) (Figure 2.2). Trabecular bone structure is typically described in terms of bone volume fraction (BV/TV; %), trabecular thickness (Tb.Th; mm), and trabecular number (Tb.N; mm^{-1}). Bone volume fraction is the ratio of bone tissue volume to total volume (inclusive of marrow space).

Trabecular thickness refers to the average diameter of trabecular struts, and trabecular number is related to the number of struts within a given volume. High bone volume fraction, with high trabecular thickness and number, is indicative of a stiffer trabecular region.

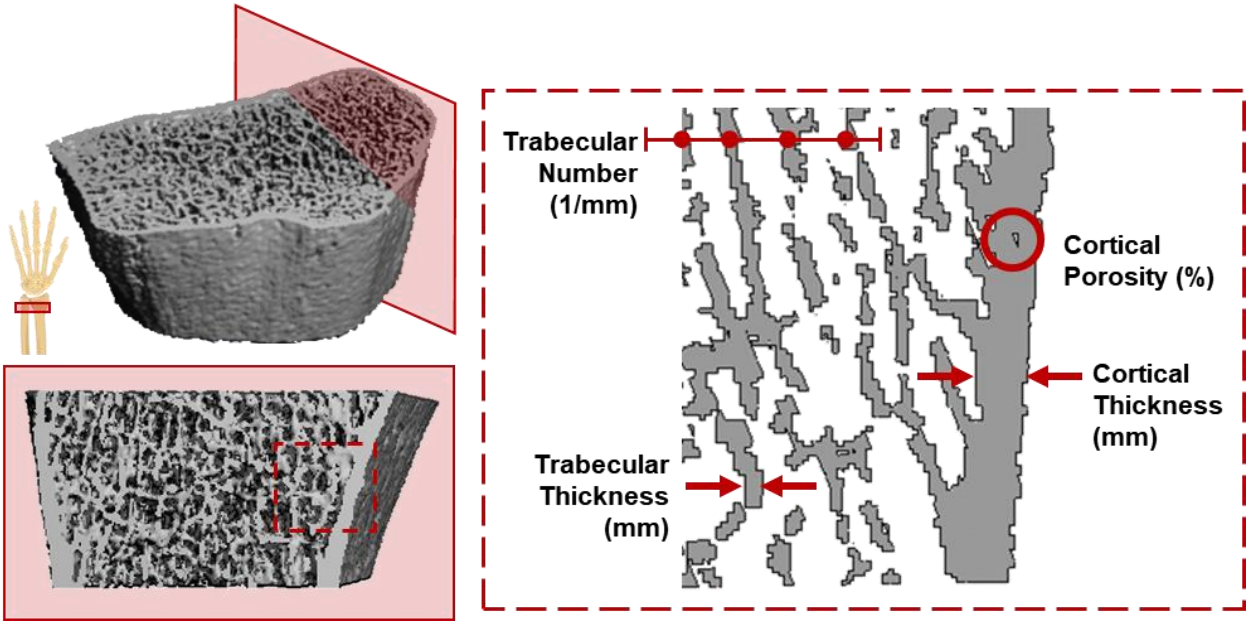

Figure 2.2: Common bone microstructure parameters used to describe trabecular and cortical bone structure. Trabecular number quantifies the number of bone struts per millimeter, and trabecular thickness reflects the average strut thickness. Cortical porosity is a relative measure of pore volume, and cortical thickness refers to the average thickness of the cortical shell.

The quantity of bone tissue is typically described in terms of bone mass or density. Bone mass reflects the total amount of mineral present within a region, and is typically referred to as bone mineral content (BMC; g). Bone density reflects the amount of mineral within a given region, normalized to the size of the region. When bone mineral density is measured using DXA, the two-dimensional image yields density in terms of mass per unit area, or areal BMD (aBMD; g/cm^2). When bone density is measured using three-dimensional imaging modalities, the result is a volumetric bone mineral density in terms of mass per unit volume (vBMD; g/cm^3). It is also important to distinguish between apparent and tissue mineral density, where apparent density refers to the average density of a region, inclusive of pores. Tissue mineral density, on the other

hand, refers to the density of mineralized tissue only, exclusive of pores. Tissue and apparent density are generally similar for cortical bone, while apparent density is much lower for trabecular bone and is driven largely by bone volume fraction.

Bone mass and strength change over the course of an individual's lifetime (Figure 2.3). Bone mass increases during childhood as the skeleton undergoes substantial growth, with 39% of mass acquired between ages 12 and 16 (Weaver et al., 2016). In women, 80-90% of lifetime bone mass is accrued by age 16 (Henry et al., 2004), and peak bone mass is achieved at the hip at age 19 and the lumbar spine at age 20 (Xue et al., 2020). Maximizing peak bone mass in early adulthood has a meaningful effect of lifetime fracture risk, with one statistical model predicting that each 1% increase in peak bone mass corresponds to a 1.3 year delay in the onset of post-menopausal osteoporosis (Hernandez et al., 2003). Peak bone mass is generally thought to be maintained into the fourth decade, but newer high resolution imaging studies suggests that deterioration of bone microstructure, especially within the trabecular compartment, may begin by age 30 (Riggs et al., 2008). Therefore, early adulthood is a critical and relevant age range for targeting interventions that increase bone strength and prevent early bone loss.

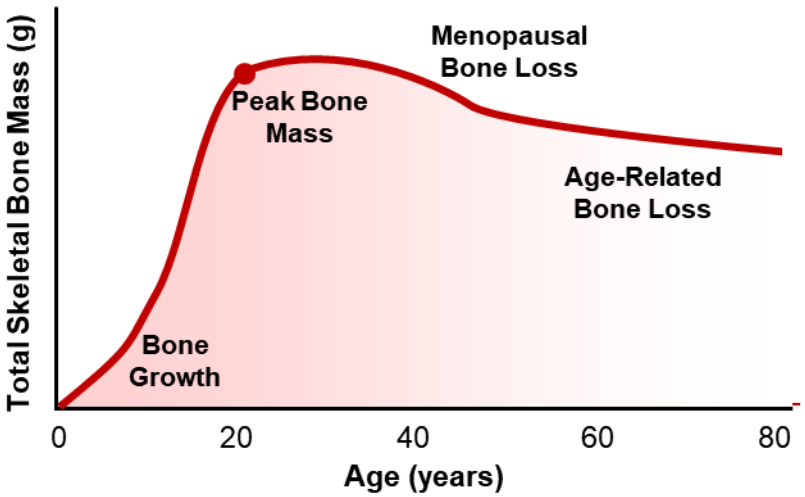

Figure 2.3: Typical lifetime trajectory of bone mass in females. Bone mineral accrual occurs during childhood and adolescence, with bone mass reaching a peak between ages 18-20. Rapid

bone loss occurs perimenopausally, followed by slower loss later in life (adapted from Weaver (2016) *Osteoporosis International*).

2.3 Assessment of Human Bone Structure via In Vivo Medical Imaging

There are several imaging modalities available clinically and/or in research settings for the visualization of human bone structure in vivo (Figure 2.4). As previously mentioned, DXA is the most widely used imaging tool for the clinical estimation of bone fracture risk. An important benefit of DXA over 3D X-ray imaging is relatively low radiation dose, which makes it safe to image central sites including the lumbar spine and proximal femur. The major limitations of DXA are lack of 3D structural information, the inability to separate cortical and trabecular compartments, and the confounding influence of bone size and shape on areal density.

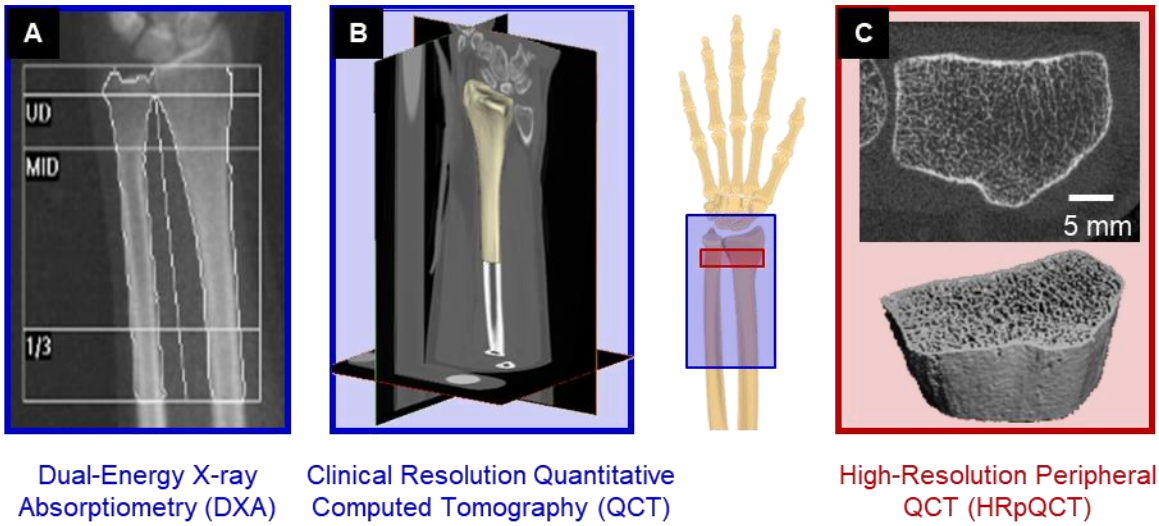

Figure 2.4: Current available methods for the assessment of bone strength and fracture risk. **(A)** DXA forearm scan with standard ultradistal (UD), middle (MID) and one-third of arm length (1/3) regions, used to calculate aBMD (g/cm^2). **(B)** Clinical CT scan of the distal radius, acquired with a transverse pixel size of 234 µm and slice thickness of 625 µm. **(C)** HRpQCT image of the distal radius, acquired with isotropic voxel size of 82 µm.

Computed tomography (CT) is a clinically available 3D imaging modality that uses X-rays to visualize bone structure in vivo (Figure 2.5). Quantitative computed tomography (QCT) analysis measures aspects of bone structure within a region of interest, and the cortical and

trabecular compartments can be assessed separately. Calibration phantoms with known potassium phosphate-equivalent density or calcium hydroxyapatite equivalent density standards can be used to calculate a linear relationship between CT attenuation values and apparent bone mineral density (Troy and Edwards, 2018). Clinical CT scans are typically acquired with an in-plane resolution and slice thickness less than 1.5 mm, enough to visualize the cortical shell but insufficient to resolve trabecular microstructure. QCT is most often used to calculate cortical and trabecular density, volume, and bone mineral content (Table 2.1). The volume of a region of interest is the product of voxel size and the number of voxels, and bone mineral content (g) is the product of average apparent density (g/cm^3) and bone volume (cm^3). Several structural indices can also be determined using QCT, including moment of inertia, compressive strength index, and bending strength index. Overall, QCT consistently outperforms DXA in estimating bone fracture strength (Cody et al., 1999; Edwards et al., 2013; Johannesdottir et al., 2017), but CT imposes a much larger ionizing radiation dose (Shepherd et al., 2015). Therefore, QCT is generally limited to research settings, but is seen as a valuable tool for clinical trials of novel pharmaceuticals because of its sensitivity to detect bone changes.

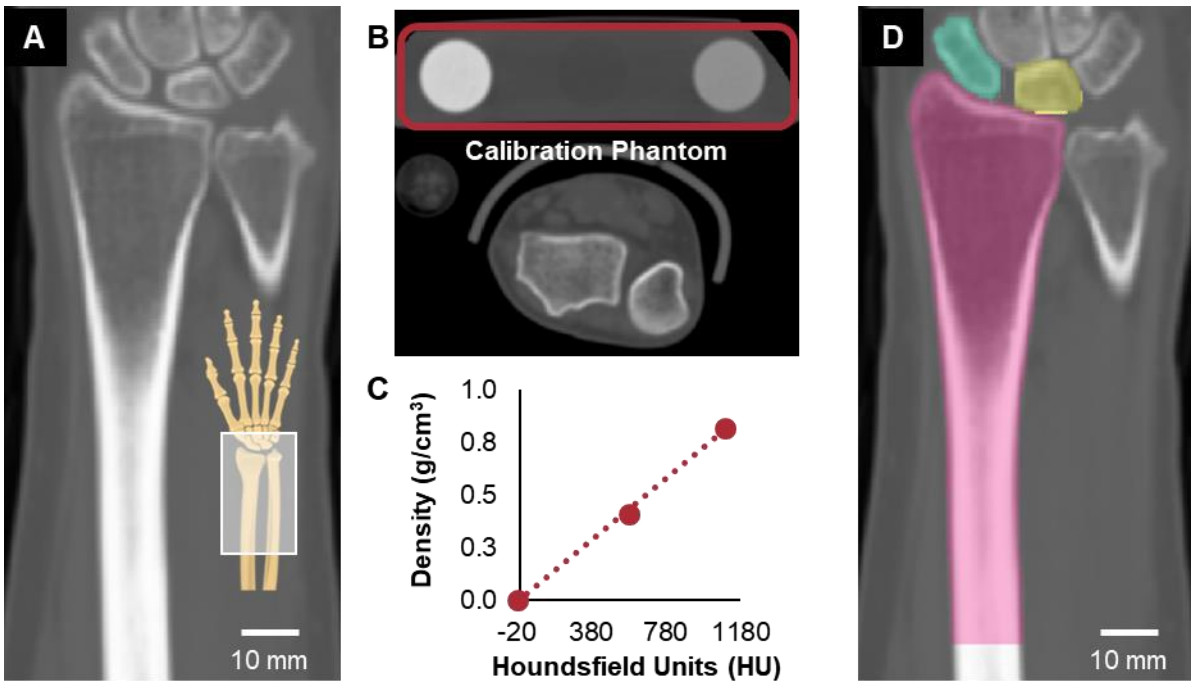

Figure 2.5: (A) Clinical resolution CT scan of the distal radius and wrist carpals, used to perform QCT analysis to measure changes in bone macrostructure, as well as generate patient-specific continuum finite element models. **(B)** A calibration phantom containing three compartments of synthetic material with known density is included in each scan. **(C)** A linear calibration equation is used to determine the CT greyvalue threshold to **(D)** segment the region of interest based on density.

Table 2.1: Common quantitative computed tomography (QCT) parameters calculated for a region of interest (ROI)

Metric	Description	Calculation
Volumetric Bone Density (vBMD; g/cm^3)	Average grey value within ROI, converted to density using calibration phantom	$vBMD = \frac{\sum_i^{n_{vox}} vBMD_i}{n_{vox}}$
Bone Volume (BV; cm^3)	Calculated from number of voxels and voxel volume within a given ROI	$BV = n_{vox} * vol_{vox}$
Bone Mineral Content (BMC; g)	Calculated from vBMD and BV for a given ROI	$BMC = vBMD * BV$
Cross-Sectional Area (CSA; cm^2)	Calculated separately for each transverse slice and averaged over ROI	$CSA = \frac{\sum_j^{n_{slice}} n_{vox,j} * area_{vox}}{n_{slice}}$
Compressive Strength Index (CSI; g^2/cm^4)	Empirical relationship considering bone density and bone size (Lang et al., 2004). Based on average area and density in transverse ROI	$CSI = CSA * vBMD^2$
Bending Strength Index (BSI; cm^3)	Effective polar moment of inertia (Corcoran et al., 1994) normalized to bone size (Lang et al., 2004). Calculated separately for each transverse slice and averaged over ROI. Assumes bone cross-section can be approximated as a circle	$BSI = \frac{\sum_j^{n_{slice}} \frac{(I_{x,j}+I_{y,j})}{W_j}}{n_{slice}}$, where $I_{x,j} = \frac{1}{e_b}\sum_i e_{i,j} * \left(y_{i,j} - \bar{y}_j\right)^2 * area_{vox}$ $I_{y,j} = \frac{1}{e_b}\sum_i e_{i,j} * \left(x_{i,j} - \bar{x}_j\right)^2 * area_{vox}$ $W_j = 2 * \sqrt{\frac{CSA_j}{\pi}}$

n_{vox} : Total number of voxels in ROI

vol_{vox} : Volume of each voxel, defined by the image voxel size in the X, Y, and Z directions

n_{slice} : Total number of transverse slices in ROI

$area_{vox}$: Area of each voxel in the transverse plane

$(I_{x,j}+I_{y,j})$: Polar moment of inertia of the j^{th} transverse slice

e_b : Elastic modulus of cortical bone

$e_{i,j}$: Elastic modulus of the i^{th} voxel in the j^{th} transverse slice

$(x_{i,j},y_{i,j})$: Coordinates of the i^{th} voxel in the j^{th} transverse slice

$(\bar{x}_j, \bar{y}_j)$: Centroid of the j^{th} transverse slice

W_j : Effective diameter of the j^{th} transverse slice, assuming circular cross section

In the last two decades, high-resolution peripheral quantitative computed tomography (HRpQCT) has enabled in vivo imaging of human bone microstructure at peripheral sites (distal radius and tibia) (Laib et al., 1998). With an isotropic voxel size of 82 µm, HRpQCT is capable of resolving individual trabeculae and larger cortical pores (Figure 2.6) (Buie et al., 2007; MacNeil and Boyd, 2007). A standard HRpQCT scan consists of a stack of 110 transverse slices covering a 9.02 mm axial length. The axial scan size is limited because of long scan times (~3 minutes per stack) and large volumes of data generated for high-resolution images. It is important to note that because the image resolution is similar to that of true trabecular thickness, the built-in analysis scripts rely on assumptions for the indirect calculation of some parameters (Table 2.2) that can be directly measured from micro-CT in animals or using *ex vivo* histomorphometry of human bone biopsies. Nonetheless, HRpQCT parameters have been shown to successfully distinguish women with and without history of forearm fracture (Nishiyama et al., 2013; Sornay-Rendu et al., 2017). The newest generation of HRpQCT has a 61 µm voxel size (Manske et al., 2015), and further improvements may enable direct trabecular microstructure quantification in the future.

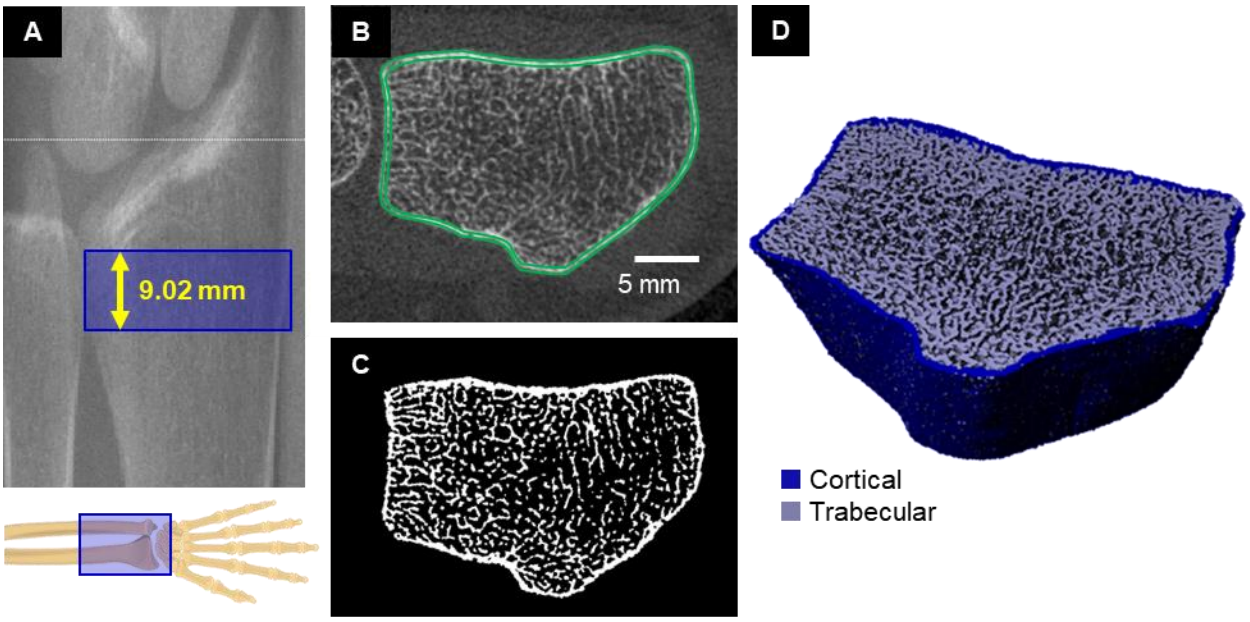

Figure 2.6: HRpQCT is used to measure changes in human bone microstructure. **(A)** A two-dimensional scout view indicating the transverse position of a standard distal radius scan, consisting of 110 slices with an isotropic voxel size of 82µm. **(B)** Transverse view of a distal radius scan, with periosteal and endosteal contours generated using the semi-automatic contouring procedure in green. **(C)** Segmented image obtained using contours, which is used to define **(D)** the cortical and trabecular compartments in three dimensions.

Table 2.2: Common HRpQCT parameters used to characterize bone microstructure at the distal radius and tibia (*Calculated using the Scanco Extended Cortical Analysis (Burghardt et al., 2010))

Parameter	Description
Total Density (Tt.BMD; g/cm^3)	Apparent density of total area within periosteal boundary, inclusive of cortical pores and marrow spaces
Trabecular Density (Tb.BMD; g/cm^3)	Apparent density of area within the endosteal boundary, inclusive of marrow spaces. Can be defined separately for the Inner (inner 60%) and Meta (outer 40%) regions
Cortical Density* (Ct.BMD; g/cm^3)	Apparent density of cortical region, inclusive of cortical porosity
Total Area (Tt.Area; mm^2)	Average cross sectional area of total area within periosteal boundary
Trabecular Number (Tb.N; mm^{-1})	Average number of trabeculae per linear mm, calculated directly using 3D ridge extraction methods (Hildebrand and Rüegsegger, 1997)
Trabecular Thickness (Tb.Th; mm)	Calculated indirectly using $Tb.Th = \frac{Tt.BMD}{1200 g/cm^3 * Tb.N}$, where 1200 g/cm^3 is the density of fully mineralized bone
Cortical Thickness* (Ct.Th; mm)	Average distance between endosteal and periosteal boundaries
Cortical Porosity* (Ct.Po; %)	Cortical pore volume normalized to the total cortical volume inclusive of pores

2.4 Bone Cells and the Dynamics of Bone Structure

Bone tissue contains cells that drive dynamic processes including growth, repair, and adaptation. There are four main cell types present in bone tissue: osteoclasts, osteoblasts, bone lining cells, and osteocytes. Osteoclasts are responsible for bone resorption. They are large (20-100 μm diameter), multinucleated cells derived from mononuclear/phagocytic cells in the bone marrow. Osteoclasts seal to the bone surface and release protons and proteolytic enzymes, forming a closed acidic microenvironment to dissolve mineral and degrade matrix proteins (Xu and Teitelbaum, 2013). Osteoblasts are responsible for bone formation. They are cuboidal cells (~10 μm in width) derived from mesenchymal stem cells that synthesize and secrete type I collagen and other proteins (Martin et al., 2015). Bone lining cells are flat, quiescent osteoblasts that form a continuous monolayer covering periosteal, endosteal, and trabecular bone surfaces. While bone lining cells do not secrete new bone, they are thought to play a role in mechanosensation and the regulation of osteoblast and osteoclast activity (Eriksen, 2010). Osteocytes, which make up 90% of bone cells, are mechanosensitive cells embedded within a complex network of bone pores. Osteocyte cell bodies reside within lacunar pores (0.5-1 μm), with cell processes extending into canalicular channels (50-100 nm) to form a communication network with nearby osteocytes and bone lining cells (Cowin, 2001; Schaffler et al., 2014). Osteocytes in the lacunar-canalicular network are surrounded by fluid, which allows for transport of metabolic and biochemical signaling molecules and generates flow-based mechanical stimuli during skeletal loading.

The collective activity of osteoblasts and osteoclasts result in bone remodeling and adaptation. In bone remodeling, osteoblast and osteoclast activity are coupled spatially and temporally, with cells working in “basic multicellular units” to resorb and replace small packets

of tissue (Martin et al., 2015). Remodeling is important for replacing older tissue with microdamage, and occurs throughout the lifespan. In healthy remodeling, bone formation and resorption are generally balanced, with no net changes in bone volume. However, there is a temporary increase in porosity and decrease in mechanical properties as formation lags behind resorption. Therefore, rapid increases in the initiation of new remodeling sites, such as during menopause, contribute to increased skeletal fragility and fracture risk. During bone adaptation, osteoblasts and osteoclasts are uncoupled, and add and remove tissue at distinct locations, resulting in net changes in bone size and shape. Bone adaptation is driven by mechanical stimuli, whereby osteocytes sense local tissue loading and recruit osteoblasts to build bone in areas of high loading and osteoclasts to areas of low loading (Figure 2.7). Adaptation can lead to net increases in bone mass, such as in response to increased physical activity, or bone loss during extended periods of bed rest, spinal cord injury, or space flight.

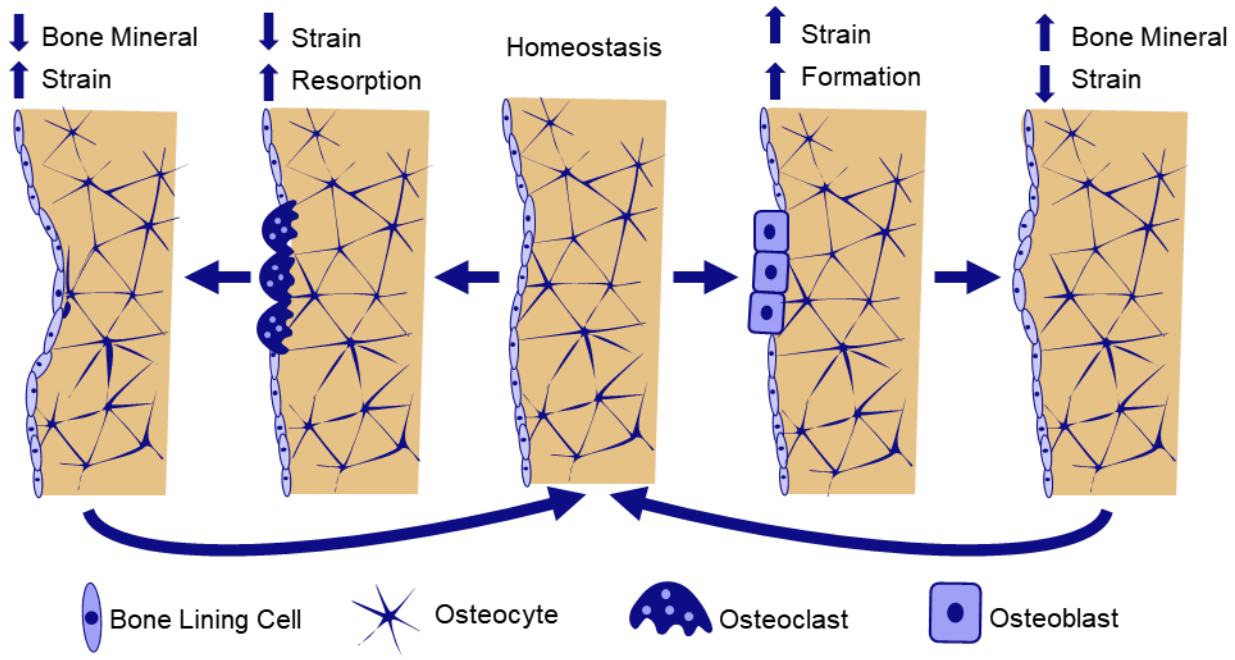

Figure 2.7: Hypothesized mechanism of strain-driven bone adaptation. Osteocyte cells embedded throughout bone tissue sense local mechanical strains. When strains are lower than the homeostatic setpoint, osteocytes release biochemical signals to recruit osteoclasts to nearby bone surfaces. Osteoclasts resorb bone, decreasing bone volume and stiffness, bringing strain back

toward homeostasis. Alternatively, when bone strains are greater than the homeostatic setpoint, osteocytes release biochemical signals to upregulate osteoblast differentiation, leading to increased bone formation. As a result, bone volume and stiffness increase, and strains decrease toward homeostasis.

Recent advances in cell culture, microscopy, and molecular biology techniques have allowed researchers to identify several mechanisms by which osteocytes sense mechanical loading and regulate adaptation. Potential mechanosensors within osteocytes include integrin proteins, primary cilia, G protein-coupled receptors, and stretch-mediated ion channels (Hughes and Petit, 2010). Once stimulated, osteocytes undergo cellular changes such as increased intracellular calcium signaling (Lewis et al., 2017) and release of adenosine triphosphate (ATP) (Kringelbach et al., 2015), nitric oxide (NO), and prostaglandins (PGE_2), which upregulate bone formation (Schaffler et al., 2014). Mechanical loading also decreases osteocyte expression of sclerostin (Galea et al., 2017), a protein that inhibits osteoblast differentiation by downregulating the canonical Wnt signaling pathway. Thus, loading increases Wnt signaling and promotes bone formation. During periods of disuse, lack of mechanical loading leads to osteocyte apoptosis, triggering the release of nuclear factor κB ligand (RANKL), a critical biochemical stimulant of osteoclast differentiation and activity (Cabahug-Zuckerman et al., 2016; Kogianni et al., 2008; Nakashima et al., 2011). While there are likely additional pathways yet to be identified, these studies provide strong evidence of a biological basis for load-driven bone adaptation.

2.5 Origins of the Theory of Load-Driven Bone Adaptation

While the cellular mechanisms governing load-driven bone adaptation have been identified relatively recently, the relationship between bone form and (mechanical) function has been appreciated for centuries. In 1638, Galileo noted that larger vertebrates have stouter bones than smaller vertebrates, and suggested that there is an evolutionary relationship between body

size and bone dimensions (Galileo, 1638; Martin, 2007). In 1892, Julius Wolff published *The Law of Bone Remodeling,* which outlined his "trajectorial hypothesis" that trabecular bone is "designed" to follow stress trajectories within bone. This hypothesis was inspired by the work of anatomist Georg Hermann von Meyer and structural engineer Karl Culmann, who recognized the similarity between trabecular bone structure in the femur, as observed by von Meyer, and stress trajectories within a similarly shaped curved crane designed by Culmann (Huiskes, 2000). While "Wolff's Law" has largely dominated the bone adaptation narrative, it was in fact Roux who first, in 1881, hypothesized that bone is a self-regulating tissue in which cells align themselves and their matrix with principal stress trajectories (Martin et al., 2015). This description of bone as an adaptive tissue was further developed by Harold Frost, who in 1987 published his "mechanostat" theory (Figure 2.8) (Frost, 1987). Frost described bone adaptation as a homeostatic feedback mechanism, where non-customary loads act as a controlling stimulus driving activity of effector cells (osteoblasts and osteoclasts). He suggested that, like a thermostat, the bone mechanostat has threshold loading values; below a disuse threshold bone is removed, and above a minimum effective load threshold bone is added. Removing tissue from an underloaded trabecular strut decreases its cross-sectional area, increasing stress and strain and restoring homeostasis. Conversely, adding tissue to an overloaded strut decreases stress and strain toward the homeostatic setpoint. Frost's theory served as the foundation for many subsequent theoretical descriptions of bone adaptation, and inspired decades of research to further characterize the mechanostat and determine its osteogenic thresholds.

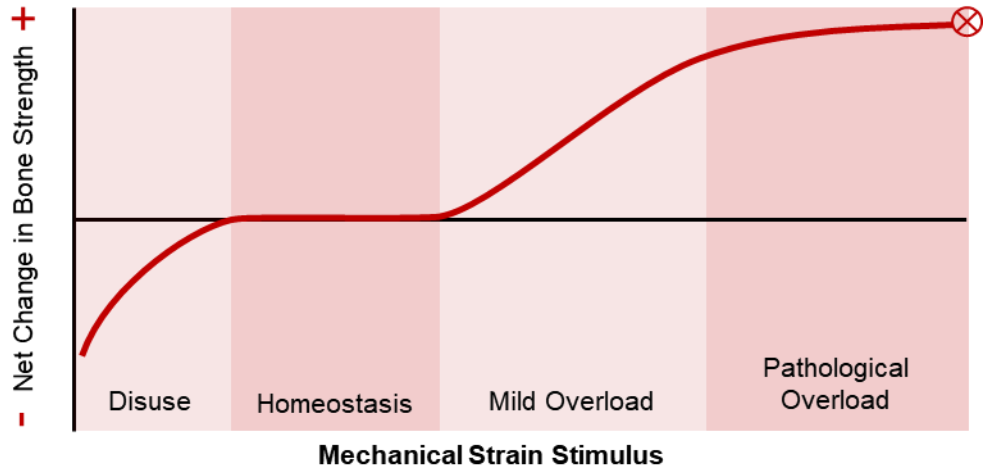

Figure 2.8: The relationship between mechanical strain and bone strength as proposed by Harold Frost's Mechanostat Theory (Frost, 2003). When mechanical stimuli are low, such as during bed rest, there is a net bone resorption response. The homeostasis window represents habitual mechanical loads to which bone is adapted and yield no net changes. In the mild overload window, such as during initiation of a new exercise intervention, there is a dose-dependent bone formation response. Ultimately, too much mechanical loading can be detrimental, with loads in the pathological overload window leading to fracture or bone stress injury. Adapted from Frost (2003) *Anat. Rec. Part A.*

2.6 Functional Bone Adaptation in Animal Models

In vivo loading animal models have been a valuable tool in characterizing the influence of specific loading parameters on adaptation. Animal models are beneficial because modifiable loading waveforms can be applied in a highly repeatable fashion using controlled, involuntary test setups. This means that loading parameters such as magnitude and rate can be systematically varied to quantify their influence on adaptation. Additionally, bone tissue loading in the region of interest can be measured directly using strain gauges placed surgically in on the periosteal bone surface. Starting in the 1960s, early models in the rabbit tibia, sheep radius, and turkey ulna applied cyclic loads between transverse pins placed surgically through the cortical shaft. These models established that dynamic rather than static loads are required for adaptation (Hert et al., 1971; Lanyon and Rubin, 1984; Rubin and Lanyon, 1984). They also demonstrated that strain

rate (O'Connor et al., 1982), strain magnitude (Rubin and Lanyon, 1985), and strain gradient (Gross et al., 1997) measured at the periosteal surface are related to changes in cortical bone area. Since the 1990s, most studies have used noninvasive models applying cyclic axial (Torrance et al., 1994) or bending (Turner et al., 1991) loads to the limbs of rats or mice, which avoid a surgery-induced wound healing response and are feasible to apply in larger experiments with more animals. These models have provided further evidence of the importance of strain magnitude (Mosley et al., 1997; Sugiyama et al., 2012), strain rate (Mosley and Lanyon, 1998; Turner et al., 1995), and the interaction of magnitude and rate (Hsieh and Turner, 2001) in generating a cortical response. They also demonstrated that only brief bouts of loading are needed to trigger an adaptive response, because bone becomes desensitized with continued loading cycles (Turner, 1998; Umemura et al., 1997). In the trabecular compartment, artificial mechanical loading leads to increases in BV/TV via trabecular thickening in the rabbit femur (Van Der Meulen et al., 2009), mouse tibia (Fritton et al., 2005), and mouse vertebral (Lambers et al., 2011) loading models.

In the last decade, a growing number of studies in animal models have focused on quantifying the relationship between tissue loading and trabecular bone adaptation at the local, tissue level. This requires identification of individual adaptation sites and quantification of bone strain throughout the region of interest. Identifying bone formation and resorption sites requires within-animal bone changes to be measured over time in vivo, rather than comparing animals between groups or using a contralateral limb control. Some studies have used a series of injected fluorescent bone formation markers to label new bone formation (Cresswell et al., 2016; Kim et al., 2003), but this does not allow for measurement of bone resorption. Alternatively, time-lapse micro-CT imaging (voxel size 10-80 μm (Christen and Müller, 2017)), where sequential scans

are aligned using rigid image registration, can be used to identify regions of added and removed bone (Birkhold et al., 2015; Schulte et al., 2011). Strain fields within loaded bone are estimated for the whole region of interest using micro-CT-based finite element (FE) models. Using these techniques, it has been shown that there is a measurable association between high strains and bone formation and low strains and resorption (Cresswell et al., 2016; Kim et al., 2003; Lambers et al., 2015; Schulte et al., 2013a).

The value of the large empirical data sets generated by animal models is they provided a foundation for mathematical descriptions of bone loading dose related to their osteogenic potential. Dennis Carter developed a "daily loading stimulus" metric (Carter et al., 1987), calculated as:

$$S = \left[\sum_{j=1}^{k} N_j \varepsilon_j^m\right]^{1/m} \quad \textbf{(2.1)}$$

Where N is the number of cycles at strain magnitude, ε, and m is a constant set to greater than one to account for the decay in response as number of cycles increases. Charles Turner proposed an "osteogenic index" (Turner, 1998), which describes a cyclic loading waveform in terms of frequency, magnitude, and duration as:

$$S = \log(1 + N_j)E_j \quad \textbf{(2.2)}$$

where

$$E_j = \sum_{i=1}^{n} \varepsilon_i f_i \quad \textbf{(2.3)}$$

Here, E_j represents the intensity of the waveform, calculated as the product of the strain magnitude, ε, and frequency, f, of a waveform with i frequency components. The logarithmic term accounts for "diminishing returns" of increasingly high number of cycles due to

desensitization. These and similar metrics provide an objective measure of loading that can be used to compare animal studies with varying loading parameters, and have served as the basis for mathematical models of bone adaptation capable of driving predictive simulations of adaptation to artificial loading interventions (Schulte et al., 2013b).

2.7 Functional Bone Adaptation in Humans

Substantial effort has been made to quantify the influence of mechanical loading during physical activity and exercise on human bone adaptation. This has primarily occurred through observational studies comparing athletic and sedentary populations and clinical trials assessing the prospective effect of specific interventions. In both cases, bone adaptation and mechanical loading need to be measured.

2.7.1 Measurement of Human Bone Adaptation

Load-driven changes in human bone structure are measured from medical images acquired over time. As in animal models, adaptation can be measured globally, as change in average parameters in a region of interest (i.e. density, trabecular thickness), or locally, by identifying specific regions of bone formation and resorption. When measuring global changes, it is important to select the same region of interest at each time point. With DXA, this is accomplished by standardized patient positioning and using automated manufacturer programs to define the region of interest (Scerpella et al., 2016). With QCT, in addition to standardizing patient positioning, image registration can be used to align scans during analysis (Bhatia et al., 2015; Edwards et al., 2015). A benefit of QCT is that scans typically include relatively large anatomical regions in 3D, with multiple anatomical landmarks that can facilitate repeatable definition of analysis regions. HRpQCT on the other hand, only includes a small, 9.02 mm region, meaning small differences in patient position can lead to poor overlap between scans.

Therefore, patient positioning is controlled using standardized braces made by the scanner manufacturer, and a 2D scout scan is performed prior to scanning to aid in selecting the region of interest using the joint as an anatomical reference point (MacNeil and Boyd, 2008). Remaining errors due to rotation and subjectivity in selecting the scan region are corrected in the manufacturer's standard longitudinal analysis program by only including overlapping slices as defined by 2D cross sectional area matching.

Identifying local adaptation between longitudinal scans was initially developed for micro-CT in animal models (Birkhold et al., 2015; Schulte et al., 2011; Waarsing et al., 2004). Scans acquired at different time points are aligned using 3D image registration (Boyd et al., 2006) and segmented into binary images. Voxels present in both images are labeled quiescent, those present at baseline only as resorbed, and those at follow-up only as formed. This approach has been successfully applied to relate bone adaptation to local tissue strains in the mouse tibia (Birkhold et al., 2014) and caudal vertebra (Lambers et al., 2015; Schulte et al., 2013a) loading models. This method is susceptible to precision errors related to partial volume effect and registration error, but given the high resolution of micro-CT, such errors have been shown to be small compared to real changes (Schulte et al., 2013a). Applying a similar approach to HRpQCT scans to label local adaptation in vivo in humans is more challenging, because the voxel size (82 μm) is closer to that of average trabecular thickness and is more susceptible to partial volume effect and other short-term precision errors. Therefore, if all added or removed voxels were labeled as adaptation similar to micro-CT, a larger proportion of adaptation would be associated with error versus real change, limiting the ability to detect measurable relationships between strain and adaptation. Christensen et al. (2014) developed methods to identify local areas of adaptation from registered HRpQCT images. Their algorithm operates on aligned, subtracted greyscale

images, and only includes continuous regions of a minimum size and grey value change to exclude noise. This method was applied to HRpQCT scans of the distal tibia in postmenopausal women, and adaptation was successfully correlated to bone strain (Christen et al., 2014) calculated using a reverse load estimation algorithm (Christen et al., 2013). However, local human bone adaptation has yet to be correlated to bone strain based on real, prospectively measured forces.

2.7.2 Measurement of Bone Loading in Humans

Bone strain has been identified as the controlling mechanical stimulus of adaptation in animal models, and is therefore expected to influence human bone adaptation. Direct measurement of bone strain is invasive, and therefore limited to small studies in research settings. A small number of studies in humans, the first published in 1975 (Lanyon et al., 1975), have used strain gauges applied to the outer bone surface directly or using bone staples to measure normal and shear strain during various activities (Burr et al., 1996; Földhazy et al., 2005; Milgrom et al., 2000). This technique is limited to a small region of the outer surface of sites with minimal soft tissue, and strain gauges cannot be left in the body long-term. More recently, Yang et al. (Yang et al., 2015, 2014) developed a method for measuring tibia deformations by calculating displacement of small optical markers on bone screws inserted into the periosteal bone surface. While they have produced valuable data that can be used to validate less invasive estimates of bone strain, these techniques are not feasible to implement in the clinic.

Force and acceleration sensors have been used to provide objective, indirect estimates of bone loading. Ground reaction forces have historically been used to characterize the intensity of bone loading (Fuchs et al., 2001; Hind and Burrows, 2007), but are challenging to measure for

large cohorts or in everyday use because force platforms are expensive and require a sophisticated biomechanics laboratory. Pressure-sensing insoles have been recently explored as a tool for measuring vertical ground reaction force and may enable force tracking outside laboratory settings. Alternatively, worn accelerometers are relatively inexpensive and can be easily used by participants to collect motion data in their everyday lives. Using cadaveric mechanical testing, it has been shown that statistical models considering limb acceleration measured using accelerometers and either bone cross sectional area or body mass significantly predict bone strain measured using strain gauges placed on the tibia and radius (Burkhart et al., 2012; Edwards et al., 2009). Several in vivo studies have explored accelerometer-based parameters such as counts, intensity, or slope to track physical activity and predict bone density changes (Ahola et al., 2009; Heikkinen et al., 2007; Rowlands and Stiles, 2012; Vainionpää et al., 2005). Additionally, sensor data can be used to calculate loading indices for a given activity or individual. Charles Turner suggested that his Osteogenic Index (Equation (2.2)) could be adapted to estimate the osteogenic potential of exercises based as

$$OI = loading\ Intensity\ \times \ln(N+1) \tag{2.4}$$

where loading intensity is the product of peak ground reaction force magnitude and loading rate (Turner and Robling, 2003). Ahola et al. (2010) used worn accelerometer data to calculate daily impact scores using weighted histogram analysis of acceleration intensities. Scores were calculated based on Carter's Daily Stress Stimulus (Equation (2.1)) as

$$DIS_{Exp} = \left[\sum_{j=1}^{32} N_j a_j^m\right]^{1/m} \tag{2.5}$$

where N_j is the number of impacts at the j^{th} acceleration level and m is an empirical constant set to 4. They also calculated an accelerometer-based score similar to Osteogenic Index, as

$$DIS_{log} = \sum_{j=1}^{32} a_j \ln(N_j + 1) \quad \textbf{(2.6)}$$

and showed that both scores were significantly correlated to changes in areal bone mineral density in the hip and cortical bone changes measured with QCT (Ahola et al., 2010). While accelerometers are useful for tracking activity intensity within individuals over time, they do not consider bone structure, which has a large influence on bone strain and varies widely between individuals. Additionally, sensor measurements do not reflect how strain is distributed within a region of bone.

Alternative to direct measurement of force or acceleration, several questionnaires have been developed to retrospectively estimate bone loading. Subjects report which activities they participate in as well as the average frequency and duration of participation for each activity. Activities are then weighted by loading intensity, which is based on the opinion of clinicians or in some cases, data of ground reaction forces from biomechanical studies in the literature. Multiple bone-specific surveys have been validated against densitometry (Dolan et al., 2006; Dowthwaite et al., 2015; Weeks and Beck, 2008) and HRpQCT values (Popp et al., 2019), showing that higher scores generally correlate to improved bone density and microstructure. However, these surveys are limited in that they assume equal activity-specific loading intensity between individuals, and at best, score intensity based on external forces rather than bone strain.

2.7.3 Finite Element Models for Estimating In Vivo Bone Strain

Finite element (FE) modeling allows for the non-invasive estimation of bone strain. The finite element method is a numerical technique that discretizes an object with complex geometry and/or material properties into smaller geometric regions, or “elements”, with a simple shape defined by connected node points. Each element is assigned a stiffness matrix, which defines

material properties such as Young's modulus and Poisson's ratio for a linear elastic material. The forces, displacements, and constraints applied at the edges of the model are considered boundary conditions. The finite element method solves for nodal displacements, which depend on how the boundary conditions propagate and interact with each element's stiffness matrix. Element stress and strain tensors and other metrics of interest are calculated in post-processing. FE modeling has been applied in the orthopedic biomechanics field since the 1970s (Huiskes and Chao, 1983), and complexity and patient-specificity has generally increased in parallel with growing computational power. Most relevant to the design of personalized exercise interventions, patient-specific models based on medical image scans allow bone strain to be estimated for a specific individual.

FE models of bone are also characterized by whether they are continuum or micro-FE models. Continuum models have a solid geometry, and structural heterogeneity such as cortical porosity and marrow spaces are implicitly accounted for in the element material properties (Figure 2.9). For CT-based models, this is accomplished using density-elasticity relationships (Helgason et al., 2008; Morgan et al., 2003) derived from mechanical testing of bone samples to map material properties to individual elements based average apparent density. Continuum FE models can be generated using clinical resolution CT scans, allowing for large regions of bone to be included. Boundary conditions including joint contact forces, muscle and ligament forces, and constraints are applied to simulate internal skeletal loading. When validated against cadaveric mechanical testing, continuum FE models of bone have been shown to explain 60-94% of variability in bone strain (Anderson et al., 2005; Bhatia et al., 2014; Edwards et al., 2013; Fung et al., 2017; Gupta et al., 2004; Keyak et al., 1993).

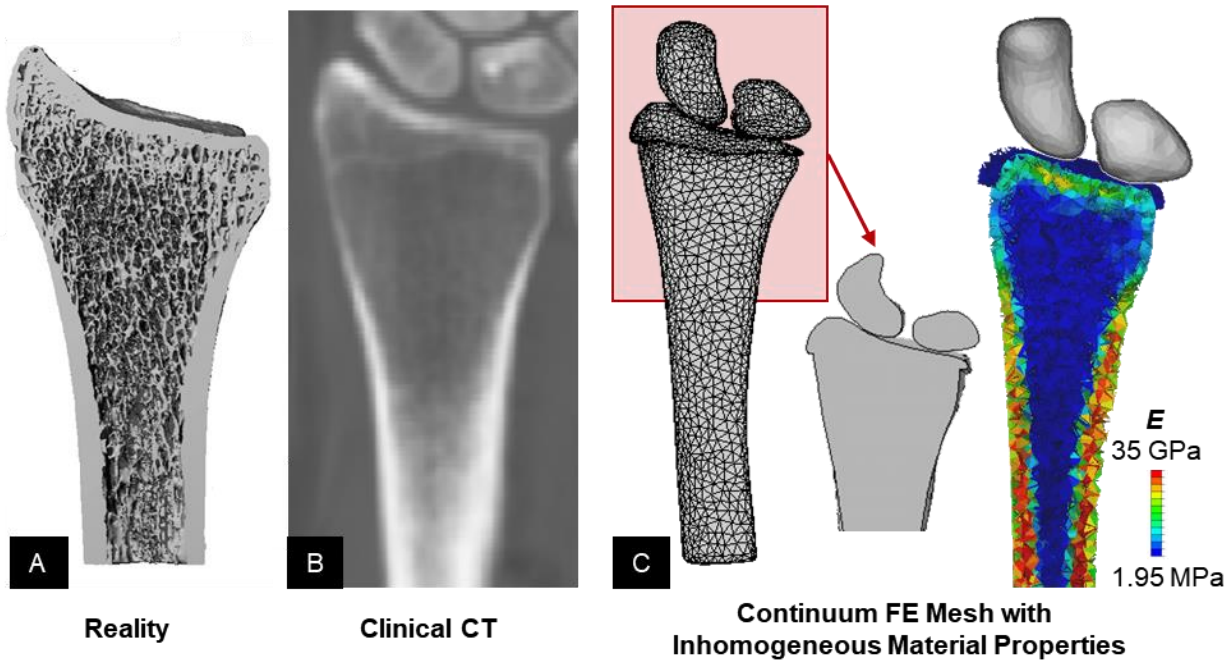

Figure 2.9: Continuum FE models approximate bone geometry, **(A)** which consists of trabecular bone struts thinner than the typical voxel size of **(B)** clinical resolution CT scans. **(C)** Therefore, continuum CT-based FE models have a solid geometry and incorporate structural heterogeneity by mapping inhomogeneous material properties such as Young's modulus (*E)* based on density-calibrated CT gray values. Part (A) adapted from MacNeil (2008) *Bone.*

Micro-FE models explicitly model trabecular microstructure separate from marrow space (Figure 2.10). Therefore, unlike continuum models, micro-FE models capture the mechanical effect of trabecular structure and orientation. The tradeoff of this detail is increased computational expense and the need for medical images with high enough resolution to capture individual trabeculae approximately 100-300 μm thick. In animals, micro-CT is capable of imaging whole bones in vivo at a resolution as low as ten micrometers, and micro-CT-based FE models are the gold standard for estimating bone strain during artificial loading interventions (Lambers et al., 2015; Schulte et al., 2013a; Webster et al., 2015). In humans, HRpQCT is capable of imaging trabecular microstructure in vivo, but is limited to small transverse regions (~1 cm thick). This limits the ability to simulate physiological boundary conditions, which has

been shown to affect bone strain distribution (Johnson and Troy, 2017b). Therefore, while HRpQCT-based micro-FE models are clinically useful to estimate overall stiffness within the scanned region as an estimate of overall fracture risk (Melton et al., 2007; Pahr and Zysset, 2016; van Rietbergen and Ito, 2015; Vilayphiou et al., 2010), they cannot accurately predict trabecular bone strain distribution during exercise.

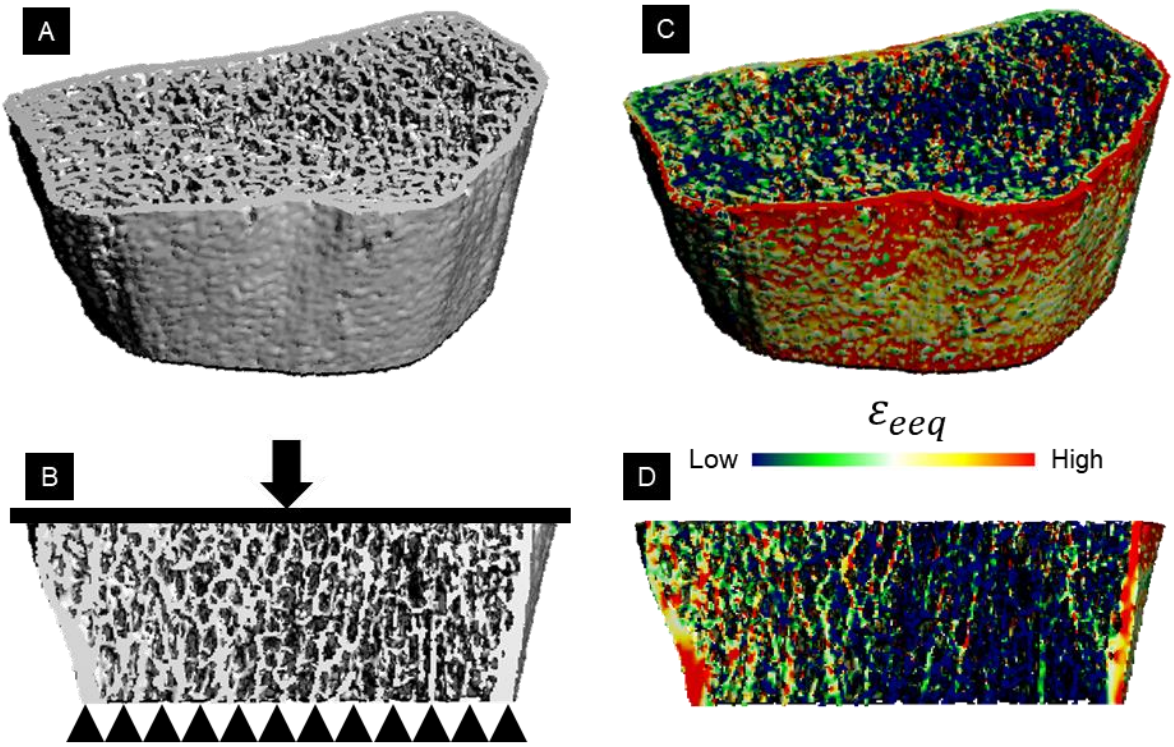

Figure 2.10: (A) HRpQCT-based micro-FE meshes are generated directly from voxel coordinates with an element size of 82µm. **(B)** Standard FE analyses of HRpQCT scans simulate platen boundary conditions applied at the proximal and distal surfaces. **(C)** Distribution of energy equivalent strain throughout the micro-FE mesh and in a **(D)** coronal view cross-section.

2.7.4 Evidence of the Role of Mechanical Loading on Human Bone Adaptation

In general, the intensity of mechanical loading during exercise is positively correlated with the magnitude of bone adaptation in humans. Compared to non-athletes, female athletes in high impact (volleyball, track and field jumping) and odd impact sports (soccer and tennis), but not low impact activities (powerlifting and swimming), have greater tibia cortical area (Nikander

et al., 2010). Female college athletes also have greater trabecular density at the distal tibia versus non-athletes, and moderate and high-impact sports (cross-country, volleyball, basketball) lead to increases in bending moment of inertia over the competitive season, while odd-impact sports (soccer) improve polar moment of inertia (i.e. torsional resistance) (Weidauer et al., 2014). Longitudinal studies also suggest that long-term participation in high-intensity sports leads to beneficial skeletal adaptation that is sustained into adulthood. Faulkner et al. (2003) showed that total body, lumbar spine, and hip aBMD were significantly greater for elite prepubertal female gymnasts versus age-matched controls (Faulkner et al., 2003), and a follow-up study showed that differences were maintained even when gymnasts had been retired for ten years on average (Erlandson et al., 2012). Looking at the upper extremity, gymnastics is associated with increased forearm aBMD and BMC (Bareither et al., 2008; Scerpella et al., 2016). Among adult female professional tennis players, BMC at the proximal humerus, humeral shaft, and distal radius has been shown to be 9-16% higher in the playing versus non-playing arms, compared to 3-5% side-to-side differences in age-matched controls (Kannus et al., 1995). These side-specific loading adaptations were generally maintained five years later, despite decreases in average training volume (Kontulainen et al., 2001).

In addition to observational studies in athletic populations, novel mechanical loading can also initiate bone adaptation in average individuals. A meta-analysis of nine controlled trials in premenopausal women showed that on average, impact loading interventions lead to significant increases in lumbar spine and femoral neck aBMD (Martyn St James and Carroll, 2010). When impact interventions with and without resistive loading were compared, impact-only interventions (vertical jumping, skipping) showed a significant effect at the femoral neck only, while combined impact-resistive interventions (circuit training, group fitness) showed a

significant effect at both sites (Martyn St James and Carroll, 2010). A separate meta-analysis of six trials of brief (<30 min) high impact exercise protocols (vertical jumping) showed significant increases in bone density at the hip but not the spine (Babatunde et al., 2012). This is in agreement with Zhao et al. (2014), who also showed that jumping interventions increased bone density at the hip only (Zhao et al., 2014). Looking at bone microstructure measured with HRpQCT, Hughes et al. (2018) showed that eight weeks of basic combat training resulted in trabecular bone formation and increased intracortical remodeling, with significant increases in micro-FE estimated stiffness and failure load (Hughes et al., 2018).

Very few studies have systematically measured the influence of specific loading parameters on adaptation. Wang et al. (2004) conducted a prospective trial of 24 healthy premenopausal women who performed a simple, controlled upper extremity "dynamic impact loading" task over 24 weeks, and showed that reaction force magnitude was significantly and positively related to change in distal radius and total forearm aBMD (Wang and Salem, 2004). Warden et al. (2019) compared bone strain distribution within the proximal humerus of the throwing and non-throwing arm in a single representative player, and showed that FE-estimated strain energy density was lower and more uniformly distributed in the throwing arm (Warden et al., 2019). Several studies have calculated the Osteogenic Index (Turner and Robling, 2003) (Equation (2.2)) or other loading scores to characterize their loading interventions (Santos-Rocha et al., 2006; Tolly et al., 2014), but data actually correlating loading scores to bone changes is limited and inconsistent (Erickson and Vukovich, 2010; Lester et al., 2009; Rantalainen et al., 2011). Jamsa et al. (2006) found that among adult women wearing accelerometers for 12-months, experiencing more large vertical peak accelerations was associated with larger increases in femoral neck aBMD (Jämsä et al., 2006). In the same group, high numbers of accelerations

with large slope, indicative of high loading rate, was also shown to positively correlate with density at the hip (Heikkinen et al., 2007). Ultimately, data from this study was adapted to calculate daily impact scores using formulations based on Carter's Daily Stress Stimulus (Equation (2.1)) and Turner's Osteogenic Index (Equation (2.2)), and both scores were significantly correlated (R up to 0.550) to change in bone density at the hip (Ahola et al., 2010). These and similar accelerometer-based loading scores (Hannam et al., 2017; Kelley et al., 2014; Pennline, 2014; Rowlands and Stiles, 2012) may prove useful in monitoring bone loading, but lack of information about how accelerations generate strain distributions within bone tissue limit their application for characterizing bone adaptation.

2.8 Prediction of Load-Driven Adaptation

Accurate predictions of load-driven bone adaptation could be used to inform the design of personalized exercise interventions or orthopedic implants, and to explore the interaction of pharmaceuticals and loading in silico. Toward this aim, several forward bone adaptation simulations combining mathematical and FE modeling have been developed. In these simulations, loading is applied to an FE mesh to calculate a bone loading stimulus, typically related to strain. This stimulus is fed into a mathematical algorithm that determines where bone should be added, removed, or remain quiescent. These changes are implemented by modifying the geometry and/or material properties of the FE mesh, which is resubmitted for FE analysis under the same loading condition. This iterative loop continues until some predetermined convergence or time-related criteria is met.

Early bone adaptation simulations modeled bone as a solid, continuum material, and updated Young's moduli of elements based on FE-estimated stress and strain (Beaupré et al., 1990a; Carter et al., 1987; Fyhrie and Carter, 1986; Hart et al., 1984; Huiskes et al., 1987).

Earlier models were also mostly phenomenological, meaning stress or strain directly control density without explicit consideration of cell behavior. For example, Fyhrie and Carter (1986) developed a theoretical framework describing bone as a self-optimizing material that undergoes changes in apparent density, ρ, in response to an "effective stress,"σ_{eff}, as

$$\rho = A \times \sqrt{\sigma_{eff}^2} \quad \textbf{(2.7)}$$

where *A* is an empirical constant (Fyhrie and Carter, 1986). This algorithm was implemented using a generic 3D model of a human proximal femur with homogenous trabecular density, and showed that given

$$\sigma_{eff}^2 = 2EU \quad \textbf{(2.8)}$$

where *E* is elastic modulus and *U* is strain energy density, produced a realistic density distribution (Fyhrie and Carter, 1990). Huiskes et al. (1987) incorporated a "lazy zone" (Table 3), with modulus increasing linearly above and below thresholds centered around a homeostatic level (Huiskes et al., 1987). This can be written mathematically as

$$\frac{dE}{dt} = \begin{bmatrix} C(U-(1+s)U_n) & U > (1+s)U_n \\ 0 & (1-s)U_n \le U \le (1+s)U_n \\ C(U-(1-s)U_n) & U < (1-s)U_n \end{bmatrix} \quad \textbf{(2.9)}$$

where U_n is the homeostatic setpoint for strain energy density, $(1+s)U_n$ is the threshold for formation, $(1-s)U_n$ is the threshold for resorption, and *C* is the slope of the line defining remodeling velocity outside of the lazy zone. In contrast to phenomenological algorithms, mechanistic simulations were proposed to explicitly model osteoclast and osteoblast behavior, with high strains or tissue microdamage initiating local, time-dependent changes based on apposition and resorption rates measured histologically (Beaupré et al., 1990b; Hart et al., 1984; Hazelwood et al., 2001; Martin, 1995). Overall, continuum simulations of bone adaptation have

been shown to provide reasonable estimates of bone adaptation to normal and modified loading conditions, but are fundamentally limited by lack of trabecular microstructure data.

The development of improved imaging techniques sparked interest in modeling trabecular bone adaptation at the tissue level. Weinans et al. (1992) showed in a two-dimensional plate model that a strain energy density-driven remodeling algorithm yielded a discontinuous density distribution similar to trabecular bone struts. Building upon this work, Mullender et al. (1994) separated the behavior of sensor cells (osteocytes) from actor cells (osteoclasts, osteoblasts) (Mullender et al., 1994). The model assumes that osteocytes are distributed throughout bone tissue, and each sense a local mechanical strain stimuli, S_i, and release biochemical signals in proportion to the difference between S_i and some reference stimulus, k. At a given location x on the bone surface at time t, the overall adaptation stimulus (sensed by osteoblasts and osteoclasts), Φ, is the cumulative sum of biochemical signals received from N nearby osteocytes, written as

$$\Phi(x,t) = \sum_{i=1}^{N} f_i(x)(S_i - k) \qquad \textbf{(2.10)}$$

Where $f_i(x)$ is the spatial influence function accounting for the decay of biochemical signals further from an osteocyte. Given $d_i(X)$ as the distance between location x and osteocyte i, the spatial influence function is written as

$$f_i(x) = e^{-[di(x)/D]} \qquad \textbf{(2.11)}$$

Where D is the decay constant giving the distance at which the signal is equal to 36.8% of its original strength. Change in bone density at location x is proportional to the stimulus Φ. When applied to the same plate model as Weinans et al. (1992), the simulation generated realistic trabecular shapes capable of realigning in response to modified loading conditions. Importantly,

the model incorporating mesh-independent osteocyte mechanosensors avoided a checkerboard artifact noted by Weinans caused by stress-shielding of adjacent elements. In a subsequent publication, the Mullendar algorithm was applied to a 3D micro-FE model generated from an *ex vivo* micro-CT scan of human vertebral trabecular bone (Mullender et al., 1998), marking a shift toward 3D simulations relying on increasing computational power.

Several simulations modeling 3D trabecular bone adaptation using micro-FE models of bone structure have been proposed. Ruimerman et al. (2005) extended the framework of Mullender to have separate terms for osteocyte sensing, load-driven osteoblast formation, and spatially random osteoclast resorption. This algorithm was used to study the influence of selecting different mechanical stimuli (i.e. SED versus principal stresses and strains) (Ruimerman et al., 2005b), but has only been implemented using small (3x33 mm^3) artificial bone cubes. Morgan et al. (2015) also used Equation (2.11) from Mullender et al. (1994) to calculate an osteocyte mechanical stimulus for a 3D simulation of trabecular bone adaptation in an in vivo rabbit bone loading model (Morgan et al., 2015). Micro-FE models were generated for 3.6x3.6x3.6 mm^3 trabecular bone cubes, and simulation predictions were compared to experimentally measured differences between loaded and non-loaded limbs. Simulations captured average group trends in trabecular histomorphometric parameters and structural anisotropy, but not all specimen-specific changes.

Table 2.3: Summary of bone adaptation theories applied in several examples of strain-driven trabecular bone adaptation simulations in the literature.

	Mechanical Stimulus	Adaptation Behavior
Huiskes et al. (1987) *J. Biomechanics.*	Difference between FE-estimated strain energy density and homeostatic strain energy density $U - U_n$	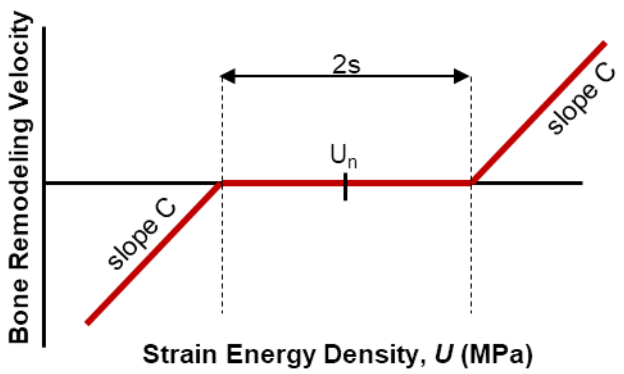
Adachi et al. (2001) *J. Biomech. Eng.*	Stress non-uniformity, Γ, (eq. 12-13)	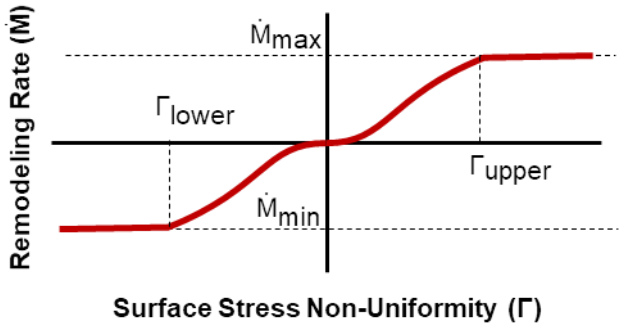
Schulte et al. (2013) *Bone.*	Neighborhood strain energy density osteocyte stimulus, *P(x)* (eq. 11)	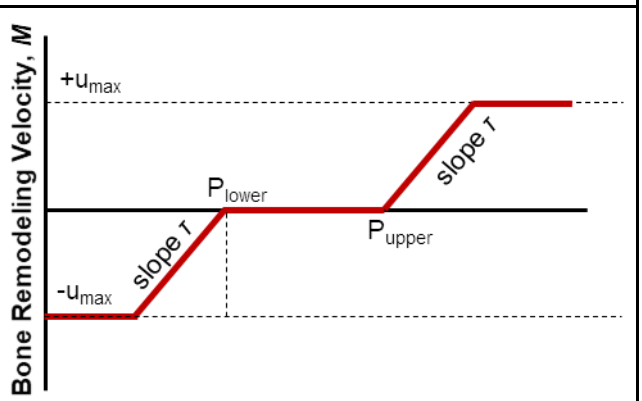
Morgan et al. (2015) *J. Biomechanics.*	Neighborhood strain energy density osteocyte stimulus, *F(x)* (eq.14)	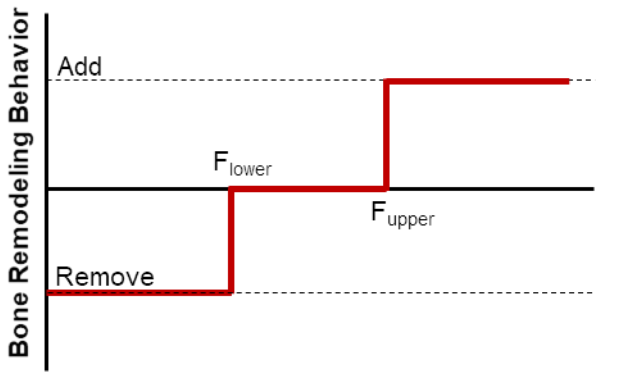

Adachi et al. developed a theoretical framework in which trabecular bone adapts to achieve uniform stress distribution on bone surfaces (Adachi et al., 2001, 1997). Stress is calculated for each micro-FE element, and at each surface location x_c, stress non-uniformity, Γ, is calculated as

$$\Gamma(x_c) = \ln\left(\frac{\sigma_c}{\sigma_d}\right) \quad \textbf{(2.12)}$$

where σ_c is the stress at x_c and σ_d is a distance-weighted average stress of neighboring elements. Neighborhood stress is calculated over the trabecular surface, S, as

$$\sigma_d = \int_s w(l)\sigma_r dS \,/\, \int_s w(l) dS \quad \textbf{(2.13)}$$

Where σ_r is the stress at a neighboring point a distance l from x_c, and $w(l)$ is a linear distance weighting function such that closer osteocytes have a larger relative contribution. Stress non-uniformity determines remodeling behavior (Table 2.3), with positive values favoring formation and negative values favoring resorption. When stress at a location is similar to that of its neighborhood (i.e. $\frac{\sigma_c}{\sigma_d} \approx 1$), Γ approaches zero, and no net change occurs. When stress at a location is greater than its neighborhood, Γ is positive and new elements are added to the surface, decreasing stress and creating a more uniform distribution. In contrast, elements are removed in low stress areas. This stress non-uniformity algorithm was applied to a micro-CT derived 5x5x5 mm^3 trabecular bone cube acquired from the unloaded limb in a canine bone loading experiment, and produced qualitatively similar changes as observed in the loaded limb (Adachi et al., 2001).

Schulte et al. (2013) developed and validated a load-driven adaptation simulation using in vivo time-lapse micro-CT scans acquired before and after a vertebral loading intervention in mice. The remodeling algorithm was driven by local strain energy density, with a loading stimulus $P(x)$ calculated for each surface voxel at location x as

$$P(x) = \sum_{i=1}^{N} e^{-\frac{(x-x_i)^2}{2\sigma^2}} SED(x_i) \quad \textbf{(2.14)}$$

where x_i is the location of a nearby voxel and σ is the distance from which osteoblasts and osteoclasts can sense osteocyte signals. The mechanical stimulus *P(x)* determines the net surface movement velocity, according to

$$M\big(P(x)\big) = \begin{cases} -u_{max}, & P(x) < P_{lower} - \dfrac{u_{max}}{\tau} \\ -(P_{lower} * \tau) + \tau * P(x), & P_{lower} - \dfrac{u_{max}}{\tau} < P(x) < P_{lower} \\ 0, & P_{lower} < P(x) < P_{upper} \\ -\big(P_{upper} * \tau\big) + \tau * P(x), & P_{upper} < P(x) < P_{upper} + \dfrac{u_{max}}{\tau} \\ u_{max}, & P_{upper} + \dfrac{u_{max}}{\tau} < P(x) \end{cases} \quad \textbf{(2.15)}$$

Such that *M(P(x))* increases linearly when *P(x)* exceeds the formation threshold P_{upper}, and becomes saturated at some velocity u_{max}. Similarly, *M(P(x))* is negative and linearly decreases when *P(x)* falls below the resorption threshold P_{lower}, until it becomes saturated at $-u_{max}$. Surface changes are implemented using a nonlinear advection equation applied to a grey-scale image generated from the binary micro-FE mask using a Gaussian blur filter. When applied to baseline micro-CT scans (n=9) from a vertebral loading experiment, the simulation predicted changes in average BV/TV with 2.4% error, and changes in trabecular thickness, separation, and number with error less than 7.8%. When assessing local accuracy on a point-by-point basis, the simulation accurately predicted 55.4±3.9% of adaptation behavior, with 72.2±3.8% for formation versus only 29.0±8.3% for resorption (Schulte et al., 2013b). In a second, larger study, Levchuck et al. (2014) conducted a validation against experimental measurements of 180 mice from multiple loading studies with or without additional pharmaceutical treatment (Levchuk et al., 2014). Across experimental groups and time points, the simulation predicted change in BV/TV with absolute error of means between 0.1-4.5%, and up to 18.1% for trabecular parameters.

Looking forward, large-scale, tissue-level bone adaptation simulations in humans could help predict how loading interventions and other changes influence trabecular bone structure. Such simulations have only recently become feasible with advancing computational power and imaging ability. Tsubota et al. (2009) applied the stress non-uniformity adaptation algorithm of Adachi et al. (2001) to a generic micro-FE model of a human proximal femur with a uniform, isotropic distribution of artificial trabeculae. The predictive simulation produced a final distribution consistent with what is generally observed in humans, showing that the algorithm controlled by loading at the microscale was capable of generating realistic macro-level trabecular structures (Tsubota et al., 2009). Badilatti et al. (2016) applied the bone adaptation algorithm of Schulte et al. (2013) to micro-FE models of whole human vertebra specimens (n=2) scanned ex vivo using micro-CT imaging. Due to the lack of patient-specific loading information and the complexity of internal in vivo spinal loading mechanics, boundary conditions for the micro-FE simulation were estimated using a retrospective load estimation method (Christen et al., 2012) that back-calculates the loads to which bone structure is currently adapted to resist. In a second publication, Badilatti et al. (2016) showed that adaptation parameters could be modified to produce reasonable patterns of trabecular bone loss associated with healthy aging and osteoporosis. While qualitative comparisons to biopsies support the realistic nature of simulation predictions, it is currently impossible to fully validate this framework because there are no imaging modalities capable of in vivo measurement of human trabecular microstructure at the spine. Thus, the largest bottleneck in further development of patient-specific bone adaptation simulations is lack of experimental data with prospectively measured changes in trabecular bone microstructure and known loading conditions.

2.9 Establishing a Human Bone Loading Model

Lack of experimental data relating tissue-level bone loading stimuli to adaptation in humans is a critical obstacle in the development of effective bone-building exercise interventions. To address this challenge, prior work in our lab established an upper-extremity in vivo loading model that can be used to deliver a diverse range of strain signals that can be prospectively correlated to changes in bone structure. This is accomplished using a voluntary upper-extremity loading task, in which participants lean their palm on and off a flat surface to deliver a cyclic force to the distal radius bone within the forearm (Figure 2.11). The distal radius was selected as the region of interest because it is a common fracture site that can be imaged non-invasively using DXA, clinical CT, and HRpQCT. Additionally, the forearm is favorable to the lower limbs, which experience confounding cyclic loads during locomotion and other activities. Cadaveric mechanical testing replicating the forearm loading task showed that a 300 N load generated a minimum principal strain of -1695±396 με in the radius (Troy et al., 2013). An in vivo pilot study found that over 28 weeks, premenopausal women who performed the loading task (n=19, 50 cycles/day, 3 days/week) experienced small increases in bone mineral content versus control subjects (n=7) who lost bone (+0.25±2.37% versus -1.70±1.16%, $p<0.05$). Changes in ultradistal radius structure were measured using QCT of clinical resolution scans.

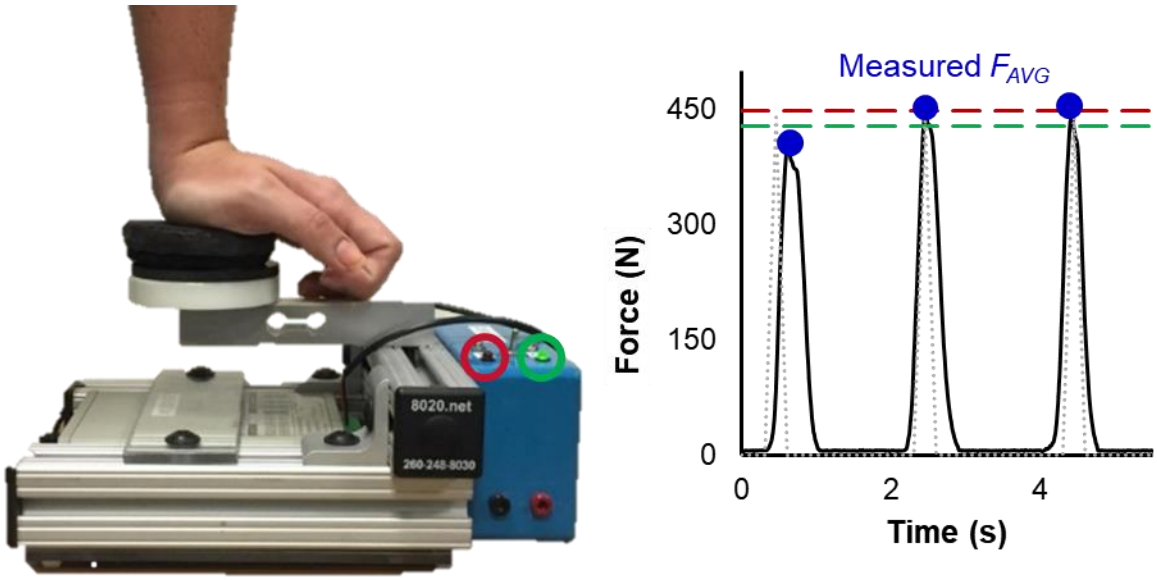

Figure 2.11: The upper-extremity loading model uses a forearm loading task to apply cyclical, compressive force to the radius bone through the palm of the hand. Loading is performed using a custom loading device that guides and records applied vertical force. Biofeedback is provided by programmable LED indicator lights that turn on at ±10 N of the target load. Recorded load cell waveforms can be used to calculate achieved loading parameters such as average peak force, F_{AVG}.

Additionally, our lab developed and validated subject-specific continuum and multiscale (continuum plus micro-FE), CT-based FE models simulating the forearm loading task (Figure 2.12). Continuum models generated from clinical resolution CT scans consist of 3D tetrahedral meshes of the distal 10 cm of the radius, the radius cartilage, and the scaphoid and lunate carpals. When compared to cadaveric mechanical testing, the FE models predicted experimentally measured strains at matching locations (R^2=0.86, RMSE 11.1% of maximum measured strain) (Bhatia et al., 2014). Data from the pilot loading study showed that when the distal radius was divided into 12 subsections, average FE-estimated energy equivalent strain magnitude was positively correlated with 14 week changes in QCT parameters (Bhatia et al., 2015). To quantify tissue-level bones strain on the level of individual trabeculae, Johnson et al. (2017) developed and validated a multiscale FE model that combines clinical resolution CT and HRpQCT-based

meshes (Johnson and Troy, 2017c). A micro-FE mesh at the distal radius HRpQCT scan site is tied between distal and proximal continuum sections, which allows boundary conditions to reflect physiological loading through the wrist while estimating tissue-level trabecular strains in the ultradistal region. When model-predicted strains were compared to strain gauge measurements, values were significantly and linearly related ($r=0.70$, $p<0.001$).

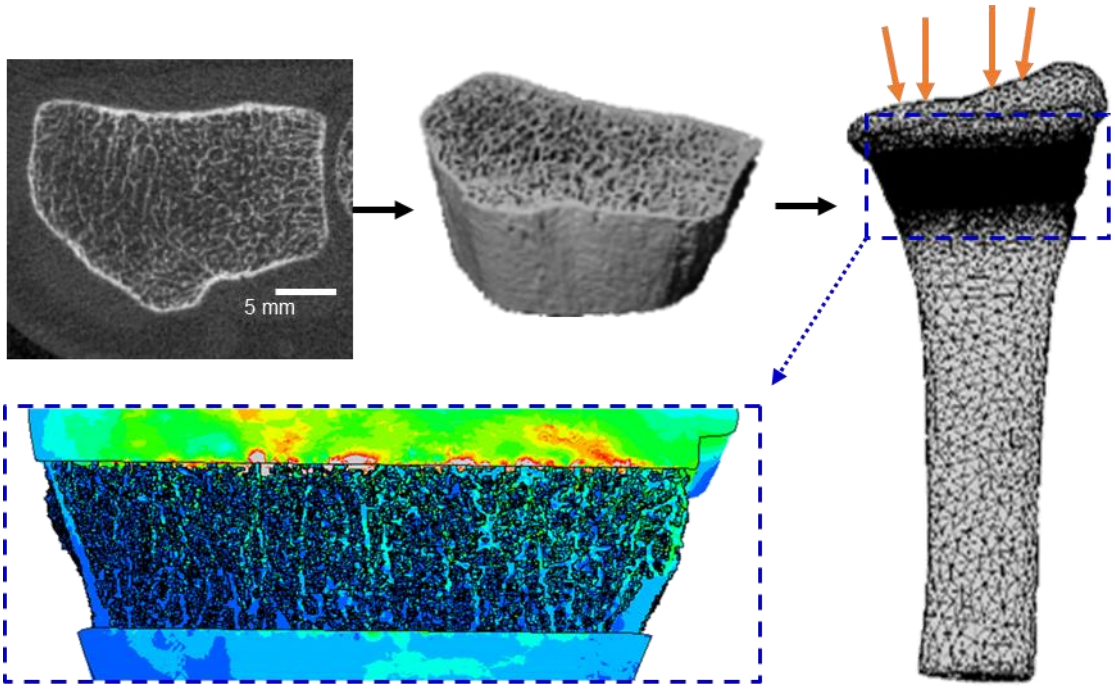

Figure 2.12: Multiscale FE model. HRpQCT scans are converted to voxel-based micro-FE meshes, which are inserted into the continuum model to estimate tissue-level trabecular strain during forearm loading.

This Dissertation builds upon previous efforts, introducing HRpQCT and multiscale-FE as well as predictive simulations to our subject-specific approach to understanding bone adaptation. This project is based a prospective, controlled, randomized clinical experiment involving 102 healthy premenopausal women using the forearm loading model. Study participants were assigned to one of five groups: low (1800 με) strain magnitude, high (3600 με) strain magnitude, low (4500 με/s) strain rate, high (36000 με /s) strain rate, or non-loading

control. Strain-based loading assignments were made using subject-specific FE models, and changes in bone structure are evaluated using serial bone imaging. In Chapter 3, we perform a cross-sectional analysis to explore the factors influencing bone strain at baseline. In Chapters 4 and 5, we will compare changes in bone structure between experimental groups, and relate bone strain and adaptation of bone macro- and microstructure. While Chapters 4 and 5 retrospectively describe the relationship between strain and adaptation, Chapter 6 explores the use of a forward bone adaptation simulation, driven by bone strain, to predict changes in radius bone structure.

Chapter 3: Aim 1, Quantify the Relationship between Mechanical Loading History, Bone Structure, and FE-Estimated Bone Strain in the Human Forearm

Published in *Bone Reports* as:

Mancuso, Megan E., Joshua E. Johnson, Sabahat S. Ahmed, Tiffiny A. Butler, and Karen L. Troy. 2018. "Distal Radius Microstructure and Finite Element Bone Strain Are Related to Site-Specific Mechanical Loading and Areal Bone Mineral Density in Premenopausal Women." *Bone Reports* 8 (July 2017): 187–94. https://doi.org/10.1016/j.bonr.2018.04.001.

3.1 Introduction

Peak bone mass, achieved during late adolescence (Bass et al., 1999; Bonjour et al., 1991; Haapasalo et al., 1996; Theintz et al., 1992), is a critical determinant of lifetime bone health. Increased peak bone mass in females has been linked to lower fracture risk (Bonjour et al., 2009; Boot et al., 2010; Tabensky et al., 2001; Zebaze et al., 2007) and delayed onset of osteoporosis (Hernandez et al., 2003). Therefore, bone-building strategies targeting young adults have the potential to make a substantial impact in fracture prevention. However, premenopausal women are not routinely counseled on methods to improve their bone health (Kling et al., 2014), and screening tools such as dual energy X-ray absorptiometry (DXA) and fracture risk calculators are expensive and invalid for young adults, respectively (Cosman et al., 2014). While mechanical loading consistently promotes bone formation in animal models (Rubin and Lanyon, 1987; Srinivasan et al., 2002; Umemura et al., 2008), human trials have yet to result in widespread adoption of weight-bearing activity as a means of increasing peak bone mass (Babatunde et al., 2012). Inconsistent outcomes may be due to the variability in how complex motions load bone at the tissue level. Importantly, two individuals performing the same activity may experience greatly different bone strains depending on how the activity is performed, the

internal forces produced by contracting muscles, and variability in bone mineralization and structure.

Although considered the gold-standard estimate of fracture risk, DXA areal densitometry measurements are inherently limited by their two-dimensional nature. Most distal radius fractures occur in women who are osteopenic rather than osteoporotic as measured using DXA (Siris et al., 2004), indicating that factors besides areal bone mineral density (aBMD) affect bone strength and fracture risk. Indeed, a combination of density, structure, and other factors comprising bone quality can explain differences in the biomechanical behavior of bone better than bone mass or density alone (Bhatia et al., 2014; Hernandez and Keaveny, 2006). Finite element (FE) models based on 3D computed tomography (CT) scans allow for the accurate estimation of bone mechanical behavior under physiological loading conditions (Bhatia et al., 2014). Such models have been shown to predict fracture strength better than DXA for the tibia (Edwards et al., 2013), and FE-estimated bone strain is predictive of structural adaptation due to mechanical loading in the radius (Bhatia et al., 2015). Additionally, high-resolution peripheral quantitative computed tomography (HRpQCT) allows for the in vivo assessment of bone microstructure in the forearm, which informs bone quality and complements FE bone strain. Together, these technologies may allow specific individuals who may benefit from exercise-based interventions for bone health to be identified. Additionally, such interventions could be engineered to produce known strains resulting in consistent, clinically meaningful skeletal adaptation.

With the long-term goal of developing targeted fracture prevention strategies for young adult women, the current work aims to compare currently available measures of bone quality and determine the degree to which estimates of site-specific mechanical loading are related to bone

microstructure and finite-element estimated bone strain. Previous studies have highlighted weight, height, and physical activity as potential determinants of bone quality, but have generally focused on whole-body loading and bone mass measured by DXA (Greenway et al., 2015; Ho and Kung, 2005; Petit et al., 2004; Rubin et al., 1999). Attempts to relate site-specific loading and radius bone structure have compared athletes and non-active controls (Dowthwaite et al., 2015; Nikander et al., 2006; Schipilow et al., 2013), but have not considered the effects of loading due to recreational exercise habits across average women. In the current work, we assessed the ability of DXA-based measurements of aBMD, the current clinical gold standard, to predict FE-estimated bone strain during physiologic loading. Second, we aimed to identify intrinsic and modifiable factors that affect bone strain and distal radius microstructure in average adult women. We hypothesized that greater site-specific loading, indicated by high levels of physical activity, grip strength, and body mass, would predict stronger bone structure and thus lower strain for a given external force, independent of age and height.

3.2 Materials and Methods:

3.2.1 Participants

Healthy females age 21-40 were recruited from the greater Worcester area as part of a larger, institutionally approved longitudinal experiment (Figure 3.1). The present study reports baseline cross-sectional data from the parent study. Women responding to online advertisements were contacted and screened via telephone survey. Individuals with irregular menstrual cycles, body mass indices outside the range 18-25 kg/m^2, no regular calcium intake, or those taking medications known to affect bone metabolism were excluded. Because subjects were being screened for a prospective loading intervention study, individuals with a history of radius fracture or injury of the non-dominant shoulder or elbow, and those regularly participating (> 2

time per month) in sports that apply high-impact loads to the forearm (e.g. gymnastics, volleyball) were also excluded. Those satisfying the initial inclusion criteria were screened for 25-hydroxyvitamin D serum levels and forearm DXA T-score during a prescreening visit (Hologic; Marlborough, MA). DXA scans were performed on the non-dominant forearm according to the manufacturer's standard protocol, and used to calculate T-score and areal density within the ultradistal and total forearm regions (Figure 3.2A). Qualified subjects had 25-hydroxyvitamin D serum above 20 ng/ml and a total forearm DXA T-score between -2.5 and 1.0. Data for qualified subjects (n=82) were collected either during the screening or a single visit within approximately two weeks of screening. All participants provided written, informed consent between January 2014 and November 2016.

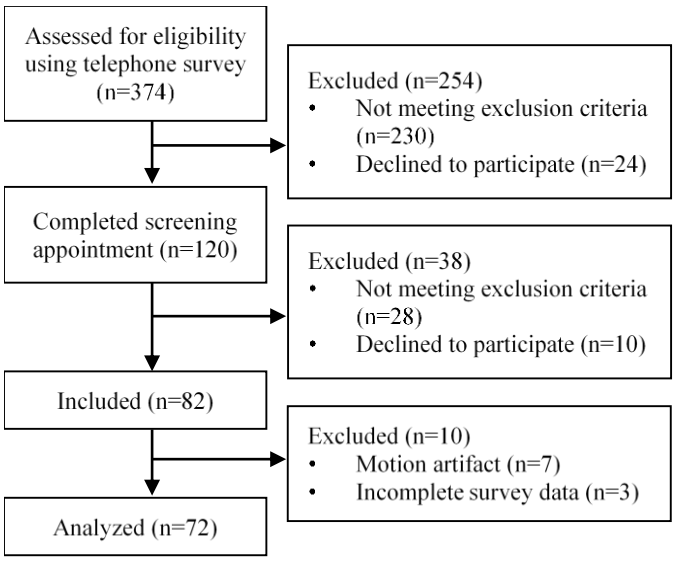

Figure 3.1: Flow diagram describing recruitment, screening, and enrollment.

3.2.2 Anthropometrics and Loading Assessments

Height was measured using a wall-mounted stadiometer, and body mass was measured using an analog scale. Non-dominant grip strength was measured using a hydraulic hand-grip

dynamometer (Baseline; White Plains, NJ) three times and averaged. Grip strength measurements were taken in a seated position with the elbow bent ninety degrees in flexion. Average daily calcium intake (mg/day) was estimated using a 10-item questionnaire that tallied weekly consumption of calcium-containing foods and beverages ("Getting Enough Calcium? Patient Calcium Questionnaire," n.d.).

To estimate forearm loading due to physical activity, a site-specific arm bone loading index (*armBLI*) algorithm (Dowthwaite et al., 2015) was used to score activity histories. The *armBLI* algorithm scores activities based on the magnitude, rate, and frequency (days/week) of loads applied to the non-dominant arm as:

$$armBLI=\Sigma[(Magnitude + Velocity) \times Frequency \times Non\text{-}Dominance] \quad \textbf{(3.1)}$$

where the non-dominance multiplier corrects for activities loading the dominant arm preferentially. The multiplier is 0.33 for predominantly unilateral activities (e.g., tennis), 0.66 for somewhat unilateral activities (e.g. softball), and 1.0 for bilateral activities (e.g. gymnastics). For each individual, an overall score is calculated as the products of activity-specific training volumes and *armBLI* indices summed over all activities performed. For the present study, physical activity training volumes were generated using the validated Bone Loading History Questionnaire (BLHQ) (Dolan et al., 2006), which was used to collect physical activity history in this group. Briefly, training volume is calculated as the product of years of participation, the seasons participated per year (fraction out of four), and a frequency score ranging from 1 to 4 reflecting training sessions per week (1=1-3 times per month, 2=1-2 times per week, 3=3-5 times per week, and 4=>5 times per week). To assess the relative importance of upper-extremity physical activity during different stages of development, separate mean annual scores (armBLI/year) were calculated for adolescent (age 10-18) and adult (age 19-current age) loading.

3.2.3 High-Resolution Peripheral Quantitative Computed Tomography

High-resolution peripheral quantitative computed tomography (HRpQCT; XtremeCT, Scanco Medical; Brüttisellen, Switzerland) scans of the distal radius in the non-dominant arm were performed according to the manufacturer's standard in vivo scanning protocol (Figure 3.2B). The scans consisted of 110 slices with an isotropic voxel size of 82 μm, encompassing a 9.02 mm axial region beginning 9.5 mm proximal to a reference line placed at the distal endplate. All scans were performed by trained technicians, and daily and weekly quality control scans were performed. Each scan was graded for motion on a scale from 1 (no motion) to 5 (severe motion artifact) (Pialat et al., 2012), and only scans scoring 3 or better were included in the analysis.

HRpQCT scans were analyzed using the manufacturer's semi-automatic standard morphological (MacNeil and Boyd, 2007) and cortical (Buie et al., 2007; Andrew J Burghardt et al., 2009; Burghardt et al., 2010; Nishiyama et al., 2009) analyses. Total BMD ($mgHa/cm^3$), trabecular BMD ($mgHa/cm^3$), mean cross-sectional area (CSA; mm^2), and trabecular number (mm^{-1}) were calculated using the standard manufacturer's analysis, and cortical BMD ($mgHa/cm^3$), cortical thickness (mm), and cortical porosity (%) were calculated using the dual-threshold method (Buie et al., 2007; Andrew J Burghardt et al., 2009; Burghardt et al., 2010; Nishiyama et al., 2009).

3.2.4 Continuum FE Modeling

Clinical resolution CT scans were used to construct three-dimensional continuum FE models including the distal articulating surface to simulate physiologic loading through the scaphoid and lunate. CT scans of the distal-most 12 cm of the non-dominant forearm were acquired using established methods with a transverse voxel size of 234 μm and slice thickness of

625 μm (BrightSpeed, GE Healthcare; Chicago, IL) (Bhatia et al., 2015). A calibration phantom with known calcium hydroxyapatite equivalent concentrations was included for conversion from Hounsfield Units to apparent density to determine inhomogeneous density-based material properties. Mechanical behavior of the entire distal radius under physiologic loading was estimated from FE models (Bhatia et al., 2014) simulating distal compressive forearm loading of 300 N (approximately one half body-weight) through the palm of the hand (Figure 3.2C). Energy equivalent strain ($\bar{\varepsilon}$) was selected as the primary FE outcome because it has been previously related to bone adaptation (Bhatia et al., 2015). This scalar quantity represents the total work done on the bone tissue, provided by the multi-axial stress-strain state:

$$\bar{\varepsilon} = \sqrt{\frac{2U}{E}} \quad \textbf{(3.2)}$$

where E is the elastic modulus, and U is the strain energy density calculated as:

$$U = \frac{1}{2}[\sigma_1\varepsilon_1 + \sigma_2\varepsilon_2 + \sigma_3\varepsilon_3] \quad \textbf{(3.3)}$$

where σ_n and ε_n are the principal stress and strain components, respectively. Mean energy equivalent strain within the region corresponding to the HRpQCT-scanned region was identified using a custom MATLAB (Mathworks; Natick, MA) script that implemented a mutual information image registration algorithm considering pixel intensities. A laboratory precision study yielded mean rotation errors of 0.47±0.38°, 0.46±0.41°, and 0.32±0.24° in the x, y, and z directions, respectively, for a similar data set (Johnson and Troy, 2017c).

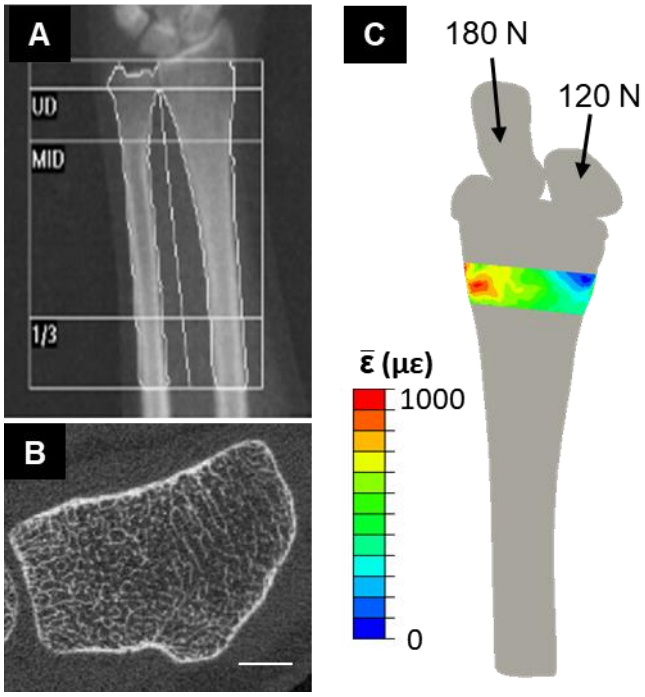

Figure 3.2: (A) Representative forearm DXA scan including ultradistal (UD), Middle (MID) and 1/3 regions, and **(B)** distal radius HRpQCT scan (scale bar 5 mm). **(C)** Three-dimensional continuum FE model used to estimate energy equivalent strain ($\bar{\varepsilon}$) within the HRpQCT scanned region.

3.2.5 Statistical Analysis

The normality of each measured variable was assessed by visual inspection of histogram distributions. To assess the ability of DXA-based measures to predict FE strain, a power regression model was constructed with ultradistal aBMD as the independent variable and mean energy equivalent strain as the dependent variable. Power regression was selected based on previous studies characterizing the relationship between bone density and mechanical properties (Helgason et al., 2008). Correlation and multiple regression analyses were used to identify intrinsic and modifiable factors that affect bone strain and distal radius microstructure. Pearson and Spearman correlation coefficients were calculated between subject characteristics, FE-strain, and HRpQCT parameters with normal and non-normal distributions, respectively. A series of hierarchical linear regression models were fitted for each structure and strain variable, with age

and height entered as intrinsic covariates and body mass, grip strength, and loading scores included as extrinsic, modifiable predictors. Covariates were added as a first block of independent variables, and then a single modifiable factor was entered in a second block, allowing the total variance explained by the intrinsic factors as a group and the predictive capability of each loading factor to be determined. The overall model residuals were visually inspected for normality and homoscedasticity using a plot of residuals versus predicted values. An alpha level of 0.05 was used to detect significance. All statistical analyses were performed using SPSS v22.0.

3.3. Results

3.3.1 Subject Characteristics

Descriptive statistics, presented as means and standard deviations, are summarized in Table 3.1. Ten enrolled subjects were excluded from analyses due to incomplete physical activity data (n=3) or HRpQCT motion artifact (n=7). Thus, all results are reported for the seventy-two subjects for whom complete data were available. Daily calcium intake was below the average intake reported for women ages 19-50 in the United States (Bailey et al., 2010), while grip strength was similar to previously reported values for young adult women (Massy-Westropp et al., 2011; Wong, 2016). Correlation coefficients between predictors and bone structure and strain parameters are provided in Table 3.2. Mean energy equivalent strain within the distal region was significantly correlated several HRpQCT parameters, DXA aBMD, and body mass.

Table 3.1: Descriptive statistics for all subjects (n=72).

Subject Characteristics	Mean	SD
Age (years)	28.3	5.3
Body Mass (kg)	63.6	8.6
Height (cm)	164.6	6.9
ND Grip Strength (kg)	26.4	5.2
Vit D (ng/mL)	32	9
Daily calcium intake (mg/day)	682	400
Adolescent Loading Score (armBLI/year)	50	48
Adult Loading Score (armBLI/year)	54	47

Vit D Serum Vitamin D level, ArmBLI Arm Bone Loading Index

Table 3.2: Correlation coefficients between subject characteristics, bone structure, and strain parameters. *p<0.05, **p<0.01

		Mean Energy Eqiv. Strain (με)	Age (years)	Height (cm)	Body Mass (kg)	ND Grip Strength (kg)	Adolescent Loading (armBLI/year)	Adult Loading (armBLI/year)
FE	Mean Energy Eqiv. Strain (με)		-0.004	-0.014	**-0.261***	-0.092	-0.029	-0.177
HRpQCT	Total BMD (mg HA/cm^3)	**-0.684****	0.022	**-0.253***	-0.099	**-0.254***	-0.182	0.005
	Trabecular BMD (mg HA/cm^3)	**-0.689****	**-0.334****	-0.076	-0.005	0.089	0.075	**0.237***
	Cortical BMD (mg HA/cm^3)	**-0.256***	**0.301***	**-0.262***	0.029	**-0.472****	-0.085	-0.220
	Total Area (mm^2)	0.092	-0.181	**0.550****	**0.343****	**0.620****	0.145	0.190
	Trabecular Number (1/mm)	**-0.327****	**-0.457****	0.080	0.190	0.069	0.162	0.153
	Cortical Thickness (mm)	**-0.498****	0.157	-0.160	-0.031	-0.165	**-0.232***	-0.024
	Cortical Porosity (%)	0.001	-0.184	0.159	-0.027	**0.285***	0.034	0.228
DXA	areal BMD (mg HA/cm3)	**-0.708****	-0.107	0.110	**0.291***	0.209	-0.057	0.149

3.3.2 Prediction of FE-Estimated Bone Strain and HRpQCT Microstructure

Results of the nonlinear power regression between DXA aBMD and mean energy equivalent strain within the ultradistal region are presented in Figure 3.3. Areal BMD explained 51.47% of the variability in strain, with higher density values associated with lower strains under a given load.

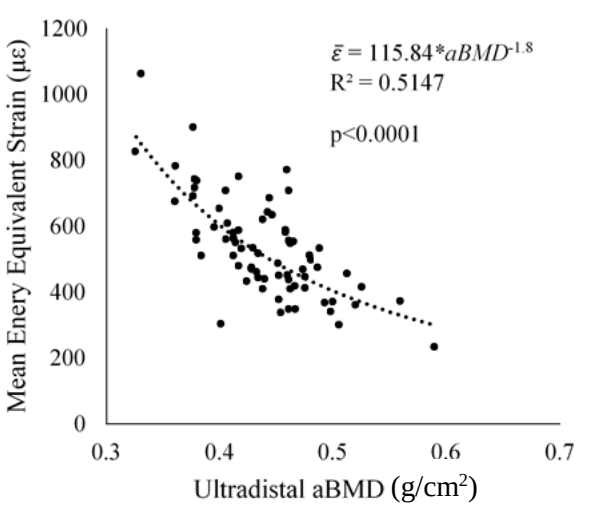

Figure 3.3: Mean energy equivalent strain within the ultradistal region matching the volume scanned with HRpQCT versus areal bone mineral density measured using DXA within the standard ultradistal site.

Mean and standard deviations for all bone parameters, as well as the corresponding hierarchical regression results, are presented in Tables 3.3 and 3.4. Mean values for HRpQCT-measured parameters agree well with those reported for young adult women (Burt et al., 2014). Energy equivalent strain was not significantly predicted by age or height. Adding body mass to the model significantly improved the prediction of strain, explaining an additional 10.0% of the variance (p=0.008).

Table 3.3: HRpQCT parameter values (mean±SD) and hierarchical linear regression results.

Parameter	Mean	SD	Predictors	R^2	ΔR^2	p	Beta
Mean Energy Eqiv. Strain (με)	534.69	151.27	Age, Height	<0.001		0.987	
			+Weight	**0.101**	**0.100**	**0.008**	**-0.394**
			+Grip Strength	0.010	0.010	0.421	-0.110
			+Adolescent Loading	0.006	0.006	0.523	0.078
			+Adult Loading	0.033	0.033	0.134	-0.184
DXA aBMD (mg Ha/cm3)	439.4	48.85	Age, Height	0.016		0.582	
			+Weight	**0.107**	**0.091**	**0.010**	**0.375**
			+Grip Strength	0.048	0.032	0.133	<0.001
			+Adolescent Loading	0.032	0.016	0.287	<0.001
			+Adult Loading	0.033	0.017	0.276	<0.001

R^2 Total variance explained by the model, *ΔR^2* Additional variance explained by predictor, *p* significance of F-value change, *Beta* Standardized coefficient

Looking at HRpQCT parameters, age and height accounted for 9.6% of the variance in trabecular BMD (p=0.031) as intrinsic factors, and adding adult loading score to the model accounted for an additional 7.1% of the variance (p=0.019). Intrinsic factors alone explained 11.9% of the variance in cortical BMD (p=0.013), and adding grip strength to the model explained an additional 17.0% of the variance (p<0.001). Total cross sectional area was strongly predicted by age and height, which explained 31.6% of the variance (p<0.001). Adding grip strength to the model significantly improved the prediction of total area, explaining an additional 17.9% of the variance (p<0.001). Intrinsic factors alone explained 17.4% of the variance in trabecular number (p=0.001), and body mass accounted for an additional 7.6% percent of the variance (p=0.011). Cortical porosity was not significantly predicted by intrinsic factors alone, but adding either grip strength or adult loading score improved model predictions by 5.6% (p=0.043) and 8.3% (p=0.013), respectively. None of the models predicting total BMD or cortical thickness was significant.

Table 3.4: HRpQCT parameter values (mean±SD) and hierarchical linear regression results.

Parameter	Mean	SD	Predictors	R^2	ΔR^2	p	Beta
Total BMD (mg Ha/cm^3)	298.23	51.53	Age, Height	0.064		0.101	
			+Body Mass	0.067	0.003	0.640	0.068
			+Grip Strength	0.088	0.024	0.184	-0.175
			+Adolescent Loading	0.068	0.004	0.584	-0.065
			+Adult Loading	0.076	0.012	0.360	0.110
Trabecular BMD (mg Ha/cm^3)	162.86	30.03	**Age, Height**	**0.096**		**0.031**	
			+ Body Mass	0.110	0.014	0.309	0.146
			+Grip Strength	0.122	0.026	0.164	0.181
			+Adolescent Loading	0.101	0.005	0.525	0.074
			+Adult Loading	**0.167**	**0.071**	**0.019**	**0.272**
Cortical BMD (mg Ha/cm^3)	969.24	44.06	**Age, Height**	**0.119**		**0.013**	
			+ Body Mass	0.147	0.028	0.142	0.207
			+Grip Strength	**0.289**	**0.170**	**<0.001**	**-0.464**
			+Adolescent Loading	0.120	0.001	0.749	-0.037
			+Adult Loading	0.139	0.020	0.215	-0.144
Total Area (mm^2)	274.23	49.23	**Age, Height**	**0.316**		**<0.001**	
			+ Body Mass	0.321	0.005	0.493	0.086
			+Grip Strength	**0.494**	**0.179**	**<0.001**	**0.477**
			+Adolescent Loading	0.316	<0.001	0.945	-0.007
			+Adult Loading	0.325	0.009	0.354	0.095
Trabecular Number (1/mm)	2.00	0.26	**Age, Height**	**0.174**		**0.001**	
			+ Body Mass	**0.249**	**0.076**	**0.011**	**0.342**
			+Grip Strength	0.178	0.004	0.564	0.072
			+Adolescent Loading	0.195	0.022	0.179	0.148
			+Adult Loading	0.198	0.024	0.158	0.158
Cortical Thickness (mm)	0.77	0.15	Age, Height	0.047		0.189	
			+ Body Mass	0.049	0.002	0.738	0.049
			+Grip Strength	0.060	0.013	0.337	-0.128
			+Adolescent Loading	0.072	0.025	0.178	-0.159
			+Adult Loading	0.048	0.001	0.846	0.024
Cortical Porosity (%)	1.20	0.67	Age, Height	0.050		0.169	
			+ Body Mass	0.091	0.041	0.084	-0.252
			+Grip Strength	**0.106**	**0.056**	**0.043**	**0.267**
			+Adolescent Loading	0.050	<0.001	0.946	0.008
			+Adult Loading	**0.133**	**0.083**	**0.013**	**0.294**

R^2 Total variance explained by the model, *ΔR^2* Additional variance explained by predictor, *p* significance of F-value change, *Beta* Standardized coefficient

3.4. Discussion

The first purpose of this study was to compare the current clinical measure of fracture risk, areal BMD measured by DXA, with FE-estimated bone strain. While aBMD and FE strain are correlated, over forty-eight percent of the variability in strain is left unexplained by its relationship with density. Thus, while aBMD may help identify those most in need of bone-building interventions, it does not fully describe the mechanical behavior of bone tissue under loading, which is critical to predicting cell-driven adaptation. Secondly, we aimed to identify measureable factors affecting bone strain and microstructure in healthy adult women. As intrinsic factors, age and height were significant predictors of trabecular number, trabecular and cortical BMD, and cross-sectional area but not total BMD, cortical thickness, cortical porosity or bone strain. Higher grip strength predicted lower cortical density and greater cross-sectional area and cortical porosity. Similar trends were seen in individuals with higher levels of site-specific adult loading, who tended to have more porous cortices and greater trabecular density. Neither grip strength nor adult loading significantly predicted strain, suggesting that differences in microstructure may compensate for each other with respect to mechanics. Finally, greater body mass predicted higher trabecular number and lower ultradistal strain. This suggests that within the normal BMI range, greater body mass is associated with improved mechanical behavior (i.e. lower strains under a given load), which may be attributed to more interconnected trabeculae supporting the distal region. Taken together, these results suggest that meaningful differences in bone morphology and mechanical behavior can be predicted by measurable subject characteristics.

In the current study, the contribution of upper extremity mechanical loading was considered through the inclusion of body mass, grip strength, and questionnaire-based physical

activity scores. These measures are to some extent related, as more active individuals may have greater muscle mass, which affects both grip strength and body mass. However, each has been previously related to bone quality and may characterize different aspects or modes of loading. For example, individuals with greater body mass experience larger compressive loads during weight-bearing exercises, to which bone adapts. This is consistent with the observation that heavier individuals experienced lower-magnitude strains for a given compressive force, indicating stronger bone. This also supports the previously reported effects of body mass on lower-extremity mechanical loading (Bareither et al., 2006), areal BMD (Gnudi et al., 2007), and fracture risk (Morin et al., 2009). Grip strength is a functionally useful measure of muscle mass and strength, and has been associated with bone density, macrostructure, and strength using peripheral QCT (Greenway et al., 2015; Hasegawa et al., 2001; Lorbergs et al., 2011). The relationship between muscle mass and bone quality is complex. Individuals may be genetically predisposed to having larger muscles and bones or build muscle over time, which drives bone adaptation to increasing forces. In the current study grip strength was positively related to cross sectional area but not strain, suggesting that grip strength may describe global body size rather than adaptation to specific loads.

Physical activity during growth and adulthood has been associated with improvements to bone structure (Kato et al., 2009). However, there is a lack of consensus whether loading during adolescence or early adulthood are more significant in determining peak bone mass (Bass et al., 1998; Daly and Bass, 2006; MacKelvie et al., 2002). We found that adolescent loading did not significantly contribute to the prediction of any bone structural or strength parameter, while adult loading was associated with favorable trabecular BMD. Variations between previous and the current results may be related to differences in questionnaires or anatomic sites. As opposed to

other skeletal loading questionnaires, the *armBLI* scores activities based on the magnitude and frequency of forearm loading rather than using ground reaction forces (Weeks and Beck, 2008) or estimations of loading at the hip and spine (Dolan et al., 2006). The relationship between loading and structure may also be site-specific, especially considering the differences in habitual loading between the upper and lower extremities.

Cortical porosity was significantly predicted by grip strength and adult loading score. However, correlation coefficients in both cases were negative, indicating that more active individuals with greater muscle mass have more porous cortices. This is somewhat surprising, as increased cortical porosity is associated with diminished structural integrity and increased fracture risk (Nishiyama et al., 2009). However, increased cortical porosity in this population may reflect more active remodeling units rather than degradation, driven by adaptation to increased applied loading.

The current study is not without limitations. Our sample size was relatively small, and subjects were recruited as part of a longitudinal study with inclusion criteria developed for the evaluation of a loading intervention. To target individuals who would most likely benefit from new loading, anyone already regularly participating in activities involving frequent, high impact loading of the upper extremities was excluded. Additionally, only women with a DXA total forearm T-score falling within the range -2.5 to 1.0 were included. Therefore, the current results cannot be generalized to women with extreme levels of upper-extremity loading, those with bone mass below the expected range for their age, or those with T-score more than 1.0 SD above the population mean. Additionally, there may have been limitations in applying the *armBLI* algorithm to adult women with retrospective rather than prospective, calendar-based training histories. The accuracy with which adolescent activity was recalled may have been limited and

introduced additional variability, contributing to the lack of significant predictions by adolescent loading. Further, the *armBLI* was validated against DXA areal density measurements (Dowthwaite et al., 2015) rather than volumetric structure or FE-derived strain. Considering these differences, a more rigorous validation of the *armBLI* may be required in adult women using CT-based measurements.

In summary, we have explored the relationships between clinical measures of bone quality, showing that the current gold-standard, DXA aBMD, does not capture the wide range of strains experienced during typical physiologic loading. Additionally, we have shown that individuals with higher levels of adult physical activity, grip strength, and body mass tend to have favorable bone microstructure structure. Women with higher body mass within a normal BMI range also had lower levels of strain under a given force, suggestive of adaptation to increased loads during functional activities. Overall, these results suggest the importance of engaging in bone-building behaviors in early adulthood, and contribute to the systematic design of prescribed loading interventions to better address the growing incidence of osteoporotic fracture.

Acknowledgements

This work was supported by the National Institutes of Health [grant number R01AR063691]; and the National Science Foundation [grant numbers DGE1106756 (MM), DGE1144804 (MM)]. The content is solely the responsibility of the authors and does not necessarily represent the official views of the funding agencies.

Chapter 4: Aim 2A, Relate Changes in Average Bone Macro- and Microstructure in the Distal Radius to Strain

Published in the *Journal of Bone and Mineral Research* as:
Troy, K.L., Mancuso, M.E., Johnson, J.E., Wu, Z., Schnitzer, T.J., Butler, T.A., 2020. Bone Adaptation in Adult Women Is Related to Loading Dose: A 12-Month Randomized Controlled Trial. J. Bone Miner. Res. 35, 1300–1312. https://doi.org/10.1002/jbmr.3999
Author Contributions: Study conceived by KLT and designed by KLT with assistance from TJS. Data collection by MEM, KLT, JEJ, and TAB. Data analysis and interpretation: MEM, KLT, JEJ, TAB, ZW, TJS. Manuscript writing and revision: KLT and MEM. Manuscript approval: MEM, KLT, JEJ, TAB, ZW, TJS.

4.1 Introduction

Exercise-based interventions have long been considered a viable option for preserving and enhancing bone strength (Howe et al., 2011) because bone adapts to best resist its habitual mechanical loading environment. Individuals who play sports and load with highly variable, off-axis loads (e.g., soccer, squash) have been observed to have better bone mechanical properties than those who do not (Martyn St James and Carroll, 2010; Weidauer et al., 2014). Clinical trials have shown that high impact activities such as jumping and hopping can improve bone density in growing children (Kontulainen et al., 2002) and young adults (Bailey and Brooke-Wavell, 2010) and maintain bone density in older adults (Korpelainen et al., 2006). However, while the evidence is strong that certain activities can increase bone density and structure in some individuals, it is not clear what specific mechanical factors govern the response. Furthermore, these factors interact with individual physiology to create a variable response, which is not well understood.

Animal in vivo loading models demonstrate that mechanical signals related to strain rate (LaMothe et al., 2005; Mosley and Lanyon, 1998; O'Connor et al., 1982) and magnitude (Mosley et al., 1997; Rubin and Lanyon, 1985) regulate bone adaptation. There is no consensus

on which specific signal(s) osteocytes sense; evidence supports lacunar-canalicular fluid flow (Donahue et al., 2003; Steck et al., 2003), flow of ions and the resulting electromagnetic signal (Kowalchuk and Pollack, 1993), direct damage of osteocytes (Hazenberg et al., 2006), microdamage of the surrounding bone that results in altered stress or strain (Burr et al., 1985; Muir et al., 2007) and other candidates (Nguyen and Jacobs, 2013). Regardless of the exact mechanism, all of these signals are closely related to (and driven by) mechanical strain. In vivo loading models have also established that, to elicit an adaptive response, the mechanical signal must be both dynamic and unaccustomed (Turner, 1998). Despite extensive animal literature, the degree to which mechanical strain magnitude and rate govern bone adaptation in humans has never been prospectively tested.

One major challenge is that bone strain is difficult to measure noninvasively. As a result, indirect measures, such as surveys for physical activity, which include weighting factors based on experimentally measured ground reaction force (GRF) and rate of GRF, have been proposed (Dolan et al., 2006; Weeks and Beck, 2008). Others have proposed "bone loading" indices that are based on similar measures (e.g. accelerometry) (Ahola et al., 2010; Turner and Robling, 2003). While these can be helpful in identifying the types of activities that should theoretically elicit an osteogenic response, they do not account for individual differences in bone structure, which have a large influence on bone strain (Bhatia et al., 2014). Alternatively, validated subject-specific FE models can provide accurate estimates of bone strain (Gray et al., 2008; Taddei et al., 2007; Troy et al., 2013) when the proper boundary conditions (magnitude, direction, and locations of application) are known.

Our previously validated upper extremity loading model (Troy et al., 2013) provides a well-controlled framework to understand the degree to which strain magnitude and rate influence

bone adaptation in people. In this model, an individual produces a compressive force through the radius by leaning onto the palm of the hand. Feedback is given using a scale or load cell, and individuals are given sound cues to assist in achieving a regular and consistent load/unload cycle. In a pilot group of 19 young adult women, we found that a mean energy equivalent strain of 734 ± 238 με applied 50 cycles per day, 3 days per week elicited modest increases in distal radius bone mineral content (BMC) and prevented seasonal loss of BMC observed in a control group (Troy et al., 2013). We also observed that high strain regions of the radius gained significantly more bone than low strain regions, suggesting that the local mechanical signals were, in part, driving the response (Bhatia et al., 2015). Although these results were promising, the study was limited in scope and duration.

Here, our purpose was to quantify the degree to which bone strain influences bone adaptation in the upper extremity of healthy adult women during a twelve-month prospective study period. Based on previous findings in humans (Bhatia et al., 2015; Troy et al., 2013) and small animals (Donahue et al., 2003; Hsieh and Turner, 2001; Mosley and Lanyon, 1998), we hypothesized that (1) bone accrual would be proportional to strain magnitude and strain rate, and (2) structural changes would include increased cross-sectional area and cortical thickness, and increased trabecular bone mass near the endosteal surface.

4.2 Methods

4.2.1 Participant Characteristics

Healthy women age 21-40 were recruited from the community for this mechanistic randomized controlled trial (NCT04135196). This group is at peak bone mass (Baxter-Jones et al., 2008; Henry et al., 2004), and compared to men, have increased risk of osteoporosis later in life. An initial telephone interview of 497 potential participants was used to exclude individuals

with self-reported BMI outside the range 18-29 kg/m^2, irregular menstrual cycles, no regular calcium intake, use of medications affecting bone health, history of radius fracture or injury to the non-dominant shoulder or elbow, or regular participation (>2 times per month) in activities with high loads at the forearm (e.g. gymnastics, volleyball). These criteria were selected to reduce possible adverse events and exclude individuals who were unlikely to respond to, or achieve, the loading stimulus. After a positive telephone interview, 159 potential participants provided written informed consent to be screened with dual energy x-ray absorptiometry (DXA; Hologic; Marlborough, MA) of the non-dominant radius and measurement of circulating levels of 25-hydroxyvitamin vitamin D and estradiol. Exclusion criteria were 25-hydroxyvitamin D serum levels below 20 ng/ml, and DXA T-score outside the range -2.5 to 1.0. In total, 102 participants were eligible after screening and opted to enroll in this institutionally approved study. All participants were recruited at a single site between December 2013 and June 2017 via social media, posters, email newsletters, and word of mouth at nearby universities, hospitals, and community events. The trial was conducted in accordance with Good Clinical Practice Guidelines. Compliance and adverse events data were reviewed annually with a study monitor.

4.2.2 Study Design

This was a 12 month, prospective, mechanistic randomized controlled trial that utilized a distal radius compressive loading intervention to investigate the effect of strain on bone adaptation. After meeting eligibility criteria from screening tests, participants were assigned into either control or one of two exercise arms that manipulated strain magnitude (Experiment 1: low and high strain magnitude) or strain rate (Experiment 2: low and high strain rate, detailed in Table 4.2). Group assignments were made by drawing slips of paper from an envelope (e.g. LOW, HIGH, CONTROL), and control participants were randomized during Experiment 1.

Participants were blinded to the study hypotheses and were not aware of the exercises or instructions given to groups other than their own. Based on pilot data (Troy et al., 2013) and simulations that showed little benefit for loading more than 100 cycles in a single bout (Bhatia et al., 2013), exercise groups were instructed to apply 100 cycles of axial force (one bout), four times weekly, by leaning onto the palm of the hand. While participants were given a goal of four bouts per week, our experimental goal was to achieve an average of three bouts per week (75% compliance), based on the positive response we previously observed with this frequency of loading. Loading was accomplished using a custom device, consisting of a uniaxial load cell (Standard Load Cells; Gujarat, India), data logger (DATAQ DI-710, DATAQ Instruments Inc.; Akron, OH), and LED indicators that lit up when the applied force was within ±10 N of the target value. To allow participants to get used to the intervention, reduce the possibility of wrist soreness, and give the investigative team time to assign subject-specific forces, those in the exercise groups were assigned a nominal 200 N target force magnitude for the first three months of loading. Thereafter, a subject-specific target force was prescribed to achieve target strain parameters based on computed-tomography based finite element (FE) models (described below; Figure 4.1).

Due to considerations of participant safety, no participant was assigned a force larger than 450 N or what she could comfortably and consistently apply, even if the force required to achieve the target strain was larger than that. Partway through the study, in response to reports of wrist soreness from some participants, this upper limit was reduced to 350 N. Loading magnitude was controlled by adjusting LED indicators on the device, while loading rate and cycle period were controlled using verbal instructions (e.g. “load slowly and evenly” versus “load as rapidly as possible”) and sound cues recorded on a portable voice recorder. Sound cues consisted of 100

beeps (long beeps for the slow rate group, short beeps for the fast rate group) occurring at 2-second intervals. Compliance was monitored every three months using data logger recordings and log books maintained by participants.

The primary outcome was 12 month change in integral ultradistal radius bone mineral content and bone mineral density (iBMC and iBMD), as measured by quantitative CT analysis (QCT). Secondary outcomes included 12 month changes in other regions, and microstructural measures with interim timepoints. A power analysis based on pilot data (Troy et al., 2013) determined that 20 participants per group would have 80% power to detect a 12 month change in BMC of 1.0±1.1%. Partway through the experiment the randomization ratio was adjusted to over-sample the loading groups (increasing the target enrollment by 6 participants) and to under-sample the control group (reducing the target by 4 participants) going forward. This was to ensure that a sufficient number of participants had loading doses that were non-zero, even if a subset of those assigned to a loading group were non-compliant.

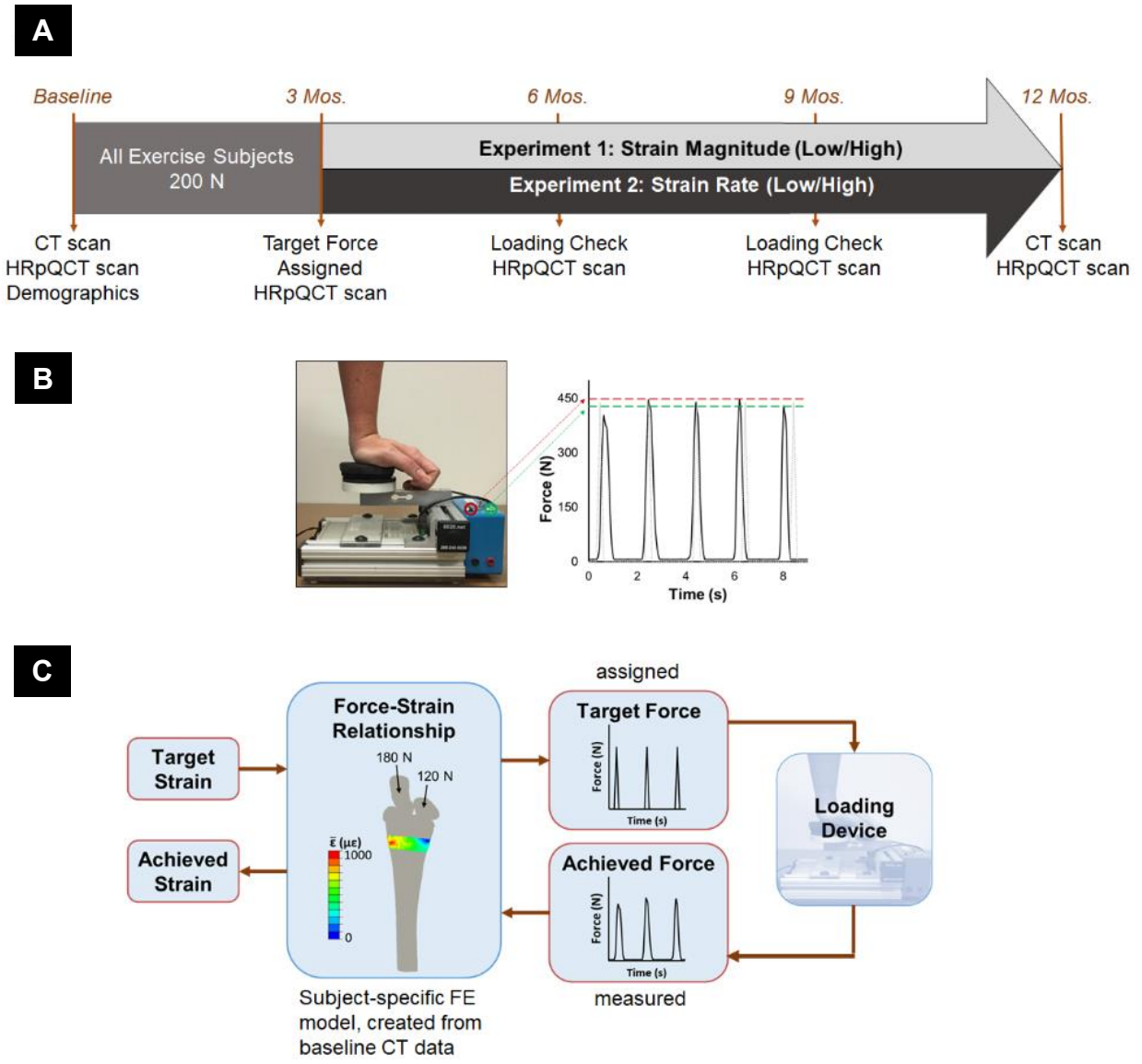

Figure 4.1: (A) Summary of the data collection timeline for participants assigned to exercise groups; **(B)** Loading device used to manipulate applied force magnitude via feedback lights (green set to target force minus 10 N, red to target force plus 10 N). Loading frequency was controlled using pre-recorded auditory cues. The force vs. time curve shows a representative load cell signal (black) versus ideal assigned loading stimulus (gray), with dashed lines indicating the forces at which feedback is given; **(C)** Linear FE model used to estimate energy equivalent strain in the transverse section matching the imaged site. The force-strain relationship was used to assign each participant a target force and calculate the resulting strain from load cell recordings.

4.2.3 Data Collection

Demographic information and imaging data (computed tomography; CT, and high resolution peripheral computed tomography; HRpQCT) were collected at baseline. Hand

dominance was determined using the Edinburgh inventory (Oldfield, 1971). CT was collected at baseline and 12 months. HRpQCT was updated every three months during the study period.

4.2.4 High Resolution Peripheral Quantitative Computed Tomography

Changes in radius microstructure were assessed using HRpQCT (Xtreme CT I, Scanco Medical; Brüttisellen, Switzerland). Bilateral scans were acquired in a standard 9.02 mm region consisting of 110 transverse slices (82 µm isotropic voxel size) beginning 9.5 mm proximal to the distal endplate. Structural changes were measured for the mutually overlapping region, using the manufacturer's 2D region-matching algorithm. Total mean cross-sectional area (CSA; mm^2) and total volumetric bone mineral density (Tt.BMD; $mgHA/cm^3$) were measured. Trabecular number (Tb.N; mm^{-1}), thickness (Tb.Th; mm) and BMD (Tb.BMD; $mgHA/cm^3$) were measured using the manufacturer's standard analysis protocol. The trabecular region was further divided into inner (central 60%; Tb.BMDinn) and outer regions (outer 40%; Tb.BMDmeta). Cortical vBMD (Ct.BMD; $mgHA/cm^3$) and cortical thickness (Ct.Th; mm) were calculated using the dual-threshold method (Buie et al., 2007; A. J. Burghardt et al., 2009; Burghardt et al., 2010). In our lab, the coefficient of variation (CV) for densitometric variables is < 0.3%. The CVs of microstructural variables range from 0.4-4.7%. All HRpQCT analyses were blinded to group assignment.

4.2.5 Quantitative Computed Tomography Analysis

At baseline and 12 months, CT scans of the distal-most 12 cm of the each forearm were acquired (GE Brightspeed, GE Medical; Milwaukee, WI; 120 kV, 180 mA, voxel size 234 µm x 234 µm x 625 µm). A calibration phantom (QRM; Moehrendorf, Germany) with known calcium hydroxyapatite equivalent concentrations was included in the field of view to relate CT attenuation (Hounsfield Units) to equivalent bone density (g/cm^3).

Changes in bone macrostructure were quantified from CT data using Mimics v15.1 (Materialise; Leuven, Belgium). Follow-up scans were registered to baseline using rigid image registration and the periosteal surface was defined using a 0.175 g/cm^3 density threshold (Troy et al., 2013). Based on methods previously established (Edwards et al., 2014), we defined integral and endocortical compartments (denoted in QCT variable names with prefixes *i* and *ec*). Briefly, the integral compartment consisted of all voxels enclosed within the periosteal surface. The endocortical compartment was comprised of the subset of integral voxels located within 2.5 mm of the periosteal surface (including all cortical bone). For each compartment bone volume (BV; cm^3), bone mineral content (BMC; g) and volumetric bone mineral density (BMD; g/cm^3) were calculated. QCT parameters for the trabecular compartment were not analyzed. Instead, HRpQCT data were analyzed, which provided a greater level of detail. Using previously established methods (Troy et al., 2013), we also calculated compressive strength index (CSI; g^2/cm^4), and bending strength index (BSI, cm^3). All parameters were calculated for total and ultradistal regions except for strength measures, which were only calculated for the ultradistal region. The total region extended 45 mm proximal from the subchondral plate and distally to the styloid tip; the ultradistal region extended 9.375 mm proximal from the subchondral plate. The CV for these QCT measures in our lab ranges from 0.7 to 2.3% (ultradistal region); 0.3 to 0.6% (total region); 0.9 to 2.3% (strength indices). All QCT analyses were blinded to group assignment.

4.2.6 Continuum Finite Element Modeling

Finite element models were constructed from the QCT scans using methods validated with cadaveric mechanical testing (Edwards and Troy, 2012). Models were used to simulate one cycle of axial loading to determine the subject-specific force needed to achieve the desired target

strain within the distal radius using Abaqus CAE (v2016, Simulia, Dassault Systèmes; Vélizy-Villacoublay, France). We used energy-equivalent strain as the measure of interest, since it provides a scalar value that has been related to bone adaptation (Bhatia et al., 2015; Mikić and Carter, 1995). Force values were assigned to each participant based on the maximum energy-equivalent strain within the ultra-distal region of the radius, as calculated using the continuum FE model for that participant. This value was used to adjust the custom loading device so that the LEDs would light up when that individual achieved her target strain. At all subsequent time points, data recorded from the load cell were applied to the FE model to calculate the *actual* mean strain within the region achieved by the participant, based on applied force (Figure 4.1C).

4.2.7 Load Cell Analysis

At each follow-up visit, load cell recordings were analyzed using custom code in MATLAB (Mathworks; Natick, MA). The beginning, peak and end of each loading waveform were identified using a custom algorithm, and the resulting frequency spectrum calculated using Fast Fourier Transform. Based on subject-specific FE models, frequency data were used to calculate the loading stimulus using the relationship suggested by Turner (Turner, 1998),

$$E = \sum_{i=0\ Hz}^{5\ Hz} \varepsilon_i f_i \qquad \textbf{(4.1)}$$

where E is the strain stimulus for the entire loading bout, f_i is the frequency value for bin i, and ε_i is the peak-to-peak energy-equivalent strain magnitude of frequency component i. A cutoff of 5 Hz was selected based on analysis of the load cell frequency content, which showed that over 95% of the signal power was <2 Hz. We also calculated peak-to-peak strain magnitude and average strain rate for the loading portion of each cycle for each participant and loading bout. Because voluntary loading produced variable and sometimes inconsistent loading signals, we

evaluated several candidate measures of "loading dose", which was intended to serve as an overall metric of mechanical loading, considering strain parameters and protocol compliance. We considered the following candidate measures of "loading dose":

$$\text{StrainStim} = E^{*}[\#\text{bouts}] \quad \textbf{(4.2)}$$

$$\text{Strain\_Mag} = \text{mean(Peak-to-Peak Strain Magnitude)}^{*}[\#\text{bouts}] \quad \textbf{(4.3)}$$

$$\text{Strain\_Rate} = \text{mean(Strain Rate)}^{*}[\#\text{bouts}] \quad \textbf{(4.4)}$$

$$\text{Strain\_MagRate} = \text{mean(Peak-to-Peak Strain Magnitude)}^{*}\text{mean(Strain Rate)}^{*}[\#\text{bouts}] \quad \textbf{(4.5)}$$

4.2.8 Statistical Analysis

Descriptive statistics were calculated and data normality was assessed. Group demographics and loading dose received were compared using ANOVA and Bonferroni-corrected *post hoc* t-tests. The hypothesis that bone mass would increase proportionally to the applied strain magnitude (Experiment 1) was tested in two ways. First, participants were analyzed by group using intention to treat (control vs. low and high strain magnitude groups). For this analysis, the 12-month change in ultradistal iBMC was analyzed as the primary dependent variable in a linear regression model with coefficients representing contrasts between each of the two experimental groups and the control group. The secondary outcome measures were also compared between groups using regression models based on the change scores at each of the time points (change from baseline). Similar analyses were performed to examine the effect of strain rate on bone (Experiment 2).

In the second analysis, we considered "loading dose" achieved by each participant as a continuous variable, with the dose for control participants being zero. Because dose includes both magnitude and frequency components, all groups were combined into a single regression model with the 12-month change in radius ultradistal iBMC as the primary outcome. The

secondary outcome measures were also considered. To test the hypothesis that bone structural changes would include increased cross-sectional area and cortical thickness, and increased endocortical density, these factors were treated as dependent variables in linear regression models, similar to the previous analyses. We assessed the F-statistic of the overall regression, and the t-statistic of each explanatory variable, considering α=0.05 to be significant. As an exploratory *post hoc* analysis, participants were ranked by change in ultradistal iBMC, and then divided into tertiles (greatest, medium, and least gain in iBMC). To gain insight into what factors were associated with the greatest gains in ultradistal iBMC, participant demographics, baseline values, and metrics describing loading dose were compared between the tertiles using ANOVA. Where significant effects were observed, Bonferroni-adjusted *post hoc* t-tests were used to compare values between individual tertiles.

4.3 Results

4.3.1 Participant Characteristics

One hundred and two women, age: 28 ± 6 years, height: 165 ± 6 cm, mass: 64 ± 9 kg were enrolled and randomized. Baseline characteristics are summarized in Table 4.1 and were not different between groups. Sixty-six participants completed the study and were included in the 12-month analysis. Seventy-seven participants had some follow-up data available and were included in our analyses of interim time points (Figure 4.2). On average, participants assigned to one of the loading groups completed 85 (SD: 92) loading bouts in total (41% of the total prescribed umber). However, the total number of loading bouts varied considerably, from 0 to 357. Strain magnitude and rate were significantly higher in the high versus low groups for Experiments 1 and 2, respectively ($p \leq 0.03$). However, the high strain magnitude and rate groups

failed to achieve the prescribed target values. All measures of loading dose were significantly greater for loading groups than for controls ($p \leq 0.046$; Table 4.2)

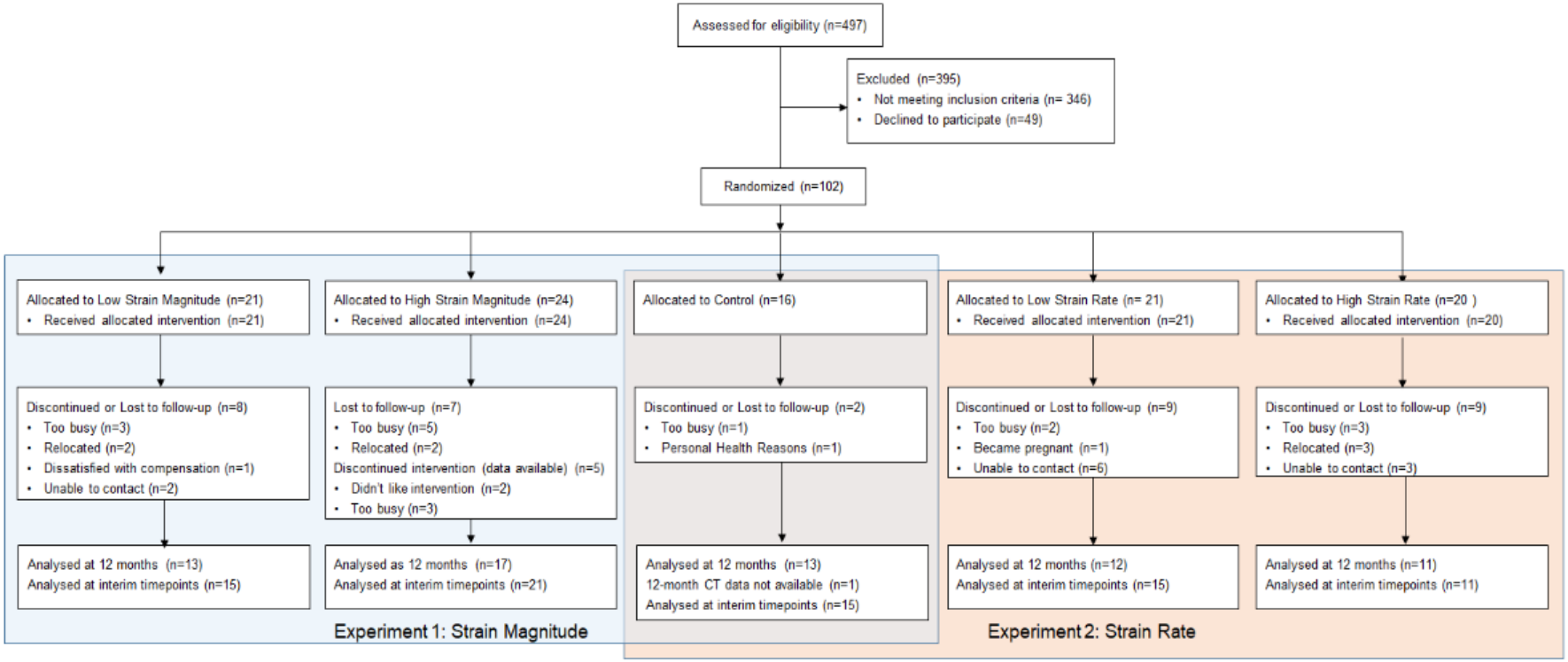

Figure 4.2: Consort chart describing participant flow through recruitment, data collection, and analysis.

Table 4.1: Mean (SD) baseline participant characteristics by group.

Treatment Group	Low Strain Magnitude n=21	High Strain Magnitude n=24	Low Strain Rate n=21	High Strain Rate n=20	Control n=16	Total n=102
Participant Characteristics						
Age (years)	30.3 (5.5)	29.3 (6.3)	27.2 (5.1)	27.1 (5.4)	28.2 (5.3)	28.4 (5.6)
Height (cm)	165.8 (6.1)	161.9 (6.1)	165.0 (6.2)	164.9 (5.7)	167.3 (7.6)	164.8 (6.4)
Body Mass (kg)	65.2 (8.8)	61 (5.9)	65.4 (9.8)	65.4 (10.0)	65 (8.9)	64.3 (8.7)
Serum Vitamin D (ng/mL)	33.7 (9.9)	31.5 (8.9)	31.1 (12.2)	29.1 (7.8)	33.2 (7.5)	31.7 (9.5)
DXA total forearm aBMD (g/cm^2)	0.586 (0.0)	0.568 (0.03)	0.576 (0.04)	0.569 (0.04)	0.570 (0.04)	0.574 (0.04)
DXA total forearm T-score	0.138 (0.8)	-0.187 (0.63)	0.138 (0.76)	-0.175 (0.74)	-0.162 (0.67)	-0.087 (0.70)
Ethnicity n (%)						
Hispanic or Latino	2 (10)	5 (21)	1 (5)	2 (10)	2 (13)	12 (12)
Non-Hispanic	19 (90)	18 (75)	20 (95)	18 (90)	14 (87)	89 (87)
Not Reported	0 (0)	1 (4)	0 (0)	0 (0)	0 (0)	1 (1)
Race n (%)						
African American	0 (0)	0 (0)	0 (0)	1 (5)	0 (0)	1 (1)
Caucasian	16 (76)	17 (71)	16 (76)	14 (70)	13 (81)	76 (75)
Asian	3 (14)	2 (8)	4 (19)	3 (15)	0 (0)	12 (12)
Pacific Islander	0 (0)	0 (0)	0 (0)	1 (5)	0 (0)	1 (1)
More Than One Race	1 (5)	2 (8)	1 (5)	1 (5)	2 (13)	7 (7)
Not Reported	1 (5)	3 (13)	0 (0)	0 (0)	1 (6)	5 (5)

Table 4.2: Mean (SD) baseline of the pooled data, and percent change at 12 months in QCT variables, by group.

Treatment Group	Low Strain Magnitude n=21	High Strain Magnitude n=24	Low Strain Rate n=21	High Strain Rate n=20
Prescribed Loading				
Number of Sessions	208	208	208	208
Ultradistal Mean Strain Magnitude (με)	490 (103)	748 (143)	632 (138)	641 (157)
Strain Rate (με/s)	1485 (312)	2267 (434)	790 (173)	6410 (1570)
Achieved Loading				
Number of Participants Completing No Loading	2	4	6	4
Number of Sessions	126 (100)	81 (76)	70 (71)	83 (115)
Ultradistal Mean Strain Magnitude (με)*	456 (125)	572 (171)	549 (147)	552 (147)
Ultradistal Median Strain Magnitude (με)*	376 (86)	468 (135)	458 (113)	447 (105)
Ultradistal Maximum Strain Magnitude (με)*	2074 (1199)	2291 (775)	2372 (883)	2494 (1108)
Ultradistal Mean Strain Rate (με/s)*	1018 (604)	1510 (1094)	945 (499)	1698 (1167)
StrainStim ($\mu\varepsilon*s^{-1}*Files*10^{-7}$)	141 (193)	118 (240)	36 (73)	78 (14)
Strain_MagRate ($\mu\varepsilon^{2}*s^{-1}*Files*10^{-5}$)	319 (353)	428 (651)	204 (255)	407 (533)
Strain_Mag ($\mu\varepsilon*Files*10^{-2}$)	493 (435)	463 (518)	343 (364)	413 (522)
Strain_Rate ($\mu\varepsilon*s^{-1}*Files*10^{-3}$)	130 (135)	141 (186)	71 (90)	156 (214)

*Calculations of Ultradistal Strain Magnitude and Strain Rate excluded participants who completed no loading.
Number of Sessions and loading dose calculations include all participants randomized in each group
Strain magnitude calculated as energy equivalent strain, which is a positive scalar

4.3.2 Adverse Events

There were no serious adverse events. Temporary soreness of the loaded wrist was the most commonly reported adverse event (28% of participants; 29 reports). Two of these participants noted that this briefly affected their daily activities (did fewer chores or avoided exercises that weighted the hands), and one took ibuprofen. Eight participants reported soreness at other sites (elbow, shoulder, hand), which included aggravation of previous injuries (e.g. shoulder pain from an injury that was several years old) that they thought might be due to the intervention. All participants reported that soreness resolved within 3-14 days. Five participants reported that pain from previous injuries temporarily prevented them from completing the assigned loading, but did not believe this was caused or aggravated by the intervention.

Radiology reports indicated no visible changes in wrist anatomy between initial and 12-month visits. Lack of time or relocation were the most common reasons expressed for dropping out (22 participants).

4.3.3 Effect of Strain on 12-month Change in Bone Mass and Structure (QCT)

None of the regression models that included strain magnitude groups were significant for overall model fit, although the membership in the low strain magnitude group was associated with slight gains in ultradistal iBMC ($p=0.041$), and consistent and significant increases in CSA, iBV and ecBV that indicated periosteal expansion (Table 4.3). Achieved strain magnitude was only 25% higher for the high versus low group, and the low magnitude group completed more loading sessions on average than the high magnitude group. Therefore, the favorable outcomes in the low group may be attributable to practical limitations of the assigned loading regimen. The groups in which strain rate was manipulated had greater 12-month changes in QCT variables than those in which strain magnitude was manipulated (Figure 4.3). In models comparing the low and high strain rate groups to the control group, both loading groups were significantly and positively associated with the increases to total and ultradistal iBMC, iBMD, ecBMC, and ecBMD. Fifty-six and 52% of the variance in change to ultradistal and total iBMD, respectively, was explained by group membership of these participants (Table 4.4). Increases to ultradistal compressive and bending strength indices were significantly and positively associated with Experiment 2 loading group membership.

Table 4.3: Mean (SD) baseline of the pooled data, and percent change at 12 months in QCT variables, by group.

	Total (n=66) **Baseline**	**Control** (n=13) **%ΔV5**	**Low Magnitude** (n=13) **%ΔV5**	**High Magnitude** (n=17) **%ΔV5**	**Low Rate** (n=12) **%ΔV5**	**High Rate** (n=11) **%ΔV5**
Ultradistal						
iBV (cm^3)	3.84 (0.40)	-1.17 (2.51)	**0.75 (2.14)**	-0.01 (2.23)	-0.29 (1.29)	0.35 (1.86)
iBMC (g)	0.91 (0.15)	-1.31 (2.68)	**0.46 (1.52)**	-0.33 (2.03)	**2.73 (2.07)**	**3.42 (2.21)**
iBMD (g/cm^3)	0.24 (0.03)	-0.59 (2.08)	-0.23 (0.96)	-0.33 (1.19)	**3.03 (1.08)**	**3.07 (1.46)**
ecBV (cm^3)	1.99 (0.15)	-0.41 (1.49)	**0.89 (1.39)**	0.34 (1.58)	-0.01 (1.25)	0.41 (1.46)
ecBMC (g)	0.63 (0.18)	-0.19 (4.87)	0.12 (2.46)	-0.10 (2.62)	**4.84 (3.64)**	**4.45 (3.47)**
ecBMD (g/cm^3)	0.31 (0.08)	0.21 (4.52)	-0.74 (2.79)	-0.43 (2.59)	**4.85 (3.46)**	**4.03 (3.30)**
Total						
iBV (cm^3)	12.96 (1.55)	-0.06 (0.47)	-0.25 (0.52)	-0.13 (0.45)	0.16 (0.64)	0.38 (0.41)
iBMC (g)	5.10 (0.60)	-0.23 (1.20)	-0.45 (0.80)	-0.19 (0.78)	**1.97 (0.86)**	**1.93 (0.75)**
iBMD (g/cm^3)	0.39 (0.04)	-0.17 (1.14)	-0.19 (0.58)	-0.06 (0.78)	**1.81 (0.63)**	**1.55 (0.86)**
ecBV (cm^3)	8.24 (0.72)	0.17 (0.71)	-0.07 (0.57)	0.18 (0.44)	0.45 (0.62)	0.35 (0.64)
ecBMC (g)	4.09 (0.55)	0.15 (1.78)	-0.26 (1.11)	0.00 (1.01)	**2.06 (1.40)**	**1.72 (1.37)**
ecBMD (g/cm^3)	0.50 (0.05)	-0.02 (1.28)	-0.20 (0.76)	-0.18 (0.98)	**1.60 (0.84)**	**1.36 (0.83)**
Ultradistal Strength						
CSA (cm^2)	4.15 (0.42)	-0.67 (1.67)	**0.65 (1.45)**	0.00 (1.48)	-0.26 (1.23)	0.35 (1.75)
CSI (g^2/cm^4)	0.24 (0.07)	-1.81 (4.40)	0.18 (1.96)	-0.65 (2.85)	**5.90 (3.05)**	**6.62 (3.26)**
BSI (cm^3)	0.12 (0.03)	-0.59 (4.31)	0.32 (1.90)	-0.29 (2.30)	**4.74 (2.44)**	**4.81 (2.70)**

Data presented as mean (SD). Bold indicates significant regression coefficient representing contrast with control group for raw change

Baseline is for participants with follow-up data available

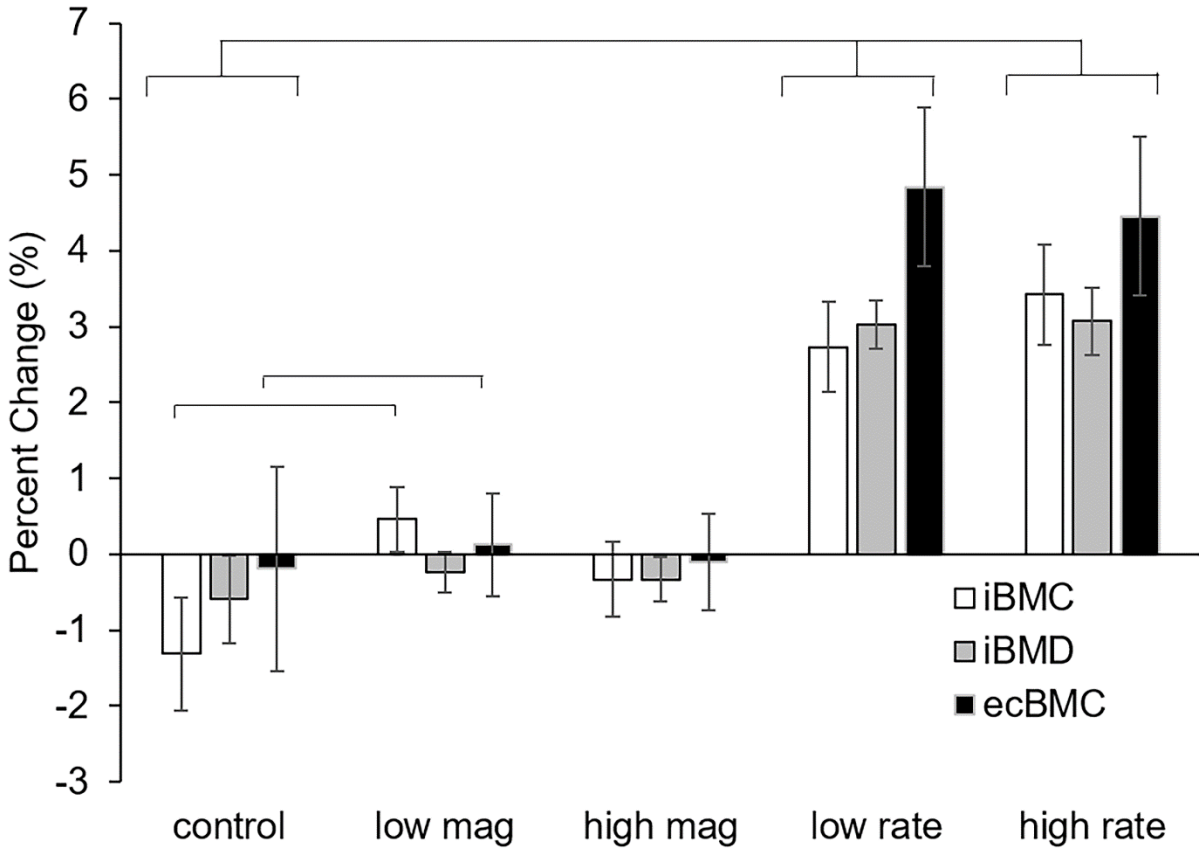

Figure 4.3: 12-month changes in QCT-derived primary outcome variables. Both the low and high rate groups had significant differences compared to the control group in all three variables.

Table 4.4: Standardized regression coefficients for QCT, by group and by loading dose. Low1 and High1 indicate low and high strain magnitude groups from Experiment 1. Low2 and High2 indicate low and high strain rate groups from Experiment 2.

	Model Definition	R^2	β_1	β_2
UD iBMC (g)	β1*Low1+β2*High1+ε	0.101	**0.374**	0.221
	β1*Low2+β2*High2+ε	**0.438**	**0.599**	**0.678**
	β1*StrainStim+ε	0.039	0.197	
	β1*Strain_MagRate+ε	**0.117**	**0.342**	
	β1*Strain_Mag+ε	**0.124**	**0.352**	
	β1*Strain_Rate+ε	**0.102**	**0.320**	
UD iBMD (g/cm^3)	β1*Low1+β2*High1+ε	0.009	0.091	0.101
	β1*Low2+β2*High2+ε	**0.563**	**0.739**	**0.716**
	β1*StrainStim+ε	0.003	0.051	
	β1*Strain_MagRate+ε	0.041	0.203	
	β1*Strain_Mag+ε	0.045	0.212	
	β1*Strain_Rate+ε	0.044	0.209	
Total iBMC (g)	β1*Low1+β2*High1+ε	0.019	-0.119	0.028
	β1*Low2+β2*High2+ε	**0.545**	**0.743**	**0.687**
	β1*StrainStim+ε	0.001	-0.028	
	β1*Strain_MagRate+ε	0.008	0.091	
	β1*Strain_Mag+ε	0.011	0.106	
	β1*Strain_Rate+ε	0.012	0.109	
Total iBMD (g/cm^3)	β1*Low1+β2*High1+ε	0.005	-0.018	0.059
	β1*Low2+β2*High2+ε	**0.520**	**0.756**	**0.627**
	β1*StrainStim+ε	0.001	0.027	
	β1*Strain_MagRate+ε	0.023	0.153	
	β1*Strain_Mag+ε	0.036	0.189	
	β1*Strain_Rate+ε	0.012	0.166	

Bold For R^2 indicates $p<0.05$ for F-test of overall model fit
Bold For β_1 or β_2 indicates $p<0.05$ for t-test of significance for coefficient

In models examining the effects of loading dose on the changes to bone, ultradistal iBMC, iBV, and ecBV were all positively and consistently associated with measures of loading dose, especially Strain_MagRate (Figure 4.4A). However, in all cases, loading dose explained less than 15% of the variance in the change values. The StrainStim metric was not related to change in any variable.

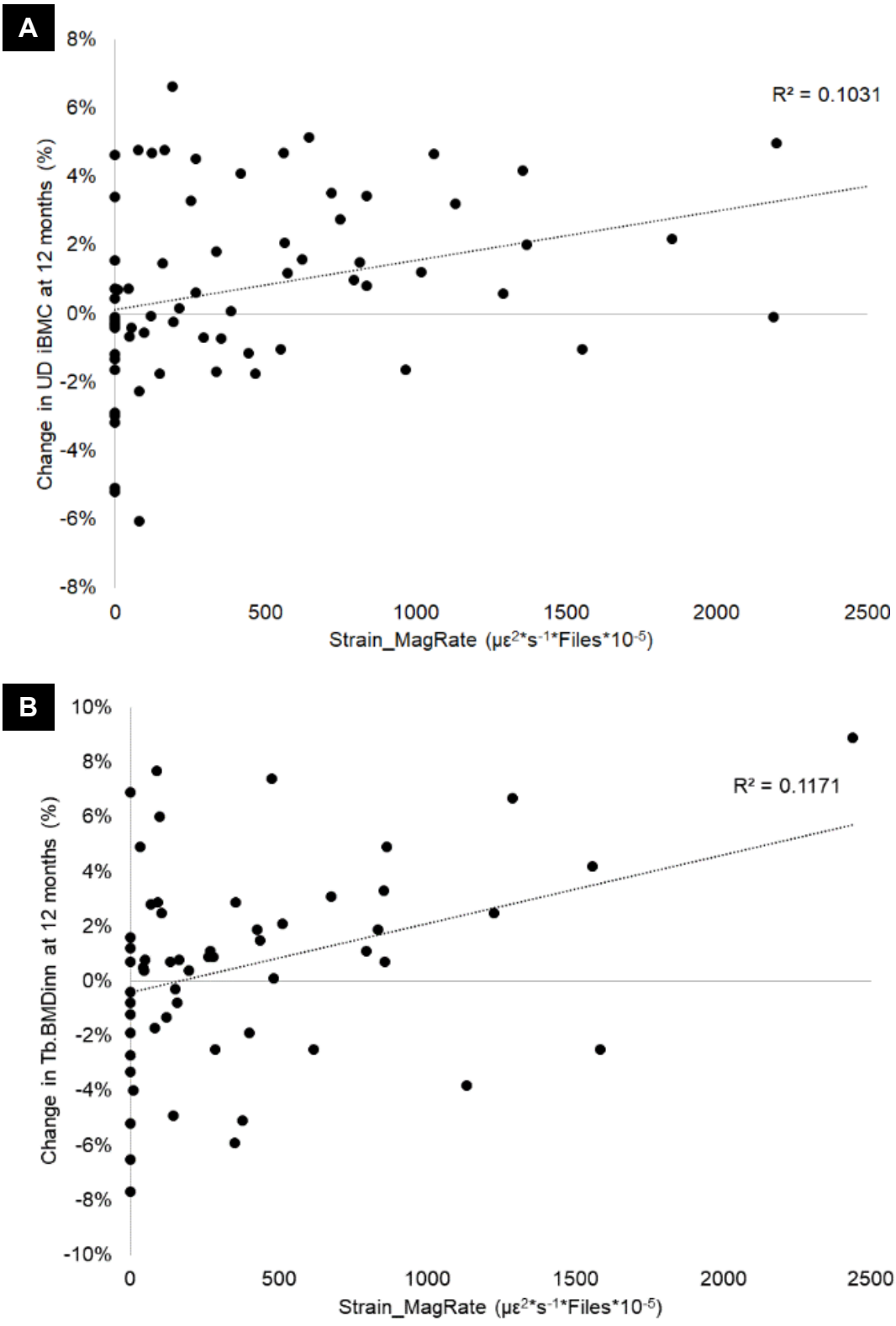

Figure 4.4: (A) Percent change in ultradistal iBMC versus Strain_MagRate. (**B)** Percent change in Tb.BMDinn versus Strain_MagRate. Both plots represent 12-month change for all participants with available data.

4.3.4 Effect of Strain on 3, 6, 9, and 12 Month Bone Microstructure (HRpQCT)

After three months, membership in the low and high magnitude loading groups explained up to 17% of the increases in Tt.BMD compared to the control group (Table 4.5). Similarly, high loading rate was significantly associated with three-month increases to Tt.BMD, Ct.BMD and Ct.Th. Strain_MagRate, Strain_Mag, and Strain_Rate were all significant predictors for the change in Tt.BMD and Ct.Th, although 12% or less of the variance in these measures was explained by loading dose.

At six months, none of the microstructural changes were different between groups. However, at nine months, the low strain magnitude group was significantly and positively associated with increases to Tt.BMD, Tb.BMD, Tb.BMDinn, and Tb.BMDmeta (Figure 4.5). Similarly, the high strain magnitude and low strain rate groups were positively associated with changes to Tb.BMDinn. Strain_MagRate and Strain_Rate were positively associated with the increase to Tb.BMDinn in nine months. These changes persisted at 12 months, with Strain_MagRate being associated with increases to Tb.BMD and Tb.BMDinn (Figure 4.4B).

Table 4.5: Mean (SD) of baseline and percent changes of HRpQCT measures during each visit (V1 at baseline through V5 at 12 months), by group.

		Baseline		%ΔV2		%ΔV3		%ΔV4		%ΔV5	
Control	**Tt.BMD (g/cm^3)**	292.46	(45.29)	-1.35	(1.16)	1.29	(2.90)	0.36	(2.25)	1.52	(3.67)
	Tb.BMD (g/cm^3)	168.94	(36.08)	-1.21	(1.75)	-0.54	(2.14)	-1.78	(2.30)	-0.15	(3.61)
	Tb.BMD$_{Meta}$ (g/cm^3)	226.58	(37.12)	-0.71	(1.19)	-0.14	(2.09)	-0.83	(1.88)	0.76	(3.75)
	Tb.BMD$_{Inn}$ (g/cm^3)	129.13	(37.03)	-2.01	(2.87)	-1.04	(2.49)	-2.96	(3.08)	-1.43	(3.91)
	Ct.BMD (g/cm^3)	851.54	(42.73)	-0.79	(0.80)	1.46	(2.65)	1.83	(2.03)	2.14	(1.69)
	Tb.N (mm^{-1})	2.09	(0.27)	-1.40	(5.81)	0.55	(12.01)	2.20	(7.55)	4.70	(7.90)
	Tb.Th (mm)	0.07	(0.01)	0.40	(4.94)	0.19	(11.92)	-3.35	(7.55)	-4.18	(8.63)
	Ct.Th (mm)	0.72	(0.09)	-0.42	(2.46)	0.47	(2.46)	-0.33	(2.94)	0.49	(3.38)
	Ct.Po (%)*	0.01	(0.01)	-3.61	(15.33)	3.29	(18.50)	10.98	(21.33)	12.47	(18.81)
Low Magnitude	**Tt.BMD (g/cm^3)**	305.66	(56.40)	**0.39**	**(1.98)**	0.70	(3.06)	**2.59**	**(2.28)**	1.23	(2.71)
	Tb.BMD (g/cm^3)	157.28	(28.74)	-0.23	(1.73)	0.62	(2.41)	**1.06**	**(1.46)**	-0.04	(1.96)
	Tb.BMD$_{Meta}$ (g/cm^3)	220.84	(28.96)	-0.08	(1.74)	0.55	(2.01)	**0.91**	**(1.94)**	-0.37	(1.57)
	Tb.BMD$_{Inn}$ (g/cm^3)	113.34	(30.02)	-0.42	(2.55)	0.71	(3.36)	**1.35**	**(1.55)**	0.43	(3.13)
	Ct.BMD (g/cm^3)	883.92	(46.19)	0.38	(1.57)	0.50	(1.77)	2.58	(2.28)	2.12	(1.84)
	Tb.N (mm^{-1})	1.95	(0.24)	-2.56	(6.43)	-1.86	(8.31)	0.57	(8.51)	-1.07	(10.21)
	Tb.Th (mm)	0.07	(0.01)	2.74	(6.21)	2.99	(7.36)	0.99	(7.34)	1.90	(10.31)
	Ct.Th (mm)	0.81	(0.17)	0.23	(2.36)	-0.09	(4.64)	0.28	(2.05)	-0.98	(3.25)
	Ct.Po (%)*	0.01	(0.00)	-7.19	(13.85)	11.33	(30.73)	7.59	(34.34)	9.83	(32.27)
High Magnitude	**Tt.BMD (g/cm^3)**	292.59	(55.28)	**0.29**	**(1.92)**	0.90	(1.94)	1.98	(1.84)	2.16	(3.07)
	Tb.BMD (g/cm^3)	162.39	(31.41)	0.20	(2.16)	-0.32	(2.30)	-0.23	(1.99)	0.72	(2.39)
	Tb.BMD$_{Meta}$ (g/cm^3)	220.08	(30.15)	0.05	(1.98)	-0.34	(1.71)	-0.25	(1.17)	0.47	(1.84)
	Tb.BMD$_{Inn}$ (g/cm^3)	122.55	(32.84)	0.43	(2.80)	-0.36	(3.52)	**-0.26**	**(3.30)**	0.95	(3.65)
	Ct.BMD (g/cm^3)	856.44	(45.47)	0.19	(1.74)	1.16	(1.94)	2.50	(2.35)	2.23	(2.08)
	Tb.N (mm^{-1})	2.00	(0.22)	-1.52	(6.33)	2.00	(6.78)	0.32	(11.14)	2.06	(9.07)
	Tb.Th (mm)	0.07	(0.01)	2.22	(7.40)	-1.90	(6.49)	0.53	(10.37)	-0.57	(8.25)
	Ct.Th (mm)	0.75	(0.16)	-0.94	(4.89)	0.11	(2.97)	-0.34	(6.12)	-0.16	(3.60)
	Ct.Po (%)*	0.01	(0.01)	4.24	(24.66)	10.71	(28.76)	21.13	(70.73)	15.54	(28.43)

Table 4.5 continued on next page

Low Rate	**Tt.BMD (g/cm^3)**	317.87	(54.93)	1.01	(4.28)	1.00	(3.47)	1.13	(3.10)	2.64	(3.75)
	Tb.BMD (g/cm^3)	165.17	(31.53)	-1.21	(3.14)	0.73	(2.01)	0.19	(1.85)	0.90	(2.32)
	Tb.BMD$_{Meta}$ (g/cm^3)	221.74	(28.89)	-0.88	(2.85)	0.56	(1.78)	-0.03	(1.44)	0.17	(1.91)
	Tb.BMD$_{Inn}$ (g/cm^3)	126.03	(34.34)	-1.61	(3.66)	0.89	(2.74)	**0.44**	**(3.07)**	1.83	(3.56)
	Ct.BMD (g/cm^3)	905.71	(54.85)	0.96	(2.33)	0.84	(2.37)	0.93	(1.98)	1.69	(2.36)
	Tb.N (mm^{-1})	2.06	(0.29)	-3.43	(6.50)	3.25	(11.80)	3.19	(10.83)	1.93	(8.22)
	Tb.Th (mm)	0.07	(0.01)	2.69	(7.29)	-1.31	(11.11)	-1.99	(10.40)	-0.33	(8.44)
	Ct.Th (mm)	0.80	(0.15)	1.46	(4.27)	0.91	(3.26)	0.73	(2.63)	2.16	(2.54)
	Ct.Po (%)*	0.01	(0.01)	-5.38	(22.23)	4.76	(37.46)	7.34	(20.28)	7.05	(24.78)
High Rate	**Tt.BMD (g/cm^3)**	313.83	(42.68)	**2.78**	**(3.09)**	0.87	(3.73)	0.34	(3.03)	0.94	(3.06)
	Tb.BMD (g/cm^3)	156.46	(28.97)	-0.04	(1.82)	0.34	(2.05)	-0.56	(2.49)	0.40	(2.43)
	Tb.BMD$_{Meta}$ (g/cm^3)	215.45	(28.07)	-0.09	(1.29)	0.05	(1.64)	-1.01	(2.06)	0.11	(2.01)
	Tb.BMD$_{Inn}$ (g/cm^3)	115.66	(30.34)	-0.22	(3.65)	0.91	(3.73)	0.23	(3.63)	0.80	(3.96)
	Ct.BMD (g/cm^3)	913.44	(40.74)	**1.13**	**(2.28)**	0.52	(2.94)	0.64	(2.65)	0.69	(2.31)
	Tb.N (mm^{-1})	1.93	(0.24)	3.37	(9.27)	5.15	(10.97)	0.17	(9.69)	0.28	(9.84)
	Tb.Th (mm)	0.07	(0.01)	-2.66	(7.35)	-3.66	(9.25)	-0.09	(8.89)	0.87	(8.29)
	Ct.Th (mm)	0.83	(0.11)	**3.74**	**(3.64)**	0.47	(3.18)	-1.06	(2.61)	0.41	(3.29)
	Ct.Po (%)*	0.01	(0.01)	-3.93	(23.04)	0.26	(21.38)	-2.21	(27.96)	7.00	(25.33)

Table 4.5 continued. *****The %CV for cortical porosity (Ct.Po) is 13%, Other CVs are ≤4.7% and are reported in the main text of the manuscript.

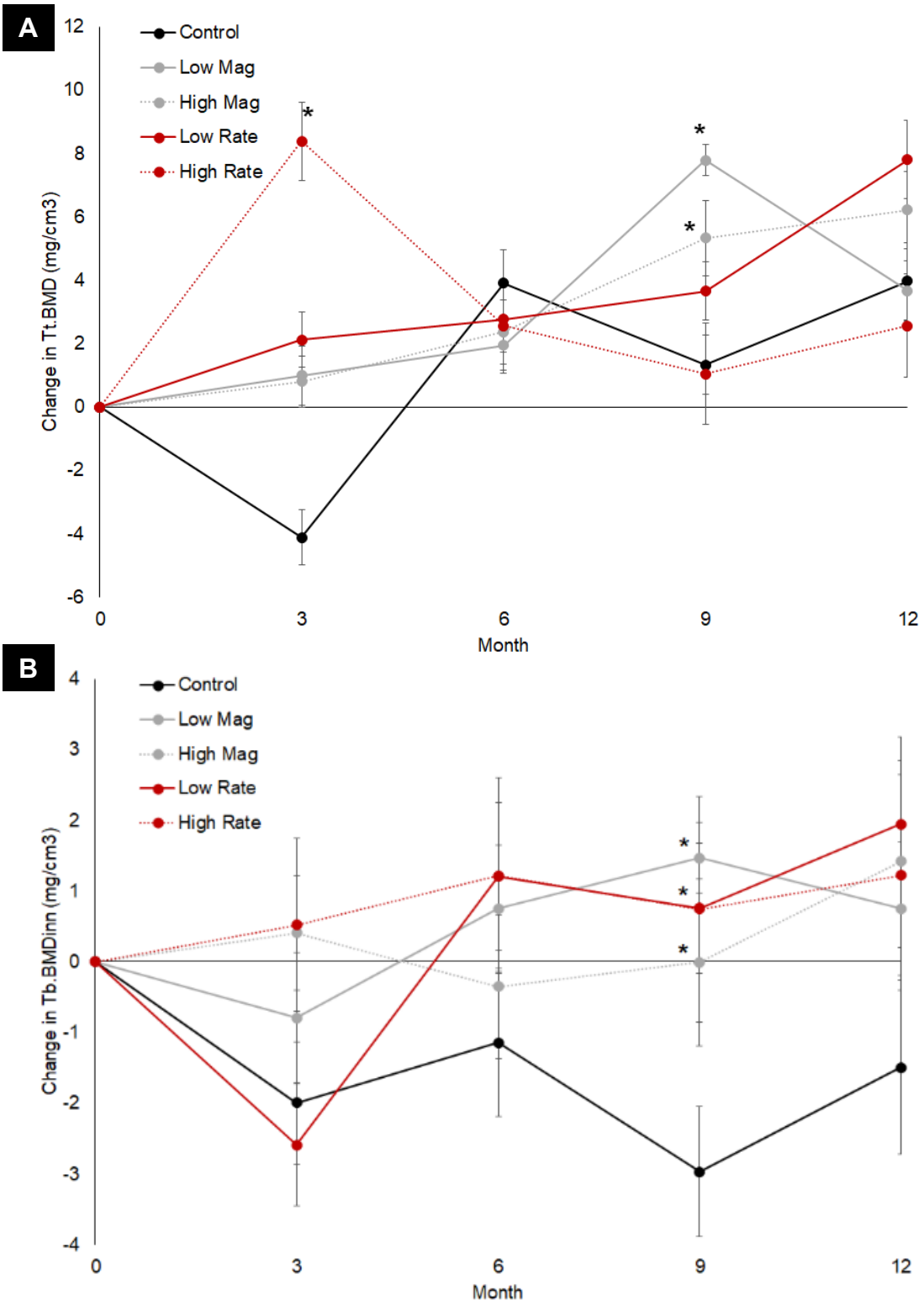

Figure 4.5: (A) Change in Tt.BMD, and **(B)** Tb.vBMDinn from baseline versus time, per group. Significant group changes versus control group at specific timepoints are labeled with *. Error bars represent standard error.

4.3.5 Comparison between change in ultradistal iBMC tertile groups

Participant characteristics at baseline were not different between tertile groups (Table 4.6). Nearly all loading-related variables were significantly different across the three tertiles. However, after Bonferroni adjustment for multiple comparisons, only the highest versus lowest tertiles were different.

Table 4.6: Mean (SD) grouped by change in ultradistal iBMC tertile. P-values indicate significant between-group differences. Symbols indicate significant Bonferroni-adjusted post hoc comparisons between specific tertiles.

	Highest Tertile	**Middle Tertile**	**Lowest Tertile**	**p-value**
Demographics				
Age (years)	27.7 (4.7)	29.4 (5.8)	29.3 (5.6)	0.510
Height (cm)	166 (7)	165 (6)	165 (7)	0.847
Body Mass (kg)	64.9 (8.1)	65.2 (9.2)	63.7 (7.3)	0.817
Serum Vitamin D (ng/mL)	30 (10)	29 (7)*	36 (10)+	**0.015**
Total Forearm aBMD (g/cm^2)	0.59 (0.04)	0.57 (0.04)	0.58 (0.03)	0.425
Group Membership (n; control/exercise)	2/20	3/19	8/14	-
Applied Loads				
Peak force (N)	297 (103)*	230 (135)	167 (139)	**0.005**
Loading rate (N/s)	865 (586)*	540 (515)	344 (407)	**0.010**
Number of Bouts	128 (85)	96.8 (84)	72 (87)	0.098
Peak Strain (με)	575 (246)*	490 (347)	323 (283)	**0.020**
Strain rate (με/s)	1878 (1428)*	1206 (1031)	918 (1077)	**0.029**
StrainStim ($με*s^{-1}*Bouts*10^{-7}$)	208 (278)	92.3 (119)	121 (224)	0.195
Strain_MagRate ($με^2*s^{-1}*Bouts*10^{-5}$)	799 (723)*	428 (531)	249 (383)	**0.007**
Strain_Mag ($με*Bouts*10^{-2}$)	847 (620)*	641 (639)	382 (497)	**0.038**
Strain_Rate ($με*s^{-1}*Bouts*10^{-3}$)	280 (257)*	149 (165)	105 (143)	**0.012**
Bone QCT values				
Baseline ultradistal iBMC	0.949 (0.172)	0.889 (0.141)	0.881 (0.114)	0.244
Visit 5 change (mg)	36 (13)*+	5 (7)*	-17 (13)+	**<0.001**
Visit 5 percent change (%)	3.8 (1.3)*+	0.6 (0.7)*	-2.0 (1.6)+	**<0.001**

* $p<0.05$ vs. lowest tertile after Bonferroni adjustment

+$p<0.05$ vs. middle tertile after Bonferroni adjustment

Data presented as mean(SD)

4.4 Discussion

We conducted a randomized controlled trial to characterize the relationship between mechanical strain magnitude and rate and changes to bone in healthy adult women. We found that the application of mechanical strain produced small but significant changes to the ultradistal radius after one year. However, our first hypothesis, that bone accrual would be *proportional* to strain magnitude and strain rate, was not fully tested. The relatively small ranges of strain magnitude and rate achieved by experimental participants limits the ability to draw conclusions regarding their independent roles. This was further complicated by differences in compliance between groups. In light of this challenge, the analysis considering loading dose is potentially most informative. Loading dose includes a combination of strain magnitude, rate, and number of loading bouts, and reflects achieved loading without issues associated with participant compliance. In fact, aligned with the scientific premise of our first hypothesis, we observed a dose-dependent relationship between measures of loading dose versus changes in iBMC and BMD across all participants.

Our second hypothesis, that structural changes would include increased cortical diameter and thickness, and increased trabecular bone mass near the endosteal surface, was only partly supported. This hypothesis was based on the structural mechanics principle that bone added near the cortical surface would result in the greatest gains in moment of inertia and structural resistance to bending. Endocortical BV, BMC, and BMD increased at 12 months, indicating bone apposition on both the periosteal and endosteal surfaces due to loading. At 3, 9, and 12 months, increases to overall density and trabecular density were observed with HRpQCT, and were dependent on loading dose. However, contrary to our expectation, the inner trabecular density (Tb.BMDinn) rather than more peripheral regions appeared to be primarily affected.

During aging, trabecular structure is first lost from this region, and later from more peripheral regions (Sode et al., 2010), thus maximizing moment of inertia for a given quantity of bone. We previously reported age-associated declines in Tb.BMDinn within a large subset of the participants measured here (Mancuso et al., 2018). It is possible that in our cohort of young, healthy women, trabecular microstructure in the more peripheral regions was already at its physiologic maximum, limiting the degree to which it might be improved. We observed Tb.BMDinn was lower than Tb.BMDmeta (Table 4.5), suggesting that there was greater capacity to improve the inner region with anabolic physical activity.

We observed significant positive effects of loading on Tt.BMD, Tb.BMDinn, and Ct.BMD after three months. Interestingly, all participants were assigned the same loading magnitude (200 N) during this ramp-up period, rather than a group-specific strain. Compliance was also the best during the first three months. Therefore, it is not surprising that both low and high magnitude groups had increases in these variables, since they both received the same stimulus. Overall, this supports the notion that loads must be novel to elicit an osteogenic response (Turner, 1998). However, the ramp-up period may have diminished the possible osteogenic response by stimulating cellular accommodation (Schriefer et al., 2005) to initially lower loads. Furthermore, it diminished the between-group differences in achieved strain. The improved response in the low magnitude group, who completed more loading bouts in total than other groups, also suggests that regular performance of exercise is as important as strain magnitude and rate. This is in agreement with studies in mice showing that separating loading cycles into multiple bouts is more osteogenic than a single bout with the same total number of cycles (Hsieh and Turner, 2001; Srinivasan et al., 2002), potentially due to desensitization of osteocytes.

We observed significant increases to bone mass in the strain rate experiment; however, both low and high strain rate groups demonstrated positive results and the regression coefficients were similar between groups. Although strain rates were significantly different between the high and low groups, participants in the high group fell far short of the target values. This may explain the similar response between groups. Surprisingly, in Experiment 1 (strain magnitude) only the low strain magnitude group showed even slight increases in ultradistal iBMC after 12 months, with no observable changes in the high strain magnitude group. In fact, despite being given different target strains and strain rates, the different loading groups did not achieve the expected range of rates and magnitudes (Table 4.2). This, combined with varying participant compliance may partly explain these counterintuitive results. The analysis by tertile change in iBMC suggests that changes to bone are indeed associated with bone loading dose. Participants in the highest tertile also had had a non-significant trend towards higher baseline BMC, suggesting that perhaps these individuals simply had a greater physiologic capacity to respond to osteogenic stimuli. We did not observe any other obvious factors related to the change (e.g. vitamin D status) that might explain this, although our measurements did not include biomarkers related to bone metabolism. The degree to which strain magnitude can be manipulated is limited due to risk of secondary injury, although greater magnitudes are possible in the lower extremities. With vibration and other external assistance, it is possible to manipulate strain rate over a much wider range than strain magnitude.

In contrast to small animal in vivo loading models, which use a materials testing machine to generate a predictable and repeatable waveform, voluntarily applied forces are variable in terms of frequency content, even when the peak magnitude is guided through visual feedback, as in our study. While many measures of bone loading dose have been proposed in the literature

(Ahola et al., 2010; Mikić and Carter, 1995; Turner, 1998; Turner and Robling, 2003), we found it impractical to implement any of them exactly as described by the authors. In addition to voluntarily produced loading signals being inconsistent, mechanical strain is non-uniform within a bone, both temporally and spatially; thus, no single strain value completely describes the strain occurring within a bone. It is not practical to place strain gages on most bones, and even when such measures are obtained (e.g. (Milgrom et al., 2015)), they only represent a small fraction of the bone surface. We previously observed that high-strain regions in the distal radius experienced the greatest gains in BMC, suggesting local control of osteogenic response (Bhatia et al., 2015). Here, we examined several candidate versions of loading dose, based on load cell recordings and subject-specific FE models. Each version included a combination of strain magnitude, frequency, and number of loading bouts. As a first attempt, we chose to examine a linear combination of the continuum strain produced within the analysis region in question (corresponding with the QCT or HRpQCT analysis region for those respective variables) and the total number of bouts achieved up to the timepoint in question. While we observed significant associations between these measures and changes to bone, we found that at best, dose explained 12% of the variance in the change. It is possible that other formulations of loading dose that include exponential scaling factors, local strain rate, strain gradient, or other measures, may be more relevant.

The magnitude and nature of the changes we observed are similar to an earlier, 6-month study using a similar loading protocol (Troy et al., 2013). In that set of 19 young women, control participants lost 1.7±1.1% ultradistal iBMC, while those in the loading group had no change in iBMC, but significant increases in trabecular BMC (1.3±2.8%). Here, we found a similar decrease in the control group iBMC (-1.3±2.7%), and increases to BMC and BMD that were associated with loading dose. The present cohort differed from the previous study in several

ways. First, present participants were generally older (28 vs. 22 years old) and many had a history of pregnancy or lactation (although not within the two years preceding enrollment). The present group were assigned loading magnitudes based on strain within the ultradistal radius at the instant of peak force production. However, due to safety limits, many participants fell short of their target strains. Thus, while high strain magnitudes may have, in theory, elicited a greater osteogenic response, they were impractical or unsafe to implement. Similarly, participants in the low and high strain rate groups were given instruction sets designed to elicit significantly different strain rates. While the rates were significantly different between groups, (low: 945 με/s, high: 1698 με/s, $p=0.02$) the sample did not vary as widely as designed and the rates were substantially lower than those occurring during impact activities such as running (Milgrom et al., 2007). Both low and high strain rate groups experienced similar increases in bone. Forearm loading is a relatively constrained activity that produces both compression and bending within the distal radius (Bhatia et al., 2014), and the ability to voluntarily manipulate the strain signal was limited.

Our results suggest that, while compressive loading in general is osteogenic, it may not be necessary to generate extremely high strain magnitudes or rates to elicit a positive response in the upper extremity. Significant gains in BMC were associated with strain rates and magnitudes within the range of those measured experimentally during activities of daily living ($\leq \sim$1300 με) (Földhazy et al., 2005) and can be achieved in a reasonable amount of time (100 loading cycles/bout, and an average of 131 loading bouts over a 12-month period for the highest tertile group). This is reassuring, since although impact loads are osteogenic (Martyn St James and Carroll, 2010), high loading rates have also been linked to increased risk of bone stress injury (Zadpoor and Nikooyan, 2011). Although we did not systematically test the effect of loading

cycles/bout, we based our target of 100 on (1) feasibility and time to complete the intervention, about three minutes, and (2) theoretical calculations of bone adaptation (Bhatia et al., 2013; Mikić and Carter, 1995) that suggested a diminished osteogenic response with additional cycles. Others have shown that breaking loading bouts into multiple sessions (Robling et al., 2001, 2000), inserting rest periods between cycles (Srinivasan et al., 2002), and changing the number of cycles (Umemura et al., 1997) all can independently influence the osteogenic response in small animal loading models. An alternative loading regimen may have produced a greater response than what was observed here, although testing these parameters was not the focus of the present investigation.

This study had several important limitations. Only 66 of the 102 original participants completed all 12 months of the study, and the results may be biased towards those who did not drop out. However, the demographics and baseline data of individuals who dropped out were not different from those who completed the study. We adjusted the randomization ratio part-way through enrollment to oversample the loading groups, which may have introduced other unknown biases. Due to the lower number of completers and lower precision, we were not powered to detect trabecular microstructural changes. However, we did observe significant changes to iBMC and Tb.BMD. The magnitude of the increases to iBMC due to the loading interventions, 1.2% across all participants, is not dissimilar to other treatment effects considered clinically relevant, and is well above (>4x) the CV for this measure. And, participants participating in Experiment 2 had much larger increases (2.9% and 3.6% for iBMC and 4.8 to 6.6% for strength indices), also several times greater than the CV. For comparison, a 3.3% increase in trochanter integral BMD over 36 months was observed in postmenopausal women given zolendronic acid (Eastell et al., 2010), and it has been estimated that each 1% increase in

peak bone mass imparts over 1 year of osteoporosis-free life in the future (Hernandez et al., 2003). While the present study examined the effects of strain magnitude and rate on bone adaptation, an underlying assumption is that the bone of each individual is already well adapted for her habitual activities; our analysis only considered the novel/added stimulus. Dominant (non-loaded) forearm data were not included in the present analysis, but would provide an indication of the systemic versus local effects of loading. Although we collected physical activity data as part of this study, they were beyond the scope of the present analysis, but may potentially explain some of the variability in response to our intervention. Our results may not be generalizable to other populations, including postmenopausal women, those with low vitamin D, men, or specific clinical populations. Finally, more research is needed to determine the specific strain requirements to elicit clinically relevant changes to lower extremity bone, given the high habitual loading stimulus in these sites.

Although other clinical trials have investigated the efficacy of various types of exercise to for improving bone mass, this study is the first to systematically investigate the effect of mechanical strain rate and magnitude on bone adaptation in humans. The data presented here fill a critical translational gap, linking in vivo animal models to clinical trials, and may be useful for informing the design of future clinical interventions targeting bone health. In particular, our data show that in healthy adult women, the distal radius is capable of modest adaptation in response to mechanical strain, and that the adaptation is associated with measures of loading dose that include strain magnitude, rate, and number of loading bouts.

In conclusion, we conducted a randomized controlled trial to systematically investigate the effect of mechanical strain rate and magnitude on bone adaptation, using an in vivo upper extremity loading model in healthy adult women. We found that compressive loading of the

forearm was osteogenic, with high and low strain rate groups having similar significant increases to bone mass. We observed that participants who gained the most bone had, on average, completed 128 compressive loading bouts, generating an average energy-equivalent strain of 575 με at 1878 με/s within the distal radius, over a period of 12 months. Individuals with the greatest gains to bone mass were similar in demographics to those with the lowest gains to bone mass. We conclude that signals related to strain magnitude, strain rate, and number of loading bouts collectively contribute to bone adaptation in healthy adult women.

Acknowledgements

This research was fully supported by NIAMS of the National Institutes of Health under award number R01AR063691.The content is solely the responsibility of the authors and does not necessarily represent the official views of the National Institutes of Health. This material is also based upon work supported by the National Science Foundation Graduate Research Fellowship Program under Grant No. DGE-1106756. We thank Sabahat Ahmed for her organization and dedication as research coordinator, and Dr. Jane Marone for serving as our Independent Safety Monitor.

Chapter 5: Aim 2B, Relate Changes in Bone Microstructure to Local Strain Parameters at the Individual Trabecular Level

In press in the *Journal of Biomechanical Engineering* as*:*

Megan E. Mancuso & Karen L. Troy. "Relating Bone Strain to Local Changes in Radius Microstructure Following 12 Months of Axial Forearm Loading in Women." *In Press.*

5.1 Introduction

Osteoporotic fractures represent a significant clinical burden, with 1 in 3 women over age fifty experiencing a fragility fracture in their lifetime ("National Osteoporosis Foundation. Osteoporosis Exercise for Strong Bones.," 2017). Exercise may have the potential to increase bone mass and offset age-related bone loss. Athletes applying high-intensity mechanical loads over extended periods of time have higher bone density than their peers (Bareither et al., 2008; Stewart and Hannan, 2000), and develop site-specific loading adaptations such as increased cortical thickness in the dominant arms of tennis (Bass et al., 2002; Kontulainen et al., 2003) and baseball (Warden et al., 2019) players. In normal healthy adults, clinical trials have shown that high-impact and resistive exercises consistently elicit a 1-3% increase in bone density at the hip over 6-24 months (Martyn St James and Carroll, 2010; Wallace and Cumming, 2000; Zhao et al., 2017, 2014). However, moving towards a more personalized approach that tunes interventions to deliver the optimal "dose" of loading for an individual requires a detailed understanding of the relationship bone tissue loading and changes in bone structure.

Animal models have provided insight into the local relationship between bone loading and adaptation. Early models established a controlling role of mechanical strain magnitude (Goodship et al., 1979; Rubin and Lanyon, 1985) and the novelty of strain distribution (Lanyon et al., 1982; Rubin and Lanyon, 1984) on the amount of new bone formed following a dynamic

loading intervention. Focusing on the local relationship between bone strain and adaptation, it has been shown that cortical bone formation is related to local strain magnitude (Kotha et al., 2004) and spatial gradient (Gross et al., 1997; Judex et al., 1997). In murine vertebral loading models focusing on the trabecular bone response, principal stresses, principal strains, strain energy density, and the spatial gradient of strain moderately predict the initiation of trabecular bone formation and resorption (Cresswell et al., 2016; Kim et al., 2003; Schulte et al., 2013b; Webster et al., 2015). It is generally suggested that these tissue-level deformations drive cellular-level mechanical stimuli, such as fluid streaming potentials and membrane shear stresses, which are transduced by osteocytes into biochemical cues regulating osteoblast and osteoclast activity (Hinton et al., 2018; Paul et al., 2018). While the mechanisms linking bone strain and cell behavior are likely similar in humans, the strength of the relationship between strain and adaptation may differ due to greater genetic variability and the influence of systemic factors such as hormones, diet, and exercise history. However, due to technical challenges in measuring bone strain and changes in bone microstructure in vivo in humans, data addressing this question are extremely limited.

Previously, we established a voluntary forearm loading model (Troy et al., 2013), in which human participants lean onto their palm to compress a padded load cell that provides feedback to guide load magnitude. We also validated participant-specific finite element (FE) models (Bhatia et al., 2014) of the forearm to simulate this loading task, enabling us to characterize the strain environment within the radius bone. These methods can be combined to prospectively assign and measure radius bone strain during the axial loading task. In a previously published pilot study that included twenty-three women, we found that 14-week changes in integral bone density in the distal radius, divided into local regions by quadrant, were positively

correlated with continuum FE-estimated energy equivalent strain (Bhatia et al., 2015). While these results provide preliminary support for local, strain-driven adaptation, the continuum FE models do not explicitly consider the effect of trabecular microstructure.

High-resolution peripheral quantitative computed tomography (HRpQCT) allows for the in vivo imaging of human bone microstructure in ~1 cm sections of the distal radius (Laib et al., 1998). Applying this technology, we validated a multiscale modeling approach (Johnson and Troy, 2017c), which incorporates a micro-FE section based on HRpQCT into continuum forearm FE models. Here, we used this technique and serial HRpQCT imaging to investigate the relationship between tissue-level bone strain and local bone adaptation in the distal radius of healthy, premenopausal women participating in a 12-month, prospective study using our forearm loading model. Our overall hypothesis was that bone formation occurs preferentially in high-strain (magnitude and gradient) regions, while bone resorption occurs preferentially in low-strain regions.

5.2 Methods

5.2.1 Participants and Loading Intervention

The data reported here were collected as part of a larger, institutionally approved randomized controlled trial enrolling 102 women (Troy et al., 2020). Full enrollment criteria are reported elsewhere (Mancuso et al., 2018). Briefly, women ages 21-40 with healthy BMI, menstrual cycles, serum vitamin D levels, calcium intake, and forearm areal bone density were included. Women were excluded if they had a history of medical conditions or use of medications affecting bone metabolism, a previous injury to the non-dominant arm, or regularly participated in activities applying high-impact loads to the forearm. The current analysis includes a subset of twenty-one participants from the control (non-loading, n=10) and loading (n=11)

groups. Control subjects with high-quality HRpQCT (motion ≤ 3) (Pialat et al., 2012) scans available at baseline and 12 months we included. In addition to having good quality scans, we further limited the load group to individuals in the top 50% of participants for achieved loading dose and who were "responders," meaning they experienced increases in bone density above the least significant change (details below).

The purpose of the parent study was to determine the influence of average strain magnitude and strain rate within the distal radius on changes in average bone structure parameters. Participants were randomized into either a non-intervention control group, or one of several loading groups with a range of target strain magnitudes and loading rates. The applied force required to generate the desired strain magnitude within the distal radius was determined for each individual using subject-specific continuum finite element models. Loading was performed on a custom device with visual LED cues to guide force magnitude and auditory beeps to guide loading rate (Figure 5.1A). Participants were asked to complete three sessions of axial compressive loading of their non-dominant forearm per week. Achieved loading was monitored by the device, which included a uniaxial load cell (Standard Load Cells; Gujarat, India) and data logger (DATAQ DI-710, DATAQ Instruments Inc.; Akron, OH) to record applied vertical force at 100 Hz. Load cell signals were analyzed in MATLAB (Mathworks; Natick, MA), and an overall "loading dose" was calculated for each participant as the product of average peak force (N), average loading rate (N/s), and number of loading sessions performed. For the present study, loading participants were ranked by loading dose and only the top 50% were included.

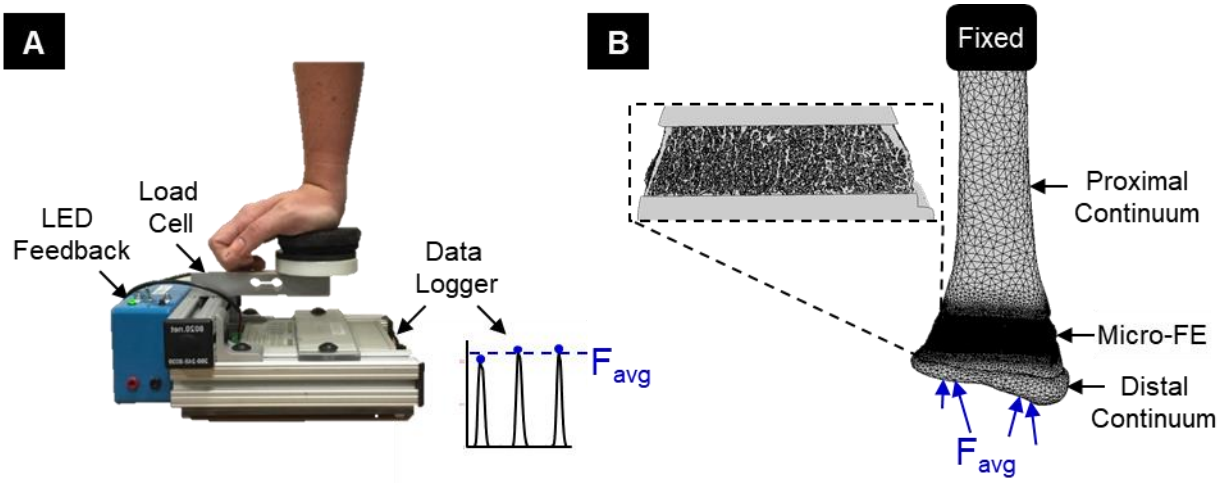

Figure 5.1: (A) Loading device used to perform forearm loading task. The vertical force was recorded and used to calculate the average applied force, F_{avg}, for each participant in the load group. **(B)** Multiscale FE models were generated from participant-specific CT scans. For the load group, an axial force equal to the participant-specific average was applied at the distal end. For the control group, the applied force was equal to the overall average across the load group participants.

5.2.2 Measurement of Bone Adaptation

Local regions of bone formation and resorption within the distal radius were identified from HRpQCT scans (Xtreme CT I, Scanco Medical; Brüttisellen, Switzerland) acquired at baseline and twelve months (isotropic voxel size: 82 µm, 0.9 mA, 60 kV). Scans included 110 axial slices covering a 9.02 mm region beginning 9.5 mm proximal to a reference line placed at the distal endplate of the radius. Adaptation sites were identified by aligning, subtracting and thresholding the baseline and follow-up greyscale images (Figure 5.2) similar to Christen et al. (2014) (Christen et al., 2018, 2014). Three-dimensional rigid registration (Image Processing Language, V5.16, Scanco Medical AG, Bruttisellen, Switzerland) was used to calculate the transformation matrix needed to align the follow-up image to the baseline image coordinates. The baseline and transformed follow-up images were cropped to the mutually overlapping region and subtracted to obtain voxel-by-voxel changes in density, where increases indicate bone

formation and decreases indicate resorption. To reduce the effect of noise and other short-term precision errors, the density difference map was thresholded to include only clusters of at least five voxels with differences ≥225 mgHA/cm^3 as adaptation sites (Christen et al., 2014). Adaptation sites were separated into the cortical and trabecular compartment by taking the Boolean intersection of formation and resorption site masks with the trabecular and cortical masks generated by the Scanco Standard Analysis program (MacNeil and Boyd, 2007). To capture periosteal bone formation added outside the baseline bone surface, the cortical mask was dilated seven voxels (574 micrometers) in the transverse plane. A sensitivity analysis of the 11 loading group participants showed that further increasing the dilation size changed the amount of labeled adaptation sites by less than 0.5%.

To assess repeatability, this adaptation labeling method was applied to a separate short-term precision data set including eight pairs of repeat distal radius scans acquired within two weeks of each other. The least significant change in average trabecular density for 3D registered scans was calculated as 2.77*CV%$_{RMS}$ (Baim et al., 2005). Next, the number of voxels labeled as formation and resorption as a percent of baseline bone volume were then determined for the cortical and trabecular compartments. As no real measurable bone changes are expected within two weeks, these values reflect the amount of erroneously labeled adaptation caused by short-term precision errors. Finally, in our data set, to select "responders," who we were confident experienced real bone changes, loading participants were included only if they experienced increases greater than this value (1.73%).

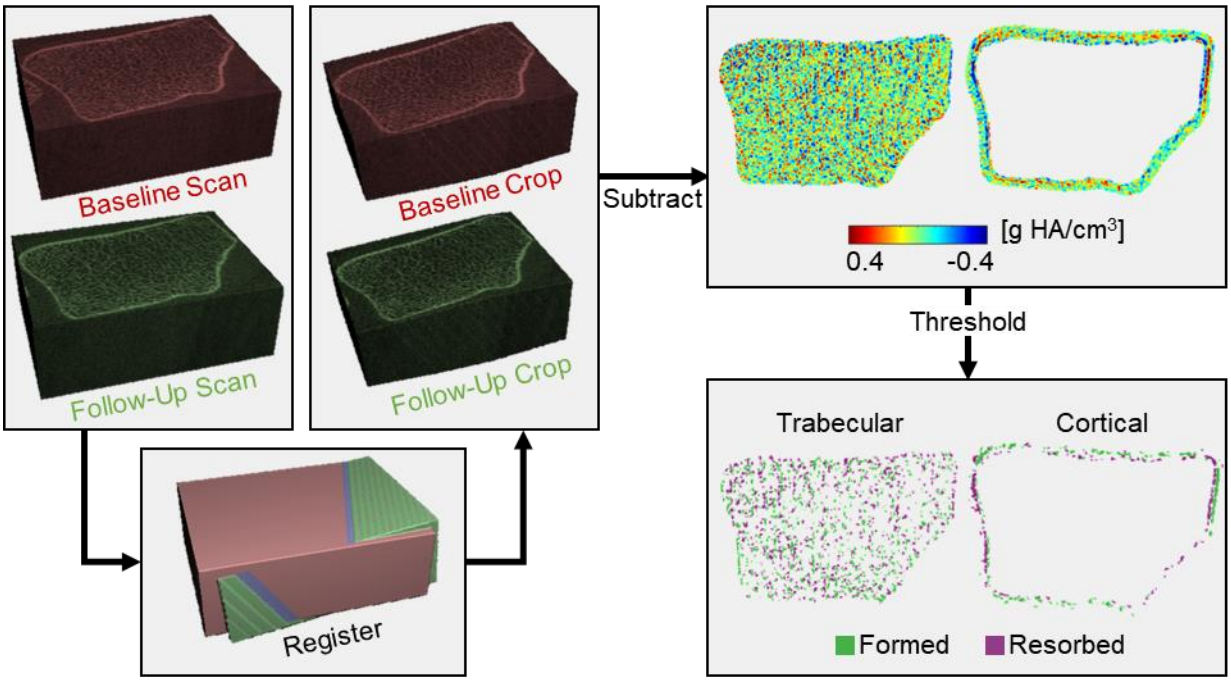

Figure 5.2: Workflow used to identify local bone formation and resorption sites. Baseline and follow-up HRpQCT greyscale images were aligned and cropped to the overlapping region. Cropped images were subtracted to obtain density difference maps for the trabecular and cortical compartments, which were thresholded to include continuous clusters of at least five voxels with a minimum change of 225 mg HA/cm^3.

5.2.3 Estimating Local Bone Strain

Bone strain magnitude and gradient were calculated using validated (Johnson and Troy, 2017c), participant-specific multiscale FE models. These models include the distal 10 cm of the radius, from the wrist joint articular surface to the mid-diaphysis. The radius is divided into two continuum sections (distal, proximal), which flank a micro-FE mesh at the HRpQCT distal radius scanned region (Figure 5.1B). Continuum mesh regions were generated from baseline clinical resolution CT scans (GE Brightspeed, GE Medical; Milwaukee, WI, in-plane resolution 234 µm, slice thickness 625 µm) of the non-dominant forearm. Three dimensional masks of the scaphoid, lunate, and distal 10 cm of the radius were segmented from the image using a 0.175 g/cm^3 density threshold (Bhatia et al., 2014). For the radius, the segmented baseline HRpQCT

mask was registered to the clinical resolution mask, and regions of the clinical resolution mask outside the HRpQCT region were converted into ten-node tetrahedral FE meshes with a nominal edge length of 3 mm. Continuum radius bone elements were assigned heterogeneous linear elastic material properties (E=1.95 MPa to 35 GPa, v=0.4) based on and established density-elasticity relationship using apparent density (Morgan et al., 2003). For the micro-FE section, the HRpQCT mask was converted to voxel-based hexahedral elements with an 82 μm edge length and homogenous linear elastic material properties (E=15 GPa, v=0.4). To accurately model radio-carpal contact, a 2 mm thick cartilage surface was generated by dilating the distal radius surface, and modeled with 2 mm ten-node tetrahedrons with hyperelastic neoHookean material properties (E=10 MPa, v=0.45) (Anderson et al., 2005). The scaphoid and lunate were modeled as rigid non-deformable solids, with ten-none tetrahedral meshes with a nominal edge length of 3 mm.

One cycle of the forearm loading task was simulated in Abaqus CAE (v2016, Simulia, Dassault Systèmes; Vélizy-Villacoublay, France). To reduce computational time, the continuum-only model was used to model full contact at the wrist, which included the scaphoid and lunate carpal bones. Ramped, quasistatic loading was applied through the centroids of each carpal toward the fixed proximal radius, such that the resultant force was axial and equal in magnitude to the participant's average achieved peak force measured by the loading device. The resulting normal and shear contact forces at radius cartilage nodes were exported from continuum simulations and applied directly at matching nodes in the multiscale model of the radius only. For participants assigned to the control group (who did not perform loading), a simulation was run with applied force set to the average applied force across all loading participants (324 N). The purpose of the control simulations was to determine an "average" mechanical strain state, to

provide a null comparison against the loading group. Multiscale models contained 3,062,520±557,518 nodes and 9,187,560±1,672,555 degrees of freedom (mean ± SD), and simulations were solved on a UNIX server with 54 processors (2.1-3.2 GHz) and 200 GB RAM in 3.4±1.9 hours.

Strain magnitude and gradient were calculated for each element in the distal radius micro-FE region. Principal stresses and strains at element centroids were exported from Abaqus used to calculate energy equivalent strain as

$$\varepsilon_{eeq} = \sqrt{\frac{2U}{E}} \quad \textbf{(5.1)}$$

Where *E* is elastic modulus and *U* is strain energy density calculated as

$$U = \frac{1}{2}[\sigma_1\varepsilon_1 + \sigma_2\varepsilon_2 + \sigma_3\varepsilon_3] \quad \textbf{(5.2)}$$

with σ_n and ε_n being the principal stress and strain components, respectively. Bone strain gradient was calculated as the norm of the gradient of energy equivalent strain in the x, y, and z directions. Gradient in each direction was calculated similar to (Huiskes et al., 2000) using the central difference formulation, with simple forward and backward differences calculated for surface elements. For example, gradient in the *x* direction for voxel *i* is calculated as

$$\frac{\partial \varepsilon_{eeq}}{\partial x} = \frac{\varepsilon_{eeq_{i+1}} - \varepsilon_{eeq_{i-1}}}{2 \times xres} \; for\; 1 < i < N$$

$$\frac{\partial \varepsilon_{eeq}}{\partial x} = \frac{\left(\varepsilon_{eeq_{i+1}}\right) - (\varepsilon_{eeq_i})}{xres} \; for\; i = 1 \quad \textbf{(5.3)}$$

$$\frac{\partial \varepsilon_{eeq}}{\partial x} = \frac{\left(\varepsilon_{eeq_i}\right) - (\varepsilon_{eeq_{i-1}})}{xres} \; for\; i = N$$

where *xres* is the element side length (82 μm) and *N* is the number of continuous voxels in the *x*-direction between two surfaces (i.e. of cortical shell or individual trabeculae). The norm of the spatial gradient was calculated for each element as

$$\nabla \varepsilon_{eeq} = \sqrt{\left(\frac{\partial \varepsilon_{eeq}}{\partial x}\right)^2 + \left(\frac{\partial \varepsilon_{eeq}}{\partial y}\right)^2 + \left(\frac{\partial \varepsilon_{eeq}}{\partial z}\right)^2} \quad \textbf{(5.4)}$$

To allow strain and adaptation to be compared spatially, formation and resorption mask coordinates were registered to the multiscale FE coordinates using mutual information 3D registration in MATLAB (Mathworks, Natick, MA). A precision analysis demonstrated rotation errors of 0.47 ±0.38°, 0.46 ±0.41°, 0.32 ±0.24° in the x,y,z directions for this method.

5.2.4 Relating Bone Strain and Adaptation

The hypothesis that bone adaptation is influenced by local tissue strains was tested using four approaches (Table 5.1). First, we compared strain near sites of formation versus resorption. Second, we compared the percent of bone formation and resorption sites occurring near high versus low strain regions. Third, we compared the percent of high and low strain elements occurring near formation versus resorption. Finally, we characterized the distribution of adaptation and strain within the cortical bone compartment across sixteen angular sectors. All analyses included both the load and control groups.

For each formation and resorption site, the average strain magnitude and gradient was calculated as the average value for all FE elements within 200 μm, corresponding to 23.8 ±10.3 and 40.0 ±8.3 elements for formation and resorption sites, respectively. Two hundred micrometers was selected as the distance within which osteocyte sense local strains. This falls within the range of previous studies (Adachi et al., 1997; Christen et al., 2014; Morgan et al., 2015; Ruimerman et al., 2005b) and is equal to 2.44 element edge lengths. For formation and resorption sites more than 200 μm from a mesh element, the value for the nearest element was used. The median, 25th percentile, and 75th percentile values for average strain magnitude and gradient near formation and resorption in both the trabecular and cortical compartments were determined.

To assess the spatial relationship between adaptation and extreme strain, very high and low strain elements for strain magnitude and gradient were defined using the 9th and 95th percentile values for each metric (Figure 5.3). Very high and low strain element sets were defined separately for the trabecular and cortical compartments. The percent of formation sites near very high strain was calculated as the number of formation sites with a high strain element within 200 µm, divided by the total number of formation sites. Conversely, the percent of very high strain elements near formation was calculated as the number of very high strain elements with a formation site within 200 µm, divided by the total number of very high strain elements. Similar calculations were performed for resorption sites and very low strain elements within each bone compartment.

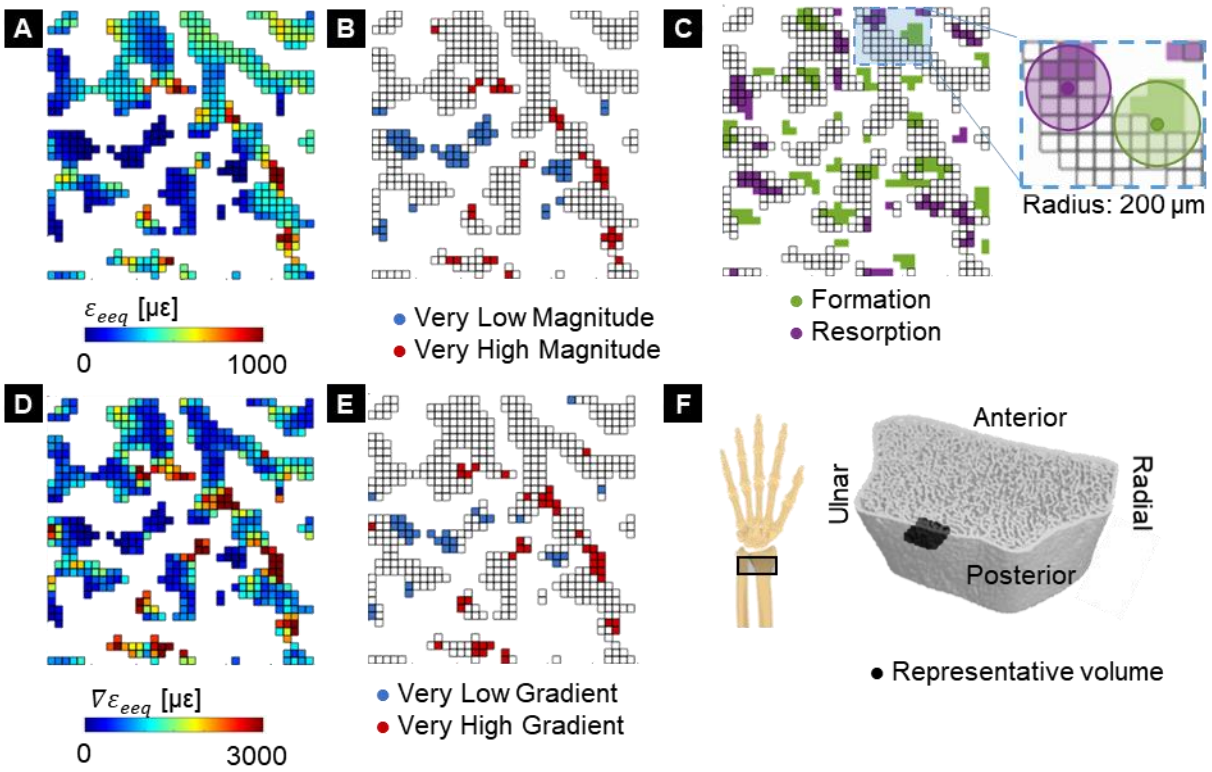

Figure 5.3: Energy equivalent strain **(A)** magnitude, $\boldsymbol{\varepsilon_{eeq}}$, and **(D)** gradient, $\boldsymbol{\nabla\varepsilon_{eeq}}$, used to define very low and very high **(B)** magnitude and **(E)** gradient elements based on the 5th and 95th

percentile values within the trabecular compartment. **(C)** Formation and resorption sites, with edges indicating elements present in the FE mesh based on the baseline scan. Inset shows 200 µm regions defining which FE elements are near formation and resorption sites. **(F)** Reconstructed HRpQCT mask of distal radius, indicating the position of the representative 3x3x0.2 mm trabecular volume in black.

To explore the distribution of cortical bone adaptation and strain, we divided the cortical compartment into sixteen equal angle sectors and determined the number of formation versus resorption and high versus low strain elements within each sector (Figure 5.4).

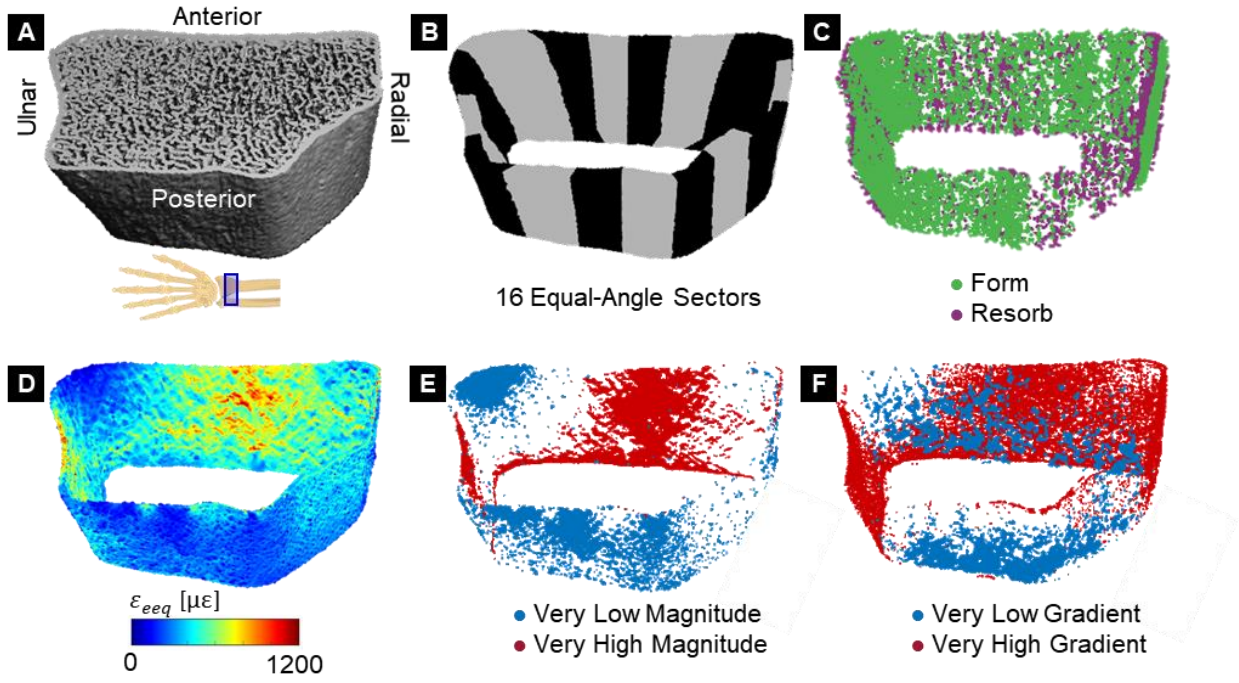

Figure 5.4: (A) Reconstructed HRpQCT mask of distal radius. **(B)** The cortical compartment was divided into sixteen equal-angle sectors defined relative to the radius centroid. **(C)** Cortical formation and resorption sites. **(D)** Energy equivalent strain within the cortical compartment, used to define very low and high strain **(E)** magnitude and **(F)** gradient elements based on 5th and 95th percentile values within the cortical bone compartment.

Table 5.1: Summary of analyses performed to spatially relate bone adaptation (formation and resorption) to FE-estimated strain. Each predictor had two levels: formation or resorption for adaptation type, control or load for group, and very high or very low for strain level. For each outcome, separate models were fit for the trabecular and cortical compartments, as well as for strain magnitude and strain gradient for analyses considering strain.

Question	Predictor(s)	Outcome(s)
Do strain metrics differ near formation versus resorption?	• Adaptation type • Group	• 25^{th} percentile strain (με or με/mm) • Median strain (με or με/mm) • 75^{th} percentile strain (με or με/mm)
What percent of formation or resorption sites are near high and low strain elements?	• Adaptation type • Strain level • Group	• Percent of formed or resorbed voxels (%)
What percent of high or low strain elements are near formation and resorption sites?	• Adaptation type • Strain level • Group	• Percent of very high or very low strain elements (%)
How are adaptation and bone strain distributed around the cortical shell?	• Group	Within each sector: • Number of very high strain elements • Number of very low strain elements • Formed volume (% of baseline) • Resorbed volume (% of baseline)

5.2.5 Statistics

To characterize adaptation in each group (loading versus control), the volume of formed and resorbed bone within each compartment was compared between groups using a mixed effects linear model. When significant interactions between group and adaptation type were found, formed and resorbed volumes were compared within each group separately.

Strain parameters were compared between adaptation type (formation versus resorption) and group (load versus control) using a mixed effects linear model. Separate models were fit for median, 25^{th} percentile, and 75^{th} percentile strain magnitude and strain gradient within the trabecular and cortical compartments. When significant adaptation by group interactions were found, strain metrics near formation and resorption were compared separately for each group.

The percent of adaptation sites near extreme strain elements was compared using a mixed effects model with adaptation type (formation versus resorption) and strain level (very high versus very low) as repeated measures and group as a between-subjects factor. When significant interactions involving strain level and adaptation type were found, strain level was compared separately within formation and resorption. Similarly, the percent of extreme strain elements near adaptation sites were compared with adaptation type, strain level, and group as factors. When significant interactions involving strain level and adaptation type were found, adaptation type was compared separately within high and low strain elements. Separate models were fit for strain magnitude and gradient within each of the trabecular and cortical bone compartments.

To verify that cortical strains were similarly distributed for load and control groups, independent samples t-tests compared the number of low and high strain elements between groups within each sector. To determine where loading may promote bone formation or prevent resorption within the cortical surface, the number of formation and resorption sites, as a percent of baseline cortical bone volume, was compared between groups within each sector using independent samples t-tests. All statistics were performed in SPSS v25.0, and $p<0.05$ was used to define statistical significance. Unless otherwise stated, data are expressed as mean±standard deviation.

5.3 Results

5.3.1 Participants

The participants included in this analysis were 28.7±4.9 years old. On average, the load group participants performed 139±86 sessions of loading over 12 months, applying an average peak force of 324.2±40.7 N.

5.3.2 Characterization of Local Adaptation

Within the load group, significantly more trabecular bone was formed than resorbed (Figure 5.5), consistent with the selection criteria that limited the load group to "responders" with gains in bone density. As a percent of baseline bone volume, 4.1±2.0% more bone was formed than resorbed. Within the control group, formed and resorbed bone volumes were similar, with 1.0±5.5% more bone resorbed than formed.

In the cortical bone compartment, the load group experienced significantly more formation than resorption, corresponding to a net increase equivalent to 4.0±4.4% of baseline cortical bone volume. Within the control group, cortical formation and resorption were similar, with 2.5±4.4% more bone resorbed than formed.

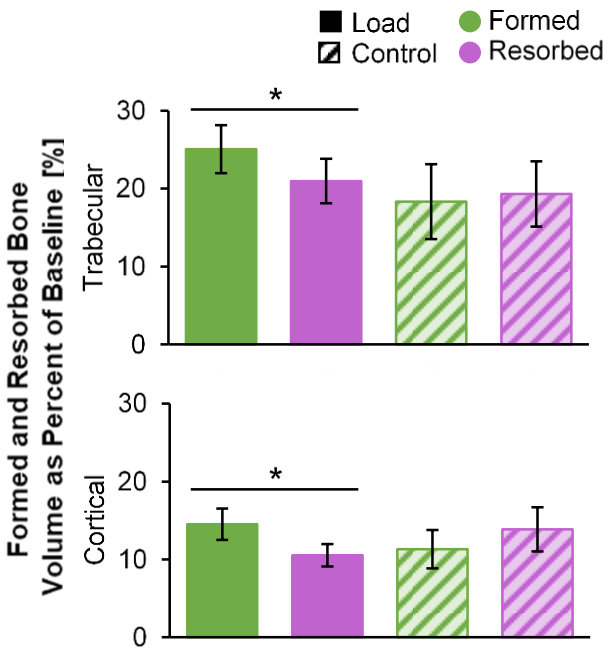

Figure 5.5: Formed and resorbed bone volume, presented as a percent of baseline bone volume, within the trabecular (top) and cortical (bottom) compartments for the load (n=11) and control (n=10) groups. *Given significant adaptation by group interaction, indicates significant difference between formed and resorbed volume within the load group.

Looking at the short-term precision data set, in which no real change occurred, 10.5±4.5% of trabecular bone volume was erroneously labeled as formation and 9.9±4.3% was erroneously labeled as resorption. In the cortical compartment, 4.7±1.9% of baseline bone volume was labeled as formation and 4.9±2.1% was labeled as resorption. The root mean square coefficient of variation for net change for trabecular bone density was 0.62%. Net adaptation within the precision group was not significantly different from zero ($p>0.05$, one-sample t-test) for both trabecular and cortical compartments, suggesting no systematic bias toward formation versus resorption. The average formed and resorbed volumes in experimental groups were a minimum of 1.7 times those associated with precision error due to partial volume and image registration.

5.3.2 Do Strain Metrics Differ near Formation versus Resorption?

Trabecular strain magnitude and gradient were higher near formation versus resorption sites for both the load and control groups, except for the 25th percentile of strain magnitude (Figure 5.6). While statistically significant, the differences between formation and resorption were relatively small, on the order of 5-10%. This corresponds to an average difference of 11.8±17.2 με between formation and resorption for median strain magnitude, and 45.7±38.6 με/mm for median strain gradient. Thus, the distribution of strain (magnitude and gradient) among formation sites was shifted slightly higher than that of resorption, but the distributions were still mostly overlapping. In the cortical compartment, strain magnitude was similar in formed versus resorbed sites, except at the 25th percentile value, which was higher near resorption. The 25th percentile and median of cortical strain gradient were higher for formation versus resorption in the control group only, with median strain gradient 138.9±98.6 με/mm higher near formation versus resorption. The 75th percentile of cortical strain gradient was

higher for formation versus resorption in both groups. Differences between formation and resorption for cortical strain gradient were relatively high, between 30-40%.

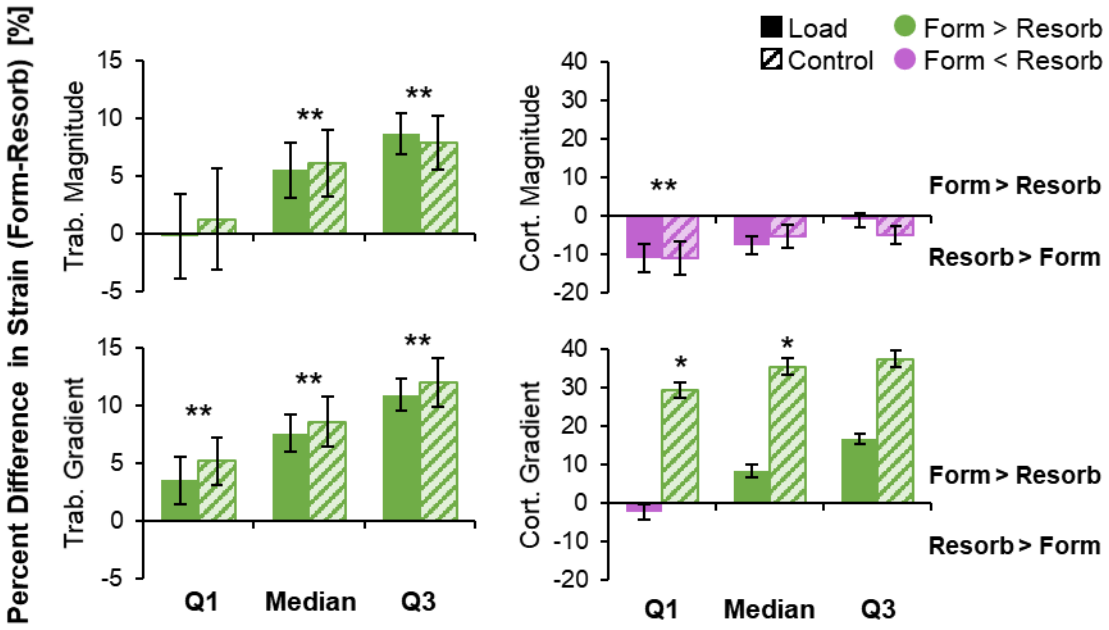

Figure 5.6: Percent difference in strain metrics between formation and resorption in the trabecular (left) and cortical (right) compartments for the load (n=11) and control (n=10) groups. For each subject, the 25th percentile (Q1), median, and 75th percentile (Q3) of strain magnitude (top) and gradient (bottom) were calculated for formation and resorption. Data presented as group means of within-subject percent difference between formation and resorption (error bars: SEM). Positive differences indicate strain is higher for formation than resorption. *Given significant group by adaptation interaction, indicates significant difference between formation and resorption within the control group only. **Indicates significant difference between formation and resorption for both groups.

5.3.3 What Percent of Formation or Resorption Sites are Near High and Low Strain Elements?

A greater proportion of trabecular formation and resorption sites were near very high versus very low strain magnitude elements in both the load and control groups (Figure 5.7). Similarly, a greater proportion of trabecular formation and resorption sites were near very high versus very low strain gradient elements, particularly for formation sites ($p<0.05$ for interaction). Cortical bone formation and resorption were both more likely to occur near very high versus very low strain gradient elements. These findings are in line with the hypothesis that high strains

lead to microdamage or other biophysical cues that upregulate remodeling, in which both formation and resorption occur. However, while significant differences were observed, over half of formation and resorption sites were near neither very high nor very low strain elements. In the trabecular compartment, a greater proportion of resorption sites were near very low and very high strain magnitude compared to formation sites (significant effect of adaptation type). This is likely because resorption eats into existing bone surfaces while formation builds away from existing surfaces. As the FE mesh was generated from baseline bone masks, formation sites were more likely to be distant from any given FE element.

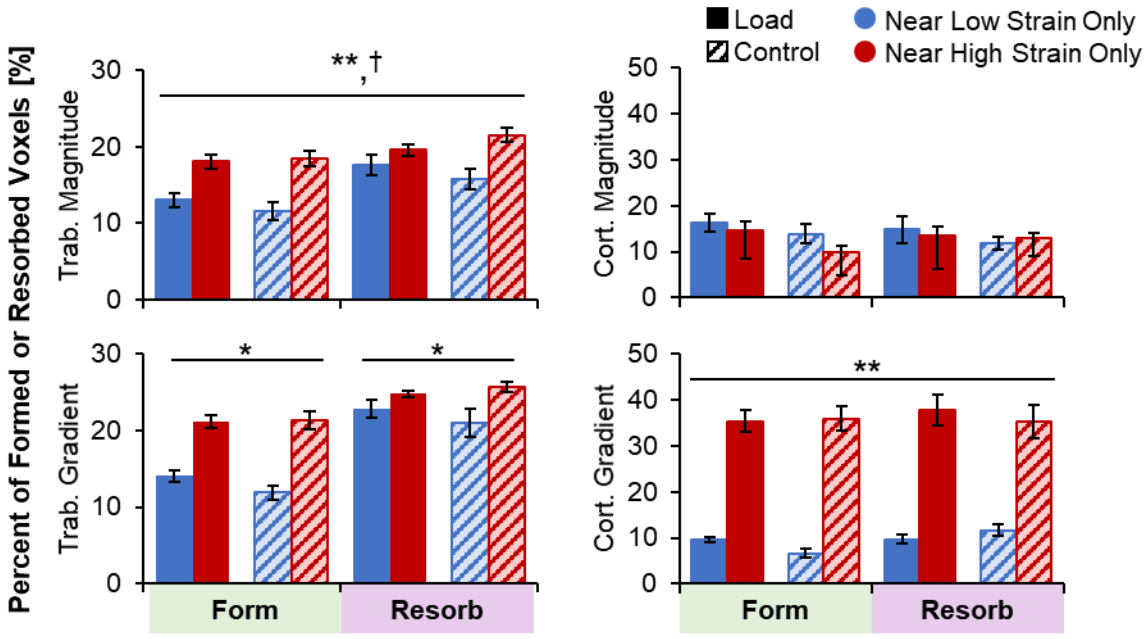

Figure 5.7: Percent of trabecular (left) and cortical (right) formation and resorption sites near very high or very low strain magnitude (top) and gradient (bottom) elements for the load (n=11) and control (n=10) groups. Data presented as group means (error bars: SEM). *Given significant strain by adaptation interaction, indicates significant difference between very low and very high strain within formation or resorption for both groups. **Indicates significant main effect of strain level (very high versus very low). †Indicates significant main effect of adaptation type (form versus resorb).

5.3.4 What Percent of High or Low Strain Elements are Near Formation and Resorption Sites?

In the trabecular compartment, a greater proportion of very low strain magnitude and gradient elements were near resorption versus formation in both the load and control groups (Figure 5.8). The proportion of very high strain magnitude and gradient elements near formation and resorption were similar. Therefore, trabecular bone resorption is associated with low bone strain. In the cortical compartment, very high and very low strain elements were found near formation and resorption at similar rates. Between 21-35% of low strain elements were near resorption, and between 19-43% of high strain elements were near formation. At least 12% of very low or high elements near both or neither adaptation types. There were significant interactions between group (load versus control) and adaptation type (formation versus resorption) for all metrics. For example, in the cortical compartment, both very high and low strain magnitude elements were more likely to be near formation for the load group and near resorption for the control group. These effects were driven by having more formation sites in the load group and more resorption sites in the control group, with any given element more likely to be near the more abundant adaptation type.

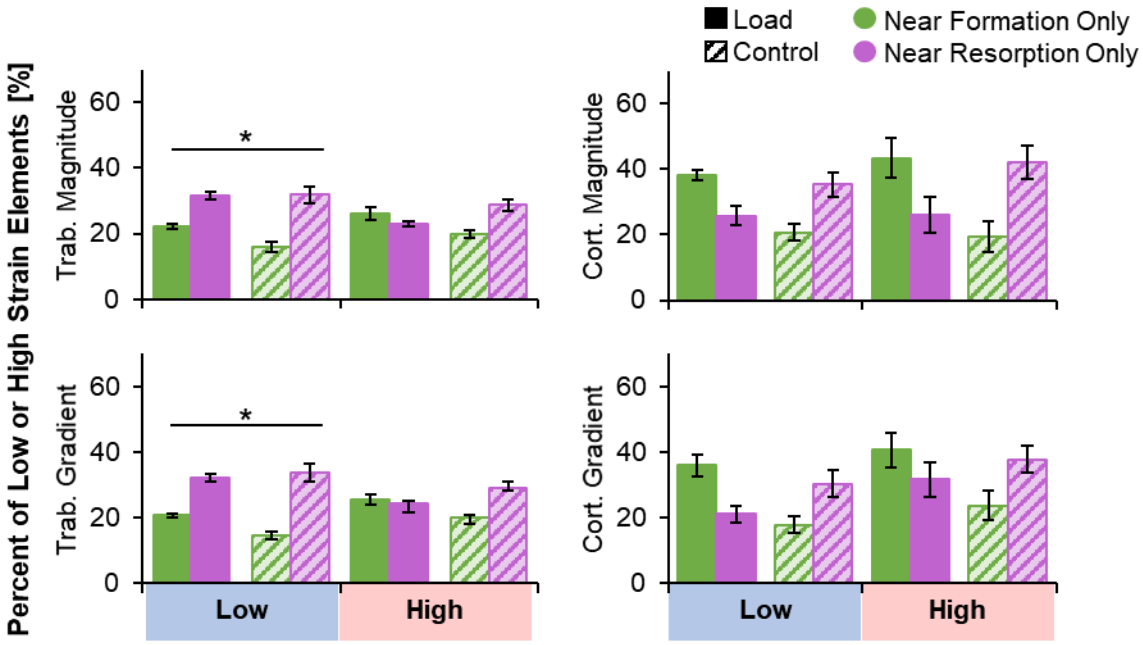

Figure 5.8: Percent of trabecular (left) and cortical (right) very low and very high strain magnitude (top) and gradient (bottom) elements near formation and resorption for the load (n=11) and control (n=10) groups. Data presented as group means (error bars: SEM). *Given significant strain by adaptation interaction, indicates significant difference between formation and resorption within very low strain elements only. Significant group by adaptation interactions were observed for all metrics but are not indicated on plot for visual clarity.

5.3.5 How are Adaptation and Bone Strain Distributed around the Cortical Shell?

There were no significant differences in cortical strain magnitude or gradient between the load and control groups in any sector. Therefore, as expected, our boundary conditions based on participant-specific force recordings for the load group and average force for control subjects generated similar bone loading. The number of formation sites was higher for the load versus control group in five out of sixteen sectors (Figure 5.9) located in the anterior and posterior surfaces ($p<0.05$). There were significantly more resorption sites in the control versus load group in one sector located in the posterior/radial quadrant.

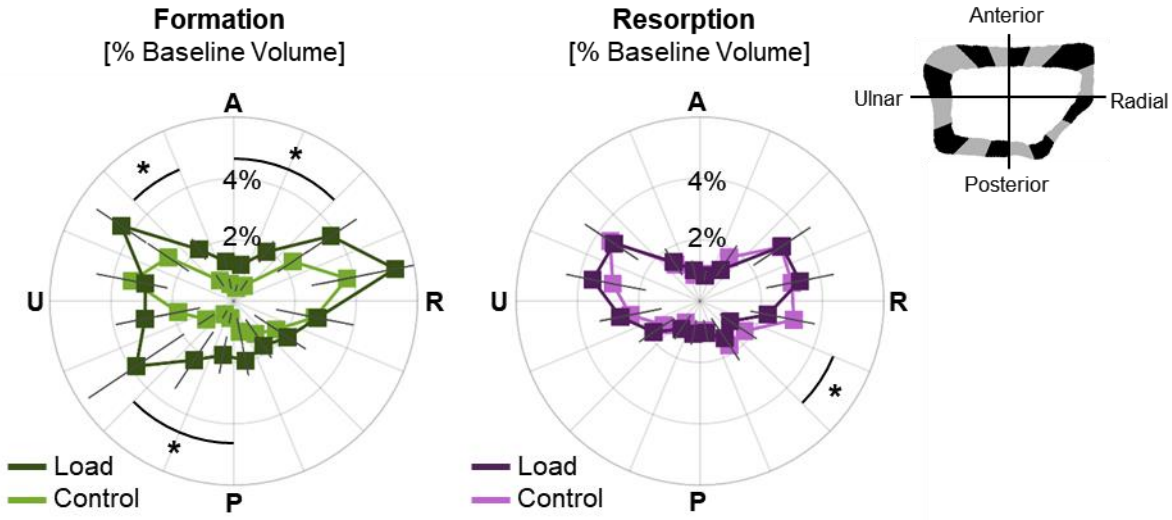

Figure 5.9: Angular distribution of formed (left) and resorbed (right) bone, as a percent of baseline cortical bone volume, in the load (n=11) and control (n=10) groups. Data presented as group means (error bars: SEM) for each sector spanning the anterior (A), ulnar (U), posterior (P), and radial (R) surfaces. *Indicates significant difference between groups.

5.4 Discussion

Our purpose was to relate tissue-level bone strain to local adaptation in the distal radius of women following 12 months of axial forearm loading. Our hypothesis that bone formation would occur preferentially in high-strain magnitude and gradient regions and bone resorption would occur preferentially in low-strain regions was partially supported. Trabecular strain magnitude and gradient were higher near formation versus resorption, and very low strain elements were more likely to be near trabecular resorption than formation. However, trabecular formation and resorption sites were both more likely to be near very high versus very low strain elements. We interpret these findings as evidence that in local regions of high strain, osteocyte stimulation and damage lead to increases in bone formation and remodeling, while in low strain regions with insufficient osteocyte stimulation, bone is removed. In the cortical compartment, the association between strain and adaptation was less clear. Strain gradient was higher near

formation versus resorption for the control group, and formation and resorption were both more likely to be near very high versus low strain gradient elements. However, there were no differences in the proportion of very low and high strain elements near formation versus resorption.

Contrary to our hypothesis, similar relationships between strain and adaptation were observed in the loading and control groups. This could be interpreted to mean that, at a local level, the same mechanical cues are driving tissue remodeling, regardless of whether there was a net gain or loss in bone mass. It is unsurprising that in the absence of a novel intervention, bone adaptation is still regulated in part by bone strain generated during activities of daily living. Since the control group did not participate in the loading intervention, we did not expect measurable relationships between FE-estimated strain and adaptation because the simulated loading task was not actually performed. However, axial compression is the primary loading mode for many common activities, and the FE-estimated strain distribution may be similar to habitual strains for the control subjects. This is in agreement with Christen et al. (2014) (Christen et al., 2014), who found that in the distal tibia of postmenopausal women with normal activity levels (i.e. no intervention), formation was more frequent in regions of high strain energy density. Troy et al. (2018) found that FE-estimated principal stresses predicted four-year circum-menarcheal changes in total BMC and cortical thickness in the distal radius of non-gymnasts, but not gymnasts (Troy et al., 2018), further suggesting that bone adaptation is related to loading even when activity levels are not above those of daily living. Additionally, by defining low and high strain elements based on 5^{th} and 95^{th} percent values within an individual participant, we did not define absolute strain "setpoints" across subjects, which may vary between individuals based on activity level and other physiological factors.

Our previous work quantified the relationship between bone strain and adaptation at the macrostructural level in a pilot group of 23 women who completed fourteen weeks of forearm loading (Bhatia et al., 2015). Strain was estimated by continuum-only FE models and changes in bone volume, density, and mineral content were measured from clinical resolution CT scans. When a 3 cm transverse section of the distal radius was divided into 12 subregions, there was a significant correlation between strain and change in density (but not volume or mineral content) for the load group only. In the present study, we found significant associations between strain and adaptation in the trabecular compartment, but did not detect many differences in the relationship of strain versus adaptation between the load and control groups. Continuum strains and micro-FE derived strains cannot be directly compared, and the local regions of formation/resorption measured in the present study cannot be compared to regional averages combining the trabecular and cortical compartments. Additionally, the analyses differed in duration (14 weeks versus 12 months), and the present analysis was limited to the overlapping region between baseline and follow-up HRpQCT scans (maximum 9.02 mm transverse region), while our previous analysis covered a larger, 3 cm region.

Our findings for the trabecular compartment are generally consistent with previous work in animal models, but the size of observed differences were smaller. In the mouse caudal vertebral loading model, Schulte et al. (2013) (Schulte et al., 2013a) found a 39% difference in strain energy density (SED) in regions with formation versus resorption after four weeks of loading, and Lambers et al. (2015) (Lambers et al., 2015) found over a 100% difference after six weeks. In comparison, we found that median trabecular energy equivalent strain magnitude and gradient were 5-8% higher in regions with formation versus resorption. In the present analysis, because all elements in micro-FE portion of our models had the same modulus and size, SED

and energy equivalent strain are directly related, with SED proportional to the square of energy equivalent strain. Therefore, the direction of differences in SED and energy equivalent strains near formation and resorption should be similar, with differences in SED likely magnified compared to energy equivalent strain because of their mathematical definitions. Looking at remodeling probabilities, Cresswell et al. (2016) (Cresswell et al., 2016) found that after one week of vertebral loading in mice, 47% of high SED regions (defined as top 20%) were within 25 μm of bone formation. After four weeks, Schulte et al. (2013) found conditional probabilities of formation and resorption at high and low SED regions, respectively, were between 40-50%. In our participants, at most 33% of very low trabecular strain elements were near resorption only, and 23% of very high trabecular strain elements were near formation only. One explanation for the weaker relationships between strain and adaptation in our study is that adaptation in animal models is measured using micro-CT, which has a higher resolution than HRpQCT with a typical voxel size of 10-25 μm. Therefore, the amount of erroneously labeled adaptation due to partial volume effect is likely higher using HRpQCT (82 μm voxel size), limiting the strength of the measurable relationship. Additionally, there are several physiological and lifestyle factors that cannot be controlled but likely influence bone adaptation in humans. Further work is needed to determine the individual roles that age, physical activity, calcium and Vitamin D intake, genetics, and hormonal factors plan in adaptation of bone to mechanical loading.

The current analysis did not find consistent evidence that cortical bone changes were directly related to bone strain magnitude. The 75^{th} percentile of cortical strain gradient was significantly higher for formation versus resorption, but the proportion of very low and high strain elements near formation and resorption sites were similar. We found that significantly more formation than resorption sites were located near high cortical strain gradients in both the

control and loading groups. This is likely driven by the fact that cortical strain gradients are largest at the periosteal surface due to the presence of the surface itself, and that bone formation occurs on bone surfaces. Taken together, these findings suggest that cortical strain gradient, rather than magnitude, is related to adaptation. This is in agreement with loading studies in a turkey ulna exogenous loading model (Gross et al., 1997) and rooster tarsometatarsus running model (Judex et al., 1997). In these models, circumferential strain gradients, but not strain magnitude, predicted areas of new bone formation with R^2 values between 0.36 and 0.63. The lack of definitive strain-adaptation relationships observed in the cortical compartment in the current study may also be related to the intervention being overall more osteogenic in the trabecular compartment. The macrostructural changes, described in detail elsewhere (Troy et al., 2020), showed that the largest loading related changes were in trabecular density, especially in the inner 60% of the trabecular compartment. Additionally, we found that across subjects, age was negatively correlated with trabecular density at baseline (Mancuso et al., 2018), even within our relatively young age range of 21-40. Therefore, it is possible that in this group, trabecular bone is the first to undergo age-related deterioration and has the most potential for improvement due to mechanical loading. Furthermore, trabecular bone has abundant surface area available for bone apposition, in contrast to the relatively limited cortical shell. Finally, cortical bone may be at its physiological maximum, or changes in the cortical compartment may be dominated by physiological factors not directly controlled here that overshadow the influence of loading.

This study has several limitations. First, the labeling of adaptation from HRpQCT images is subject partial volume and registration error, which leads to some bone being erroneously labeled as formation or resorption. Our 10-11% error rates in the trabecular compartment are approximately double those reported by Schulte et al. using micro-CT with a 10.5 μm voxel size

(Schulte et al., 2013a). While micro-CT is not safe for use in humans, future studies may be improved by using newer, higher resolution HRpQCT scanners, which currently scan at a 61 μm voxel size (Manske et al., 2015). Looking at other technologies used in humans, clinical resolution CT can be registered to measure regional changes in apparent density and bone mineral content with high repeatability (coefficient of variation <0.7% in (Bhatia et al., 2015)), but cannot capture adaptation at the sub-millimeter, tissue level. Despite relatively high short-term precision errors, we found that the amount of formation and resorption observed longitudinally was at least 1.7 times that for a short-term precision data set. Additionally, there was no bias toward mislabeling formation or resorption, suggesting that precision error may limit the strength, but not the direction of the measurable relationship between strain and adaptation. Overall, this supports the validity of the significant trends we have observed, but it is possible that we have underestimated absolute differences in strain parameters and the spatial association between strain and adaptation. Second, our findings may overestimate strain/adaptation relationships due to selection of "responders" within the loading group. However, the relationships between local strain and adaptation type were consistent in both loading and control subjects. Third, the FE model boundary conditions used participant-specific load magnitudes but assumed an axial direction. While we instruct participants to perform loading with their arm directed axially, measuring the exact positioning was outside the scope of this investigation. The potential influence of variability in loading position on FE-estimated bone strain is part of our ongoing work. We focused on the magnitude and norm of the spatial gradient of energy equivalent strain, as energy equivalent strain is a scalar representative of the multiaxial strain state, and has been shown to relate to adaptation in our pilot study (Troy et al., 2013). Additionally, the norm of strain gradients in the axial and transverse directions as a scalar

representation of spatial variability has been used in previous studies (Koontz et al., 2002; Ruimerman et al., 2005b). However, it is possible that other bone strain parameters have a controlling role in functional bone adaptation. Bone tissue strain gradient was selected as an upstream measure of fluid flow, as spatially varying strains yield pressure gradients and therefore flow within lacunar-canalicular and marrow spaces. A more direct estimate of fluid flow using poroelastic modeling (Carriero et al., 2018; Pereira et al., 2015; Scheiner et al., 2016) or inclusion of marrow as a separate material (Webster et al., 2015) may provide a more detailed description of the local mechanical environment and have shown potential in predicting adaptation in animal loading models, but is outside the scope of the present study.

In summary, we related tissue-level bone strain to 12-month changes in radius microstructure in young healthy women who performed axial forearm loading or participated as non-loading controls. We found that local regions of high strain magnitude and gradient are associated with increased trabecular formation and remodeling, while low strain magnitude and gradient are associated with trabecular bone resorption. Cortical strain gradient was higher near formation versus resorption in the control group, and both adaptation types occurred preferentially near high strain gradients at the periosteal surface. While we observed a significant measurable relationship between strain and adaptation, only half of very high and low strain elements were near formation or resorption only. The similarity of the strain/adaptation relationship between loading and control groups suggest that, at a local level, the same mechanical cues drive tissue remodeling, regardless of the net stimulus or change. Overall, our results show that participant-specific bone strain and adaptation can be estimated using currently available non-invasive imaging techniques. Our results also highlight that bone strain has a measurable, controlling influence on the adaptive response in healthy adult women. To the best

of our knowledge, this is the first study to relate prospectively measured changes in human bone structure to subject-specific bone strain, based on real force measurements. This is an important first step toward defining loading thresholds above or below which bone formation or resorption occur, quantifying the extent to which changes in human bone structure can be predicted based on strain, and characterizing the influence of physical activity history, age, and other physiological factors on these thresholds. Ultimately, such knowledge could inform predictive models of bone adaptation, enabling the in silico comparison and optimization of targeted loading interventions to maximize bone strength and prevent fragility fractures.

Acknowledgements

This work was supported by NIAMS of the National Institutes of Health under award number R01AR063691. This material is based upon work supported by the National Science Foundation Graduate Research Fellowship Program under Grant No. DGE-1106756. This research was performed using computational resources supported by the Academic & Research Computing group at Worcester Polytechnic Institute and the National Science Foundation under Grant No. DMS-1337943. Any opinions, findings, and conclusions or recommendations expressed in this material are those of the author(s) and do not necessarily reflect the views of the National Science Foundation or the National Institutes of Health. We thank Joshua Johnson, Tiffiny Butler, and Sabahat Ahmed for their role in data collection for the parent study. We thank Michael DiStefano for his assistance with local adaptation image analysis.

Chapter 6: Aim 3, Develop a Forward Bone Adaptation Simulation for the Human Forearm Loading Model

6.1 Introduction

Osteoporotic bone fractures are experienced by 1 in 3 women over age 50 (Melton, 1995). Exercise is a cost-effective, non-pharmacologic strategy for increasing bone strength and preventing fractures. Several meta-analyses have shown that impact and resistive exercise elicits consistent, modest (~1-3%) increases in bone density (Babatunde et al., 2012; Ireland and Rittweger, 2017; Zhao et al., 2014), but there are no established methods for personalizing interventions for specific clinical populations or individuals.

Computer simulations of load-driven bone adaptation are a promising approach for comparing loading interventions in silico, potentially reducing the need for expensive and time-consuming clinical exercise trials. In particular, medical image-based, patient-specific models could be used to simulate several versions of an intervention for an individual, allowing physicians to prescribe the intervention with the greatest predicted increases in bone formation. To date, several simulations have been proposed, combining mathematical theories of bone adaptation and finite element modeling. Earlier models generally modeled bone as a continuum solid (Beaupré et al., 1990a; Fyhrie and Carter, 1990; Huiskes et al., 1987), but more recently, there has been an increased focus on predicting trabecular adaptation at the microstructural level (Adachi et al., 2001; Huiskes et al., 2000; Ruimerman et al., 2005a; Schulte et al., 2013b). In animal models, micro-CT allows simulations to be run on micro-FE models of real bone geometries with boundary conditions based on experimental loading conditions from in vivo studies. Importantly, predicted changes can be compared to follow-up micro-CT scans from the

animal studies to validate the mathematical remodeling rules (Adachi et al., 2001; Levchuk et al., 2014; Morgan et al., 2015; Schulte et al., 2013b).

Looking toward human application, Badilatti et al. (2016) established a load-driven adaptation simulation of the human vertebra using ex vivo micro-CT scans and bone strain estimated using a retrospective load estimation method (Badilatti et al., 2016). While qualitative comparison to biopsies from different patients support that the simulation generally produces realistic results, lack of prospective bone imaging prohibits patient-specific validation. Overall, lack of experimental data describing in vivo bone loading and tissue-level structural changes represents the largest bottleneck in further development of patient-specific bone adaptation simulations.

Previously, our lab established a human bone loading model to study the relationship between bone strain and adaptation in the distal radius. Participants lean the palm of their hand onto a padded load cell to apply cyclic, axial loading to the forearm. Bone strain within the distal radius during loading is estimated using computed tomography (CT) based finite element (FE) models, and strain is related to changes in bone structure measured using high resolution peripheral quantitative CT (HRpQCT). FE boundary conditions consist of two forces applied at the scaphoid and lunate carpals directed toward the centroid of the proximal radius, representing an axial load distributed through the wrist. This is based on verbal directions to participants to load evenly with the forearm vertical, but the extent to which achieved loading varies between and within individuals has not been systematically tested.

In Aim 2B, we showed that following 12 months of the forearm loading task, trabecular bone adaptation was related to local, tissue-level bone energy equivalent strain. Here, our purpose was to use this experimental data to develop and apply an iterative, in silico bone

adaptation algorithm for the forearm loading task, with a particular focus on the influence of FE boundary conditions on simulation results. This was accomplished in three parts. First, we assessed the ability of the bone adaptation algorithm with simple, axial boundary conditions to predict prospectively measured changes in trabecular bone volume fraction (BV/TV) measured over 12 months using HRpQCT. We hypothesized that the simulation would predict participant-specific trabecular changes similar to those measured experimentally. Second, we measured variability in task execution of forearm loading using experimental motion capture, and assessed the influence of variability on FE-estimated bone strain in a sensitivity analysis of FE boundary conditions. We hypothesized that FE-estimated trabecular strain distribution, but not overall magnitude, would be dependent on boundary conditions. Third, we compared trabecular changes predicted by the adaptation simulation with simple axial and variable loading conditions. We hypothesized that simulation predictions would be dependent on boundary conditions, such that the simulation is capable of producing distinct adaptation patterns for different versions of loading interventions.

6.2 Methods

6.2.1 Experimental Loading Intervention

The experimental bone adaptation data reported here were collected as part of a larger, institutional approved randomized controlled trial enrolling 102 women ages 21-40 (Troy et al., 2020). Inclusion criteria included healthy normal BMI, menstrual cycles, serum vitamin D, calcium intake, and forearm areal bone mineral density. Exclusion criteria included history of medical conditions or use of medications known to affect bone health, previous injury to the non-dominant arm, and regular participation in heavy forearm loading activities (i.e. gymnastics, volleyball, and racket sports).

For the parent study, participants were randomized into one of five loading groups or a non-loading control group. Participants in loading groups were asked to complete three sessions of 100 cycles of loading per week for the 12-month study period. Participants were assigned individualized target force magnitudes to generate the average bone strain for their experimental group using continuum FE models (Bhatia et al., 2014). Loading was performed using custom devices consisting of a padded uniaxial load cell (Standard Load Cells; Gujarat, India), data logger (DATAQ DI-710, DATAQ Instruments Inc.; Akron, OH), and custom LED circuit. Loading magnitude was guided by the LED circuit, with indicator lights turning on when applied force was equal to 10 N below and above the target magnitude. Loading rate was guided using auditory beeping cues played on a digital voice recorder. Vertical applied force was recorded at 100 Hz, and loading waveforms were analyzed using a custom MATLAB (Mathworks; Natick, MA) script to calculate the peak force (N) and loading rate (N/s) for each cycle. An overall "loading dose" was calculated for each participant as the product of average peak force, average loading rate, and number of loading sessions performed during the study period. Bone structure was measured every three months using HRpQCT (XtremeCT I, Scanco Medical; Brüttisellen, Switzerland) at the distal radius (Laib et al., 1998). The data used here includes subjects who were assigned to the loading intervention who had good quality baseline and 12-month HRpQCT scans (motion ≤ 3 (Pialat et al., 2012)) and were in the top two quartiles for loading dose.

6.2.2 Estimation of Tissue-Level Bone Strain

Bone strain during forearm loading was estimated using validated (Johnson and Troy, 2017a) participant-specific multiscale FE models of the distal 10 cm of the radius (Figure 6.). Multiscale models consist of continuum FE meshes generated from clinical resolution CT scans (GE Brightspeed, GE Medical; Milwaukee, WI; 120 kV, 180 mA, voxel size 234 µm x 234 µm x

625 μm) flanking a micro-FE mesh at the HRpQCT scan site (82 μm isotropic voxel size). Continuum elements were ten-node tetrahedrons with a 3 mm nominal edge length, and were assigned inhomogeneous, density-based linear elastic material properties (E=1.95 MPa to 35 GPa) according to (Morgan et al., 2003). The voxel-based micro-FE mesh consisted of hexahedral elements generated directly from HRpQCT voxel coordinates, and were assigned homogeneous linear elastic material properties (E=15 GPa, v=0.4). At the transition between continuum and micro-FE meshes, continuum element size was refined to facilitate a tie constraint between meshes.

FE boundary conditions simulated one cycle of the forearm loading task, with forces distributed at the distal articular cartilage to apply physiological loading. As a preprocessing step outside the bone adaptation simulation, as previously described (Johnson and Troy, 2017b), cartilage contact forces were calculated using a continuum-only FE model including non-deformable CT-based meshes of the scaphoid and lunate carpals. Ramped quasistatic forces were applied at the centroid of each carpal directed toward the centroid of the fixed proximal radius. Carpal forces were calculated so the resultant magnitude was equal to the participant-specific average achieved force recorded by the loading device, with 40% of force applied at the lunate and 60% and the scaphoid. Models were solved using Abaqus CAE (v2016, Dassault Systèmes; Vélizy-Villacoublay, France), and the resulting normal and shear contact forces at the cartilage nodes were exported for application to matching nodes in multiscale models. The same cartilage forces were applied during each iteration of the bone adaptation simulation.

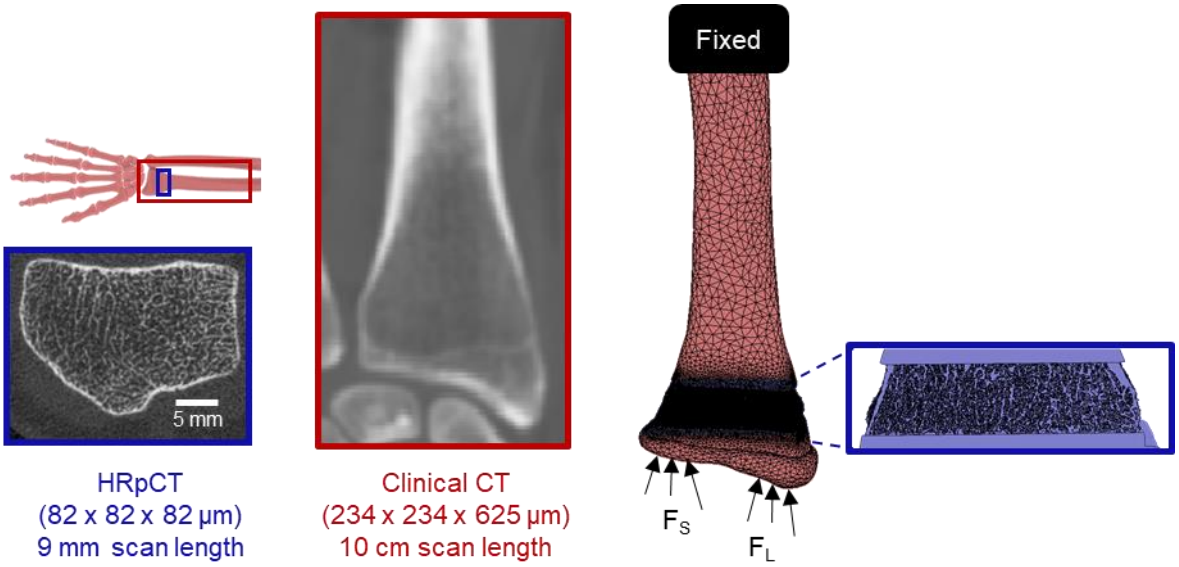

Figure 6.1: Multiscale FE models used to estimate tissue-level bone strain during the forearm loading task. Participant-specific meshes are generated from clinical resolution CT and HRpQCT scans, and boundary conditions simulate axial loading through the scaphoid (S) and lunate (L) carpals at the wrist.

6.2.3 Development of the Strain-Driven Bone Adaptation Algorithm

The bone adaptation algorithm assumes that trabecular bone adapts to mechanical loading, such that bone formation is more likely in high strain regions and resorption is more likely at low strain regions. The adaptation algorithm is applied only to the micro-FE section of the multiscale model, and is limited to the trabecular compartment. At each iteration, energy equivalent strain is calculated for each micro-FE element as

$$\varepsilon_{eeq} = \sqrt{\frac{2U}{E}} \quad \textbf{(6.1)}$$

where E is elastic modulus and U is strain energy density, calculated as

$$U = \frac{1}{2}[\sigma_1\varepsilon_1 + \sigma_2\varepsilon_2 + \sigma_3\varepsilon_3] \quad \textbf{(6.2)}$$

where σ_n and ε_n are the principal stress and strain components, respectively. It is assumed that osteocytes throughout bone tissue (one per elements center) release biochemical signals in proportion to local mechanical strain, S, which we assume is energy equivalent strain. Bone

adaptation occurs at bone surfaces, where osteoblast and osteoclast effector cells respond to a cumulative, density-weighted stimulus, *P(X)*, calculated based on (Mullender et al., 1994) as

$$P(x) = \sum_{i=1}^{N} e^{-d_i(x)/D} S_i(t) \quad \textbf{(6.3)}$$

where $S_i(t)$ is the strain stimulus at osteocyte *i* a distance $d_i(x)$ from effector cells at surface location *x*. The distance decay factor, *D*, defines the neighborhood of osteocytes that contribute to *P(x)*, and reflects the decrease in biochemical signal strength for osteocytes further from the bone surface. The contribution of osteocyte *i* to *P(x)* is equal to e^{-1}~=37% of its initial strength when $d_i(x)=D$, and only osteocytes within distance *D* contribute to the signal at *x*. The remodeling stimulus $P_i(x)$ is entered into probability density functions that determine whether the element is removed, an adjacent element is added, or the surface remains quiescent. Whereas most published remodeling simulations are deterministic in that high strains trigger formation only and low strains resorption only, our model accounts for our experimental observation that adaptation is more stochastic, with formation occurring more often near high strains but also near low strains (and vice versa for resorption). The probability density functions are depicted in Figure 6.2, showing that at any given value of *P(x)* there is a nonzero probability of resorption, formation, and quiescence, and these three probabilities add to one hundred percent. The probabilities of formation ($Prob_{form}$) and resorption ($Prob_{resorb}$) are dependent on *P(x)* such that:

$$Prob_{form} = \begin{cases} Prob_{form,min} & P(x) \le P_{sat,min} \\ Prob_{form,min} + \left(\frac{Prob_{form,max} - Prob_{form,min}}{P_{sat,max} - P_{sat,min}}\right) * \left(P(x) - P_{sat,min}\right) & , P_{sat,min} < P(x) \le P_{sat,max} \\ Prob_{form,max} & P(x) > P_{sat,max} \end{cases}$$

and **(6.4)**

$$Prob_{res} = \begin{cases} Prob_{res,max} & P(x) \le P_{sat,min} \\ Prob_{res,max} - \left(\frac{Prob_{res,max} - Prob_{res,min}}{P_{sat,max} - P_{sat,min}}\right) * \left(P(x) - P_{sat,min}\right) & , P_{sat,min} < P(x) \le P_{sat,max} \\ Prob_{res,min} & P(x) > P_{sat,max} \end{cases}$$

where $P_{sat,min}$ and $P_{sat,max}$ are thresholds of stimulus P, below and above which the probabilities of formation and resorption are saturated, respectively. Between the saturation thresholds, the probability of formation linearly increases from $Prob_{form,min}$ to $Prob_{form,max}$, and the probability of resorption linearly decreases from $Prob_{res,max}$ to $Prob_{res,min}$. This probabilistic approach was implemented for each trabecular surface element by determining the probabilities of formation, resorption, or neither based on the P stimulus value for that element, and selecting one option using a random number generator that selects an integer between zero and one hundred.

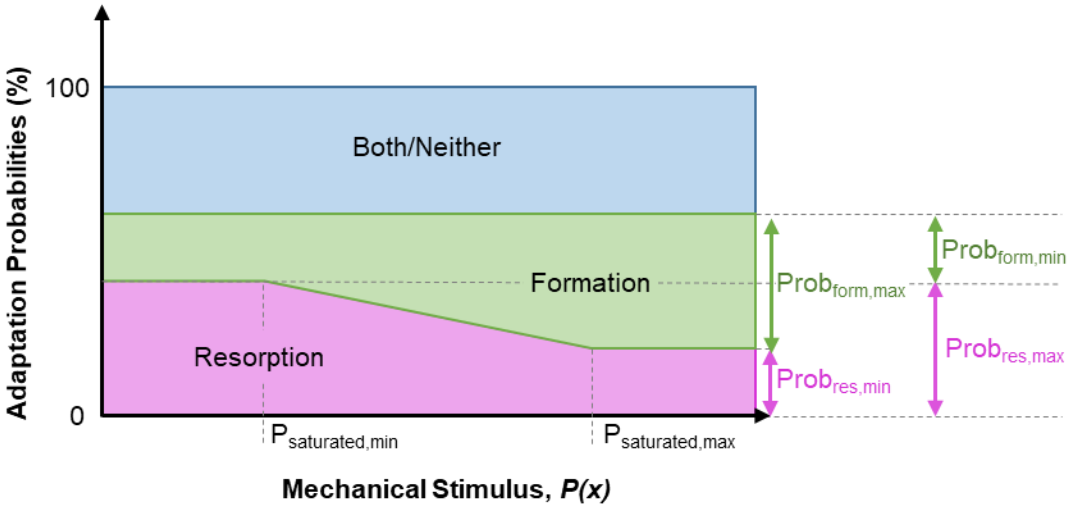

Figure 6.2: Probability density function used to determine adaptation behavior for each surface trabecular element as a semi-stochastic function of mechanical stimulus *P(x).*

6.2.4 Bone Adaptation Simulation Parameter Selection and Implementation

For the current analysis, a single set of parameter values was selected for all participants, assuming that the mechanostat has the same regulatory setpoints across individuals. Due to the iterative nature of the simulation, parameter values cannot be directly fitted to match experimental data. Therefore, we calculated iteration 1 predicted changes for five participants using several candidate parameter values, and selected those generating changes in the correct direction as experimental changes most often. Overall, the P value thresholds influenced the

balance between formed and resorbed volumes, while the minimum and maximum probabilities had a larger influence and regulated the magnitude of the adapted volumes. $P_{sat,min}$ and $P_{sat,max}$ were set to the average 5th and 80th percentile strain values (435 με and 5182 με) calculated across a subgroup of thirteen participants (same as the sensitivity analysis described below). These percentile cutoffs were selected such that a greater percent (20% versus 5%) of elements would be at the maximum probability of formation than resorption to achieve the net increase in BV/TV observed experimentally.

The minimum and maximum probabilities for formation and resorption were set to 1% and 4%, respectively. The 1:4 ratio for the minimum and maximum probabilities was based on the maximum and minimum volumes of formed and resorbed bone found at extremely high and extremely low strain regions in Aim 2B (~10% and ~40%). Probabilities were initially set directly to 10% and 40%, but were scaled down to allow for a gradual change in net adaptation over the total number of iterations. This was necessary to prevent large areas of the micro-FE mesh from becoming disconnected and subsequently removed in excess of resorption predicted by the algorithm. For a subset of five participants, simulations with probabilities set to 2% and 8% and to 1% and 4% were run for eight iterations. The error in average group change, as well as average absolute error for each participant was lower for 1% and 4% and thus were selected as the final values.

The bone adaptation simulation was fully automated and implemented on a UNIX server cluster. A custom MATLAB shell script controlled the iterative process of running FE loading simulations in Abaqus (v2016, Simulia, Dassault Systèmes; Vélizy-Villacoublay, France), obtaining the resulting element stress and strain tensors within the HRpQCT micro-FE mesh, calculating the mechanical stimulus and adaptation behavior for each trabecular element, and

updating the micro-FE mesh geometry (Figure 6.3). The MATLAB shell script was run on 12 parallel processors (2.1-3.2 GHz) and 80 GB RAM, with the implementation of the adaptation algorithm and update of the micro-FE mesh taking approximately 15-40 minutes at each iteration. Each multiscale FE model was solved using 54 parallel processors (2.1-3.2 GHz) and 200 GB RAM in 3.4±1.9 hours. The simulations were run for ten iterations, and the final micro-FE mesh geometry was exported for comparison with experimental follow-up scans. Ten iterations was selected to achieve model convergence based on a preliminary version of the simulation not incorporating the probabilistic density functions, which showed a decrease in the net change at each iteration from 0.65% to 0.07% over ten iterations. For the current simulation algorithm, average error in raw change in total trabecular BV/TV continued to decrease over the simulation (Figure 6.4). However, we observed that changing the number of iterations from 8 to 10 did not affect the interpretation of statistical comparisons of simulated and experimental changes. Future work in improving model tuning should confirm whether additional iterations improve simulation performance.

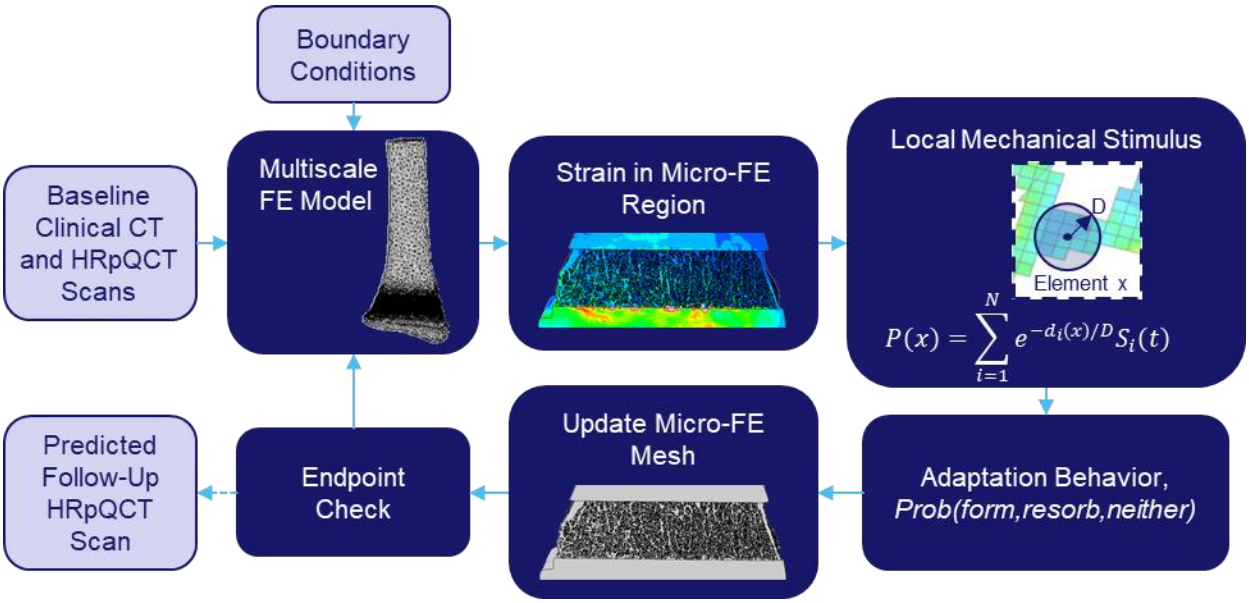

Figure 6.3: Workflow of the strain-driven bone adaptation simulation. Clinical resolution CT and HRpQCT scans acquired at baseline are used to define the initial multiscale FE model, with boundary conditions simulating the forearm loading task. Energy equivalent strain is calculated within the micro-FE region, and at each trabecular surface element the mechanical stimulus *P(x)* is calculated and the probabilistic adaptation behavior is determined. The updated micro-FE mesh is integrated back into the multiscale FE model for the next iteration. The final simulation outputs are compared to experimental follow-up HRpQCT scans.

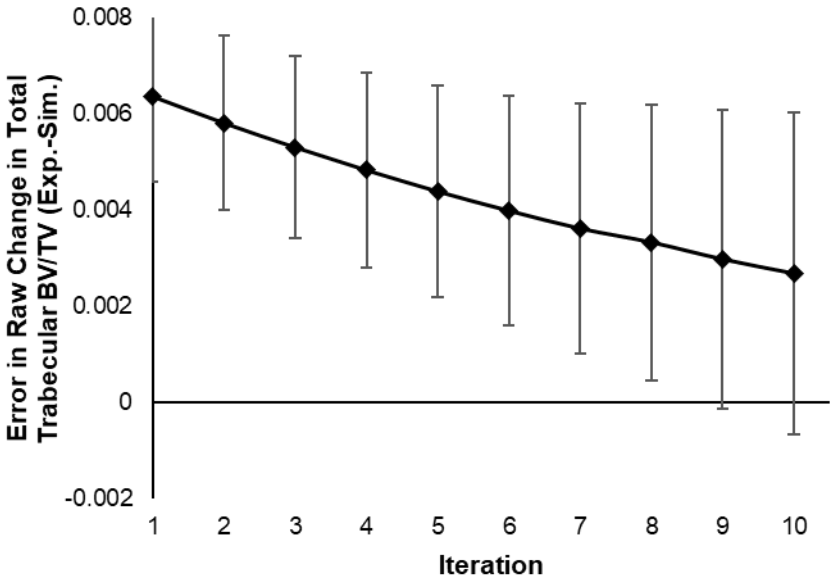

Figure 6.4: Error in simulation prediction of raw change in total trabecular BV/TV versus experimental changes over the number of simulation iterations. Error bars indicate standard error.

6.2.5 Comparison of Experimental and Predicted Trabecular Bone Adaptation

The validity of the bone adaptation simulation was assessed by comparing participant-specific predicted changes in trabecular BV/TV to experimental changes measured from 12-month HRpQCT scan data. BV/TV was used as the adaptation outcome because the micro-FE mesh geometry generated by the simulation is binary, and calculation of BV/TV does not require full greyscale information.

Experimental change in BV/TV was determined from baseline and 12-month follow-up HRpQCT scans. The baseline and follow-up scans were contoured and segmented using the manufacturer's standard, semi-automatic method (MacNeil and Boyd, 2007). The transformation matrix required to align the baseline to the follow-up image was calculated using three-dimensional rigid registration of the greyscale images (Image Processing Language, V5.16, Scanco Medical AG; Bruttisellen, Switzerland). The transformation matrix was used to transform the trabecular mask for the baseline scan, generated by the standard analysis program, into the follow-up image coordinate system. The non-transformed trabecular mask was applied to the segmented baseline scan and the transformed mask was applied to the segmented follow-up scan to determine BV/TV in matching regions using Mimics v15.1 (Materialise; Leuven, Belgium). The trabecular region was also divided into inner (60%) and outer (40%) regions (Figure 6.5) to assess whether the adaptation simulation accurately estimates the regional distribution of bone changes. Due to the limitations of only having binary information for the micro-FE mesh, a direct estimate of BV/TV was calculated as the number of bone voxels to total voxels in the region of interest. The measurement of experimental change in BV/TV has some short-term precision error, mostly due to partial volume effect of the HRpQCT scans and participant repositioning error. The root mean square coefficients of variation for change in

BV/TV, calculated from two repeat scans of eight individuals acquired with less than two weeks between scans, were 1.27%, 1.45%, and 1.41% for total, inner, and outer trabecular compartments, respectively.

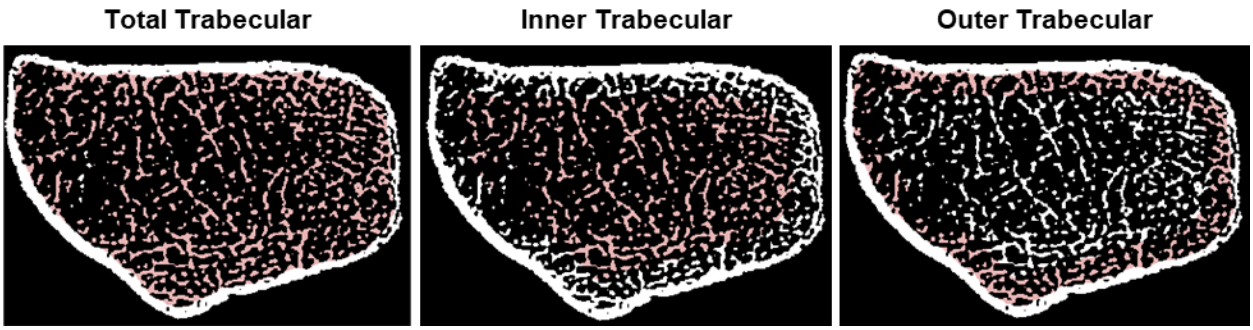

Figure 6.5: Definition of total, inner (60%) and outer (40%) trabecular bone compartments.

6.2.6 Measurement of Forearm Loading Task Execution Variability

Six women ages 21-40 participated in an institutionally approved motion capture study to quantify the realistic range of variability in loading direction. Individuals with fractures or other injuries to the non-dominant arm in the past five years were excluded.

Each participant completed one laboratory visit, during which four sessions of 25 cycles of forearm loading were performed while forearm motion and force applied to the hand were measured. Each loading session took approximately one minute to complete, and had varying target load magnitudes and rates (Table 6.1) selected to reflect the range of loading conditions applied in the parent study. Loading was performed using the same loading devices as the parent study.

.

Table 6.1: Target loading parameters for each loading session during the biomechanics motion capture experiment. Parameters were selected to generate the range of values observed in the parent bone loading study.

Condition	Target Force Magnitude (N)	Time to Reach Peak Force (s)	Target Loading Rate (N/s)
Low Magnitude, Moderate Rate	200 N	0.33 s	667 N/s
High Magnitude, Moderate Rate	350 N	0.33 s	1,167 N/s
Moderate Magnitude, Low Rate	300 N	0.8 s	375 N/s
Moderate Magnitude, High Rate	300 N	0.1 s	3,000 N/s

Reflective markers (6.4 mm sphere Pearl Markers, B&L Engineering, Santa Ana, CA) were placed at the third metacarpal, radial styloid, ulnar styloid, and medial and lateral elbow, consistent with recommendations of the International Society of Biomechanics (Wu et al., 2005). Bony landmarks were located using palpitation by a single investigator. Marker positions during loading were recorded using a six-camera Optitrak Motive motion capture system (Optitrack Flex 13, Natural Point Inc.; Corvalis, OR) at a sampling frequency of 120 Hz. Cameras were focused on the loading device, which was placed on top of a force plate set on a hip-high table. The force plate (AMTI OPTIMA, Advanced Mechanical Technology; Watertown, MA) was used in conjunction with Netforce software (Advanced Mechanical Technology; Watertown, MA) to record force and moment data in three dimensions at a sampling frequency of 1200 Hz. Camera and force plate data were synchronized by setting the motion capture system as an external trigger for the force plate.

Raw motion and force data were used to calculate the relative position of the 3D force vector relative to the long axis of the forearm using a custom MATLAB script. Force data were down sampled to 120 Hz to match camera data, and the instance of peak force magnitude was identified for each loading cycle. Center of pressure coordinates were calculated for each peak as

$$COP_x = \frac{-M_y + COP_z * F_x}{F_z}, COP_y = \frac{M_x + COP_z * F_y}{F_z} \quad \textbf{(6.6)}$$

Where $[F_x, F_y, F_z]$, $[M_x, M_y, M_z]$, and $[COP_x, COP_y, COP_z]$ define the force, moment, and center of pressure in the force plate local coordinate system. Here, COP_z is constant and equal to the vertical distance between the force plate origin and the top of the loading device (15 cm). The center of pressure coordinates and force were transformed into the global coordinate system of the marker data using a calibration triangle placed at a known location within the force plate coordinate system.

Marker coordinate data were used to define a local coordinate system for the forearm at the instance of each force peak. The Y axis points from the wrist joint center (midpoint between the radial styloid and ulnar styloid markers) towards the elbow joint center (midpoint between medial and lateral elbow markers). The Z axis points from the wrist joint center toward the radial styloid, and the X axis is defined by the cross product of Y and Z pointing anteriorly toward the palm (Figure 6.6). The coordinate system definition was based on the International Biomechanics Society standards (Wu et al., 2005), adapted to move the origin of the Y axis from the ulnar styloid to the wrist joint center to facilitate interpretation within the context of the FE model. The Euler angle sequence needed to rotate the global coordinate system into the forearm local coordinate system was calculated and applied to the force vector and COP coordinates. For each of the six motion capture participants, the average peak force vector was calculated and normalized to its magnitude to determine the unit vector describing the mean direction of force relative to the forearm. The overall average unit vector was calculated over all participants for use in the FE sensitivity analysis.

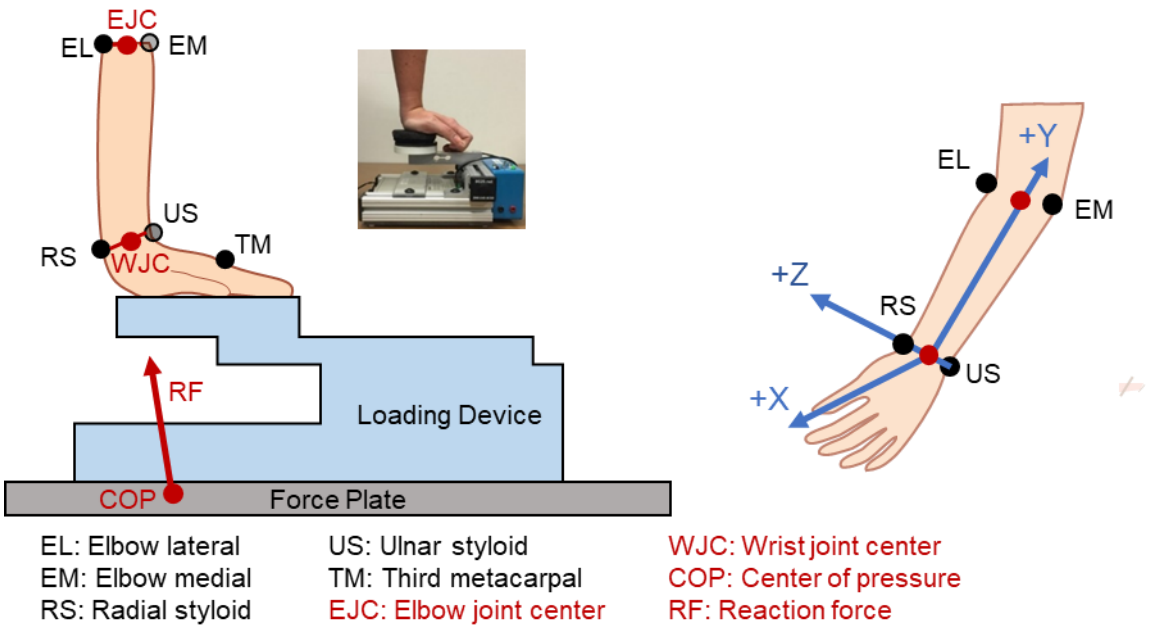

Figure 6.6: (Left) Experimental setup for the biomechanics loading variability study, including relative position of loading device and force plate, as well as reflective marker locations used to define (Right) the local forearm coordinate system.

6.2.7 FE Model Boundary Condition Sensitivity Analysis

Based on the measured loading variability, four sets of boundary conditions were applied to multiscale FE models for thirteen participants. Axial boundary conditions are the same as previously described, with two forces directed from the centroids of the scaphoid and lunate toward the proximal radius, yielding an axially directed resultant load. To account for measured variability in center of pressure, we modeled the two extreme cases, such that 100% of the resultant load is applied at the scaphoid ("scaphoid" condition), and 100% of the resultant load is applied at the lunate ("lunate" condition). Finally, tilted boundary conditions consisted of two distributed forces rotated to represent the average measured tilt relative to the forearm. For the tilted condition, the rotation matrix between a vertical vector and the average unit vector calculated across motion capture participants was applied to the axial condition force vectors. For each loading condition, a separate continuum-only model with the scaphoid and lunate

carpals was solved using the corresponding force vectors, and the resulting cartilage contact forces were exported for use in multiscale FE models.

Metrics of FE-estimated strain reflecting loading magnitude and distribution were compared between loading conditions. Strain magnitude was measured as the median value of energy equivalent strain, $\varepsilon_{eeq,med}$. Multiple metrics were used to characterize bone strain distribution. The standard deviation of ε_{eeq} was used to characterize overall loading variability, where a greater standard deviation indicates that strain values are, on average, further from the mean. We also calculated the percent of bone volume with ε_{eeq} greater than 75% of the 95th percentile value, where a smaller high strain volume indicates a more concentrated, less uniform strain distribution.

6.2.8 Comparison of Predicted Trabecular Bone Adaptation under Axial versus Tilted Loading

To measure the sensitivity of the adaptation simulation to changes in loading, predicted changes for simulations with axial and tilted FE boundary conditions were compared for the subset of thirteen participants from the sensitivity analysis. Simulations were run with all other parameters equal to those for the axial loading condition. Predicted changes in BV/TV for each loading condition were calculated for the total trabecular region. Additionally, as tilting the loading vector likely influences the radial distribution of strain and therefore mechanical stimulus *P(x)*, predicted changes were also compared within angular quadrants. Posterior, anterior, radius, and ulna quadrants were defined at 45° angles relative to the axes of anatomically aligned FE models (Bhatia et al., 2015).

6.2.9 Statistics

Experimental and simulation predicted changes in BV/TV were compared using a paired t-test (α=0.05), with separate tests performed for the total, inner, and outer trabecular bone

compartments. To explore potential factors that may influence adaptation outside of strain, we compared participant characteristics between participants for which the direction of change in BV/TV (i.e. net increase or decrease) was predicted correctly versus incorrectly using independent t-tests (α=0.05).

For the FE boundary condition sensitivity analysis, strain magnitude and distribution metrics were compared between conditions using repeated measures ANOVA with Bonferroni-corrected posthoc t-tests (α=0.05). For each strain metric, one model was used to compare axial, scaphoid, and lunate loading, and a second model was used to compare axial and tilted loading. For each model, the dependent variable was the strain outcome metric, and boundary condition was treated as a within-subject repeated measure. Separate models were fit for the integral, total trabecular, inner trabecular, outer trabecular, and cortical compartments.

The sensitivity of the bone adaptation simulation to FE boundary conditions was assessed by comparing change in total trabecular BV/TV between axial and tilted conditions using a paired t-test (α=0.05). Additionally, simulated changes and median trabecular strain were compared within each quadrant between axial and tilted loading conditions using paired t-tests (α=0.05).

6.3 Results

6.3.1 Bone Adaptation Simulation

The average increase in total trabecular BV/TV across participants was similar for experimental measurements and simulation predictions (simulation (p=0.31, effect size=0.25) (Table 6.2, Figure 6.7). However, the simulation failed to capture the experimental increase in inner trabecular BV/TV, instead predicting an average group decrease (p=0.01, effect size=0.66). This was balanced in the outer trabecular compartment, for which the simulation overestimated

the average group increase in BV/TV (p=0.01, effect size=0.65). Looking at individual changes (Figure 6.8), the direction of change in BV/TV (increase versus decrease) was predicted correctly for 11 out of 18 participants. Qualitatively, we observed that net changes between baseline and the final simulation mesh consisted of relatively large resorbed regions where entire trabeculae were removed, while formation tended to occur as thin layers on existing trabecular struts (Figure 6.9). Larger resorption regions were generally more common in participants and regions within bone with lower BV/TV, where trabecular connectivity is more susceptible to disruption. We also noted a trend in participants for which the simulation over and underestimated change that formation was more common in the distal portion of the micro-FE mesh, and resorption was more common near the proximal end. This may be related to loading distribution, as well as generally lower BV/TV in the proximal end closer to the marrow cavity.

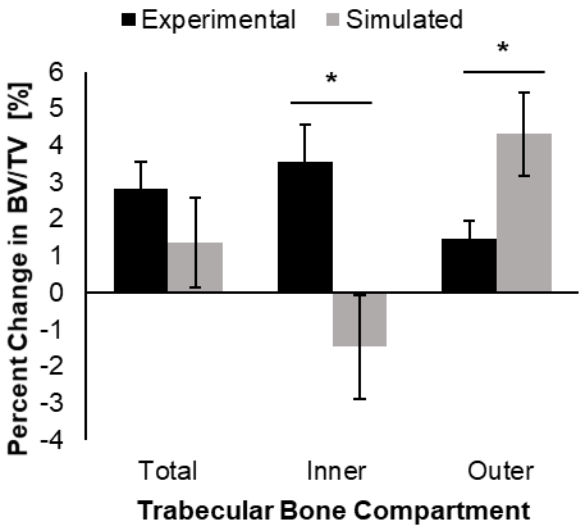

Figure 6.7: Average within-participant percent changes in BV/TV measured experimentally versus predicted by the adaptation simulation. Percent changes are calculated for the total, inner, and outer trabecular bone compartments as a percent of the baseline value within the given compartment. Error bars indicate standard error, *indicates significant difference between experimental and simulated change within the compartment ($p<0.05$).

Table 6.2: Individual and group average values for baseline BV/TV and experimental and predicted percent changes in BV/TV in the total, inner, and outer trabecular bone compartments. For the total trabecular compartment, it is indicated whether the simulation correctly predicted the direction (increase or decrease) of change in BV/TV as measured experimentally. **Bold** indicates significant difference between experimental and simulated change within the compartment ($p<0.05$).

	Total Trabecular				**Inner Trabecular**				**Outer Trabecular**			
Direction correct?	Baseline BV/TV	Exp. Change (%)	Sim. Change (%)	Diff. (S-E) (%)	Baseline BV/TV	Exp. Change (%)	Sim. Change (%)	Diff. (S-E) (%)	Baseline BV/TV	Exp. Change (%)	Sim. Change (%)	Diff. (S-E) (%)
yes	0.26	3.5	3.8	0.3	0.22	3.3	1.4	-1.9	0.30	2.2	6.4	4.2
yes	0.28	6.4	6.0	-0.4	0.25	7.7	6.5	-1.2	0.34	4.4	5.4	1.1
yes	0.34	0.4	0.9	0.5	0.31	-0.4	-3.6	-3.3	0.39	0.5	6.1	5.5
yes	0.25	3.0	4.1	1.2	0.22	4.5	2.3	-2.2	0.29	0.8	5.7	4.9
yes	0.33	-2.7	-0.9	1.8	0.31	-3.8	-2.6	1.2	0.38	-0.5	1.6	2.2
yes	0.26	2.5	0.6	-1.9	0.22	4.8	-0.1	-4.9	0.31	-1.0	1.4	2.4
yes	0.26	1.0	3.1	2.1	0.23	0.8	-0.5	-1.3	0.32	1.7	6.7	5.0
yes	0.28	3.7	0.5	-3.2	0.25	2.1	-4.9	-7.0	0.32	5.1	5.4	0.3
yes	0.31	2.0	6.2	4.2	0.28	2.3	4.4	2.1	0.35	0.8	8.1	7.3
yes	0.26	6.4	0.5	-5.9	0.21	7.7	-3.0	-10.6	0.32	4.1	4.3	0.2
yes	0.27	5.6	11.6	6.0	0.24	6.1	9.4	3.4	0.32	4.3	14.5	10.2
no	0.24	0.9	-1.1	-2.0	0.19	4.4	-6.2	-10.6	0.30	-1.7	3.0	4.8
no	0.33	-1.3	1.6	2.9	0.29	-2.2	-1.6	0.6	0.37	-0.2	4.5	4.7
no	0.28	1.9	-1.5	-3.4	0.24	2.7	-4.5	-7.2	0.34	0.5	1.8	1.3
no	0.24	-0.4	7.7	8.0	0.21	-1.4	5.3	6.7	0.29	0.9	10.5	9.6
no	0.22	7.4	-3.9	-11.3	0.19	9.2	-5.5	-14.7	0.28	3.6	-1.9	-5.5
no	0.18	8.6	-2.9	-11.4	0.14	13.3	-7.8	-21.1	0.25	2.7	2.0	-0.7
no	0.24	2.0	-11.9	-14.0	0.18	2.8	-15.8	-18.6	0.35	-1.8	-8.0	-6.2
Mean	0.27	2.84	1.36	-1.47	0.23	3.55	-1.48	**-5.03**	0.32	1.46	4.31	**2.85**
SD	0.04	3.08	5.15	6.01	0.05	4.27	5.95	**7.61**	0.04	2.16	4.81	**4.39**

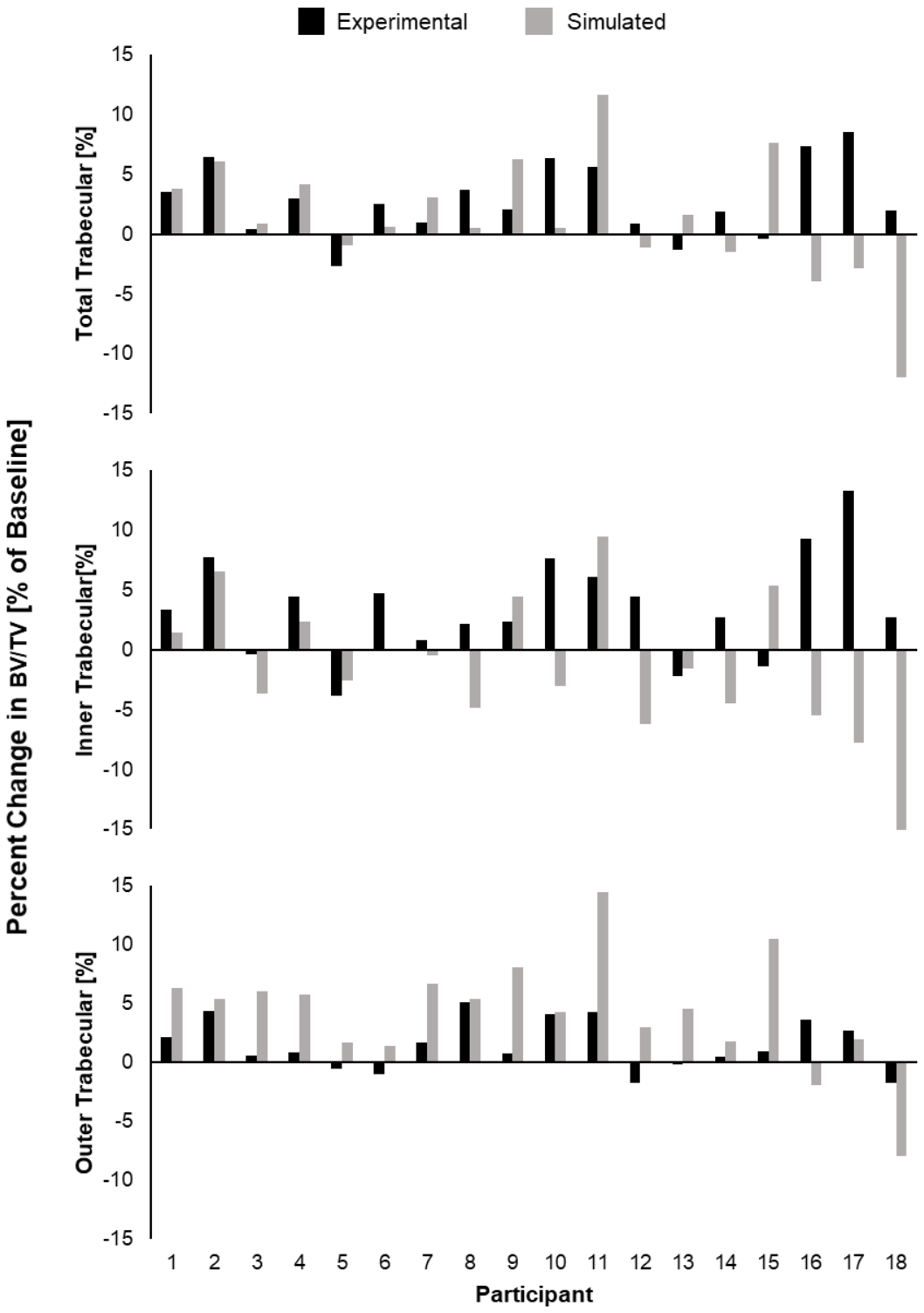

Figure 6.8: Experimental versus simulation-predicted change in BV/TV, calculated for the total, inner, and outer trabecular bone compartments as a percent of the baseline value for the given compartment. Data are presented individually for each participant. Positive change values indicate an increase from baseline to follow-up while negative values indicate a decrease in BV/TV.

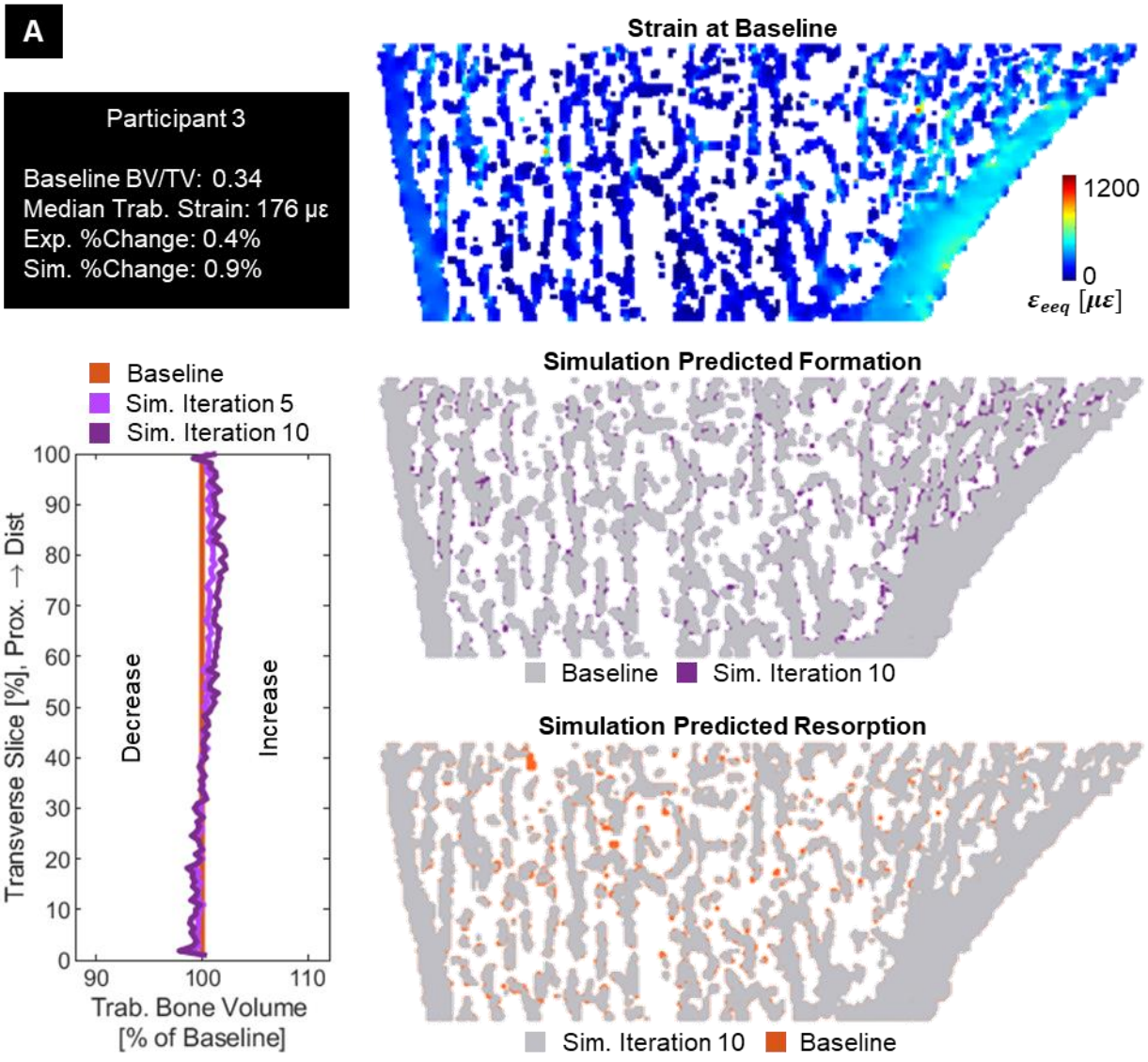
A
Participant 3
Baseline BV/TV: 0.34
Median Trab. Strain: 176 με
Exp. %Change: 0.4%
Sim. %Change: 0.9%
Strain at Baseline
1200
0
ε_{eeq} [$\mu\varepsilon$]
Baseline
Sim. Iteration 5
Sim. Iteration 10
Transverse Slice [%], Prox. → Dist
Decrease
Increase
Trab. Bone Volume
[% of Baseline]
Simulation Predicted Formation
Baseline
Sim. Iteration 10
Simulation Predicted Resorption
Sim. Iteration 10
Baseline

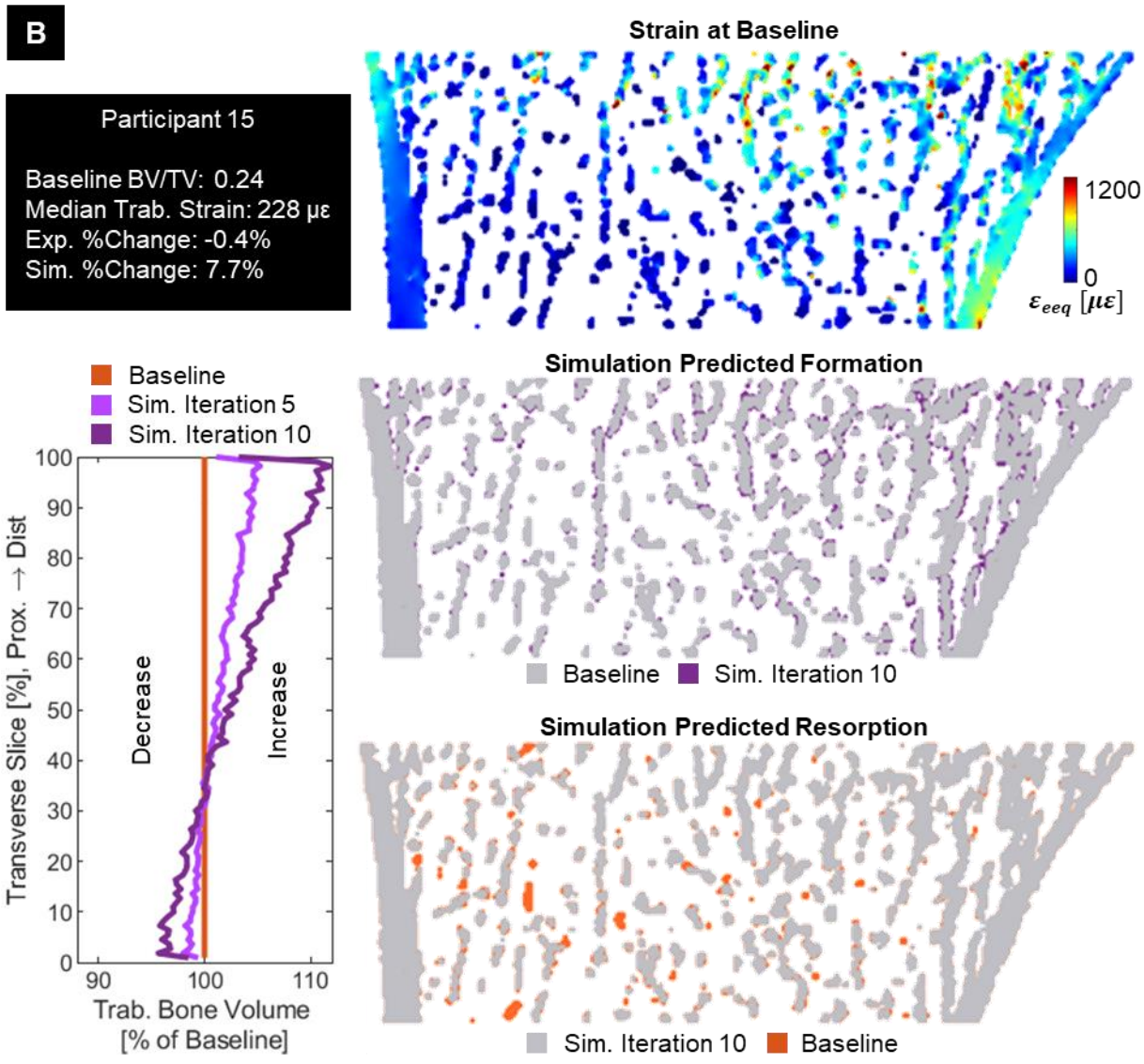
B
Participant 15
Baseline BV/TV: 0.24
Median Trab. Strain: 228 με
Exp. %Change: -0.4%
Sim. %Change: 7.7%
Strain at Baseline
1200
0
ε_{eeq} [$\mu\varepsilon$]
Baseline
Sim. Iteration 5
Sim. Iteration 10
Transverse Slice [%], Prox. → Dist
Decrease
Increase
Trab. Bone Volume
[% of Baseline]
Simulation Predicted Formation
Baseline
Sim. Iteration 10
Simulation Predicted Resorption
Sim. Iteration 10
Baseline

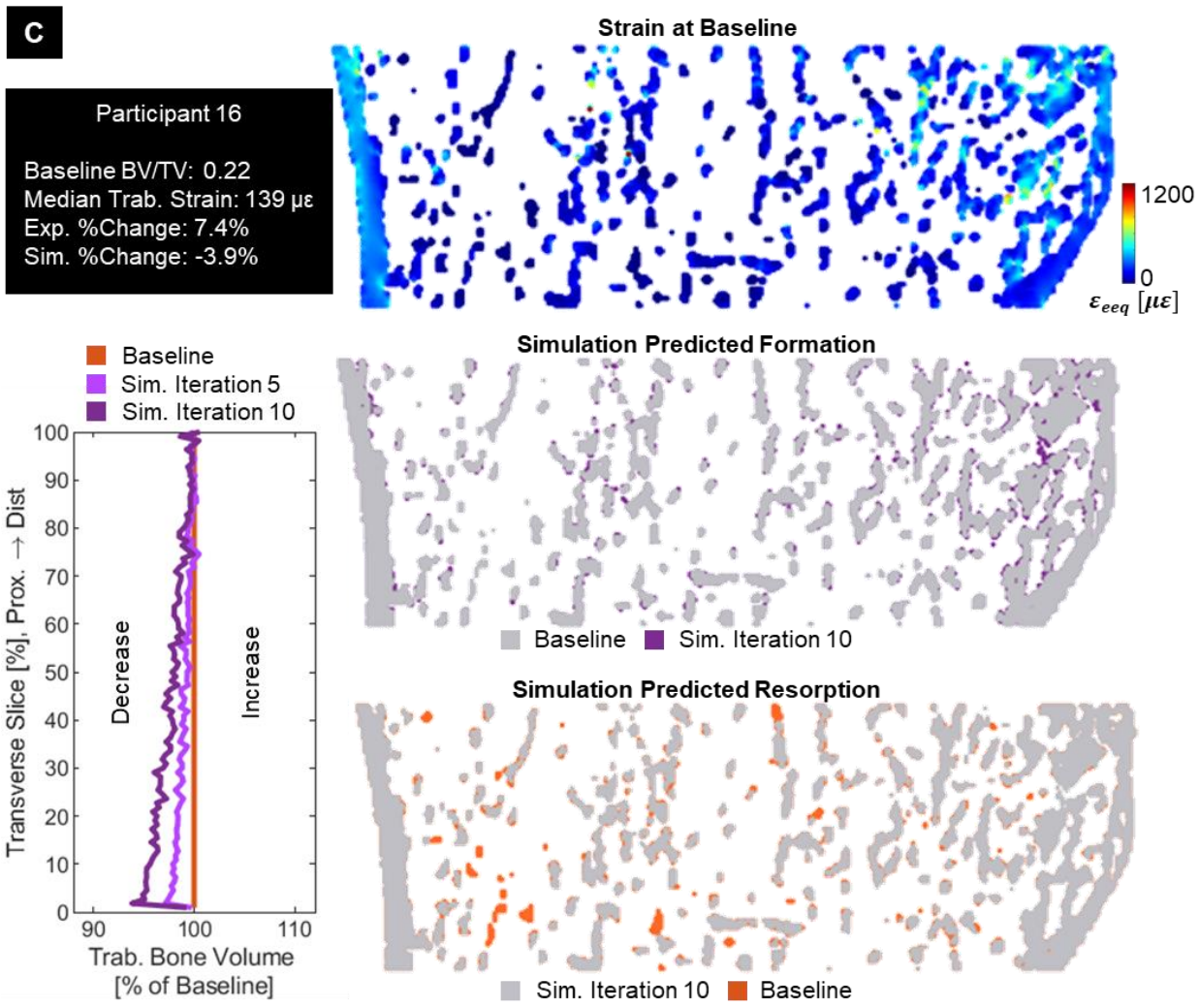

Figure 6.9: Representative illustrations of the bone adaptation simulation behavior for participants for which the simulation **(A)** closely matched experimental change, **(B)** incorrectly predicted an increase, and **(C)** incorrectly predicted a decrease in total trabecular BV/TV. Participant numbers correspond to those reported in Figure 6.6. Strain and adaptation behavior is visualized for a single, central coronal slice of the micro-FE region. Strain shows energy equivalent strain ($\boldsymbol{\varepsilon_{eeq}}$). Predicted formation is visualized by overlaying the baseline (gray) and final simulation mesh (purple), with purple elements indicating areas added during the simulation. Similarly, for resorption, orange voxels are those present at baseline but not in the final simulation mesh. The plot shows bone volume in each transverse slice, normalized to the within-slice volume at baseline. Values less than 100 indicate a net decrease in bone elements within a slice, and values greater than 100 indicating a net increase.

Among subjects for whom the simulation correctly predicted the direction of change in BV/TV, average absolute peak force was significantly greater than those with incorrect

simulation predictions (Table 6.3, Figure 6.10). There were no significant differences in loading rate or number of loading sessions completed. There was a non-significant trend towards higher median trabecular strain magnitude for those with correctly predicted direction of change. In terms of bone structure, baseline BV/TV was significantly higher for the correctly predicted group, but there was no difference in the experimentally measured percent change in BV/TV. Thus, correct prediction of the direction of net change in BV/TV was associated with generating higher magnitude loads and having a higher relative bone volume at baseline.

Table 6.3: Comparison of participant loading and bone parameters between individuals for which the simulation predicted the direction of change (increase or decrease) in BV/TV correctly or incorrectly. Differences were assessed using independent samples t-test, with p-values and Cohen's d effect size listed and **bold** indicating statistical significance.

	Direction Predicted Correctly (n=11)	Direction Predicted Incorrectly (n=7)		
	Mean (SD)	Mean (SD)	p-value	Effect Size
Number of Loading Sessions	180.6 (60.5)	176.4 (64.5)	0.89	0.07
Average Peak Force (N)	329.8 (41.2)	258.0 (85.2)	**0.03**	**1.17**
Average Loading Rate (N/s)	870.8 (629.6)	924.7 (527.3)	0.85	-0.09
Median Trabecular Strain (με)	196.6 (38.2)	158.0 (42.6)	0.06	0.96
Baseline BV/TV	0.282 (0.032)	0.245 (0.046)	0.06	1.00
Experimental Change in BV/TV (%)	2.9 (2.7)	2.7 (3.8)	0.91	0.06

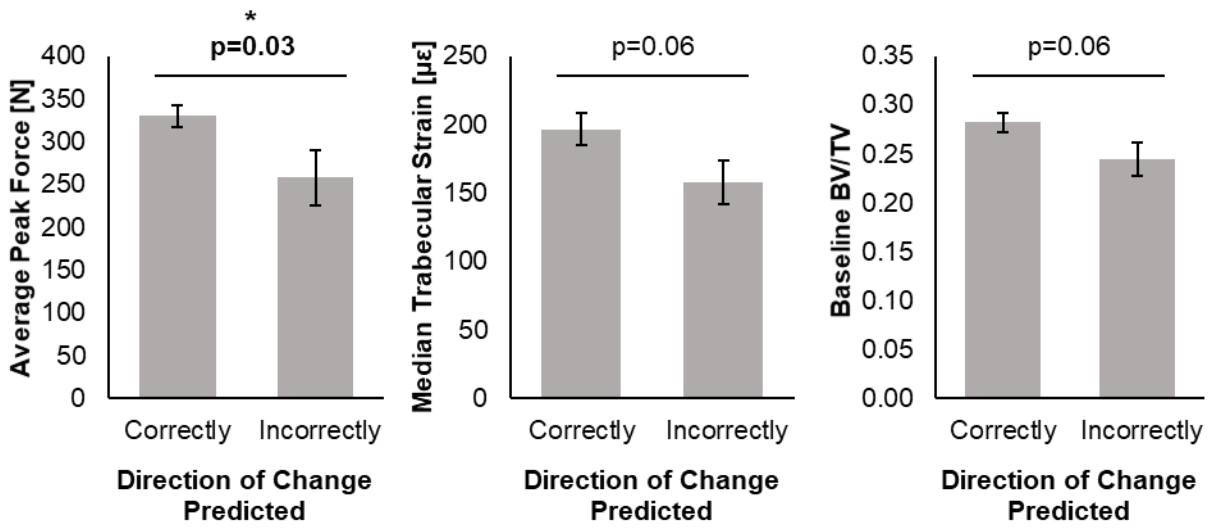

Figure 6.10: Comparison of loading parameters and baseline bone status between individuals for which the simulation predicted the direction of change (increase or decrease) in BV/TV correctly (n=11) versus incorrectly (n=7). *Indicates significant difference ($p<0.05$), with p-values also indicating non-significant trends.

6.3.2 Influence of Forearm Loading Task Execution on FE-Estimated Bone Strain

In the biomechanics study, we found that participants tended to perform loading with the center of pressure shifted toward either the scaphoid or lunate, with the side preference consistent within each participant. The average absolute distance of the center of pressure from the wrist joint center was 14.4±3.7 mm along the radioulnar axis. Across subjects, the ground reaction force was tilted 0.4-24.7° relative to the long axis of the forearm. When the elevation angle between the long axis of the forearm and the ground reaction force vector was calculated for each individual (not considering the direction of GRF in the horizontal plane), the average tilt was 8.4±4.3°. The ground reaction force was consistently tilted dorsally and radially relative to the forearm long axis.

In the FE boundary condition sensitivity analysis, shifting the distributed axial load to the lunate only had no effect on strain magnitude in any compartment (Table 6.4). Shifting the distributed axial load to the scaphoid only led to significant, 12-17% decreases in strain

magnitude in the integral and trabecular (inner, outer, and total) compartments. Tilting the distributed force vectors had no effect on strain magnitude in any compartment.

Changing FE model boundary conditions generated visibly different strain distributions (Figure 6.11). The standard deviation of strain for the lunate loading condition was 63-88% greater versus the distributed axial loading condition, with significant changes for all compartments (Figure 6.12). Standard deviation was also significantly greater for the scaphoid loading condition for the integral, total trabecular, outer trabecular, and cortical compartments, but changes were smaller relative to the scaphoid condition, between 18-73%. There were no significant differences in standard deviation of strain between distributed axial and tilted loading conditions.

The volume of bone with high strain (>75% of the 95^{th} percentile) was 14-37% lower for the lunate loading condition and 11-20% lower for the scaphoid condition ($p<0.05$ for all compartments). Therefore, high strains were concentrated within a smaller volume, indicative of a less uniform loading distribution. For the tilted loading condition, the high strain volume was significantly larger in the total, inner, and outer trabecular regions, indicating a more uniform trabecular strain distribution versus the distributed axial condition.

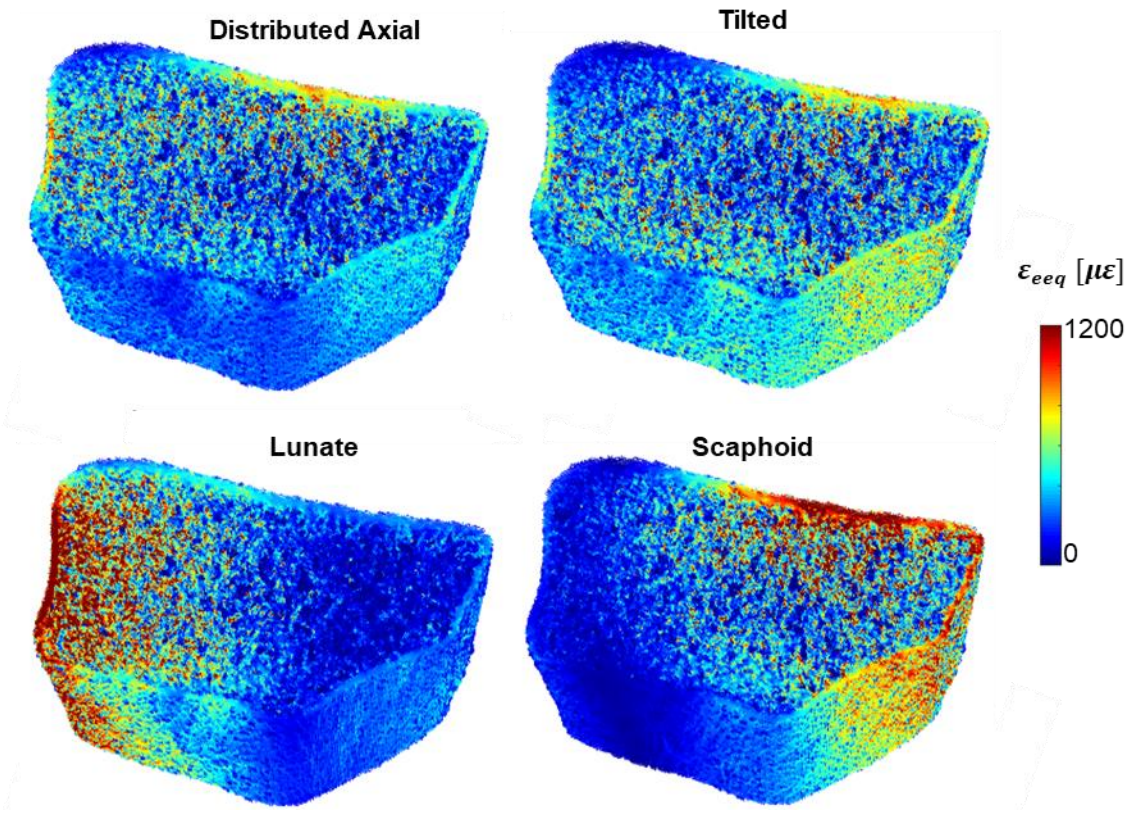

Figure 6.11: Energy equivalent strain (ε_{eeq}) in a representative distal radius micro-FE mesh under distributed axial, tilted, lunate (L), and scaphoid (S) loading conditions.

Table 6.4: Strain magnitude and distribution metrics compared across loading conditions applied in the FE boundary condition sensitivity analysis. Mean and standard deviation (SD) values are provided for each loading condition, and for the modified conditions percent change versus the axial condition is provided (**bold** indicates significant difference, $p<0.05$). High strain volume was calculated as the percent of bone volume with energy equivalent strain greater than 75% of the 95th percentile value within the bone compartment of interest.

	Axial	**Lunate**		**Scaphoid**		**Tilted**	
	Mean (SD)	Mean (SD)	Mean (SD) %Change vs. Axial	Mean (SD)	Mean (SD) %Change vs. Axial	Mean (SD)	Mean (SD) %Change vs. Axial
Integral							
Median (με)	215.3(64.5)	237.6(81.5)	8.5(7.1)	179.6(53.2)	**-16.9(3.0)**	250.6(121.6)	14.2(8.7)
SD (με)	180.9(58.6)	308.3(88.2)	**73.5(10.9)**	243.4(62.1)	**39.3(6.9)**	173.7(72.1)	-3.3(7.6)
High Strain Volume (%)	16.2(2.1)	11.9(1.4)	**-25.8(2.9)**	12.8(0.6)	**-19.8(3.3)**	17.9(4.6)	9.8(6.2)
Total Trabecular							
Median (με)	177.2(50.1)	220.1(83.1)	7.6(6.6)	151.5(45.0)	**-15.1(3.6)**	203.9(93.6)	12.6(7.7)
SD (με)	181.5(62.3)	303.7(88.2)	**72.4(11.0)**	206.7(56.6)	**18.2(5.7)**	174.3(73.6)	-3.6(7.1)
High Strain Volume (%)	12.2(1.5)	11.5(2.3)	**-14.4(2.1)**	10.6(0.5)	**-12.9(2.3)**	13.0(1.6)	**6.1(2.4)**
Inner Trabecular							
Median (με)	169.0(50.1)	176.9(55.8)	4.4(6.4)	149.5(46.1)	**-11.7(4.4)**	193.0(88.2)	12.4(8.1)
SD (με)	188.4(65.8)	299.6(89.7)	**63.1(9.9)**	199.6(60.7)	9.3(5.3)	183.5(80.3)	-2.5(7.1)
High Strain Volume (%)	11.6(1.2)	9.9(0.8)	**-14.2(1.7)**	10.3(0.7)	**-10.8(2.3)**	12.2(1.3)	**5.6(1.7)**
Outer Trabecular							
Median (με)	184.6(54.6)	208.9(66.4)	12.0(7.3)	154.0(46.4)	**-17.2(3.5)**	213.7(100.6)	13.1(7.6)
SD (με)	171.2(61.5)	308.2(94.6)	**85.2(13.3)**	212.6(56.1)	**30.9(7.9)**	161.5(66.9)	-4.6(7.1)
High Strain Volume (%)	13.1(1.9)	11.0(1.0)	**-15.2(2.5)**	11.2(0.7)	**-12.7(2.6)**	13.9(2.0)	**7.0(3.3)**
Cortical							
Median (με)	277.5(84.9)	285.0(106.8)	-0.3(5.8)	272.9(91.7)	-2.7(3.4)	318.5(154.3)	12.7(8.7)
SD (με)	163.4(57.9)	296.9(91.7)	**88.1(17.5)**	264.6(72.7)	**73.2(14.0)**	153.1(65.6)	-3.8(8.8)
High Strain Volume (%)	23.1(2.8)	14.4(3.1)	**-37.2(4.2)**	18.8(1.6)	**-17.8(3.2)**	26.0(7.3)	12.8(8.6)

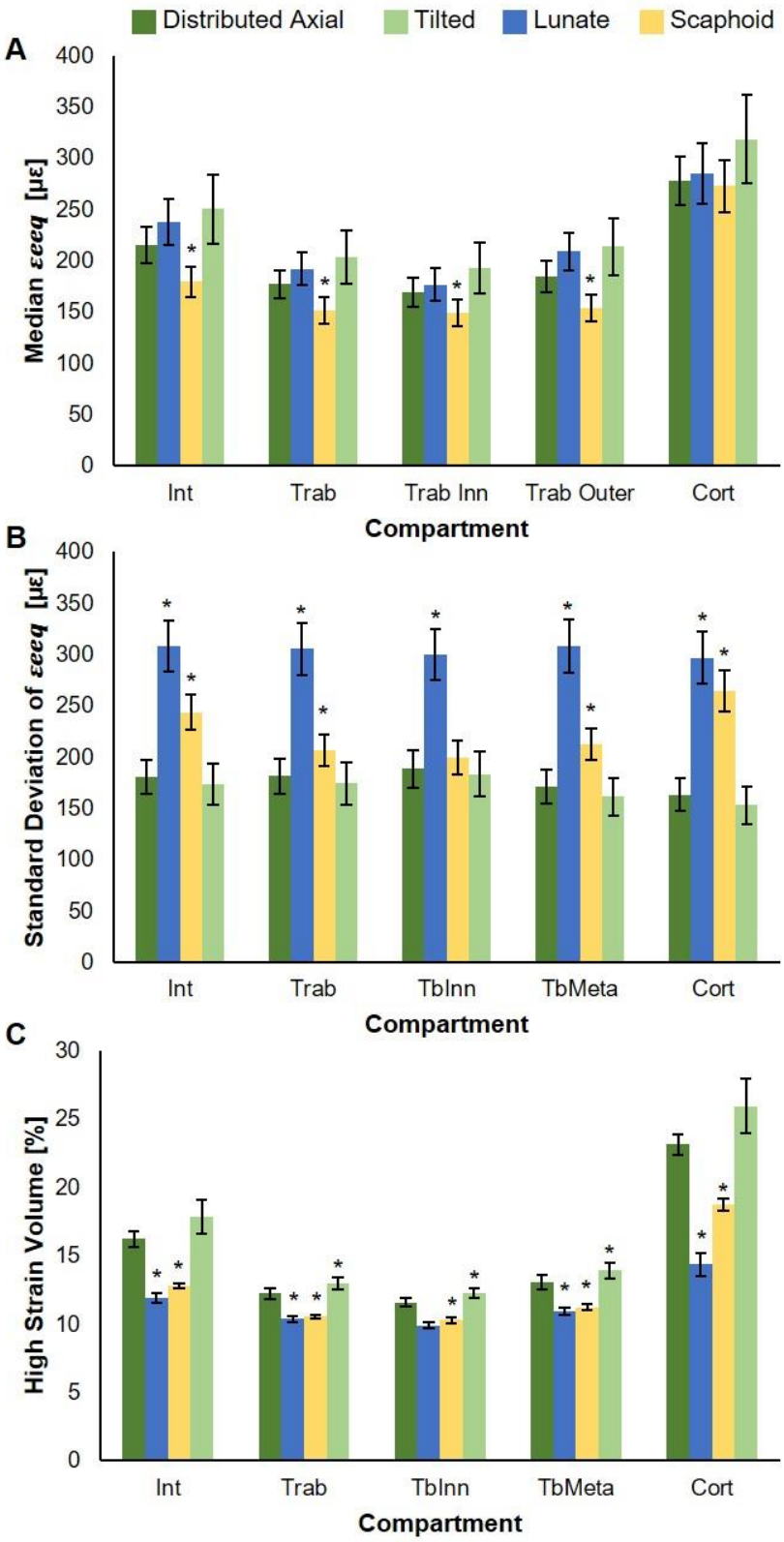

Figure 6.12: Strain magnitude and distribution metrics compared across loading conditions applied in the FE boundary condition sensitivity analysis. Values are provided for the integral

(Int), total trabecular (Trab), inner trabecular (TbInn), outer trabecular (TbMeta), and cortical (Cort) bone compartments. High strain volume was calculated as the percent of bone volume with energy equivalent strain greater than 75% of the 95th percentile value within the bone compartment of interest. Error bars indicate standard error, *indicates significant difference versus Axial ($p<0.05$).

6.3.3 Influence of Boundary Conditions on Bone Adaptation Simulation

Tilting the force vector applied to FE models at each iteration did not significantly affect the change in total trabecular BV/TV predicted by the adaptation simulation (Table 6.5). Looking within each quadrant, there were significant differences in simulation-predicted change in BV/TV for axial versus tilted loading in the posterior, radius, and ulna quadrants (Figure 6.13A). Tilting the loading vector in the posterior-radius direction decreased the magnitude of bone loss in the posterior and radius quadrants predicted for axial loading. In contrast, the tilted loading condition showed smaller predicted increases in BV/TV in the ulna quadrant versus axial loading. These differences in simulated adaptation align with changes in regional bone strain (Figure 6.13B). Median strain in the posterior and radius quadrants were significantly higher under tilted versus axial loads, while there were non-significant trends toward lower strains in the anterior and ulna quadrants.

Table 6.5: Bone strain and simulated changes in BV/TV when axial versus tilted loading conditions are applied within the bone adaptation simulation (n=13). Mean and standard deviation (SD) values are provided for strain, baseline BV/TV, and simulated changes in BV/TV for the total trabecular region and within each quadrant. Bold indicates significant within-participant differences between loading conditions, determined using paired t-tests with Cohen's d effect sizes reported.

	Median Strain				Simulated Adaptation				
	Axial Mean (SD) (με)	Tilted Mean (SD) (με)	p-val.	Effect Size	Baseline BV/TV Mean (SD)	Axial Sim. Change (%) Mean (SD)	Tilted Sim. Change (%) Mean (SD)	p-val.	Effect Size
Total	177.2 (50.1)	203.9 (93.6)	0.15	0.43	0.274 (0.039)	1.0 (5.7)	2.6 (8.4)	0.17	0.41
Posterior	133.0 (63.1)	196.3 (123.9)	**0.02**	**0.78**	0.319 (0.041)	-4.7 (8.0)	0.7 (11.6)	**0.004**	**0.99**
Radius	139.7 (37.1)	189.1 (79.3)	**0.02**	**0.79**	0.240 (0.052)	-5.8 (5.6)	-0.6 (8.9)	**0.002**	**1.10**
Anterior	312.8 (112.4)	292.2 (128.6)	0.39	0.25	0.274 (0.035)	10.8 (7.0)	8.5 (7.9)	0.12	0.46
Ulna	233.0 (66.3)	209.9 (85.8)	0.19	0.38	0.293 (0.040)	6.7 (7.2)	3.8 (8.7)	**0.02**	**0.74**

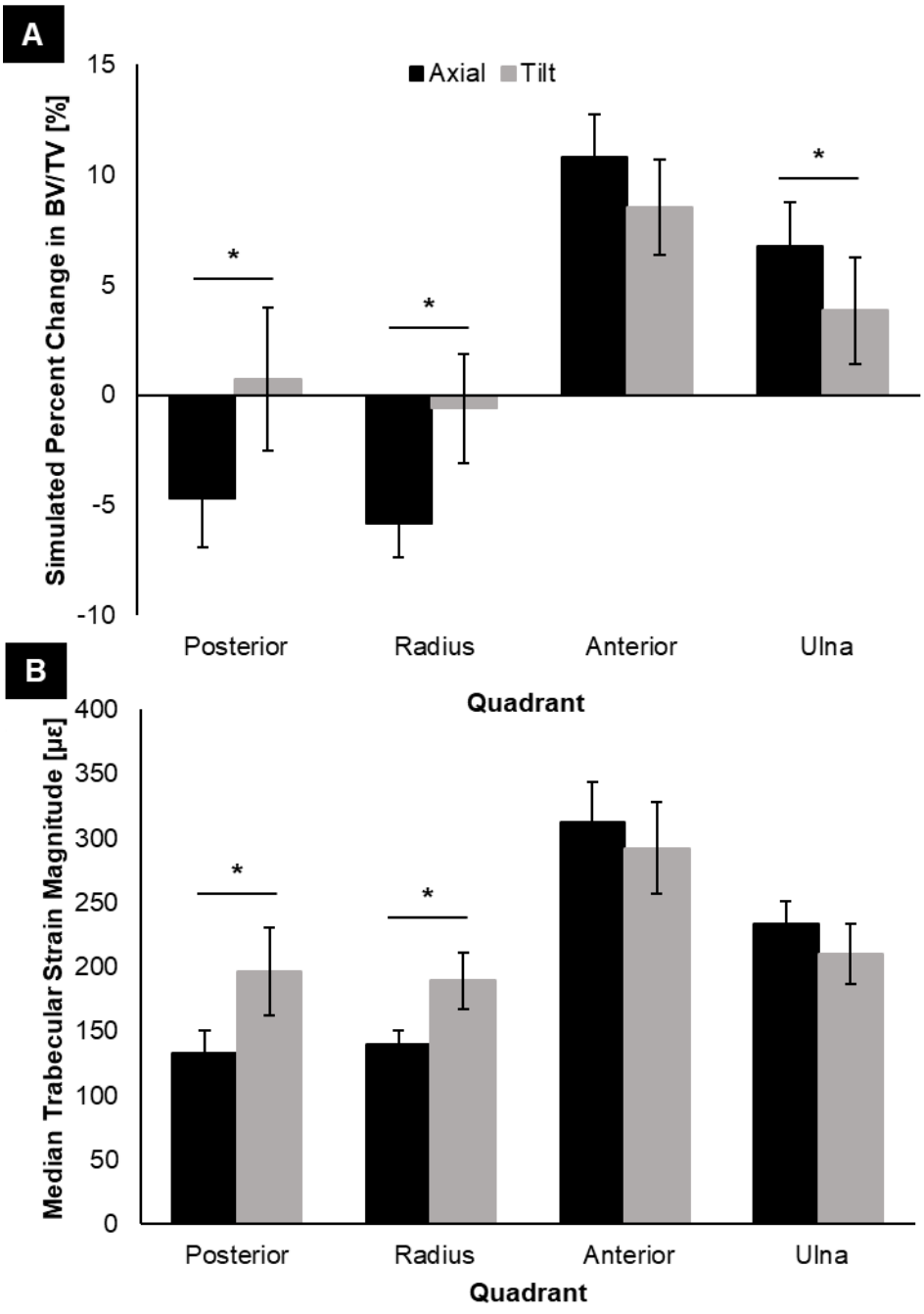

Figure 6.13: (A) Average simulated changes in BV/TV for the axial versus tilted loading conditions. **(B)** Median trabecular energy equivalent bone strain estimated using baseline FE models with axial versus tilted loading. Percent changes are calculated for each quadrant of the trabecular region relative to the baseline value within the quadrant. Error bars indicate standard error, *indicates significant difference between axial and tilted loading ($p<0.05$).

6.4 Discussion

Here we investigated whether a bone adaptation simulation, driven by local bone tissue strain, was capable of predicting experimentally measured changes in distal radius bone structure following 12 months of axial compressive loading. Additionally, we measured variability in applied force during the forearm loading task, and quantified its influence on FE-estimated bone strain and predictions in bone adaptation.

Our first hypothesis was that the simulation would predict trabecular changes similar to those measured experimentally. Overall, the bone adaptation simulation predicted average group trends in change in total trabecular bone, but did capture regional changes in the inner and outer trabecular regions or participant-specific changes. This suggests that across individuals, bone strain influences adaptation of bone structure to mechanical loading in our upper extremity model. However, the relationship between strain and the magnitude of the adaptive response varies between individuals, and may be regulated by additional systemic, non-mechanical factors. This is in agreement with research showing that adaptation to mechanical loading is influenced by parathyroid hormone, estrogen and selective estrogen receptor modulators, and the adipocyte-secreted hormone leptin (Price et al., 2011). Diet may affect the cellular response to mechanical loading by influencing availability of vitamin D, vitamin K, and phytoestrogens (Willems et al., 2017), and insufficient caloric intake has been associated with delayed or interrupted menstruation and diminished bone structure in young female athletes (De Souza et al., 2014). Additionally, it has been suggested that the ability of bone to adapt in response to mechanical loading may diminish with advanced age, potentially in women due to decreased estrogen levels (Hughes et al., 2016; Razi et al., 2015). There are several physiological factors that may have influenced the individual adaptive response in our cohort. Women who had

previously been pregnant were included, as long as the last pregnancy was not within two years of enrollment. Women were excluded if they had no current regular calcium intake or low serum vitamin D, but it is possible that long-term intake history or other dietary factors may have influenced the adaptive response within individuals. Further work is required to systematically study the individual influence of physiological factors on load-driven bone adaptation in women.

While physiological factors likely influence adaptation, the agreement between our simulation and experimental changes may also be improved by further model tuning. For this initial study, our approach was to identify a set of parameters that would capture the overall trend of increasing BV/TV across subjects. Due to the iterative nature of the simulation, directly relating parameter values to simulation outputs would require the trial and error of running the full simulations, where the current set of simulations reported here (eighteen axial loading plus thirteen tilted loading simulations) represent over 1000 hours of computational time. Therefore, we selected $P_{saturated,min}$ and $P_{saturated,max}$ by comparing the simulated changes during iteration 1 for several percentile value cutoffs of stimulus $P(x)$, calculated for a subset of 13 participants. The minimum and maximum probabilities were selected based on the 1:4 ratio observed in Aim 2B, and the observation that when the probabilities were increased, there were larger decreases in inner trabecular connectivity due to more voxels being resorbed in each iteration. An alternative tuning approach that may be explored in future work could be to identify the parameter values that best predict experimental changes for each individual and determining overall mean values.

We also compared loading and bone parameters for individuals for whom the simulation correctly predicted the direction change in BV/TV. We found that average applied force was significantly higher among participants with correctly predicted direction. Median trabecular strain was also higher on average for correctly predicted individuals, but the difference was not

statistically significant. Additionally, baseline BV/TV was significantly higher in correctly versus incorrectly predicted individuals. One potential explanation for these findings is that individuals with greater BV/TV are less susceptible to the simulation artifact of inner trabecular bone loss due to disconnection of sparse trabecular struts. Individuals with greater BV/TV will generally have stiffer bones, and therefore may have been assigned higher target forces to achieve the desired strain for their experimental groups in the parent study. This finding may also indicate that lower mechanical stimulus generated by participants in the incorrect predicted group did not elicit a strain-driven adaptive response, and therefore the experimental changes we observed reflect random or physiologically regulated bone turnover. In this case, we would not expect our strain-driven simulation to predict experimental changes not driven by strain.

It is also important to consider our findings in the context of previous bone adaptation simulations. Using data from a rabbit femoral bone loading model, Morgan et al. (2015) showed that a surface-based trabecular adaptation simulation driven by strain energy density successfully predicted the direction of a significant average group difference in BV/TV between loaded and control specimens, but underestimated the size of the difference (69.4% experimental versus 18.9% simulated). Schulte et al. (2013) and Levchuk et al. (2014) validated a trabecular surface adaptation simulation against data from vertebral loading experiments in mice, and found errors in average group change in BV/TV of 2.4% and 4.5%, respectively (Levchuk et al., 2014; Schulte et al., 2013b). We found that while there was no significant difference between experimental and predicted change in total trabecular BV/TV, the simulation underpredicted the average experimental change by 52% (1.4% versus 2.8% for simulated versus experimental). This could potentially be improved with further parameter tuning. However, our simulation is

also limited by the poorer resolution of HRpQCT in humans versus micro-CT in animals and greater genetic and physiological variability in humans versus animal models.

This initial version of the strain-driven bone adaptation algorithm was relatively simple, and increasing the sophistication of the model may increase the overall accuracy of the simulation. FE models simulated one cycle of forearm loading, and peak energy equivalent strain magnitude was the mechanical strain metric driving stimulus $P(x)$. Future versions may benefit from incorporating participant-specific information about the average number of loading cycles per session and number of sessions performed. Other loading variables besides energy equivalent strain magnitude may be more appropriate. We selected strain magnitude because in Aim 2B (Chapter 5), the relationships between trabecular adaptation and strain were similar for strain magnitude and spatial gradient, and magnitude requires less computational time and resources to implement. Additionally, the simulation directly considered strain during forearm loading, rather than the difference between habitual strains and the loading intervention, which others have suggested may be a more appropriate driving stimulus (Huiskes et al., 1987). Incorporating an error term would require knowledge about each participant's habitual radius bone strains, which depends on activities of daily living and physical activity habits. This could potentially be accomplished using wrist-worn accelerometer sensors to estimate forces at the wrist, but would require further validation. Alternatively, habitual strains could be estimated using the reverse load estimation algorithm developed by Christen et al. (2013) (Christen et al., 2013), which assumes that bone structure is already completely adapted to habitual loads, such that one can assume habitual forces are those generating the most uniform strain distribution within a bone. This approach has been shown to generate accurate force estimates when applied to mouse vertebrae with known applied forces (Christen et al., 2012), and reasonable wrist joint forces

when applied to the human radius (Christen et al., 2013). However, the reverse load estimation approach is limited in that it does not consider the potential influence of physiological factors besides habitual loading that may influence bone structure, especially in humans.

Our second hypothesis, that FE-estimated trabecular strain distribution, but not magnitude, would be dependent on boundary conditions, was generally supported. While the scaphoid loading condition led to a statistically significant decrease in overall trabecular strain magnitude, there were no changes in magnitude for the lunate or tilted conditions. Strain distribution was more sensitive to changes in loading condition, as we observed significant differences in standard deviation and high strain volume for the scaphoid and lunate conditions. In general, tilting the applied force vector did not have a large influence on bone strain, and even increased strain uniformity in the trabecular compartment. Overall, these results suggest that within the normal range of variability in execution of the forearm loading task, FE boundary conditions can meaningfully influence FE outcomes. This is consistent with prior work in our lab, which showed that boundary conditions affect radius bone strain distribution (Edwards and Troy, 2011; Johnson and Troy, 2017b), and that changes in loading direction can impact FE-predicted fracture strength and location (Troy and Grabiner, 2007).

The result of the FE sensitivity analysis has several practical implications. In applications where overall strain magnitude is most important, such as calculating the average mechanical loading strain dose within a region of interest, assuming axial loading is appropriate. This is favorable for large cohort studies because the equipment required to measure force and motion in three dimensions is costly and generally unavailable outside of biomechanics laboratory settings. However, studies concerned with local strain values may benefit from measuring participant-specific three-dimensional loading to inform more realistic FE boundary conditions. Our

combined experimental-computational sensitivity study also highlights the importance of relating biomechanical factors describing task execution to our biological mechanical stimulus, bone strain. This is necessary to identify which factors ultimately need to be controlled through braces, visual or auditory biofeedback, or other means to standardize bone loading across participants. Alternatively, task execution parameters shown to influence bone strain can be intentionally modified to target loading to particular regions within a bone.

Our third hypothesis was that simulation predictions would be dependent on boundary conditions, such that the simulation is capable of producing distinct adaptation patterns for different versions of loading interventions. We found that tilting the force vector applied to FE models during the adaptation simulation affected trabecular adaptation patterns. Tilting the vector in the average direction from the biomechanics experiments increased median strain magnitude in the posterior and radius quadrants, which in turn led to smaller decreases or larger increases in BV/TV for adaptation simulations with tilted versus axial loading conditions. This illustrates that, as intended, the bone adaptation simulation is sensitive to loading condition and is suitable for testing different task execution styles of the forearm loading task to understand the potential influence on bone adaptation.

This analysis has several strengths. To the best of our knowledge, this is the first time a strain-driven bone adaptation algorithm has been validated against experimental data in humans, which has been cited as a major bottleneck in the field (Badilatti, 2015; Levchuk et al., 2014). We successfully implemented a fully automated simulation operating on participant-specific bone FE-meshes with an average of three million nodes. While the simulation did not necessarily predict experimental changes, we have demonstrated that the simulation behaves correctly as designed, adding and removing bone in local regions with high and low mechanical stimuli

(Figure 6.9). Therefore, we accomplished our goal to develop and implement a strain-driven adaptation simulation, which can be used in parallel with experimental studies to generate and test hypotheses about how strain and other factors influence the local mechanism of bone adaptation in future work. As previously mentioned, the adaptation algorithm is limited by the lack of physiological factors such as age, hormone levels, and dietary factors that may influence adaptation. Additionally, while the biomechanics study participants were demographically similar to the parent study cohort, aggregate rather than participant-specific loading variability was applied to FE models in the boundary condition sensitivity analysis. Overall, each aspect of the adaptation simulation, including FE models and the adaptation algorithm, has several variables that can be further validated, tuned, or made more complex in the future given additional experimental data.

In summary, we have developed a strain-driven bone adaptation algorithm capable of predicting average trends in change in trabeculae BV/TV following 12 months of axial forearm loading in healthy adult women. Additionally, we showed that our simulation is sensitive to changes in loading within a normal, easily achievable range of task execution variability. The ability to predict average group changes is valuable for clinical exercise trial design, as potential options for exercises could be simulated for a cohort of "virtual" research participants to identify more osteogenic intervention. Further investigation into physiological factors that influence the patient-specific relationship between strain and adaptation may enable simulations accurate on the individual level. Such knowledge could allow for patient-specific in silico exercise optimization, improving the efficacy of exercise for the prevention of fragility bone fractures.

Acknowledgements

This work was supported by NIAMS of the National Institutes of Health under award number R01AR063691. This material is based upon work supported by the National Science Foundation Graduate Research Fellowship Program under Grant No. DGE-1106756. This research was performed using computational resources supported by the Academic & Research Computing group at Worcester Polytechnic Institute and the National Science Foundation under Grant No. DMS-1337943. We thank Joshua Johnson, PhD, Tiffiny Butler, PhD, and Sabahat Ahmed, PharmD, for their role in data collection for the parent study. We thank Michael DiStefano for his assistance with the finite element sensitivity study and image analysis. We thank Chris Nycz, PhD, and Tess Meier, MS, for their assistance and expertise in the motion capture study.

Chapter 7: Conclusions and Future Directions

Osteoporotic fractures represent a significant and growing clinical burden in the United States and worldwide. Fragility fractures are the result of decreased bone mass and diminished bone structure that affects one in three women over age sixty-five. Although pharmaceutical treatments for bone loss exist, their use is limited due to cost and safety concerns and is based on bone mass screening by dual energy X-ray absorptiometry (DXA), which fails to identify more than half of individuals who go on to fracture. Alternatively, exercise is safe and accessible, and has the potential to stimulate bone formation and offset age-related bone loss. Mechanical loading increases bone mass by stimulating osteocytes to upregulate bone-building osteoblasts and suppress bone-resorbing osteoclasts. In animal models, it has been shown that bone adaptation occurs in proportion to specific strain stimuli (magnitude, rate, spatial gradient), and exercise has been associated with increased bone mass in human observational studies and clinical exercise trials. However, lack of experimental data relating bone tissue strain stimuli to adaptation in humans has prevented the design of patient-specific, evidence-based interventions.

This Dissertation used an upper extremity human bone loading model to study the relationship between bone strain and adaptation in healthy adult women. We explored the participant characteristics related to demographics and loading history that influence bone structure and strain at the start of a loading intervention period. We quantified the relationship between bone strain loading dose and average changes in distal radius structure over 12 months. We further characterized the strain-adaptation relationship at the microscale level, relating bone formation and resorption to strain magnitude and spatial gradient at the individual trabecular level. We applied the results of this prospective clinical experiment to develop a forward simulation of strain-driven bone adaptation, which we evaluated against measured changes in

trabecular bone structure. Finally, we measured variability in task execution in the forearm loading model, and quantified the influence of variable boundary conditions on finite element (FE) estimated bone strain and predicted bone adaptation.

The cross-sectional baseline analysis in Aim 1 showed that age, height, body mass, and recent physical activity were related to bone structure, and body mass was related to bone strain. Additionally, we showed that when the same force (300 N) was applied to participant-specific continuum FE models of the radius (n=72), average energy equivalent strain varied nearly five-fold (234-1110 με) compared to only a two-fold range for bone mineral content (0.56-1.25 g). This highlights the importance of considering participant-specific bone structure when estimating in vivo bone loading during exercise, a significant departure from the majority of clinical exercise trials that use surrogate estimates of bone loading. Overall, we concluded that relatively small differences in bone structure parameters, influenced by demographics and loading history, lead to large differences in bone mechanics and the strain dose delivered by a given intervention.

In Aim 2A, we compared 12-month and interim bone changes for 102 women between loading groups with varying target strain magnitudes and rates and a control group. The low strain magnitude has significant increases in several quantitative computed tomography variables relative to the control (0.46±1.52% in integral bone mineral content versus -1.31±2.68% for control), while the high strain magnitude group saw increases in BMD, driven by changes in the inner trabecular region, at interim timepoints. We observed significant changes in the low and high strain rate groups relative to the control group, including 2.73±2.07% and 3.42±2.21% increases in integral bone mineral content for the low and high rate groups, respectively. While the between-group differences need to be interpreted in the context of protocol compliance, a major strength of our overall approach is that achieved loading was measured for each individual

and can be assessed as a strain loading dose. In fact, we found that loading dose considering strain magnitude, rate, and number of loading sessions was significantly related to change in bone mineral content and bone volume. While these statistically significant relationships demonstrate that metrics related to bone strain influence adaptation, they explained less than 15% of the variance in bone changes, motivating future work to determine what physiological factors may contribute to the adaptation response. Overall, this randomized controlled trial marks the first time that strain magnitude, rate, and loading bouts have been prospectively related to changes in human bone structure.

In Aim 2B, we investigated the mechanism of bone adaptation by locally relating strain and adaptation. Multiscale FE models including bone microstructure at the high resolution peripheral quantitative computed tomography (HRpQCT) scan site estimated bone strain. Baseline and 12-month scans were used to identify formation and resorption sites. We found that trabecular bone resorption was associated with low strain magnitude and spatial gradient, while both formation and resorption were more common near high strains. Additionally, median trabecular bone strain magnitude and gradient were 11.8±17.2 με and 45.7±38.6 με/mm, greater near formation versus resorption, corresponding to 5-10% differences. This is the first evidence of local, strain-driven adaptation based on real, prospective measurements in humans. While there was a spatial relationship between bone strain and adaptation, more than half of formation and resorption could not be explained by strain. Interestingly, similar trends were observed for the load and control groups. Overall, we conclude that local bone tissue strain, likely in combination with other physiological factors, influences adaptation under normal loads and in response to novel interventions.

In Aim 3, we developed a strain-driven bone adaptation simulation that predicts changes in trabecular bone volume fraction in the HRpQCT scanned region based on strain estimated from multiscale FE models. The simulation successfully predicted trends in average group change in total trabecular bone volume fraction (2.84±3.08% increase measured experimentally versus 1.36±5.15% predicted by the simulation), but overestimated gains in outer trabecular bone and underestimated gain (and predicted average losses) in inner trabecular bone. We suggest that the predicted loss of inner trabecular bone is related to the lower bone volume fraction in this region. Generally, we observed that in areas with fewer bone struts, small areas of resorption were more likely to disrupt connectivity and create floating regions that are removed and further decrease bone volume fraction. We believe this may be somewhat improved with higher resolution imaging, which would allow smaller bone packets to be added and removed with each iteration of the adaptation simulation. This could also be accomplished by up-sampling the current micro-FE mesh, but this would increase the number of elements above what is currently feasible given available computational power. Additionally, in Aim 3 we illustrated that our simulations were sensitive to physiologically relevant changes in loading task execution, as measured using experimental motion capture.

Overall, we have built and applied a combined experimental-computational pipeline for the systematic study of strain-driven bone adaptation in humans. We demonstrated, for the first time in humans, that bone loading dose related to strain magnitude and rate are related to average change in bone mineral content, and that bone formation is spatially related to areas of high strain magnitude and spatial gradient. This is consistent with findings in animal models, which have demonstrated dose-dependent relationships between bone strain magnitude and rate with changes in bone structure parameters, as well as locally within trabecular microstructure.

However, we also found that the measurable relationship between strain and adaptation in our human model is not as strong as reported for animals. This is likely due in part to the higher resolution imaging available for small animals, which allows for more precise measurement of global and local bone adaptation. Additionally, humans are more variable than model animal species, genetically and in terms of diet, physical activity, and loading intervention compliance. Our findings suggest that future research of the various factors influencing load-driven adaptation is warranted to move closer to a patient-specific model of exercise prescription.

This project was limited to healthy adult women, and is not generalizable to men, post-menopausal women, or other clinical subpopulations. However, our approach using image-based FE models considering participant-specific bone geometry to estimate bone strain is generalizable, and can be used to study how the relationship between strain and adaptation to forearm loading may vary with age, sex, or other factors. For example, in older women, lower forces may be required to achieve similar strains because bone density and stiffness is generally lower. However, work in animal models suggests that bone mechanosensitivity may decline with age, such that higher strains are required to achieve similar adaptation patterns. Historically, it has not been possible to discern this complex relationship between applied force, bone strain, and adaptation, but may be accomplished using our loading model. Further, the data reported here for healthy women at peak bone mass can serve as a normative benchmark for future in other clinical populations.

Our approach can also be applied to develop loading models at alternative skeletal sites. Here we focused on the upper extremity because it is a common fragility fracture site, can be imaged non-invasively at the macro- and microstructural levels, and habitual loads are relatively infrequent in individuals who do not regularly participate in activities such as gymnastics

volleyball, or racquet sports. Therefore, we assume that mechanical loads outside the forearm loading task were negligible and we did not measure loads beyond loading device recordings. To develop loading models at load-bearing sites such as the tibia or femur, loads applied during gait must be considered in addition to the intervention. This could potentially be addressed using retrospective activity surveys, motion capture, musculoskeletal modeling, pedometers, insole pressure sensors, worn accelerometers, or a combination of these tools. However, such methods would require rigorous validation. Another challenge in translating this work to other skeletal sites is that building image-based FE models at central sites such as the hip or spine is complicated by radiation safety concerns. A potential alternative to CT is magnetic resonance imaging (MRI)-based models, which is generally better suited for soft tissue but does not involve ionizing radiation. Work in our lab and by others has begun to validate MRI-based FE models of the femur.

A challenge in implementing any human loading intervention is participant compliance. Here, we encouraged compliance by regularly contacting participants and providing an incentive for high (>70%) compliance at interim study visits. Nevertheless, we observed a decrease in compliance over the study duration for many participants, with 37 out of 86 loading group participants completing at least fifty percent (78) of the assigned loading sessions. The primary reasons noted by subjects for lack of compliance were lack of time, and in some cases, wrist soreness. It is possible that interventions such as ours focused on healthy adult women may be more sensitive to compliance challenges than those in older women, who have a more immediate motivation to engage in bone-building behaviors. Future work should focus on further developing strategies that encourage compliance, such as increased education of the relationship between peak bone mass in young adulthood and osteoporosis risk. Additionally, future studies

may benefit by taking advantage of existing systems, such as physical education classes, to increase motivation.

Here, we initially assigned loading group participants to complete four weekly loading sessions of 100 cycles, with target forces ranging from 200-450 N. Based on participant feedback and reports of wrist soreness, we ultimately decreased the maximum to 350 N and made additional individual adjustments as needed. A pilot study using the forearm loading model assigned 50 cycles of loading per session, three days per week, with a uniform target force of 300 N for all participants. The target sessions and loading magnitudes were increased for the current study based on the modest bone changes observed in the pilot cohort (+0.3 change versus -1.7% in control group), but this may have contributed to lower compliance overall. This is highlighted by the Aim 2A finding that the high strain magnitude group did not achieve their prescribed target load, with strain magnitude only 25% higher than that of the low magnitude group. Further, the low group, which may have found their target load more manageable, completed more loading sessions on average and experienced larger increases in bone mineral content. Additionally, the fact that loading dose considering strain magnitude, strain rate, and number of loading bouts was correlated with changes in bone structure suggests that all three metrics contributed to osteogenic potential. Overall, it is important to consider how loading parameters such as target magnitude, number of loading cycles per session, and number of sessions may influence the overall efficacy of the intervention, considering the practical constraints of participant safety and motivation.

This project relied heavily on HRpQCT imaging, with changes in average bone parameters measured in Aims 1 and 2A, local adaptation measured from registered HRpQCT scans in Aim 2B, and calculation of regional changes in bone volume fraction in Aim 3.

Additionally, HRpQCT scans were used to generate voxel-based micro-FE meshes within multiscale FE models, allowing use to estimate bone strain within individual trabecular struts in the distal radius scanned region. While this technology provided more insight into the microstructural mechanism of strain-driven adaptation compared to prior work in our lab using clinical resolution CT, its limitations should be considered. The first generation HRpQCT scanner used here has an isotropic voxel size of 82 μm, which is on the same order of magnitude for trabecular thickness. This makes imaging susceptible to partial volume effect, creating short-term precision errors that limit the ability to detect small changes in bone structural parameters. We reported precision analyses from an in-house short-term precision study where repeat scans were acquired within two weeks of each other for each of our analyses, and acknowledge that it may have influenced the strength of the relationship between strain and adaptation. For example, we reported that approximately half of local adaptation identified in Aim 2B is potentially attributed to precision error, although we still found statistically significant associations between strain and trabecular formation and resorption. Additionally, the relatively large voxel size may have influenced the calculation of strain spatial gradient in Aim 2B, due to fewer voxels being present across each trabecular strut compared to studies using micro-CT in animals (voxel size ~10 μm). We also noted in Aim 3 that the limited mesh resolution may have contributed to poor simulation predictions in regions with low bone volume fraction, as having larger resorption cavities increases the probability that whole struts become disconnected. Overall, future work may benefit from increases in resolution, which is currently available in the second generation HRpQCT scanner with a 61 μm voxel size. HRpQCT is also limited to small transverse scan regions (9.02 mm) due to relatively long scan times and large data files. This restricts the region available to study microstructural adaptation, especially in longitudinal studies where the

analysis region is further limited by small shifts in scan location due to patient positioning error. Future improvements in the scanner enabling larger scan regions, coupled with increased computational power for large FE simulations, may enable measurement of adaptation and FE-estimation of strain within in the entire radius at the microstructural level.

In conclusion, this Dissertation has established the quantitative relationship between tissue-level bone loading and adaptation in the upper extremity of young healthy adult women. This work represents an important step toward defining bone loading targets relevant to the mechanism of strain-driven adaptation. Ultimately, this approach may enable the in silico optimization of targeted loading interventions to maximize bone strength and prevent fragility fractures.

References

Adachi, T., Tomita, Y., Sakuae, H., Tanaka, M., 1997. Simulation of trabecular surface remodeling based on local stress nonuniformity. JSME Int. J. Ser. C Mech. Syst. Mach. Elem. Manuf. 40, 415–434. https://doi.org/10.1248/cpb.37.3229

Adachi, T., Tsubota, K., Tomita, Y., Hollister, S.J., 2001. Trabecular Surface Remodeling Simulation for Cancellous Bone Using Microstructural Voxel Finite Element Models. J. Biomech. Eng. 123, 403. https://doi.org/10.1115/1.1392315

Ahola, R., Korpelainen, R., Vainionpää, A., Jämsä, T., 2010. Daily impact score in long-term acceleration measurements of exercise. J. Biomech. 43, 1960–1964. https://doi.org/10.1016/j.jbiomech.2010.03.021

Ahola, R., Korpelainen, R., Vainionpää, A., Leppäluoto, J., Jämsä, T., 2009. Time-course of exercise and its association with 12-month bone changes. BMC Musculoskelet. Disord. 10, 138. https://doi.org/10.1186/1471-2474-10-138

Anderson, D.D., Deshpande, B.R., Daniel, T.E., Baratz, M.E., 2005. A three-dimensional finite element model of the radiocarpal joint: distal radius fracture step-off and stress transfer. Iowa Orthop. J. 25, 108–117.

Babatunde, O.O., Forsyth, J.J., Gidlow, C.J., 2012. A meta-analysis of brief high-impact exercises for enhancing bone health in premenopausal women. Osteoporos. Int. 23, 109–119. https://doi.org/10.1007/s00198-011-1801-0

Badilatti, S.D., 2015. Large-scale simulations of load-adaptive bone remodeling in human vertebrae from native osteoporotic to augmented bone.

Badilatti, S.D., Christen, P., Levchuk, A., Marangalou, J.H., van Rietbergen, B., Parkinson, I., Müller, R., 2016. Large-scale microstructural simulation of load-adaptive bone remodeling in whole human vertebrae. Biomech. Model. Mechanobiol. 15, 83–95. https://doi.org/10.1007/s10237-015-0715-8

Bailey, C.A., Brooke-Wavell, K., 2010. Optimum frequency of exercise for bone health: Randomised controlled trial of a high-impact unilateral intervention. Bone 46, 1043–1049. https://doi.org/10.1016/j.bone.2009.12.001

Bailey, R.L., Dodd, K.W., Goldman, J.A., Gahche, J.J., Dwyer, J.T., Moshfegh, A.J., Sempos, C.T., Picciano, M.F., 2010. Estimation of Total Usual Calcium and Vitamin D Intakes in the United States 1 – 3. J. Nutr. 817–822. https://doi.org/10.3945/jn.109.118539.817

Baim, S., Wilson, C.R., Lewiecki, E.M., Luckey, M.M., Downs, R.W., Lentle, B.C., 2005. Precision Assessment and Radiation Safety for Dual-Energy X-Ray Absorptiometry. J. Clin. Densitom. https://doi.org/10.1385/jcd:8:4:371

Bala, Y., Zebaze, R., Ghasem-Zadeh, A., Atkinson, E.J., Iuliano, S., Peterson, J.M., Amin, S., Bjørnerem, Å., Melton, L.J., Johansson, H., Kanis, J.A., Khosla, S., Seeman, E., 2014. Cortical porosity identifies women with osteopenia at increased risk for forearm fractures. J. Bone Miner. Res. 29, 1356–1362. https://doi.org/10.1002/jbmr.2167

Bareither, M. Lou, Grabiner, M.D., Troy, K.L., 2008. Habitual Site-Specific Upper Extremity Loading is Associated with Increased Bone Mineral of the Ultradistal Radius in Young Women. J. Women's Heal. 17, 1577–1581. https://doi.org/10.1089/jwh.2008.0888

Bareither, M. Lou, Troy, K.L., Grabiner, M.D., 2006. Bone mineral density of the proximal femur is not related to dynamic joint loading during locomotion in young women. Bone 38, 125–129. https://doi.org/10.1016/j.bone.2005.07.003

Bass, S., Delmas, P.D., Pearce, G., Hendrich, E., Tabensky, A., Seeman, E., 1999. The differing tempo of growth in bone size, mass, and density in girls is region-specific. J. Clin. Invest. 104, 795–804. https://doi.org/10.1172/JCI7060

Bass, S., Pearce, G., Bradney, M., Hendrich, E., Delmas, P.D., Harding, A., Seeman, E., 1998. Exercise Before Puberty May Confer Residual Benefits in Bone Density in Adulthood: Studies in Active Prepubertal and Retired Female Gymnasts. J. Bone Miner. Res. 13, 500–507. https://doi.org/10.1359/jbmr.1998.13.3.500

Bass, S.L., Saxon, L., Daly, R.M., Turner, C.H., Robling, A.G., Seeman, E., Stuckey, S., 2002. The Effect of Mechanical Loading on the Size and Shape of Bone in Pre-, Peri-, and Postpubertal Girls: A Study in Tennis Players. J. Bone Miner. Res. 17, 2274–2280. https://doi.org/10.1359/jbmr.2002.17.12.2274

Baxter-Jones, A.D.G., Kontulainen, S.A., Faulkner, R.A., Bailey, D.A., 2008. A longitudinal study of the relationship of physical activity to bone mineral accrual from adolescence to young adulthood. Bone. https://doi.org/10.1016/j.bone.2008.07.245

Beaupré, G.S., Orr, T.E., Carter, D.R., 1990a. An approach for time-dependent bone modeling and remodeling-Application: A preliminary remodeling simulation. J. Orthop. Sport. Phys. Ther. 8, 662–670.

Beaupré, G.S., Orr, T.E., Carter, D.R., 1990b. An approach for time-dependent bone modeling and remodeling--Theoretical development. J. Orthop. Sport. Phys. Ther. 8, 651–661.

Bhatia, V.A., Brent Edwards, W., Johnson, J.E., Troy, K.L., 2015. Short-Term Bone Formation is Greatest Within High Strain Regions of the Human Distal Radius: A Prospective Pilot Study. J. Biomech. Eng. 137, 011001-1–5. https://doi.org/10.1115/1.4028847

Bhatia, V.A., Edwards, W.B., Troy, K.L., 2014. Predicting surface strains at the human distal radius during an in vivo loading task - Finite element model validation and application. J. Biomech. 47, 2759–2765. https://doi.org/10.1016/j.jbiomech.2014.04.050

Bhatia, V.A., Edwards, W.B., Troy, K.L., 2013. Predicting bone adaptation at the human distal radius using cadaveric specimens and the daily strain stimulus theory., in: Proceedings of the 59th Annual Meeting of the Orthopaedic Research Society. Orthopaedic Research Society, San Antonio, TX.

Birkhold, A.I., Razi, H., Duda, G.N., Weinkamer, R., Checa, S., Willie, B.M., 2014. Mineralizing surface is the main target of mechanical stimulation independent of age: 3D dynamic in vivo morphometry. Bone 66, 15–25. https://doi.org/10.1016/j.bone.2014.05.013

Birkhold, A.I., Razi, H., Weinkamer, R., Duda, G.N., Checa, S., Willie, B.M., 2015. Monitoring in vivo (re)modeling: A computational approach using 4D microCT data to quantify bone surface movements. Bone 75, 210–221. https://doi.org/10.1016/j.bone.2015.02.027

Bjørnerem, Å., Wang, X., Bui, M., Ghasem-Zadeh, A., Hopper, J.L., Zebaze, R., Seeman, E., 2018. Menopause-Related Appendicular Bone Loss is Mainly Cortical and Results in Increased Cortical Porosity. J. Bone Miner. Res. 33, 598–605. https://doi.org/10.1002/jbmr.3333

Bonjour, J.P., Chevalley, T., Ferrari, S., Rizzoli, R., 2009. The importance and relevance of peak bone mass in the prevalence of osteoporosis. Salud Publica Mex. 51, 5–17. https://doi.org/10.1590/S0036-36342009000700004

Bonjour, J.P., Theintz, G., Buchs, B., Slosman, D., Rizzoli, R., 1991. Critical years and stages of puberty for spinal and femoral bone mass accumulation during adolescence. J. Clin. Endocrinol. Metab. 73, 555–563.

Boot, A.M., de Ridder, M.A.J., van der Sluis, I.M., van Slobbe, I., Krenning, E.P., de Muinck

Keizer-Schrama, S.M.P.F., 2010. Peak bone mineral density, lean body mass and fractures. Bone 46, 336–341. https://doi.org/10.1016/j.bone.2009.10.003

Boyd, S.K., Moser, S., Kuhn, M., Klinck, R.J., Krauze, P.L., Müller, R., Gasser, J.A., 2006. Evaluation of three-dimensional image registration methodologies for in vivo micro-computed tomography. Ann. Biomed. Eng. 34, 1587–1599. https://doi.org/10.1007/s10439-006-9168-7

Buie, H.R., Campbell, G.M., Klinck, R.J., MacNeil, J.A., Boyd, S.K., 2007. Automatic segmentation of cortical and trabecular compartments based on a dual threshold technique for in vivo micro-CT bone analysis. Bone 41, 505–515. https://doi.org/10.1016/j.bone.2007.07.007

Burghardt, A.J., Buie, H.R., Laib, A., Majumdar, S., Boyd, S.K., 2010. Reproducibility of direct quantitative measures of cortical bone microarchitecture of the distal radius and tibia by HR-pQCT. Bone 47, 519–528. https://doi.org/10.1016/j.bone.2010.05.034

Burghardt, A. J., Kazakia, G.J., Link, T.M., Majumdar, S., 2009. Automated simulation of areal bone mineral density assessment in the distal radius from high-resolution peripheral quantitative computed tomography. Osteoporos. Int. https://doi.org/10.1007/s00198-009-0907-0

Burghardt, Andrew J, Kazakia, G.J., Ramachandran, S., Link, T.M., Majumdar, S., 2009. Age and Gender Related Differences in the Geometric Properties and Biomechanical Significance of Intra-Cortical Porosity in the Distal Radius and Tibia. J. Bone Miner. Res. 25, 983–993. https://doi.org/10.1359/jbmr.091104

Burkhart, T.A., Dunning, C.E., Andrews, D.M., 2012. Predicting distal radius bone strains and injury in response to impacts using multi-axial accelerometers. J. Biomech. Eng. 134, 101007. https://doi.org/10.1115/1.4007631

Burr, D.B., Martin, R.B., Schaffler, M.B., Radin, E.L., 1985. Bone remodeling in response to in vivo fatigue microdamage. J. Biomech. https://doi.org/10.1016/0021-9290(85)90204-0

Burr, D.B., Milgrom, C., Fyhrie, D., Forwood, M., Nyska, M., Finestone, A., Hoshaw, S., Saiag, E., Simkin, A., 1996. In vivo measurement of human tibial strains during vigorous activity. Bone 18, 405–410. https://doi.org/10.1016/8756-3282(96)00028-2

Burt, L.A., Macdonald, H.M., Hanley, D.A., Boyd, S.K., 2014. Bone microarchitecture and strength of the radius and tibia in a reference population of young adults: an HR-pQCT study. Arch. Osteoporos. 9, 183. https://doi.org/10.1007/s11657-014-0183-2

Cabahug-Zuckerman, P., Frikha-Benayed, D., Majeska, R.J., Tuthill, A., Yakar, S., Judex, S., Schaffler, M.B., 2016. Osteocyte Apoptosis Caused by Hindlimb Unloading is Required to Trigger Osteocyte RANKL Production and Subsequent Resorption of Cortical and Trabecular Bone in Mice Femurs. J. Bone Miner. Res. 31, 1356–1365. https://doi.org/10.1002/jbmr.2807

Carriero, A., Pereira, A.F., Wilson, A.J., Castagno, S., Javaheri, B., Pitsillides, A.A., Marenzana, M., Shefelbine, S.J., 2018. Spatial relationship between bone formation and mechanical stimulus within cortical bone: Combining 3D fluorochrome mapping and poroelastic finite element modelling. Bone Reports 8, 72–80. https://doi.org/10.1016/j.bonr.2018.02.003

Carter, D.R., Fyhrie, D.P., Whalen, R.T., 1987. Trabecular bone density and loading history: Regulation of connective tissue biology by mechanical energy. J. Biomech. 20. https://doi.org/10.1016/0021-9290(87)90058-3

Christen, P., Boutroy, S., Ellouz, R., Chapurlat, R., Van Rietbergen, B., 2018. Least-detectable and age-related local in vivo bone remodelling assessed by time-lapse HR-pQCT. PLoS

One 13, 1–11. https://doi.org/10.1371/journal.pone.0191369
Christen, P., Ito, K., Ellouz, R., Boutroy, S., Sornay-Rendu, E., Chapurlat, R.D., van Rietbergen, B., 2014. Bone remodelling in humans is load-driven but not lazy. Nat. Commun. 5, 4855. https://doi.org/10.1038/ncomms5855
Christen, P., Ito, K., Knippels, I., Müller, R., van Lenthe, G.H., van Rietbergen, B., 2013. Subject-specific bone loading estimation in the human distal radius. J. Biomech. 46, 759–766. https://doi.org/10.1016/j.jbiomech.2012.11.016
Christen, P., Müller, R., 2017. In vivo Visualisation and Quantification of Bone Resorption and Bone Formation from Time-Lapse Imaging. Curr. Osteoporos. Rep. 15, 311–317. https://doi.org/10.1007/s11914-017-0372-1
Christen, P., Van Rietbergen, B., Lambers, F.M., Müller, R., Ito, K., 2012. Bone morphology allows estimation of loading history in a murine model of bone adaptation. Biomech. Model. Mechanobiol. 11, 483–492. https://doi.org/10.1007/s10237-011-0327-x
Cody, D.D., Gross, G.J., Hou, F.J., Spencer, H.J., Goldstein, S.A., Fyhire, D.P., 1999. Femoral strength is predicted better by finite element models than QCT and DXA. J. Biomech. 32, 1013–1020.
Corcoran, T.A., Sandler, R.B., Myers, E.R., Lebowitz, H.H., Hayes, W.C., 1994. Calculation of cross-sectional images with application in geometry of bone from ct postmenopausal women. J. Comput. Assist. Tomogr. 18, 626–633. https://doi.org/10.1097/00004728-199407000-00021
Cosman, F., de Beur, S.J., LeBoff, M.S., Lewiecki, E.M., Tanner, B., Randall, S., Lindsay, R., 2014. Clinician's Guide to Prevention and Treatment of Osteoporosis. Osteoporos. Int. 25, 2359–2381. https://doi.org/10.1007/s00198-014-2794-2
Cowin, S.C. (Ed.), 2001. Bone mechanics handbook, second edition, 2nd ed, Bone Mechanics Handbook, Second Edition. CRC Press, Boca Raton, FL. https://doi.org/10.1016/s0021-9290(01)00251-2
Cresswell, E.N., Goff, M.G., Nguyen, T.M., Lee, W.X., Hernandez, C.J., 2016. Spatial relationships between bone formation and mechanical stress within cancellous bone. J. Biomech. 49, 222–228. https://doi.org/10.1016/j.jbiomech.2015.12.011
Currey, J.D., 1988. The effect of porosity and mineral content on the Young's modulus of elasticity of compact bone. J. Biomech. 21, 131–139. https://doi.org/10.1016/0021-9290(88)90006-1
Daly, R.M., Bass, S.L., 2006. Lifetime sport and leisure activity participation is associated with greater bone size, quality and strength in older men. Osteoporos. Int. 17, 1258–1267. https://doi.org/10.1007/s00198-006-0114-1
De Souza, M.J., Nattiv, A., Joy, E., Misra, M., Williams, N.I., Mallinson, R.J., Gibbs, J.C., Olmsted, M., Goolsby, M., Matheson, G., 2014. 2014 Female Athlete Triad Coalition Consensus Statement on Treatment and Return to Play of the Female Athlete Triad: 1st International Conference Held in San Francisco, CA, May 2012, and 2nd International Conference Held in Indianapolis, IN, May 2013. Clin. J. Sport Med. 24, 96–119. https://doi.org/10.1097/JSM.0000000000000085
De Souza, R.L., Matsuura, M., Eckstein, F., Rawlinson, S.C.F., Lanyon, L.E., Pitsillides, A.A., 2005. Non-invasive axial loading of mouse tibiae increases cortical bone formation and modifies trabecular organization: A new model to study cortical and cancellous compartments in a single loaded element. Bone 37, 810–818. https://doi.org/10.1016/j.bone.2005.07.022

Dolan, S.H., Williams, D.P., Ainsworth, B.E., Shaw, J.M., 2006. Development and reproducibility of the bone loading history questionnaire. Med. Sci. Sports Exerc. 38, 1121–1131. https://doi.org/10.1249/01.mss.0000222841.96885.a8

Donahue, S.W., Donahue, H.J., Jacobs, C.R., 2003. Osteoblastic cells have refractory periods for fluid-flow-induced intracellular calcium oscillations for short bouts of flow and display multiple low-magnitude oscillations during long-term flow. J. Biomech. https://doi.org/10.1016/S0021-9290(02)00318-4

Dowthwaite, J.N., Dunsmore, K.A., Gero, N.M., Burzynski, A.O., Sames, C.A., Rosenbaum, P.F., Scerpella, T.A., 2015. Arm bone loading index predicts DXA musculoskeletal outcomes in two samples of post-menarcheal girls. J. Musculoskelet. Neuronal Interact. 15, 358–371.

Eastell, R., Lang, T., Boonen, S., Cummings, S., Delmas, P.D., Cauley, J.A., Horowitz, Z., Kerzberg, E., Bianchi, G., Kendler, D., Leung, P., Man, Z., Mesenbrink, P., Eriksen, E.F., Black, D.M., 2010. Effect of once-yearly zoledronic acid on the spine and hip as measured by quantitative computed tomography: Results of the HORIZON pivotal fracture trial. Osteoporos. Int. https://doi.org/10.1007/s00198-009-1077-9

Edwards, W.B., Schnitzer, T.J., Troy, K.L., 2014. Bone mineral and stiffness loss at the distal femur and proximal tibia in acute spinal cord injury. Osteoporos. Int. https://doi.org/10.1007/s00198-013-2557-5

Edwards, W.B., Schnitzer, T.J., Troy, K.L., 2013. Torsional stiffness and strength of the proximal tibia are better predicted by finite element models than DXA or QCT. J. Biomech. 46, 1655–1662. https://doi.org/10.1016/j.jbiomech.2013.04.016

Edwards, W.B., Simonian, N., Troy, K.L., Schnitzer, T.J., 2015. Reduction in Torsional Stiffness and Strength at the Proximal Tibia as a Function of Time since Spinal Cord Injury. J. Bone Miner. Res. 30, 1422–1430. https://doi.org/10.1002/jbmr.2474

Edwards, W.B., Troy, K.L., 2012. Finite element prediction of surface strain and fracture strength at the distal radius. Med. Eng. Phys. 34, 290–298. https://doi.org/10.1016/j.medengphy.2011.07.016

Edwards, W.B., Troy, K.L., 2011. Simulating Distal Radius Fracture Strength Using Biomechanical Tests: A Modeling Study Examining the Influence of Boundary Conditions. J. Biomech. Eng. 133, 114501. https://doi.org/10.1115/1.4005428

Edwards, W.B., Ward, E.D., Meardon, S.A., Derrick, T.R., 2009. The Use of External Transducers for Estimating Bone Strain at the Distal Tibia During Impact Activity. J. Biomech. Eng. 131, 051009. https://doi.org/10.1115/1.3118762

Erickson, C.R., Vukovich, M.D., 2010. Osteogenic index and changes in bone markers during a jump training program: A pilot study. Med. Sci. Sports Exerc. 42, 1485–1492. https://doi.org/10.1249/MSS.0b013e3181d0fa7a

Eriksen, E.F., 2010. Cellular mechanisms of bone remodeling. Rev. Endocr. Metab. Disord. 11, 219–227. https://doi.org/10.1007/s11154-010-9153-1

Erlandson, M.C., Kontulainen, S.A., Chilibeck, P.D., Arnold, C.M., Faulkner, R.A., Baxter-Jones, A.D.G., 2012. Higher premenarcheal bone mass in elite gymnasts is maintained into young adulthood after long-term retirement from sport: A 14-year follow-up. J. Bone Miner. Res. 27, 104–110. https://doi.org/10.1002/jbmr.514

Faulkner, R.A., Forwood, M.R., Beck, T.J., Mafukidze, J.C., Russell, K., Wallace, W., 2003. Strength indices of the proximal femur and shaft in prepubertal female gymnasts. Med. Sci. Sports Exerc. 35, 513–518. https://doi.org/10.1249/01.MSS.0000053724.33480.8B

Földhazy, Z., Arndt, A., Milgrom, C., Finestone, A., Ekenman, I., 2005. Exercise-induced strain and strain rate in the distal radius. J Bone Jt. Surg Br 87-b, 261–266. https://doi.org/10.1302/0301-620X.87B2.14857

Fritton, J.C., Myers, E.R., Wright, T.M., Van Der Meulen, M.C.H., 2005. Loading induces site-specific increases in mineral content assessed by microcomputed tomography of the mouse tibia. Bone 36, 1030–1038. https://doi.org/10.1016/j.bone.2005.02.013

Frost, H.M., 2003. Bone's mechanostat: A 2003 update. Anat. Rec. Part a 275A, 1081–1101. https://doi.org/10.1002/ar.a.10119

Frost, H.M., 1987. Bone "mass" and the "mechanostat": A proposal. Anat. Rec. 219, 1–9. https://doi.org/10.1002/ar.1092190104

Fuchs, R.K., Bauer, J.J., Snow, C.M., 2001. Jumping improves hip and lumbar spine bone mass in prepubescent children: A randomized controlled trial. J. Bone Miner. Res. 16, 148–156. https://doi.org/10.1359/jbmr.2001.16.1.148

Fung, A., Loundagin, L.L., Edwards, W.B., 2017. Experimental validation of finite element predicted bone strain in the human metatarsal. J. Biomech. 60, 22–29. https://doi.org/10.1016/j.jbiomech.2017.06.010

Fyhrie, D.P., Carter, D.R., 1990. Femoral head apparent density distribution predicted from bone stresses. J. Biomech. 23, 1–10. https://doi.org/10.1016/0021-9290(90)90363-8

Fyhrie, D.P., Carter, D.R., 1986. A unifying principle relating stress to trabecular bone morphology. J. Orthop. Res. 4, 304–317. https://doi.org/10.1002/jor.1100040307

Galea, G.L., Lanyon, L.E., Price, J.S., 2017. Sclerostin's role in bone's adaptive response to mechanical loading. Bone 96, 38–44. https://doi.org/10.1016/j.bone.2016.10.008

Galileo, G., 1638. Discorsi e Dimostrazioni Matematiche intorno a due nuove scienze attenenti alla mecanica & i movimenti locali.

Getting Enough Calcium? Patient Calcium Questionnaire [WWW Document], n.d. . Doylest. Heal. Orthop. Inst. URL https://www.doylestownhealth.org/medical-services/orthopedic-institute/services-and-advanced-procedures/osteoporosis-and-bone-health-program/resources (accessed 4.23.18).

Gnudi, S., Sitta, E., Fiumi, N., 2007. Relationship between body composition and bone mineral density in women with and without osteoporosis: Relative contribution of lean and fat mass. J. Bone Miner. Metab. 25, 326–332. https://doi.org/10.1007/s00774-007-0758-8

Goff, M.G., Lambers, F.M., Nguyen, T.M., Sung, J., Rimnac, C.M., Hernandez, C.J., 2015. Fatigue-induced microdamage in cancellous bone occurs distant from resorption cavities and trabecular surfaces. Bone 79, 8–14. https://doi.org/10.1016/j.bone.2015.05.020

Goodship, A.E., Lanyon, L.E., McFie, H., 1979. Functional adaptation of bone to increased stress. An experimental study. J. Bone Jt. Surg. - Ser. A. https://doi.org/10.2106/00004623-197961040-00008

Gray, H.A., Taddei, F., Zavatsky, A.B., Cristofolini, L., Gill, H.S., 2008. Experimental validation of a finite element model of a human cadaveric tibia. J. Biomech. Eng. https://doi.org/10.1115/1.2913335

Greenway, K.G., Walkley, J.W., Rich, P.A., 2015. Relationships between self-reported lifetime physical activity, estimates of current physical fitness, and aBMD in adult premenopausal women. Arch. Osteoporos. 10. https://doi.org/10.1007/s11657-015-0239-y

Gross, T.S., Edwards, J.L., Mcleod, K.J., Rubin, C.T., 1997. Strain gradients correlate with sites of periosteal bone formation. J. Bone Miner. Res. 12, 982–988. https://doi.org/10.1359/jbmr.1997.12.6.982

Gupta, S., van der Helm, F.C.T., Sterk, J.C., van Keulen, F., Kaptein, B.L., 2004. Development and experimental validation of a three-dimensional finite element model of the human scapula. Proc. Inst. Mech. Eng. Part H J. Eng. Med. 218, 127–142. https://doi.org/10.1243/095441104322984022

Haapasalo, H., Sievanen, H., Pasanen, M., 1996. Development of Mass , Density , and Estimated Mechanical Characteristics of Bones in Caucasian Females. J. Bone Miner. Res. 11.

Hannam, K., Deere, K.C., Hartley, A., Clark, E.M., Coulson, J., Ireland, A., Moss, C., Edwards, M.H., Dennison, E., Gaysin, T., Cooper, R., Wong, A., McPhee, J.S., Cooper, C., Kuh, D., Tobias, J.H., 2017. A novel accelerometer-based method to describe day-to-day exposure to potentially osteogenic vertical impacts in older adults: findings from a multi-cohort study. Osteoporos. Int. 28, 1001–1011. https://doi.org/10.1007/s00198-016-3810-5

Hart, R.T., Davy, D.T., Heiple, K.G., 1984. A computational method for stress analysis of adaptive elastic materials with a view toward applications in strain-induced bone remodeling. J. Biomech. Eng. 106, 342–350.

Hasegawa, Y., Schneider, P., Reiners, C., 2001. Age, sex, and grip strength determine architectural bone parameters assessed by peripheral quantitative computed tomography (pQCT) at the human radius. J. Biomech. 34, 497–503. https://doi.org/10.1016/S0021-9290(00)00211-6

Hazelwood, S.J., Bruce Martin, R., Rashid, M.M., Rodrigo, J.J., 2001. A mechanistic model for internal bone remodeling exhibits different dynamic responses in disuse and overload. J. Biomech. 34, 299–308. https://doi.org/10.1016/S0021-9290(00)00221-9

Hazenberg, J.G., Freeley, M., Foran, E., Lee, T.C., Taylor, D., 2006. Microdamage: A cell transducing mechanism based on ruptured osteocyte processes. J. Biomech. https://doi.org/10.1016/j.jbiomech.2005.06.006

Heikkinen, R., Vihriälä, E., Vainionpää, A., Korpelainen, R., Jämsä, T., 2007. Acceleration slope of exercise-induced impacts is a determinant of changes in bone density. J. Biomech. 40, 2967–2974. https://doi.org/10.1016/j.jbiomech.2007.02.003

Helgason, B., Perilli, E., Schileo, E., Taddei, F., Brynjólfsson, S., Viceconti, M., 2008. Mathematical relationships between bone density and mechanical properties: A literature review. Clin. Biomech. 23, 135–146. https://doi.org/10.1016/j.clinbiomech.2007.08.024

Henry, Y.M., Fatayerji, D., Eastell, R., 2004. Attainment of peak bone mass at the lumbar spine, femoral neck and radius in men and women: Relative contributions of bone size and volumetric bone mineral density. Osteoporos. Int. 15, 263–273. https://doi.org/10.1007/s00198-003-1542-9

Hernandez, C.J., Beaupré, G.S., Carter, D.R., 2003. A theoretical analysis of the relative influences of peak BMD, age-related bone loss and menopause on the development of osteoporosis. Osteoporos. Int. 14, 843–847. https://doi.org/10.1007/s00198-003-1454-8

Hernandez, C.J., Keaveny, T.M., 2006. A biomechanical perspective on bone quality. Bone 39, 1173–1181. https://doi.org/10.1016/j.bone.2006.06.001

Hert, J., Lisková, M., Landa, J., 1971. Reaction of bone to mechanical stimuli. 1. Continuous and intermittent loading of tibia in rabbit. Folia Morphol. (Warsz).

Hildebrand, T., Rüegsegger, P., 1997. A new method for the model-independent assessment of thickness in three-dimensional images. J. Microsc. 185, 67–75. https://doi.org/10.1046/j.1365-2818.1997.1340694.x

Hind, K., Burrows, M., 2007. Weight-bearing exercise and bone mineral accrual in children and adolescents: A review of controlled trials. Bone 40, 14–27.

https://doi.org/10.1016/j.bone.2006.07.006
Hinton, P. V, Rackard, S.M., Kennedy, O.D., Kennedy, O.D., 2018. In Vivo Osteocyte Mechanotransduction : Recent Developments and Future Directions 746–753.
Ho, A.Y.Y., Kung, A.W.C., 2005. Determinants of peak bone mineral density and bone area in young women. J. Bone Miner. Metab. 23, 470–475. https://doi.org/10.1007/s00774-005-0630-7
Howe, T.E., Shea, B., Dawson, L.J., Downie, F., Murray, A., Ross, C., Harbour, R.T., Caldwell, L.M., Creed, G., 2011. Exercise for preventing and treating osteoporosis in postmenopausal women. Cochrane Database Syst. Rev. CD000333. https://doi.org/10.1002/14651858.CD000333.pub2
Hsieh, Y.F., Turner, C.H., 2001. Effects of loading frequency on mechanically induced bone formation. J. Bone Miner. Res. 16, 918–924. https://doi.org/10.1359/jbmr.2001.16.5.918
Hughes, J.M., Charkoudian, N., Barnes, J.N., Morgan, B.J., 2016. Revisiting the debate: Does exercise build strong bones in the mature and senescent skeleton? Front. Physiol. 7, 1–8. https://doi.org/10.3389/fphys.2016.00369
Hughes, J.M., Ga, E., Guerriere, K.I., Taylor, K.M., Popp, K.L., Xu, C., Unnikrishnan, G., Staab, S., Matheny, R.W., Mcclung, J.P., Reifman, J., Bouxsein, M.L., 2018. Changes in tibial bone microarchitecture in female recruits in response to 8 weeks of U . S . Army Basic Combat Training ☆ 113, 9–16. https://doi.org/10.1016/j.bone.2018.04.021
Hughes, J.M., Petit, M.A., 2010. Biological underpinnings of frost's mechanostat thresholds: The important role of osteocytes. J. Musculoskelet. Neuronal Interact. 10, 128–135.
Huiskes, R., 2000. If bone is the answer, then what is the question? J. Anat. 197, 145–156. https://doi.org/10.1046/j.1469-7580.2000.19720145.x
Huiskes, R., Chao, E.Y.S., 1983. A survey of finite element analysis in orthopedic biomechanics: The first decade. J. Biomech. 16, 385–409. https://doi.org/10.1016/0021-9290(83)90072-6
Huiskes, R., Ruimerman, R., van Lenthe, G.H., Janssen, J.D., 2000. Effects of mechanical forces on maintenance and adaptation of form in trabecular bone. Nature 405, 704–706. https://doi.org/10.1038/35015116
Huiskes, R., Weinans, H., Grootenboer, H.J., Dalstra, M., Fulda, B., Sloof, T., 1987. Adaptive Bone-Remodeling Theory Applied to Prosthetic-Design Analysis. J. Biomech. 20, 1135–1150.
Ireland, A., Rittweger, J., 2017. Exercise for osteoporosis: How to navigate between overeagerness and defeatism. J. Musculoskelet. Neuronal Interact. 17, 155–161.
Jämsä, T., Vainionpää, A., Korpelainen, R., Vihriälä, E., Leppäluoto, J., 2006. Effect of daily physical activity on proximal femur. Clin. Biomech. 21, 1–7. https://doi.org/10.1016/j.clinbiomech.2005.10.003
Jimenez-Palomar, I., Shipov, A., Shahar, R., Barber, A.H., 2015. Structural orientation dependent sub-lamellar bone mechanics. J. Mech. Behav. Biomed. Mater. 52, 63–71. https://doi.org/10.1016/j.jmbbm.2015.02.031
Johannesdottir, F., Thrall, E., Muller, J., Keaveny, T.M., Kopperdahl, D.L., Bouxsein, M.L., 2017. Comparison of non-invasive assessments of strength of the proximal femur. Bone 105, 93–102. https://doi.org/10.1016/j.bone.2017.07.023
Johnson, J.E., Troy, K.L., 2017a. Validation of a new multiscale finite element analysis approach at the distal radius 0, 1–9.
Johnson, J.E., Troy, K.L., 2017b. Simplified boundary conditions alter cortical-trabecular load sharing at the distal radius; A multiscale finite element analysis. J. Biomech.

https://doi.org/10.1016/j.medengphy.2017.03.005
Johnson, J.E., Troy, K.L., 2017c. Validation of a new multiscale finite element analysis approach at the distal radius. Med. Eng. Phys. 44, 16–24. https://doi.org/10.1016/j.medengphy.2017.03.005
Judex, S., Gross, T.S., Zernicke, R.F., 1997. Strain gradients correlate with sites of exercise-induced bone-forming surfaces in the adult skeleton. J. Bone Miner. Res. 12, 1737–1745. https://doi.org/10.1359/jbmr.1997.12.10.1737
Kannus, P., Haapasalo, H., Sankelo, M., Sievänen, H., Pasanen, M., Heinonen, A., Oja, P., Vuori, I., 1995. Effect of starting age of physical activity on bone mass in the dominant arm of tennis and squash players. Ann. Intern. Med. 123, 27–31. https://doi.org/10.7326/0003-4819-123-1-199507010-00003
Kato, T., Yamashita, T., Mizutani, S., Honda, A., Matumoto, M., Umemura, Y., 2009. Adolescent exercise associated with long-term superior measures of bone geometry: a cross-sectional DXA and MRI study. Br. J. Sports Med. 43, 932–935. https://doi.org/10.1136/bjsm.2008.052308
Kelley, S., Hopkinson, G., Strike, S., Luo, J., Lee, R., 2014. An accelerometry-based approach to assess loading intensity of physical activity on bone. Res. Q. Exerc. Sport 85, 245–250. https://doi.org/10.1080/02701367.2014.897680
Keyak, J.H., Fourkas, M.G., Meagher, J.M., Skinner, H.B., 1993. Validation of an automated method of three-dimensional finite element modelling of bone. J. Biomed. Eng. 15, 505–509. https://doi.org/10.1016/0141-5425(93)90066-8
Kim, C.H., Takai, E., Zhou, H., Von Stechow, D., Muller, R., Dempster, D.W., Guo, X.E., 2003. Trabecular bone response to mechanical and parathyroid hormone stimulation: The role of mechanical microenvironment. J. Bone Miner. Res. 18, 2116–2125. https://doi.org/10.1359/jbmr.2003.18.12.2116
Kling, J.M., Clarke, B.L., Sandhu, N.P., 2014. Osteoporosis Prevention, Screening, and Treatment: A Review. J. Women's Heal. 23, 563–572. https://doi.org/10.1089/jwh.2013.4611
Kogianni, G., Mann, V., Noble, B.S., 2008. Apoptotic bodies convey activity capable of initiating osteoclastogenesis and localized bone destruction. J. Bone Miner. Res. 23, 915–927. https://doi.org/10.1359/jbmr.080207
Kontulainen, S., Kannus, P., Haapasalo, H., Sievänen, H., Pasanen, M., Heinonen, A., Oja, P., Vuori, I., 2001. Good maintenance of exercise-induced bone gain with decreased training of female tennis and squash players: A prospective 5-year follow-up study of young and old starters and controls. J. Bone Miner. Res. 16, 195–201. https://doi.org/10.1359/jbmr.2001.16.2.195
Kontulainen, S., Sievänen, H., Kannus, P., Pasanen, M., Vuori, I., 2003. Effect of long-term impact-loading on mass, size, and estimated strength of humerus and radius of female racquet-sports players: A peripheral quantitative computed tomography study between young and old starters and controls. J. Bone Miner. Res. 18, 352–359. https://doi.org/10.1359/jbmr.2003.18.2.352
Kontulainen, S.A., Kannus, P.A., Pasanen, M.E., Sievänen, H.T., Heinonen, A.O., Oja, P., Vuori, I., 2002. Does previous participation in high-impact training result in residual bone gain in growing girls? Int. J. Sports Med. 23, 575–581. https://doi.org/10.1055/s-2002-35543
Koontz, J.T., Charras, G.T., Guldberg, R.E., 2002. A Microstructural Finite Element Simulation of Mechanically Induced Bone Formation. J. Biomech. Eng. 123, 607.

https://doi.org/10.1115/1.1406951
Korpelainen, R., Keinänen-Kiukaanniemi, S., Heikkinen, J., Väänänen, K., Korpelainen, J., 2006. Effect of impact exercise on bone mineral density in elderly women with low BMD: A population-based randomized controlled 30-month intervention. Osteoporos. Int. https://doi.org/10.1007/s00198-005-1924-2
Kotha, S.P., Hsieh, Y.F., Strigel, R.M., Müller, R., Silva, M.J., 2004. Experimental and finite element analysis of the rat ulnar loading model - Correlations between strain and bone formation following fatigue loading. J. Biomech. 37, 541–548. https://doi.org/10.1016/j.jbiomech.2003.08.009
Kowalchuk, R.M., Pollack, S.R., 1993. Stress-Generated potentials in bone: Effects of bone fluid composition and kinetics. J. Orthop. Res. https://doi.org/10.1002/jor.1100110614
Kringelbach, T.M., Aslan, D., Novak, I., Ellegaard, M., Syberg, S., Andersen, C.K.B., Kristiansen, K.A., Vang, O., Schwarz, P., Jørgensen, N.R., 2015. Fine-tuned ATP signals are acute mediators in osteocyte mechanotransduction. Cell. Signal. 27, 2401–2409. https://doi.org/10.1016/j.cellsig.2015.08.016
Laib, A., Hauselmann, H.J., Ruegsegger, P., 1998. In vivo high resolution 3D-QCT of the human forearm. Technol. Heal. Care 6, 329–337.
Lambers, F.M., Kuhn, G., Weigt, C., Koch, K.M., Schulte, F.A., Müller, R., 2015. Bone adaptation to cyclic loading in murine caudal vertebrae is maintained with age and directly correlated to the local micromechanical environment. J. Biomech. 48, 1179–1187. https://doi.org/10.1016/j.jbiomech.2014.11.020
Lambers, F.M., Schulte, F.A., Kuhn, G., Webster, D.J., Müller, R., 2011. Mouse tail vertebrae adapt to cyclic mechanical loading by increasing bone formation rate and decreasing bone resorption rate as shown by time-lapsed in vivo imaging of dynamic bone morphometry. Bone 49, 1340–1350. https://doi.org/10.1016/j.bone.2011.08.035
LaMothe, J.M., Hamilton, N.H., Zernicke, R.F., 2005. Strain rate influences periosteal adaptation in mature bone. Med. Eng. Phys. 27, 277–284. https://doi.org/10.1016/j.medengphy.2004.04.012
Lang, T., LeBlanc, A., Evans, H., Lu, Y., Genant, H., Yu, A., 2004. Cortical and trabecular bone mineral loss from the spine and hip in long-duration spaceflight. J. Bone Miner. Res. 19, 1006–1012. https://doi.org/10.1359/JBMR.040307
Lanyon, L.E., Goodship, A.E., Pye, C.J., MacFie, J.H., 1982. Mechanically adaptive bone remodelling. J. Biomech. 15, 141–154. https://doi.org/10.1016/0021-9290(82)90246-9
Lanyon, L.E., Hampson, W.G.J., Goodship, A.E., Shah, J.S., 1975. Bone Deformation Recorded in vivo from Strain Gauges Attached to the Human Tibial Shaft. Acta Orthop. Scand. 46, 256–268. https://doi.org/10.3109/17453677508989216
Lanyon, L.E., Rubin, C.T., 1984. Static vs dynamic loads as an influence on bone remodelling. J. Biomech. 17, 897–905.
Lester, M.E., Urso, M.L., Evans, R.K., Pierce, J.R., Spiering, B.A., Maresh, C.M., Hatfield, D.L., Kraemer, W.J., Nindl, B.C., 2009. Influence of exercise mode and osteogenic index on bone biomarker responses during short-term physical training. Bone 45, 768–776. https://doi.org/10.1016/j.bone.2009.06.001
Levchuk, A., Zwahlen, A., Weigt, C., Lambers, F.M., Badilatti, S.D., Schulte, F.A., Kuhn, G., Müller, R., 2014. The Clinical Biomechanics Award 2012 - Presented by the European Society of Biomechanics: Large scale simulations of trabecular bone adaptation to loading and treatment. Clin. Biomech. 29, 355–362.

https://doi.org/10.1016/j.clinbiomech.2013.12.019
Lewis, K.J., Frikha-benayed, D., Louie, J., Stephen, S., Spray, D.C., Thi, M.M., Seref-ferlengez, Z., Majeska, R.J., Weinbaum, S., Schaffler, M.B., 2017. Osteocyte calcium signals encode strain magnitude and loading frequency in vivo 114, 11775–11780. https://doi.org/10.1073/pnas.1707863114
Looker, A.C., Sarafrazi Isfahani, N., Fan, B., Shepherd, J.A., 2017. Trends in osteoporosis and low bone mass in older US adults, 2005–2006 through 2013–2014. Osteoporos. Int. 28, 1979–1988. https://doi.org/10.1007/s00198-017-3996-1
Lorbergs, A.L., Farthing, J.P., Baxter-Jones, A.D.G., Kontulainen, S.A., 2011. Forearm muscle size, strength, force, and power in relation to pQCT-derived bone strength at the radius in adults. Appl. Physiol. Nutr. Metab. 36, 618–625. https://doi.org/10.1139/h11-065
MacKelvie, K.J., Khan, K.M., McKay, H. a, 2002. Is there a critical period for bone response to weight-bearing exercise in children and adolescents? a systematic review. Br. J. Sports Med. 36, 250–257; discussion 257. https://doi.org/10.1136/bjsm.36.4.250
MacNeil, J.A., Boyd, S.K., 2008. Improved reproducibility of high-resolution peripheral quantitative computed tomography for measurement of bone quality. Med. Eng. Phys. 30, 792–799. https://doi.org/10.1016/j.medengphy.2007.11.003
MacNeil, J.A., Boyd, S.K., 2007. Accuracy of high-resolution peripheral quantitative computed tomography for measurement of bone quality. Med. Eng. Phys. 29, 1096–1105. https://doi.org/10.1016/j.medengphy.2006.11.002
Mancuso, M.E., Johnson, J.E., Ahmed, S.S., Butler, T.A., Troy, K.L., 2018. Distal radius microstructure and finite element bone strain are related to site-specific mechanical loading and areal bone mineral density in premenopausal women. Bone Reports 8, 187–194. https://doi.org/10.1016/j.bonr.2018.04.001
Manske, S.L., Zhu, Y., Sandino, C., Boyd, S.K., 2015. Human trabecular bone microarchitecture can be assessed independently of density with second generation HR-pQCT. Bone 79, 213–221. https://doi.org/10.1016/j.bone.2015.06.006
Martin, B., 1995. Mathematical model for repair of fatigue damage and stress fracture in osteonal bone. J. Orthop. Res. 13, 309–316. https://doi.org/10.1002/jor.1100130303
Martin, R.B., 2007. The importance of mechanical loading in bone biology and medicine. J. Musculoskelet. Neuronal Interact. 7, 48–53.
Martin, R.B., Burr, D.B., Sharkey, N.A., Fyhrie, D.P., 2015. Skeletal tissue mechanics, American Journal of Physical Anthropology. https://doi.org/10.1002/1096-8644(200007)112:3<435::AID-AJPA12>3.3.CO;2-Z
Martyn St James, M., Carroll, S., 2010. Effects of different impact exercise modalities on bone mineral density in premenopausal women: A meta-analysis. J. Bone Miner. Metab. 28, 251–267. https://doi.org/10.1007/s00774-009-0139-6
Massy-Westropp, N.M., Gill, T.K., Taylor, A.W., Bohannon, R.W., Hill, C.L., 2011. Hand Grip Strength: age and gender stratified normative data in a population-based study. BMC Res. Notes 4, 127. https://doi.org/10.1186/1756-0500-4-127
Melton, J.L., 1995. Perspectives: How many women have osteoporosis now? J. Bone Miner. Res. 10, 175–177. https://doi.org/10.1002/jbmr.5650100202
Melton, L.J., Riggs, B.L., Van Lenthe, G.H., Achenbach, S.J., Müller, R., Bouxsein, M.L., Amin, S., Atkinson, E.J., Khosla, S., 2007. Contribution of in vivo structural measurements and load/strength ratios to the determination of forearm fracture risk in postmenopausal women. J. Bone Miner. Res. 22, 1442–1448. https://doi.org/10.1359/jbmr.070514

Mikić, B., Carter, D.R., 1995. Bone strain gage data and theoretical models of functional adaptation. J. Biomech. 28, 465–469. https://doi.org/10.1016/0021-9290(94)00085-I

Milgrom, C., Burr, D.B., Finestone, A.S., Voloshin, A., 2015. Understanding the etiology of the posteromedial tibial stress fracture. Bone. https://doi.org/10.1016/j.bone.2015.04.033

Milgrom, C., Finestone, A., Simkin, A., Ekenman, I., Mendelson, S., Millgram, M., Nyska, M., Larsson, E., Burr, D., 2000. In-vivo strain measurements to evaluate the strengthening potential of exercises on the tibial bone. J. bone Jt. Surg. Br. Vol. 82, 591–594.

Milgrom, C., Radeva-Petrova, D.R., Finestone, A., Nyska, M., Mendelson, S., Benjuya, N., Simkin, A., Burr, D., 2007. The effect of muscle fatigue on in vivo tibial strains. J. Biomech. 40, 845–850. https://doi.org/10.1016/j.jbiomech.2006.03.006

Morgan, E., Bayraktar, H., Keaveny, T., 2003. Trabecular bone modulus-density relationships depend on anatomic site. J. Biomech. 36, 897–904. https://doi.org/10.1016/S0021-9290(03)00071-X

Morgan, T.G., Bostrom, M.P.G., van der Meulen, M.C.H., 2015. Tissue-level remodeling simulations of cancellous bone capture effects of in vivo loading in a rabbit model. J. Biomech. 48, 875–882. https://doi.org/10.1016/j.jbiomech.2014.12.011

Morin, S., Tsang, J.F., Leslie, W.D., 2009. Weight and body mass index predict bone mineral density and fractures in women aged 40 to 59 years. Osteoporos. Int. 20, 363–370. https://doi.org/10.1007/s00198-008-0688-x

Mosley, J.R., Lanyon, L.E., 1998. Strain rate as a controlling influence on adaptive modeling in response to dynamic loading of the ulna in growing male rats. Bone 23, 313–318. https://doi.org/10.1016/S8756-3282(98)00113-6

Mosley, J.R., March, B.M., Lynch, J., Lanyon, L.E., 1997. Strain magnitude related changes in whole bone architecture in growing rats. Bone 20, 191–198. https://doi.org/10.1016/S8756-3282(96)00385-7

Muir, P., Sample, S.J., Barrett, J.G., McCarthy, J., Vanderby, R., Markel, M.D., Prokuski, L.J., Kalscheur, V.L., 2007. Effect of fatigue loading and associated matrix microdamage on bone blood flow and interstitial fluid flow. Bone. https://doi.org/10.1016/j.bone.2006.11.012

Mullender, M., van Rietbergen, B., Rüegsegger, P., Huiskes, R., 1998. Effect of Mechanical Set Point of Bone Cells on Mechanical Control of Trabecular Bone Architecture. Bone 22, 125–131. https://doi.org/10.1016/S8756-3282(97)00251-2

Mullender, M.G., Huiskes, R., 1995. Proposal for the regulatory mechanism of Wolff's law. J. Orthop. Res. 13, 503–512. https://doi.org/10.1002/jor.1100130405

Mullender, M.G., Huiskes, R., Weinans, H., 1994. A physiological approach to the simulation of bone remodeling as a self-organizational control process. J. Biomech. 27, 1389–1394. https://doi.org/10.1016/0021-9290(94)90049-3

Nakashima, T., Hayashi, M., Fukunaga, T., Kurata, K., Oh-Hora, M., Feng, J.Q., Bonewald, L.F., Kodama, T., Wutz, A., Wagner, E.F., Penninger, J.M., Takayanagi, H., 2011. Evidence for osteocyte regulation of bone homeostasis through RANKL expression. Nat. Med. 17, 1231–1234. https://doi.org/10.1038/nm.2452

National Osteoporosis Foundation. Osteoporosis Exercise for Strong Bones. [WWW Document], 2017. URL https://www.nof.org/patients/fracturesfall-prevention/exercisesafe-movement/osteoporosis-exercise-for-strong-bones/ (accessed 3.3.18).

National Osteoporosis Foundation, 2008. Osteoporosis Fast Facts [WWW Document]. URL https://cdn.nof.org/wp-content/uploads/2015/12/Osteoporosis-Fast-Facts.pdf (accessed

9.20.17).
Nellans, K.W., Kowalski, E., Chung, K.C., 2012. The Epidemiology of Distal Radius Fractures. Hand Clin 28, 113–125. https://doi.org/10.1016/j.hcl.2012.02.001.The
Nguyen, A.M., Jacobs, C.R., 2013. Emerging role of primary cilia as mechanosensors in osteocytes. Bone. https://doi.org/10.1016/j.bone.2012.11.016
Nikander, R., Kannus, P., Rantalainen, T., Uusi-Rasi, K., Heinonen, A., Sievänen, H., 2010. Cross-sectional geometry of weight-bearing tibia in female athletes subjected to different exercise loadings. Osteoporos. Int. 21, 1687–1694. https://doi.org/10.1007/s00198-009-1101-0
Nikander, R., Sievänen, H., Uusi-Rasi, K., Heinonen, A., Kannus, P., 2006. Loading modalities and bone structures at nonweight-bearing upper extremity and weight-bearing lower extremity: A pQCT study of adult female athletes. Bone 39, 886–894. https://doi.org/10.1016/j.bone.2006.04.005
Nishiyama, K.K., Macdonald, H.M., Buie, H.R., Hanley, D.A., Boyd, S.K., 2009. Postmenopausal Women With Osteopenia Have Higher Cortical Porosity and Thinner Cortices at the Distal Radius and Tibia Than Women With Normal aBMD: An In Vivo HR-pQCT Study. J. Bone Miner. Res. 25, 882–890. https://doi.org/10.1359/jbmr.091020
Nishiyama, K.K., Macdonald, H.M., Hanley, D.A., Boyd, S.K., 2013. Women with previous fragility fractures can be classified based on bone microarchitecture and finite element analysis measured with HR-pQCT. Osteoporos. Int. 24, 1733–1740. https://doi.org/10.1007/s00198-012-2160-1
O'Connor, J.A., Lanyon, L.E., MacFie, H., 1982. The influence of strain rate on adaptive bone remodelling. J. Biomech. 15, 767–781. https://doi.org/10.1016/0021-9290(82)90092-6
Oldfield, R.C., 1971. The assessment and analysis of handedness: The Edinburgh inventory. Neuropsychologia. https://doi.org/10.1016/0028-3932(71)90067-4
Pahr, D.H., Zysset, P.K., 2016. Finite Element-Based Mechanical Assessment of Bone Quality on the Basis of In Vivo Images. Curr. Osteoporos. Rep. 14, 374–385. https://doi.org/10.1007/s11914-016-0335-y
Paul, G.R., Malhotra, A., Müller, R., 2018. Mechanical Stimuli in the Local In Vivo Environment in Bone: Computational Approaches Linking Organ-Scale Loads to Cellular Signals. Curr. Osteoporos. Rep. 16, 395–403. https://doi.org/10.1007/s11914-018-0448-6
Pennline, J.A., 2014. Evaluating Daily Load Stimulus Formulas in Relating Bone Response to Exercise. https://doi.org/NASA/TM-2014-218306
Pereira, A.F., Javaheri, B., Pitsillides, A.A., Shefelbine, S.J., 2015. Predicting cortical bone adaptation to axial loading in the mouse tibia. J. R. Soc. Interface 12. https://doi.org/10.1098/rsif.2015.0590
Petit, M.A., Beck, T.J., Lin, H.M., Bentley, C., Legro, R.S., Lloyd, T., 2004. Femoral bone structural geometry adapts to mechanical loading and is influenced by sex steroids: The Penn State Young Women's Health Study. Bone 35, 750–759. https://doi.org/10.1016/j.bone.2004.05.008
Pialat, J.B., Burghardt, A.J., Sode, M., Link, T.M., Majumdar, S., 2012. Visual grading of motion induced image degradation in high resolution peripheral computed tomography: Impact of image quality on measures of bone density and micro-architecture. Bone 50, 111–118. https://doi.org/10.1016/j.bone.2011.10.003
Popp, K.L., Turkington, V., Hughes, J.M., Xu, C., Unnikrishnan, G., Reifman, J., Bouxsein, M.L., 2019. Skeletal loading score is associated with bone microarchitecture in young

adults. Bone 127, 360–366. https://doi.org/10.1016/j.bone.2019.06.001
Poundarik, A.A., Wu, P.C., Evis, Z., Sroga, G.E., Ural, A., Rubin, M., Vashishth, D., 2015. A direct role of collagen glycation in bone fracture. J. Mech. Behav. Biomed. Mater. 52, 120–130. https://doi.org/10.1016/j.jmbbm.2015.08.012
Price, J.S., Sugiyama, T., Galea, G.L., Meakin, L.B., Sunters, A., Lanyon, L.E., 2011. Role of endocrine and paracrine factors in the adaptation of bone to mechanical loading. Curr. Osteoporos. Rep. 9, 76–82. https://doi.org/10.1007/s11914-011-0050-7
Rantalainen, T., Hoffrén, M., Linnamo, V., Heinonen, A., Komi, P. V., Avela, J., Nindl, B.C., 2011. Three-month bilateral hopping intervention is ineffective in initiating bone biomarker response in healthy elderly men. Eur. J. Appl. Physiol. 111, 2155–2162. https://doi.org/10.1007/s00421-011-1849-8
Razi, H., Birkhold, A.I., Weinkamer, R., Duda, G.N., Willie, B.M., Checa, S., 2015. Aging leads to a dysregulation in mechanically driven bone formation and resorption. J. Bone Miner. Res. 30, 1864–1873. https://doi.org/10.1002/jbmr.2528
Riggs, B.L., Melton, L.J., Robb, R.A., Camp, J.J., Atkinson, E.J., McDaniel, L., Amin, S., Rouleau, P.A., Khosla, S., 2008. A population-based assessment of rates of bone loss at multiple skeletal sites: Evidence for substantial trabecular bone loss in young adult women and men. J. Bone Miner. Res. 23, 205–214. https://doi.org/10.1359/jbmr.071020
Riggs, L., Melton, L., 1995. The worldwide problem of osteoporosis: lessons from epidemiology. Bone 17, 2–3.
Robling, A.G., Burr, D.B., Turner, C.H., 2001. Recovery periods restore mechanosensitivity to dynamically loaded bone. J. Exp. Biol.
Robling, A.G., Burr, D.B., Turner, C.H., 2000. Partitioning a daily mechanical stimulus into discrete loading bouts improves the osteogenic response to loading. J. Bone Miner. Res. https://doi.org/10.1359/jbmr.2000.15.8.1596
Rowlands, A. V., Stiles, V.H., 2012. Accelerometer counts and raw acceleration output in relation to mechanical loading. J. Biomech. 45, 448–454. https://doi.org/10.1016/j.jbiomech.2011.12.006
Rozental, T.D., Walley, K.C., Demissie, S., Caksa, S., Martinez-Betancourt, A., Parker, A.M., Tsai, J.N., Yu, E.W., Bouxsein, M.L., 2018. Bone Material Strength Index as Measured by Impact Microindentation in Postmenopausal Women With Distal Radius and Hip Fractures. J. Bone Miner. Res. 33, 621–626. https://doi.org/10.1002/jbmr.3338
Rubin, C.T., Lanyon, L.E., 1987. Osteoregulatory nature of mechanical stimuli: Function as a determinant for adaptive remodeling in bone. J. Orthop. Res. 5, 300–310. https://doi.org/10.1002/jor.1100050217
Rubin, C.T., Lanyon, L.E., 1985. Regulation of bone mass by mechanical strain magnitude. Calcif. Tissue Int. 37, 411–417. https://doi.org/10.1007/BF02553711
Rubin, C.T., Lanyon, L.E., 1984. Regulation of Bone Formation by Applied Dynamic Loads. J. Bone Jt. Surg. 66A, 397–402.
Rubin, L.A., Hawker, G.A., Peltekova, V.D., Fielding, L.J., Ridout, R., Cole, D.E., 1999. Determinants of peak bone mass: clinical and genetic analyses in a young female Canadian cohort. J. Bone Miner. Res. 14, 633–43. https://doi.org/10.1359/jbmr.1999.14.4.633
Ruimerman, R., Hilbers, P., Rietbergen, B. Van, Huiskes, R., 2005a. A theoretical framework for strain-related trabecular bone maintenance and adaptation 38, 931–941. https://doi.org/10.1016/j.jbiomech.2004.03.037
Ruimerman, R., Van Rietbergen, B., Hilbers, P., Huiskes, R., 2005b. The effects of trabecular-

bone loading variables on the surface signaling potential for bone remodeling and adaptation, in: Annals of Biomedical Engineering. pp. 71–78. https://doi.org/10.1007/s10439-005-8964-9

Sabet, F.A., Raeisi Najafi, A., Hamed, E., Jasiuk, I., 2016. Modelling of bone fracture and strength at different length scales: a review. Interface Focus 6, 20150055. https://doi.org/10.1098/rsfs.2015.0055

Salkeld, G., Cameron, I.D., Cumming, R.G., Easter, S., Seymour, J., Kurrle, S.E., Quine, S., 2000. Quality of life related to fear of falling and hip fracture in older women: A time trade off study. Br. Med. J. 320, 341–345. https://doi.org/10.1136/bmj.320.7231.341

Santos-Rocha, R.A., Oliveira, C.S., Veloso, A.P., 2006. Osteogenic index of step exercise depending on choreographic movements, session duration, and stepping rate. Br. J. Sports Med. 40, 860–866. https://doi.org/10.1136/bjsm.2006.029413

Scerpella, T.A., Bernardoni, B., Wang, S., Rathouz, P.J., Li, Q., Dowthwaite, J.N., 2016. Site-specific, adult bone benefits attributed to loading during youth: A preliminary longitudinal analysis. Bone 85, 148–159. https://doi.org/10.1016/j.bone.2016.01.020

Schaffler, M.B., Burr, D.B., 1988. Stiffness of compact bone: Effects of porosity and density. J. Biomech. 21, 13–16. https://doi.org/10.1016/0021-9290(88)90186-8

Schaffler, M.B., Cheung, W.Y., Majeska, R., Kennedy, O., 2014. Osteocytes: Master orchestrators of bone. Calcif. Tissue Int. 94, 5–24. https://doi.org/10.1007/s00223-013-9790-y

Scheiner, S., Pivonka, P., Hellmich, C., 2016. Poromicromechanics reveals that physiological bone strains induce osteocyte-stimulating lacunar pressure. Biomech. Model. Mechanobiol. 15, 9–28. https://doi.org/10.1007/s10237-015-0704-y

Schipilow, J.D., Macdonald, H.M., Liphardt, A.M., Kan, M., Boyd, S.K., 2013. Bone micro-architecture, estimated bone strength, and the muscle-bone interaction in elite athletes: An HR-pQCT study. Bone 56, 281–289. https://doi.org/10.1016/j.bone.2013.06.014

Schneider, P., Reiners, C., Cointry, G.R., Capozza, R.F., Ferretti, J.L., 2001. Bone quality parameters of the distal radius as assessed by pQCT in normal and fractured women. Osteoporos. Int. 12, 639–646. https://doi.org/10.1007/s001980170063

Schoeb, M., Hamdy, N.A.T., Malgo, F., Winter, E.M., Appelman-Dijkstra, N.M., 2020. Added Value of Impact Microindentation in the Evaluation of Bone Fragility: A Systematic Review of the Literature. Front. Endocrinol. (Lausanne). 11. https://doi.org/10.3389/fendo.2020.00015

Schriefer, J.L., Warden, S.J., Saxon, L.K., Robling, A.G., Turner, C.H., 2005. Cellular accommodation and the response of bone to mechanical loading. J. Biomech. https://doi.org/10.1016/j.jbiomech.2004.08.017

Schuit, S.C.E., Van Der Klift, M., Weel, A.E.A.M., De Laet, C.E.D.H., Burger, H., Seeman, E., Hofman, A., Uitterlinden, A.G., Van Leeuwen, J.P.T.M., Pols, H.A.P., 2004. Fracture incidence and association with bone mineral density in elderly men and women: The Rotterdam Study. Bone 34, 195–202. https://doi.org/10.1016/j.bone.2003.10.001

Schulte, F.A., Lambers, F.M., Kuhn, G., Müller, R., 2011. In vivo micro-computed tomography allows direct three-dimensional quantification of both bone formation and bone resorption parameters using time-lapsed imaging. Bone 48, 433–442. https://doi.org/10.1016/j.bone.2010.10.007

Schulte, F.A., Ruffoni, D., Lambers, F.M., Christen, D., Webster, D.J., Kuhn, G., Müller, R., 2013a. Local Mechanical Stimuli Regulate Bone Formation and Resorption in Mice at the

Tissue Level. PLoS One 8. https://doi.org/10.1371/journal.pone.0062172
Schulte, F.A., Zwahlen, A., Lambers, F.M., Kuhn, G., Ruffoni, D., Betts, D., Webster, D.J., Müller, R., 2013b. Strain-adaptive in silico modeling of bone adaptation - A computer simulation validated by in vivo micro-computed tomography data. Bone 52, 485–492. https://doi.org/10.1016/j.bone.2012.09.008
Shepherd, J.A., Schousboe, J.T., Broy, S.B., Engelke, K., Leslie, W.D., 2015. Executive Summary of the 2015 ISCD Position Development Conference on Advanced Measures From DXA and QCT: Fracture Prediction Beyond BMD. J. Clin. Densitom. 18, 274–286. https://doi.org/10.1016/j.jocd.2015.06.013
Siris, E.S., Chen, Y.-T., Abbott, T.A., Barrett-Connor, E., Miller, P.D., Wehren, L.E., Berger, M.L., 2004. Bone Mineral Density Thresholds for Pharmacological Intervention to Prevent Fractures. Arch. Intern. Med. 164, 1108–1112. https://doi.org/10.1001/archinte.164.10.1108
Sode, M., Burghardt, A.J., Kazakia, G.J., Link, T.M., Majumdar, S., 2010. Regional variations of gender-specific and age-related differences in trabecular bone structure of the distal radius and tibia. Bone. https://doi.org/10.1016/j.bone.2010.02.021
Sornay-Rendu, E., Boutroy, S., Duboeuf, F., Chapurlat, R.D., 2017. Bone Microarchitecture Assessed by HR-pQCT as Predictor of Fracture Risk in Postmenopausal Women: The OFELY Study. J. Bone Miner. Res. 32, 1243–1251. https://doi.org/10.1002/jbmr.3105
Sornay-Rendu, E., Munoz, F., Garnero, P., Duboeuf, F., Delmas, P.D., 2005. Identification of osteopenic women at high risk of fracture: The OFELY study. J. Bone Miner. Res. 20, 1813–1819. https://doi.org/10.1359/JBMR.050609
Srinivasan, S., Weimer, D.A., Agans, S.C., Bain, S.D., Gross, T.S., 2002. Low-magnitude mechanical loading becomes osteogenic when rest is inserted between each load cycle. J. Bone Miner. Res. 17, 1613–20. https://doi.org/10.1359/jbmr.2002.17.9.1613
Steck, R., Niederer, P., Knothe Tate, M.L., 2003. A finite element analysis for the prediction of load-induced fluid flow and mechanochemical transduction in bone. J. Theor. Biol. 220, 249–259. https://doi.org/10.1006/jtbi.2003.3163
Stewart, A.A.D., Hannan, J., 2000. Total and regional bone density in male runners, cyclists, and controls. Med Sci Sport. Exerc 32, 1373–1377. https://doi.org/0195-9131/00/3208-1373/0
Sugiyama, T., Meakin, L.B., Browne, W.J., Galea, G.L., Price, J.S., Lanyon, L.E., 2012. Bones' adaptive response to mechanical loading is essentially linear between the low strains associated with disuse and the high strains associated with the lamellar/woven bone transition. J. Bone Miner. Res. 27, 1784–1793. https://doi.org/10.1002/jbmr.1599
Tabensky, a, Duan, Y., Edmonds, J., Seeman, E., 2001. The contribution of reduced peak accrual of bone and age-related bone loss to osteoporosis at the spine and hip: insights from the daughters of women with vertebral or hip fractures. J. Bone Miner. Res. 16, 1101–7. https://doi.org/10.1359/jbmr.2001.16.6.1101
Taddei, F., Schileo, E., Helgason, B., Cristofolini, L., Viceconti, M., 2007. The material mapping strategy influences the accuracy of CT-based finite element models of bones: An evaluation against experimental measurements. Med. Eng. Phys. https://doi.org/10.1016/j.medengphy.2006.10.014
Theintz, G., Buchs, B., Rizzoli, R., Slosman, D., Clavien, H., Sizonenko, P.C., Bonjour, J.P., 1992. Longitudinal monitoring of bone mass accumulation in healthy adolescents: Evidence for a marked reduction after 16 years of age at the levels of lumbar spine and femoral neck in female subjects. J. Clin. Endocrinol. Metab. 75, 1060–1065. https://doi.org/10.1210/jc.75.4.1060

Tolly, B., Chumanov, E., Brooks, A., 2014. Ground reaction forces and osteogenic index of the sport of cyclocross. J. Sports Sci. 32, 1365–1373. https://doi.org/10.1080/02640414.2014.889839

Torrance, A.G., Mosley, J.R., Suswillo, R.F.L., Lanyon, L.E., 1994. Noninvasive loading of the rat ulna in vivo induces a strain-related modeling response uncomplicated by trauma or periostal pressure. Calcif. Tissue Int. https://doi.org/10.1007/BF00301686

Torres, A.M., Matheny, J.B., Keaveny, T.M., Taylor, D., Rimnac, C.M., Hernandez, C.J., 2016. Material heterogeneity in cancellous bone promotes deformation recovery after mechanical failure. Proc. Natl. Acad. Sci. U. S. A. 113, 2892–2897. https://doi.org/10.1073/pnas.1520539113

Troy, K.L., Edwards, W.B., 2018. Practical considerations for obtaining high quality quantitative computed tomography data of the skeletal system. Bone 110, 58–65. https://doi.org/10.1016/j.bone.2018.01.013

Troy, K.L., Edwards, W.B., Bhatia, V.A., Bareither, M. Lou, 2013. In vivo loading model to examine bone adaptation in humans: A pilot study. J. Orthop. Res. 31, 1406–1413. https://doi.org/10.1002/jor.22388

Troy, K.L., Grabiner, M.D., 2007. Off-axis loads cause failure of the distal radius at lower magnitudes than axial loads: A finite element analysis. J. Biomech. 40, 1670–1675. https://doi.org/10.1016/j.jbiomech.2007.01.018

Troy, K.L., Mancuso, M.E., Johnson, J.E., Wu, Z., Schnitzer, T.J., Butler, T.A., 2020. Bone adaptation in adult women is related to loading dose: A 12-month randomized controlled trial. J. Bone Miner. Res. jbmr.3999. https://doi.org/10.1002/jbmr.3999

Troy, K.L., Scerpella, T.A., Dowthwaite, J.N., 2018. Circum-menarcheal bone acquisition is stress-driven: A longitudinal study in adolescent female gymnasts and non-gymnasts. J. Biomech. 78, 45–51. https://doi.org/10.1016/j.jbiomech.2018.07.017

Tsubota, K. ichi, Suzuki, Y., Yamada, T., Hojo, M., Makinouchi, A., Adachi, T., 2009. Computer simulation of trabecular remodeling in human proximal femur using large-scale voxel FE models: Approach to understanding Wolff's law. J. Biomech. 42, 1088–1094. https://doi.org/10.1016/j.jbiomech.2009.02.030

Turner, C.H., 1998. Three rules for bone adaptation to mechanical stimuli. Bone 23, 399–407. https://doi.org/10.1016/S8756-3282(98)00118-5

Turner, C.H., Akhter, M.P., Raab, D.M., Kimmel, D.B., Recker, R.R., 1991. A noninvasive, in vivo model for studying strain adaptive bone modeling. Bone 12, 73–79. https://doi.org/10.1016/8756-3282(91)90003-2

Turner, C.H., Owan, I., Takano, Y., 1995. Mechanotransduction in bone: role of strain rate. Am. J. Physiol. Metab. 269, E438–E442. https://doi.org/10.1152/ajpendo.1995.269.3.E438

Turner, C.H., Robling, A.G., 2003. Designing exercise regimens to increase bone strength. Exerc. Sport Sci. Rev. 31, 45–50. https://doi.org/10.1097/00003677-200301000-00009

U.S. Dept. of HHS, 2004. Bone health and osteoporosis: a report of the Surgeon General, US Health and Human Services. U.S. Department of Health and Human Services, Office of the Surgeon General, Rockville, MD. https://doi.org/10.2165/00002018-200932030-00004

Umemura, Y., Ishiko, T., Yamauchi, T., Kurono, M., Mashiko, S., 1997. Five jumps per day increase bone mass and breaking force in rats. J. Bone Miner. Res. 12, 1480–1485. https://doi.org/10.1359/jbmr.1997.12.9.1480

Umemura, Y., Nagasawa, S., Honda, A., Singh, R., 2008. High-impact exercise frequency per week or day for osteogenic response in rats. J. Bone Miner. Metab. 26, 456–460.

https://doi.org/10.1007/s00774-007-0848-7
Unal, M., Akkus, O., 2015. Raman spectral classification of mineral- and collagen-bound water's associations to elastic and post-yield mechanical properties of cortical bone. Bone 81, 315–326. https://doi.org/10.1016/j.bone.2015.07.024
Unal, M., Creecy, A., Nyman, J.S., 2018. The Role of Matrix Composition in the Mechanical Behavior of Bone. Curr. Osteoporos. Rep. 16, 205–215. https://doi.org/10.1007/s11914-018-0433-0
Vainionpää, A., Korpelainen, R., Leppäluoto, J., Jämsä, T., 2005. Effects of high-impact exercise on bone mineral density: A randomized controlled trial in premenopausal women. Osteoporos. Int. 16, 191–197. https://doi.org/10.1007/s00198-004-1659-5
Van Der Meulen, M.C.H., Yang, X., Morgan, T.G., Bostrom, M.P.G., 2009. The effects of loading on cancellous bone in the rabbit. Clin. Orthop. Relat. Res. 467, 2000–2006. https://doi.org/10.1007/s11999-009-0897-4
van Rietbergen, B., Ito, K., 2015. A survey of micro-finite element analysis for clinical assessment of bone strength: The first decade. J. Biomech. 48, 832–841. https://doi.org/10.1016/j.jbiomech.2014.12.024
Vilayphiou, N., Boutroy, S., Sornay-Rendu, E., Van Rietbergen, B., Chapurlat, R., 2016. Age-related changes in bone strength from HR-pQCT derived microarchitectural parameters with an emphasis on the role of cortical porosity. Bone 83, 233–240. https://doi.org/10.1016/j.bone.2015.10.012
Vilayphiou, N., Boutroy, S., Sornay-rendu, E., Van rietbergen, B., Munoz, F., Delmas, P.D., Chapurlat, R., 2010. Finite element analysis performed on radius and tibia HR-pQCT images and fragility fractures at all sites in postmenopausal women. Bone 46, 1030–1037. https://doi.org/10.1016/j.bone.2009.12.015
Waarsing, J.H., Day, J.S., Van Der Linden, J.C., Ederveen, A.G., Spanjers, C., De Clerck, N., Sasov, A., Verhaar, J.A.N., Weinans, H., 2004. Detecting and tracking local changes in the tibiae of individual rats: A novel method to analyse longitudinal in vivo micro-CT data. Bone 34, 163–169. https://doi.org/10.1016/j.bone.2003.08.012
Wallace, B.A., Cumming, R.G., 2000. Systematic review of randomized trials of the effect of exercise on bone mass in pre- and postmenopausal women. Calcif. Tissue Int. 67, 10–8. https://doi.org/10.1007/s00223001089
Wang, M.Y., Salem, G.J., 2004. The relations among upper-extremity loading characteristics and bone mineral density changes in young women. Bone 34, 1053–1063. https://doi.org/10.1016/j.bone.2004.01.025
Warden, S.J., Carballido-gamio, J., Avin, K.G., Kersh, M.E., Fuchs, R.K., Krug, R., Bice, R.J., 2019. Adaptation of the proximal humerus to physical activity : A within-subject controlled study in baseball players. Bone 121, 107–115. https://doi.org/10.1016/j.bone.2019.01.008
Weaver, C.M., Gordon, C.M., Janz, K.F., Kalkwarf, H.J., Lappe, J.M., Lewis, R., O'Karma, M., Wallace, T.C., Zemel, B.S., 2016. The National Osteoporosis Foundation's position statement on peak bone mass development and lifestyle factors: a systematic review and implementation recommendations. Osteoporos. Int. 27, 1281–1386. https://doi.org/10.1007/s00198-015-3440-3
Webster, D., Schulte, F.A., Lambers, F.M., Kuhn, G., Müller, R., 2015. Strain energy density gradients in bone marrow predict osteoblast and osteoclast activity: A finite element study. J. Biomech. 48, 866–874. https://doi.org/10.1016/j.jbiomech.2014.12.009
Weeks, B.K., Beck, B.R., 2008. The BPAQ: A bone-specific physical activity assessment

instrument. Osteoporos. Int. 19, 1567–1577. https://doi.org/10.1007/s00198-008-0606-2
Weidauer, L., Minett, M., Negus, C., Binkley, T., Vukovich, M., Wey, H., Specker, B., 2014. Odd-impact loading results in increased cortical area and moments of inertia in collegiate athletes. Eur. J. Appl. Physiol. 114, 1429–1438. https://doi.org/10.1007/s00421-014-2870-5
Willems, H.M.E., van den Heuvel, E.G.H.M., Schoemaker, R.J.W., Klein-Nulend, J., Bakker, A.D., 2017. Diet and Exercise: a Match Made in Bone. Curr. Osteoporos. Rep. 15, 555–563. https://doi.org/10.1007/s11914-017-0406-8
Willett, T.L., Sutty, S., Gaspar, A., Avery, N., Grynpas, M., 2013. In vitro non-enzymatic ribation reduces post-yield strain accommodation in cortical bone. Bone 52, 611–622. https://doi.org/10.1016/j.bone.2012.11.014
Wong, S.L., 2016. Grip strength reference values for Canadians aged 6 to 79: Canadian Health Measures Survey, 2007 to 2013.
Wu, G., Van Der Helm, F.C.T., Veeger, H.E.J., Makhsous, M., Van Roy, P., Anglin, C., Nagels, J., Karduna, A.R., McQuade, K., Wang, X., Werner, F.W., Buchholz, B., 2005. ISB recommendation on definitions of joint coordinate systems of various joints for the reporting of human joint motion - Part II: Shoulder, elbow, wrist and hand. J. Biomech. 38, 981–992. https://doi.org/10.1016/j.jbiomech.2004.05.042
Xu, F., Teitelbaum, S.L., 2013. Osteoclasts: New Insights. Bone Res. 1, 11–26. https://doi.org/10.4248/BR201301003
Xue, S., Kemal, O., Lu, M., Lix, L.M., Leslie, W.D., Yang, S., 2020. Age at attainment of peak bone mineral density and its associated factors: The National Health and Nutrition Examination Survey 2005–2014. Bone 131, 115163. https://doi.org/10.1016/j.bone.2019.115163
Yang, P.F., Kriechbaumer, A., Albracht, K., Sanno, M., Ganse, B., Koy, T., Shang, P., Brüggemann, G.P., Müller, L.P., Rittweger, J., 2015. On the relationship between tibia torsional deformation and regional muscle contractions in habitual human exercises in vivo. J. Biomech. 48, 456–464. https://doi.org/10.1016/j.jbiomech.2014.12.031
Yang, P.F., Sanno, M., Ganse, B., Koy, T., Brüggemann, G.P., Müller, L.P., Rittweger, J., 2014. Torsion and antero-posterior bending in the in vivo human tibia loading regimes during walking and running. PLoS One 9. https://doi.org/10.1371/journal.pone.0094525
Zadpoor, A.A., Nikooyan, A.A., 2011. The relationship between lower-extremity stress fractures and the ground reaction force: A systematic review. Clin. Biomech. 26, 23–28. https://doi.org/10.1016/j.clinbiomech.2010.08.005
Zebaze, R.M.D., Jones, A., Knackstedt, M., Maalouf, G., Seeman, E., 2007. Construction of the femoral neck during growth determines its strength in old age. J. Bone Miner. Res. 22, 1055–1061. https://doi.org/10.1359/jbmr.070329
Zhao, R., Zhang, M., Zhang, Q., 2017. The Effectiveness of Combined Exercise Interventions for Preventing Postmenopausal Bone Loss: A Systematic Review and Meta-analysis. J. Orthop. Sport. Phys. Ther. 47, 241–251. https://doi.org/10.2519/jospt.2017.6969
Zhao, R., Zhao, M., Zhang, L., 2014. Efficiency of Jumping Exercise in Improving Bone Mineral Density Among Premenopausal Women: A Meta-Analysis. Sport. Med. https://doi.org/10.1007/s40279-014-0220-8